Quasi-Optical Components
for Millimeter and Submillimeter Waves

Thesis by

Jung-Chih Chiao

喬 榮 治

Thesis Advisor: Professor David B. Rutledge

In Partial Fulfillment of the Requirements

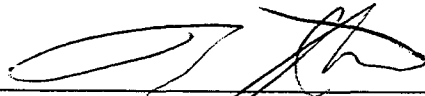for the Degree of

Doctor of Philosophy
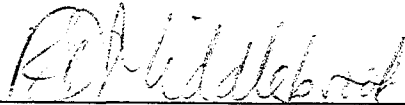
California Institute of Technology

Pasadena, California
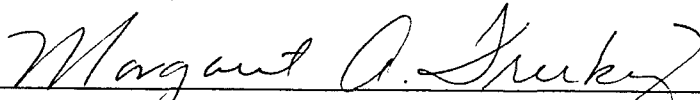
1996

(Submitted September 20, 1995)

ia

The dissertation of Jung-Chih Chiao is approved.

Professor Tatsuo Itoh, University of California, Los Angeles

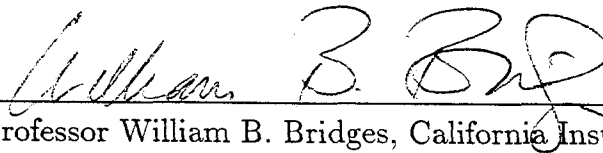Professor R. David Middlebrook, California Institute of Technology

Dr. Margaret A. Frerking, Jet Propulsion Laboratory, NASA

Professor S. James Allen, University of California, Santa Barbara

Professor William B. Bridges, California Institute of Technology

Professor David B. Rutledge, California Institute of Technology
Committee Chair

California Institute of Technology, Pasadena, California
September 20, 1995

To My Parents

獻給我的父母

You are the Wind Beneath My Wings.

您們是我翼下之風

Acknowledgements

I would like to express my gratitude to my thesis advisor, Professor David Rutledge, for his encouragement, unconditional support, and his belief in me to work in his research group. Not only his wealth of ideas, creative thinking and enthusiasm, but also his friendliness and generosity made this five-year journey very fulfilling and rewarding. I would also like to express my appreciation to Professor William Bridges. His extensive knowledge, enthusiasm on teaching and caring personality enriched my learning experiences at CalTech.

I would like to thank all the terrific people I have worked with for the past five years, not only for their helps and technical discussions, but also for their good friendships which I will treasure the most forever. It is difficult to acknowledge all of them here, so I have dedicated a section in the end of each chapter (page 120, 207 and 249) to acknowledge their contributions in my thesis work. In addition, I would like to express my appreciation to Mr. Kent Potter for providing his valuable knowledge and experience on equipments and fabrications, and Dr. Yong Guo for teaching me fabrication fundamentals.

There is no word sufficient enough to describe my gratitude to all the friendship I received over these five years, instead, I will list all their names here and say "Thank you all very much for being there for me."

For all the good friends related to the CalTech MMIC group, I would like to thank Kent Pottter; Irene Loera; the Rutledge family: Dale, Rob, Kate and Allen; Dr. Bobby Weikle and Dee Weikle; Dr. Jon Hacker and Betty Wu Hacker; Dr. Scott Wedge and Cindy Wedge; Dr. Phil Stimson and Tric Stimson; Dr. Victor Lubecke and Dr. Olga Borić-Lubecke; Michael De Lisio and Lisa De Lisio; Dr. Yong Guo and Yijin Wang Guo; Dr. Moonil Kim and Heejoa Kim; Alina Moussessian; Dr. Gabriel Rebeiz; Karen Lee; David Haub; Shijie Li; Cheh-Ming Liu; John Davis and Theresa Davis; Polly Preventza; and Dr. Minoru Saga. I also thank Dr. Jongsuck Bae; Dr. Koji Mizuno; Andrea Markelz; Yongjun

The way it can be spoken is not the way itself.
The thing it can be named is not the thing itself.

– Lao Tse, 604-531 B.C.

Quasi-Optical Components
for Millimeter and Submillimeter Waves

Abstract

Power-combining schemes involving planar grids of solid-state devices or passive elements quasi-optically coupled in free space are an efficient means of combining power that makes them ideal for millimeter/submillimeter-wave applications by eliminating waveguide sidewall losses and machining difficulties. Three quasi-optical components including grid frequency multipliers, microswitch beam-steering grids and evanescent-wave couplers are presented.

A terahertz grid frequency doubler using a 6×6 diode-grid periodically loaded with planar Schottky diodes has been developed. A peak output power of $330\,\mu$W was measured at $1.00\,$THz for 2.42-μs 500-GHz input pulses with a peak power of $3.3\,$W.

The microswitch beam-steering grid has potential advantages over mechanical-scanning devices or active beam-steering reflectors based on diode-grids such as lower losses and simple control circuits at submillimeter wavelengths. Micromechanical electrostatically-controlled SiO_xN_y-membrane switches have been fabricated on silicon wafers to provide binary reactance control. Simulations predict that a 4-bit controlled 10-layer microswitch beam-steering grid can have a phase-shift resolution of $22.5°$ over $360°$ with a maximum loss of $1.6\,$dB and a maximum phase error of $5°$ at $240\,$GHz.

The metal-mesh evanescent-wave couplers have been demonstrated to have wider bandwidths and larger modulations than Fabry-Perot couplers. The evanescent-wave coupling effect has been studied and used to increase the efficiency of an optically-controlled amplitude-modulator at $56.5\,$GHz.

Contents

Chapter 1

Introduction

Millimeterwave (30-300 GHz) and submillimeterwave (300 GHz-3 THz) systems have been attracting a growing interest in both academic studies and industrial applications. Although the technologies have not been well developed at the present time, the advantages and the expanding demands of the use of this portion of the electromagnetic spectrum have shown promise of utilizing these systems in the future [1]. The applications vary from personal communication tools [2] and automobile crash-avoidance systems [3], to remote-sensing of the earth's surface [4] and studying emission spectra of distance celestial bodies [5]. The shorter wavelengths in the millimeterwave and submillimeterwave bands allow the use of smaller and lighter components than for microwave bands, which makes possible to develop compact and portable systems, especially for air-borne and space-borne applications. They also provide broader bandwidths and higher resolution for radars and imaging systems. In addition, the atmosphere attenuation of millimeter waves is relatively low compared to infrared and optical wavelengths [6], which allows to build cameras and radars to penetrate clouds, fog and dust for remote-sensing, missile-seeking, aircraft-guiding and automobile collision-avoidance applications.

1.1 QUASI-OPTICAL SYSTEMS

Conventional millimeterwave and submillimeterwave components are based on metal cavities, waveguides and horns along with vacuum tubes or gas lasers

as sources. Although they are adequate for applications, they are usually heavy, bulky, expensive and have high losses, and also require high-power supplies and intensive manual labor for machining. Recent achievements of high-speed solid-state device technologies have made possible to develop compact, lightweight and reliable millimeter/submillimeter-wave systems. High-speed transistors, which can be operated up to 300 GHz, and diodes, which can be operated up to 1 THz, have been routinely fabricated [7]. These solid-state devices, due to the small sizes for small operating wavelengths, are inherently low-power devices. In an attempt to increase the limited output powers, a variety of power-combining methods have been developed [8]. Many of these techniques are based on scaled-down microwave circuits, transmission lines such as waveguides and microstrip lines, and resonant cavities [9]. Conventional power-combining techniques have serious limitations at higher frequencies, though they have reached high combining efficiencies at microwave frequencies. At higher frequencies, the radiation and conduction losses become too high for sensitive systems and degrade the efficiencies. The machining for single-mode waveguides become more difficult and expensive as frequencies increase. The power-combining based on resonant cavities also result in a narrow bandwidth and a limited number of devices, which make high-power operation impractical.

In 1986, Mink [10] suggested the use of quasi-optical techniques for solid-state power-combining. A grid of many planar devices quasi-optically coupled in free space does not require the construction of single-mode waveguides and can potentially overcome the power limits of high-speed solid-state devices by distributing powers among many devices. Rutledge and Schwarz [11] first demonstrated the idea of integrating solid-state devices into a periodic grid as a multimode detector array. The approach of using quasi-optical grids to combine power provides many advantages, and these advantages become more attractive when the frequencies increase, including higher powers, higher frequencies, less losses,
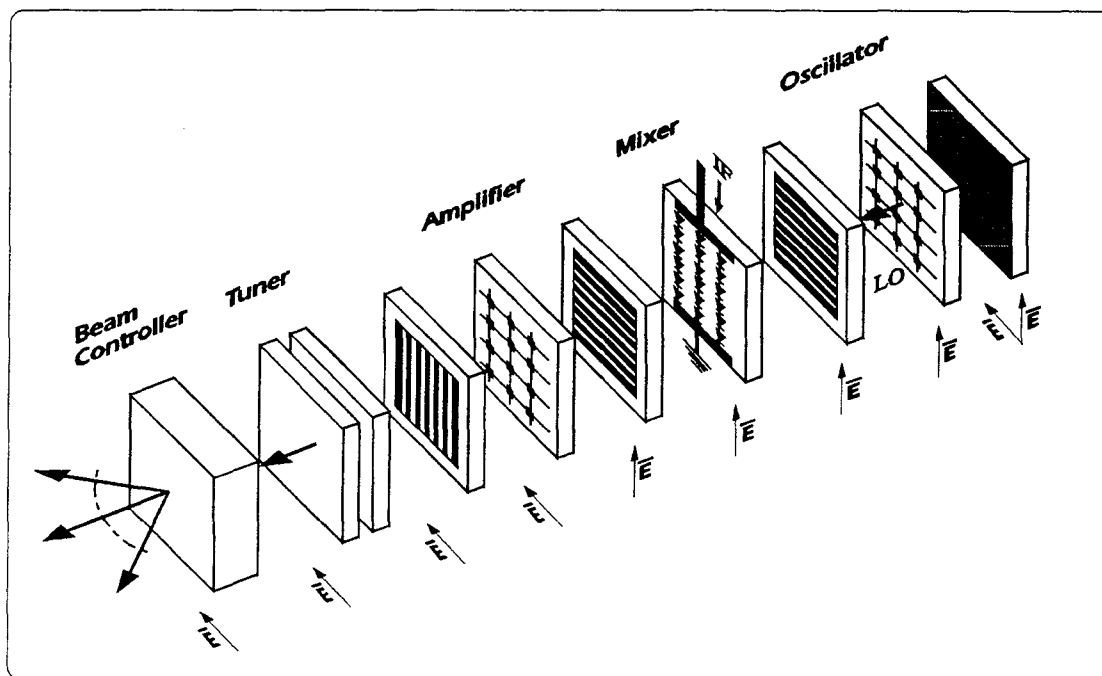
Fig. 1.1 A quasi-optical transmitter.

easier tuning, simpler analysis, monolithic feature, and better failure tolerance. A detailed description of these advantages will be discussed in Chapter 2.

Millimeterwave and submillimeterwave quasi-optical systems look more like optical systems, which the waves propagate and combine in free space, except the components. Figure 1.1 shows the configuration of a quasi-optical transmitter. The typical components are either active surfaces such as periodic circuits (grids) fabricated on dielectric substrates loaded with active devices, or passive lumped elements such as metal meshes on dielectric substrates. A variety of grids have been demonstrated including detectors [11], phase-shifters [12,13], frequency multipliers [14,15], oscillators [16,17], amplifiers [18-20], mixers [21], beam controllers [22,23], switches [24], voltage controlled oscillators (VCOs) [25] couplers [26], and power oscillators [27]. These grids show promising signs of constructing a complete quasi-optical system and solve many of the problems

which plague other power-combining methods. However, these grids, mostly have been demonstrated at microwave or millimeterwave frequencies, face new problems of their own at higher frequencies such as loss reductions and performance enhancements. In this thesis, a THz frequency doubler will be discussed to demonstrate the availability of LO sources and the feasibility of frequency multiplication at submillimeter wavelengths. A micromechanical membrane-switch beam-steering grid will be presented to demonstrate the feasibility of lower-loss grid phase-shifters at millimeter and submillimeter wavelengths. A metal-mesh evanescent-wave coupler will also be presented for demonstration of efficient beam-modulations.

1.2 QUASI-OPTICAL THz FREQUENCY MULTIPLIERS

The demand for solid-state local oscillators at submillimeter wavelengths has been steadily increasing for applications in radio astronomy [28,29] and remote sensing of the atmosphere [30]. The interest for terahertz applications has raised a strong need for submillimeter-wave receivers, mixers and sources, especially tunable high-power sources used as the local oscillators for heterodyne submillimeter-wave receivers. Traditional high-power sources in the THz region such as gas lasers and vacuum-tube oscillators are not suitable for this purpose due to their large sizes, high-voltage supplies, short lifetimes and small tuning ranges. However, frequency multipliers such as Schottky diode multipliers can be used to generate the required terahertz frequencies from lower-frequency solid-state tunable signal sources such as Gunn-diode oscillators.

Conventional diode multipliers have mostly been single-diode structures, typically consisting of a Schottky varactor diode placed in a crossed-waveguide mount with a whisker contact [31]. A grid of many planar diodes quasi-optically coupled in free space does not require the construction of single-mode waveguides and can potentially overcome the low-power inherent with solid-state devices operating at submillimeter wavelengths. Figure 1.2 shows the concept. Figure 1.3
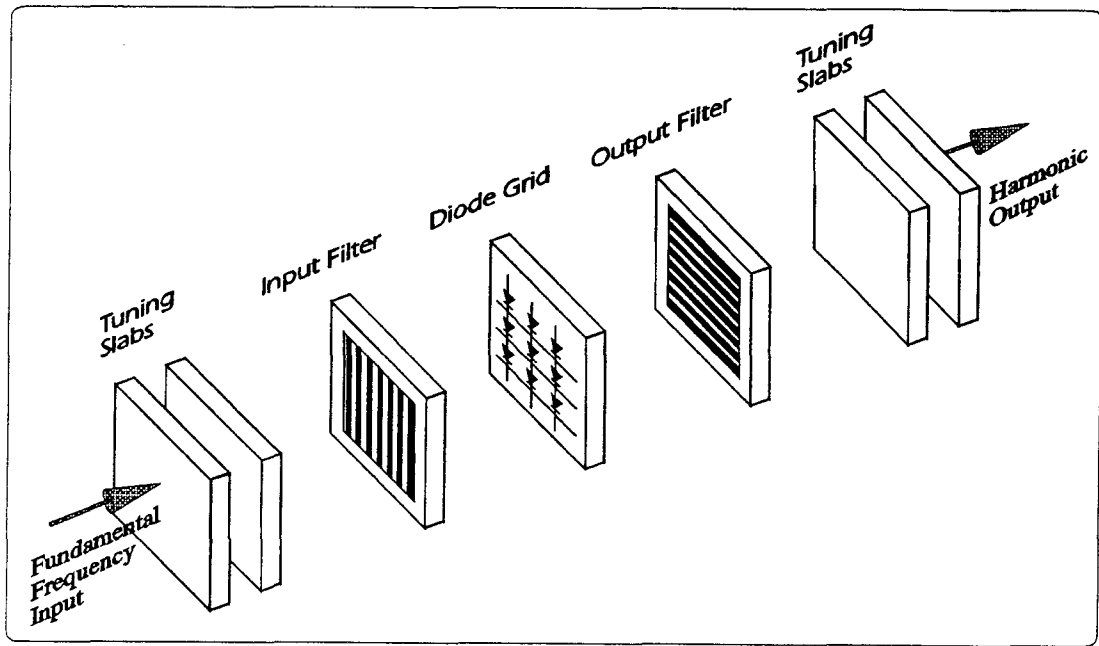
Fig. 1.2 The grid-multiplier concept. The fundamental wave enters on the left as a beam, passes through a filter, and is incident on the diode grid. The grid acts as a nonlinear surface and produces a beam at the harmonic frequencies, which passes through the output filter on the right.
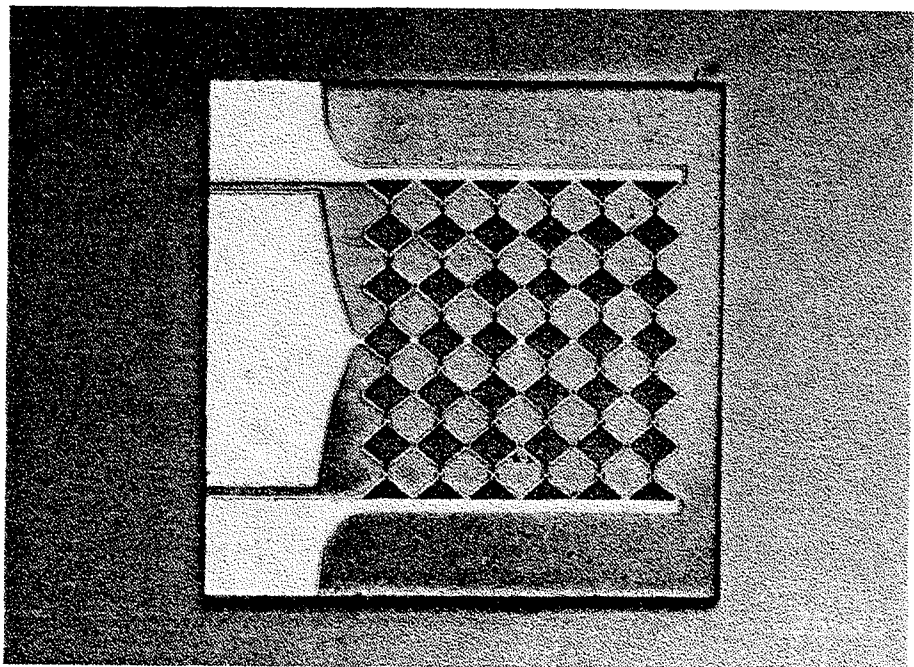
Fig. 1.3 The THz grid frequency doubler. It is a 6×6 array. The adjacent bow-ties are not connected except the center row. The diodes in the top and bottom halves of the grid have opposite orientations.

shows the THz planar Schottky diode grid used as a frequency doubler. Previous efforts of quasi-optical frequency multipliers have demonstrated the feasibility and advantages (Table 1.1).

Multipliers	Output Frequency	No. of diodes	Output power	Efficiency
Doubler [14,32]	66 GHz	760 Schottky	0.5 W	9.5%
Tripler [33]	99 GHz	6000 BIN*	2.16 mW	24%
Tripler [15,34]	99 GHz	3100 SQBV†	5 W	2%
Tripler [15,34]	99 GHz	3000 MQBV‡	1.25 W	0.7%
Doubler [Chapter 2]	1.00 THz	36 Schottky	330 μW	0.1%

Table 1.1 Achievements of quasi-optical frequency multipliers.

* BIN: barrier-intrinsic-N^+.

† SQBV: Schottky-quantum-barrier varactor.

‡ MQBV: multi-quantum-barrier varactor.

This work is a joint effort among the MMIC group at CalTech, the Semiconductor Devices Laboratory at the University of Virginia (UVA), and the Center for Free-Electron Laser Studies at the University of California, Santa Barbara (UCSB). CalTech is responsible for design, UVA is responsible for fabrication of the diode grids and the measurements are done at UCSB using the free-electron laser.

This is the first attempt to use the terahertz planar Schottky diodes developed successfully at UVA [35] on quasi-optical grids. These diode-grids, which are originally designed for the use as sideband generators [36], have been fabricated. We decided to test these diode-grids as frequency multipliers to verify the feasibility of using diode-grids for terahertz frequency multiplication. It should be emphasized that these diode-grids are originally designed for sideband generators, therefore, some design features may not be optimal or proper for the use as frequency multipliers. For example, flipping the diode orientations above and

below the center row of the grid for biasing is inappropriate for multipliers because the cancellation of electric fields from the two halves in the far field creates an undesired null in the center of the output beam.

A peak output power of $330\,\mu$W is measured at $1.00\,$THz for 2.42-μs 500-GHz input pulses with a peak power of $3.3\,$W without any impedance tuning. The relationship between the input power at $500\,$GHz and the output power at $1\,$THz follows a square-power relationship. The diode-orientations designed for sideband-generator application result in a null in the center of the output beam for multiplier applications and measurements show that only 10% of the total radiated power is received by the detector due to the null in the output beam. It should be possible to increase the output powers and multiplication efficiencies by correcting the diode-orientations since these diodes have not saturated yet.

1.3 QUASI-OPTICAL BEAM-STEERING GRIDS

A complete structure of quasi-optical transmitter or receiver requires electronic beam-controllers for beam steering, focussing and switching in the applications such as radars for aircraft-guiding and missile-seeking; automobile radars for collision avoidance systems; and millimeterwave imaging cameras which allow to see through fog. Electronic-scanning systems are more reliable, flexible and have higher scanning-speeds than mechanical scanning systems. The high-speed capability of electronic-scanning devices allows the beam to shift rapidly, so it can track or image more targets simultaneously. Conventional waveguide beam-steering systems are heavy, bulky and usually require complicated control circuits. Previous efforts of using quasi-optical monolithic diode-grids as electronic millimeterwave beam-controllers show impressive results (Table 1.2) and the advantages of lower losses and high-speed control.

Beam-steerer type	Frequency	No. of diodes	Phase shift	Reflection loss
Reflection * [12,37]	93 GHz	1600 SV† diodes	70°	6.5 dB
Reflection * [13,38]	120 GHz	7168 SV† diodes	70°	3.5 dB
Reflection * [39]	60 GHz	7100 SV† diodes	130°	2.7 dB

Table 1.2 Achievements of quasi-optical diode-grid beam steerers.

* single layer.

† SV: Schottky varactor.

Extending the quasi-optical diode-grid method for beam-control to higher frequencies faces technical challenge to reduce losses caused by the series resistances of the diodes. Past experiences show that it is extremely important to keep series resistances of diodes as low as possible to reduce losses. However, the series resistances of Schottky diodes increase when the operating frequencies increase and the series resistances will cause more serious loss problems at sub-
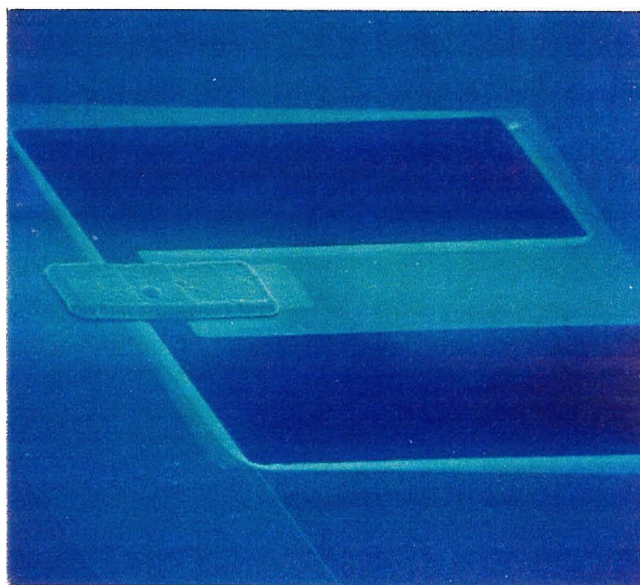
Fig. 1.4 A SiO_xN_y-membrane microswitch on silicon. By applying bias on the electrodes, the cantilever bridge will experience an electrostatic force to bend the membrane downward until the electrodes contact. The stress of the membrane will separate the contacts when the bias is removed.

millimeter wavelengths. Therefore, exploring the possibility of a novel method using passive elements instead of diodes is the main purpose of this work.

Micromechanical membrane-switches (Figure 1.4) offer the advantages of simple control circuits and very low series resistances because of the pure metal-
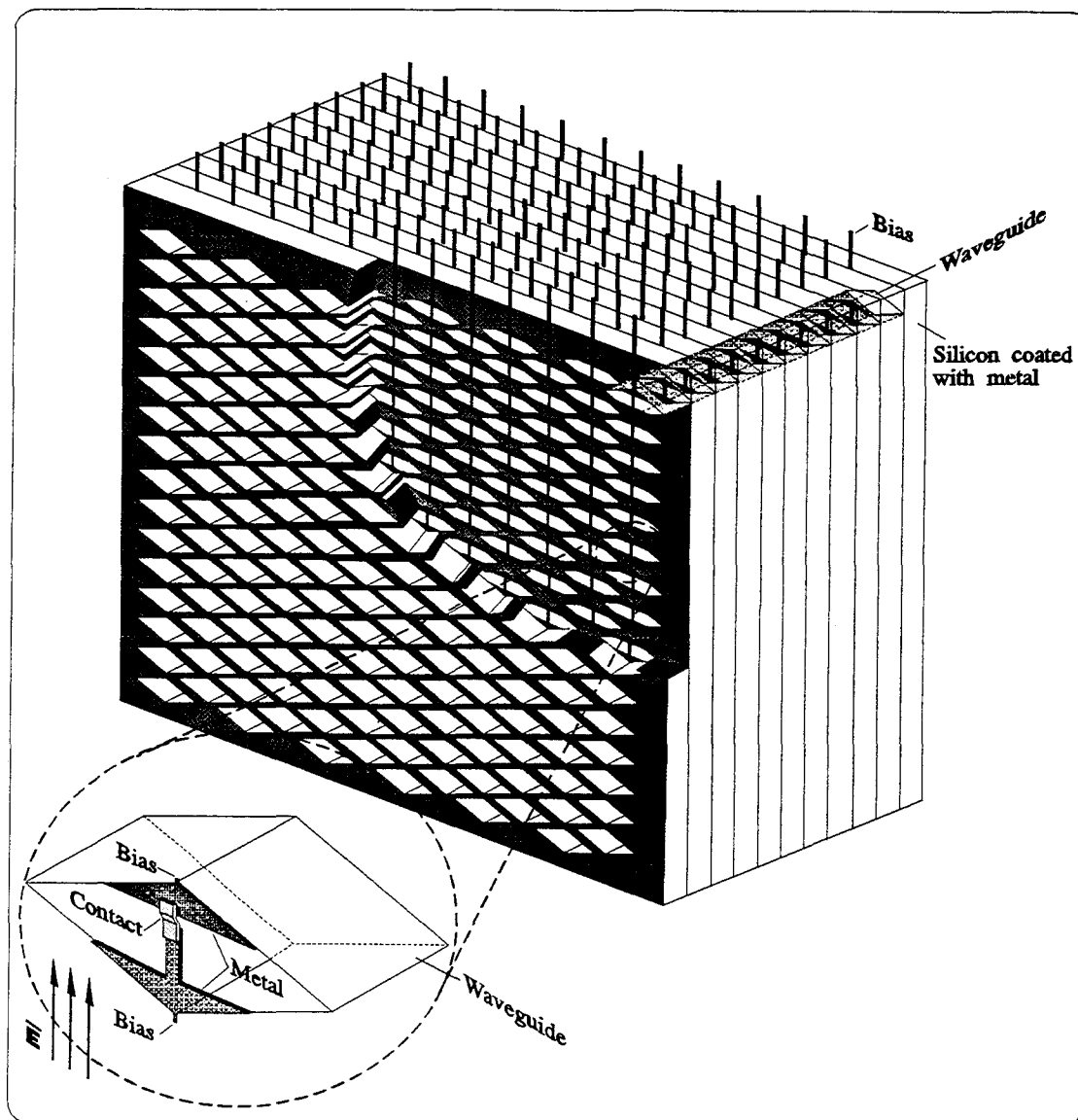
Fig. 1.5 The concept of a microswitch beam-steering grid. The incident waves enter on the left, pass through several layers of microswitches and waveguides, where different settings of microswitches add different phase shifts to the propagating waves, and transmit with deflected angle on the right. The microswitches are electrostatically controlled.

to-metal contacts. We proposed to utilize the binary changes of reactances by switching the microswitches in an array to establish a discrete transmission-type phase shifter. A multi-layer structure (Figure 1.5) provides higher resolutions of phase-shifts with low losses, which can be minimized by adjusting the spacing between layers and the unit-cell patterns. Simulations predict that a 4-bit controlled 10-layer microswitch beam-steering grid can have a phase-shift resolution of 22.5° over 360° with a maximum loss of 1.6 dB at 240 GHz, under the assumption of having a 2-Ω RF-conduction-loss resistance on each microswitch.

1.4 QUASI-OPTICAL EVANESCENT-WAVE COUPLERS

Quasi-optical amplitude controllers provide functions such as amplitude modulations, beam switching and feedback elements to provide the required feedback to reach oscillation conditions for quasi-optical coherent power-combining. Fabry-Perot interferometers have been widely used as tunable couplers and filters at millimeter and submillimeter wavelengths. These couplers consist of two reflectors and make use of interference between propagating waves to change their coupling coefficients. The large and rapid changes of the coupling coefficients with frequency result in a narrow bandwidth [40].

We proposed metal-mesh evanescent-wave couplers (Figure 1.6) which make use of the coupling effect of evanescent waves to control transmissions. The evanescent waves are induced by an incident wave on the meshes, and decay quickly away from the mesh, normally less than $\lambda/20$ from the surface [41], therefore, in contrast to a Fabry-Perot interferometer, the coupling coefficient of the evanescent wave coupler can be significantly changed by small adjustments of spacing. In principle, this type of couplers should have wider bandwidth because the transmission properties of the couplers depend primarily on the mesh parameters.

This work is a joint effort between Dr. Jongsuck Bae and Dr. Koji Mizuno's group, where the couplers were fabricated and tested, at the Research Institute of

Electrical Communication in Tohoku University, Sendai, Japan; and the MMIC group at CalTech.

Metal-mesh evanescent-wave couplers have been demonstrated as quasi-optical amplitude-modulators for millimeter wavelengths. The transmittance of a capacitive metal-mesh evanescent-wave coupler can be changed from 93% to 10% at 56 GHz by moving a tuning plate only $\lambda/21.4$. The coupling coefficient of a capacitive coupler can vary more 30% over a 13% frequency range by adjusting the spacing less than $\lambda/40$. A model is presented to explain the relationship
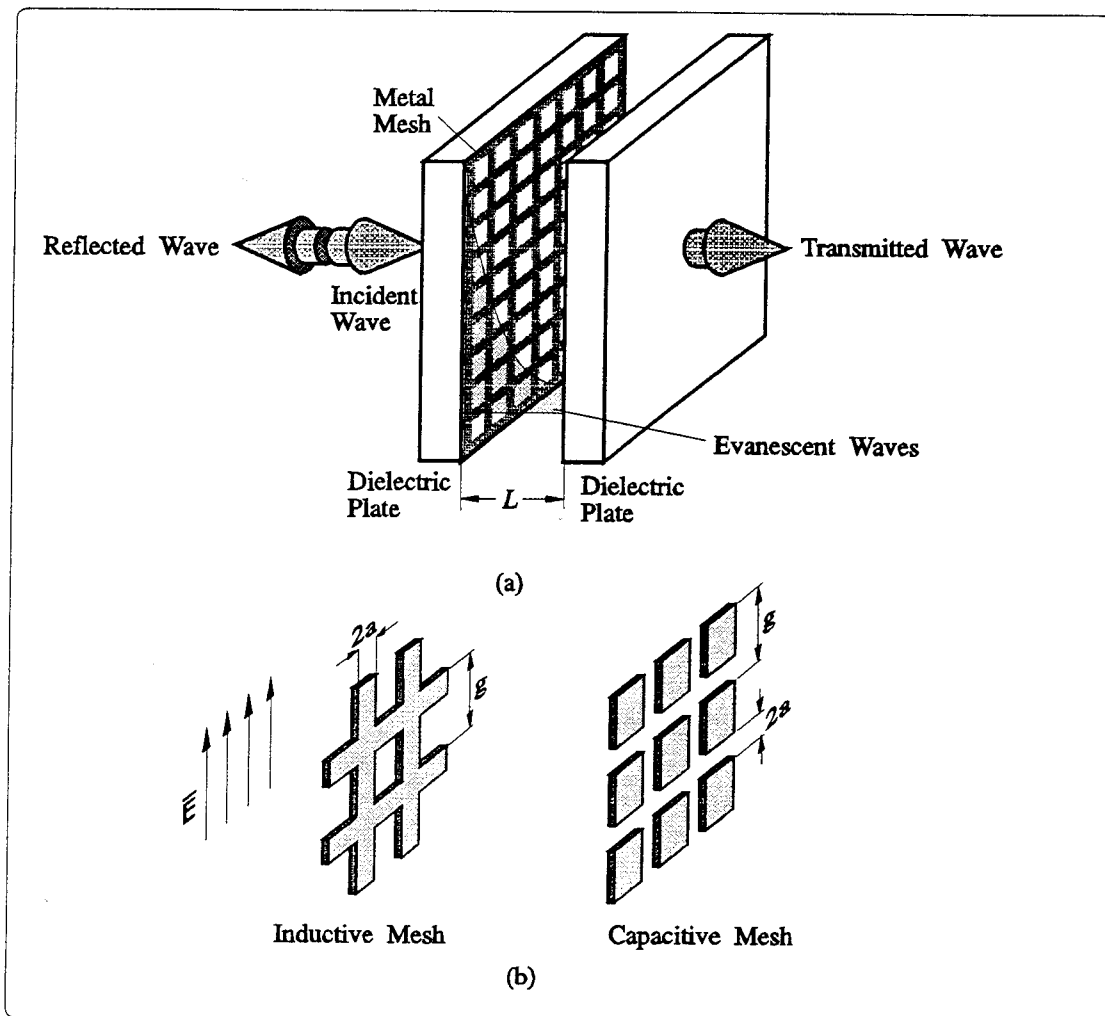
Fig. 1.6 (a) Configuration of a metal-mesh evanescent-wave coupler. (b) Capacitive meshes and inductive meshes.

between the effective dielectric constant and the evanescent-wave coupling effect. This model also explains some discrepancies between the conventional mesh theory and the measurements.

Design principles are presented to reach maximum amplitude modulations considering the mesh parameters, resonant frequencies and the thickness of the tuning plates. In a capacitive metal-mesh evanescent-wave coupler with optimal mesh parameters, changing the silicon plate thickness from 1 mm to 3 mm to tune the resonant frequencies, the coupling coefficient at the operating frequency can be increased from 45% to 70% for a variation of spacing less than $\lambda/100$. The model and design principles presented at millimeter wavelengths, achieve good agreements with measurements, provide useful information for designing a submillimeter-wave coupler.

An optical-controlled metal-mesh evanescent-wave coupler is also demonstrated. By using a laser diode to modulate the dielectric constant of silicon with the existence of the evanescent-wave coupling effect, a maximum modulation of 13% is achieved at 56.5 GHz. To compare, the modulation is only 0.6% without the evanescent-wave coupling effect using the same power of light illumination.

1.5 Organization of The Thesis

This thesis consists of three main sections. Each chapter is concerned with a different project. Chapter 2 discusses terahertz quasi-optical frequency multipliers using Schottky diode grids. Chapter 3 presents a novel approach to develop a beam-steering grid using micromechanical membrane-switches. Chapter 4 demonstrates metal-mesh evanescent-wave couplers at millimeter wavelengths. Due to the distinctive characteristics of each chapter, the motivations, previous achievements, approaches, conclusions and suggestions for future research will be discussed individually in each chapter. The general idea of quasi-optical approaches such as the advantages and the methods of analysis, the unit-cell methods, will be given in Chapter 2.

In **chapter 2**, terahertz quasi-optical grid frequency-doublers have been investigated by using Schottky diode-grids which were originally designed as sideband generators. Terahertz applications; the achievements of terahertz sources; conventional waveguide-multipliers and the achievements; and the concept, advantages and previous efforts of quasi-optical multipliers are first reviewed to emphasize the importance of developing quasi-optical submillimeter-wave frequency multipliers. The idea of terahertz sideband generators is presented for the original motivation of developing planar Schottky diode grids. Then the structures, advantages, problems and a complete fabrication procedure of surface-channel planar Schottky diodes are introduced.

The design approach (linear analysis), the unit-cell method, and the calculations for embedding impedances of grid structures are discussed and the results of linear analysis on the grid multipliers are shown. The results of DC tests and RF measurements are presented. The nulls in the output beam, due to the improper diode orientations, are shown and verified by theory. The efforts of using a dielectric lens to correct the output patterns; impedance tunings and biasing effects are shown as an endeavor to increase the multiplication efficiencies. The current saturation, RF current measurements, failure of diodes and nonlinear analysis using harmonic-balance methods are discussed providing information for future improvements.

Suggestions of future works include the improvement of the grid design, diode structures, and experimental setup. A new design of 12 × 12 arrays and the estimated output patterns are shown. The possibility of using other devices rather than Schottky varistor diodes is also discussed including a new grid frequency tripler using InAs quantum-well devices.

In **chapter 3**, a review on quasi-optical diode-grid beam-controllers is first given. Then the structures of micromechanical membrane-switches and the approach of using these microswitches on beam-steering grids are discussed. A

general system and the modelling method are shown. Two designs including practical considerations of using $\langle 110 \rangle$ and $\langle 100 \rangle$ orientation silicon wafers with anisotropic etchant KOH and EDP solutions, respectively, are presented.

Because of smaller wavelengths, submillimeter-wave beam-steering grids have TE_{10}-wave guided in a multi-layer vertical-wall rhombic-waveguide array with microswitches inside the waveguides to provide the required shunt reactances for phase-shifting. The dimensions and spacings of rhombic waveguides in the grids have been calculated to minimize the losses. Performance predictions, simulations and design principles are discussed for a 240-GHz beam-steering grid. For longer wavelengths, thin $\langle 100 \rangle$ silicon wafers are used for supporting the microswitches and the free space between layers is used for providing the proper electrical lengths. Performance predictions, simulations and design principles are discussed for a 44-GHz beam-steering grid.

Micromechanical SiO_xN_y-membrane switches are fabricated on $\langle 100 \rangle$ orientation silicon wafers to demonstrate the feasibility of fabricating long electrostatically-controlled binary switches on silicon. Rhombic waveguide arrays are also made by using $\langle 110 \rangle$ orientation silicon wafers and anisotropic etching techniques to show that it is feasible to fabricate vertical-wall waveguides on silicon.

Finally, measurements are demonstrated for the designs of 44-GHz beam-steering grids to verify the simulations.

In **chapter 4**, metal-mesh evanescent-wave couplers have been demonstrated as quasi-optical amplitude-modulators at millimeter wavelengths. In this chapter, mechanical tunable metal-mesh evanescent-wave couplers are first studied to understand the evanescent-wave coupling effect; the dependence of the coupling effects on the mesh parameters, on the the spacings, and on the thickness of tuning slab; and the relationships between the coupling effects and the resonant frequencies. A more accurate model then is presented to modify the transmission-line equivalent-circuits taking the evanescent-wave effects into con-

sideration. Finally, we used the same model and design approaches to demonstrate a non-mechanical optical-controlled metal-mesh evanescent-wave coupler for amplitude modulations at millimeter wavelengths.

REFERENCES

[1] J.W. Mink and D.B. Rutledge, "Guest Editor's Overview of the Special Issue on Quasi-Optical Techniques," *IEEE Trans. Microwave Theory Tech.*, Vol. MTT-41, No. 10, pp. 1661-1663, Oct. 1993.

[2] R. Leyshon, "Millimeter Technology Gets a New Lease on Life," *Microwave Journal*, No. 3, pp. 26-35, March 1992.

[3] G.R. Huguenin, "Millimeter Wave Radar for Automobile Crash Avoidance Systems," *Proceedings of the International Conference on Millimeter and Submillimeter Waves and Applications*, SPIE Proceedings series, Vol. 2250, Jan. 1994.

[4] J.W. Waters and P.H. Siegel, "Applications of Millimeter and Submillimeter Technology to Earth's Upper Atmosphere: Results To Date and Potential for the Future," *The 4th International Symposium on Space Terahertz Technology*, Los Angeles, CA, March 1993.

[5] T.G. Phillips, "Developments in Submillimeterwave Astronomy," *The 19th International Conference on Infrared and Millimeter Waves in Sendai, Japan*, 1994.

[6] J.C. Wiltse, "Introduction and Overview of Millimeter Waves," *Infrared and Millimeter Waves*, Vol. 4, Chap. 1, K.J. Button, Ed., Academic Press, Inc., New York, 1979.

[7] R.A. York, "Quasi-Optical Power Combining Techniques," *Millimeter and Microwave Engineering for Communications and Radar*, J.C. Wiltse, Ed., Critical Reviews of Optical Science and Technology, Vol. CR54, pp. 63-97, 1994.

[8] K. Chang and C. Sun, "Millimeter-wave Power Combining Techniques," *IEEE Trans. on Microwave Theory and Tech.*, Vol. MTT-31, No. 2, pp. 91-107, Feb. 1983.

[9] K. Kurokawa, "The Single-Cavity Multiple-Device Oscillator," *IEEE Trans. on Microwave Theory and Tech.*, Vol. MTT-19, No. 10, pp. 793-801, Oct. 1971.

[10] J.W. Mink, "Quasi-Optical Power Combining of Solid-State Millimeter-Wave Sources," *IEEE Trans. on Microwave Theory and Tech.*, Vol. MTT-34, No. 2, pp. 273-179, Feb. 1986.

[11] D.B. Rutledge and S.E. Schwarz, "Planar Multimode Detector Arrays for Infrared and Millimeter-wave Applications," *IEEE J. Quantum Electronics*, Vol. QE-17, pp. 407-414, 1981.

[12] W. Lam, C. Jou, H. Chen, K. Stolt, N. Luhmann, Jr., and D. Rutledge, "Millimeter-wave Diode-Grid Phase-Shifters," *IEEE Trans. on Microwave Theory and Techniques*, pp. 902-907, No. 5, May 1988.

[13] L.B. Sjogren, H.L. Liu, X.H. Qin, C.W. Domier, N.C. Luhmann, Jr., "Phased Array Operation of a Diode Grid Impedance Surface," *IEEE Trans. on Microwave Theory and Techniques*, Vol. MTT-42, No. 4, pp. 565-572, April 1994.

[14] C.F. Jou, W.W. Lam, H.Z. Chen, K.S. Stolt, N.C. Luhmann, Jr. and D.B. Rutledge, "Millimeter-Wave Diode-Grid Frequency Doubler," *IEEE Trans. on Microwave Theory and Tech.*, Vol. 36, No. 11, pp. 1507-1514, Nov. 1988.

[15] H-X.L. Liu, L.B. Sjogren, C.W. Domier, N.C. Luhmann, Jr., D.L. Sivco and A.Y. Cho, "Monolithic Quasi-Optical Frequency Tripler Array with 5-W Output Power at 99 GHz," *IEEE Electron Device Letters*, Vol. 14, No. 7, pp. 329-331, July 1993.

[16] Z.B. Popović, R.M. Weikle, II, M.Kim and D.B. Rutledge, "A 100-MESFET Planar Grid Oscillator," *IEEE Trans. on Microwave Theory and Tech.*, Vol. 39, pp. 193-200, 1991.

[17] R.M. Weikle, II, M.Kim, J.B. Hacker, M.P. De Lisio and D.B. Rutledge, "Planar MESFET Grid Oscillators Using Gate Feedback," *IEEE Trans. on Microwave Theory and Tech.*, Vol. 40, pp. 1997-2003, 1992.

[18] M. Kim, E.A. Sovero, J.B. Hacker, M.P. De Lisio, J.C. Chiao, S.J. Li, D.R. Gagnon, J.J. Rosenberg and D.B. Rutledge, "A 100-Element HBT Grid Amplifier," *IEEE Trans. Microwave Theory Tech.*, Vol. MTT-41, No. 10, pp. 1762-1771, Oct. 1993.

[19] M.P. De Lisio, C.-M. Liu, A. Moussessian, J.J. Rosenberg and D.B. Rutledge, "A 100-Element MODFET Grid Amplifier," *IEEE AP-S International Symposium*, Newport Beach, CA, June 1995.

[20] C.-M. Liu, E.A. Sovero and D.B. Rutledge, "40 GHz Monolithic Grid Amplifier," *53rd Annual Device Research Conference*, Charlottesville, Virginia, June 1995.

[21] J.B. Hacker, R.M. Weikle, II, M. Kim, M.P. De Lisio and D.B. Rutledge, "A 100-Element Planar Schottky Diode Grid Mixer," *IEEE Trans. Microwave Theory Tech.*, Vol. 40, No. 3, pp. 557-562, March 1992.

[22] L.B. Sjogren, H.L. Liu, F. Wang, T. Liu, X.H. Qin, W. Wu, E. Chung, C.W. Domier, N.C. Luhmann, Jr., "A Monolithic Diode Array Millimeter-Wave Beam Transmittance Controller," *IEEE Trans. on Microwave Theory and Techniques*, Vol. MTT-41, No. 10, pp. 1782-1790, Oct. 1993.

[23] X.H. Qin, W.M. Zhang, C.W. Domier, N.C. Luhmann, Jr., W. Berk, S. Duncan and D.W. Tu, "Monolithic Millimeter-Wave Beam Control Array," *Digest of IEEE Microwave Theory and Techniques Symposium*, MTT-S95, WE3F-F4, pp. 1669-1672, 1995.

[24] K.D. Stephan, F.H. Spooner and P.F. Goldsmith, "Quasioptical Millimeter-Wave Hybrid and Monolithic PIN Diode Switches," *IEEE Trans. on Microwave Theory and Techniques*, Vol. MTT-41, No. 10, pp. 1791-1798, Oct. 1993.

[25] T. Mader, S. Bundy and Z.B. Popović, "Quasi-Optical VCOs," *IEEE Trans. on Microwave Theory and Techniques*, Vol. MTT-41, No. 10, pp. 1775-1781, Oct. 1993.

[26] J. Bae, J.-C. Chiao, K. Mizuno, and D.B. Rutledge, "Metal Mesh Couplers Using Evanescent Waves at Millimeter and Submillimeter Wavelengths," *Int. Journal of Infrared and Millimeter Waves*, Vol. 6, No. 2, pp. 377-390, 1995.

[27] J. Hacker, M.P. DeLisio, M. Kim, C.-M. Liu, S.-J. Li, S.W. Wedge and D.B. Rutledge, "A 10-Watt X-Band Grid Oscillator," *IEEE MTT-S Int. Microwave Symposium Digest*, pp. 823-826, 1994.

[28] S. Gulkis, "Submillimeter Wavelength Astronomy Missions for the 1990s," *The Proceeding of the 1st International Symposium on Space Terahertz Technology*, pp. 454-457, 1990.

[29] M.A. Frerking, "The Submillimeter Mission Heterodyne Instrument," *The Proceeding of the 2nd International Symposium on Space Terahertz Technology*, pp. 17-31, 1991.

[30] J.W. Waters, "Submillimeter Heterodyne Remote Sensing of Upper Atmosphric Gases," *Microwave and Optical Technology Letter*, Vol. 4, No. 1, pp. 2-6, Jan. 1991.

[31] A. Räisänen, "Frequency Multipliers for Millimeter and Submillimeter Wavelengths," *Proceedings of the IEEE*, Vol. 80, No. 11, pp. 1842-1852, Nov. 1992.

[32] Christina Jou, "Millimeter-Wave Monolithic Schottky Diode-Grid Frequency Doublers," *Ph.D. Dissertation*, University of California, Los Angeles, 1987.

[33] R.J. Hwu, N.C. Luhmann Jr., L. Sjogren, X. H. Qin, W. Wu, D.B. Rutledge, B. Hancock, J. Maserjian, U. Lieneweg, W. Lam, and C. Jou, "Watt-Level Quasi-Optical Monolithic Frequency Multiplier Development," *The Proceeding of the 1st International Symposium on Space Terahertz Technology*, pp. 126-149, 1990.

[34] Hong-Xia Liantz Liu, "Monolithic Schottky Barrier and Quantum Barrier Device Arrays for Millimeter Wave Frequency Multiplication," *Ph.D. Dissertation*, University of California, Los Angeles, 1993.

[35] T.W. Crowe, R.J. Mattauch, H.P. Röser, W.L. Bishop, W.C.B. Peatman and X. Liu, "GaAs Schottky Diodes for THz Mixing Applications," *Proceedings of the IEEE*, Vol. 80, No. 11, pp. 1827-1841, Nov. 1992.

[36] Jonathan B. Hacker, "Grid Mixers and Power Grid Oscillators," *Ph.D. Dissertation*, California Institute of Technology, 1994.

[37] W.W. Lam, "Millimeter-wave Monolithic Schottky Diode-Grid Phase-Shifters," *Ph.D. Dissertation*, California Institute of Technology, 1987.

[38] Lance B. Sjogren, "A Multi-Function Millimeter-Wave Schottky Diode Array Electronic Beam Controller," *Ph.D. Dissertation*, University of California, Los Angeles, 1992.

[39] Xiaohui Qin, "Monolithic Millimeter Wave Beam Control Array," *Ph.D. Dissertation*, University of California, Los Angeles, 1995.

[40] V. Balakhanov, "Properties of a Fabry-Perot Interferometer with Mirrors in the Form of a Backed Metal Grid," *So. Phys. Doklady,* Vol. 10, pp. 788-790, 1966.

[41] Z. Agronovich, V. Marchenko, and V. Shestopalov, "The Diffraction of Electromagnetic Waves from Plane Metallic Lattices," *Sov. Phys. Tech. Phys.,* Vol. 7, pp. 277-286, 1962.

Chapter 2

Terahertz Grid Frequency Multipliers

The demand for solid-state local oscillators at submillimeter wavelengths has been steadily increasing for applications in radio astronomy and remote sensing of the atmosphere. The interest for terahertz applications has fostered a strong need for submillimeter-wave receivers, mixers and sources, especially tunable high-power sources used as the local oscillators for heterodyne submillimeter-wave receivers. Traditional high-power sources in the THz region such as gas lasers and vacuum-tube oscillators are not suitable for this purpose due to their large size, high-voltage supplies, short lifetime and small tuning ranges. However, frequency multipliers such as Schottky diode multipliers can be used to generate the required terahertz frequencies from lower-frequency solid-state tunable signal sources such as Gunn-diode oscillators.

This project is a joint effort among the MMIC group at CalTech, the Semiconductor Devices Laboratory at the University of Virginia (UVA), and the Center for Free-Electron Laser Studies at the University of California, Santa Barbara (UCSB). CalTech is responsible for design, UVA is responsible for fabrication of the diode-grids and the measurements are performed at UCSB. This is the first attempt to use the state-of-the-art terahertz planar Schottky diodes developed successfully at UVA on quasi-optical grids. These diode-grids which are originally designed for use as sideband generators have been fabricated and the testing for use as sideband generators is presently underway, nevertheless, we decided to test these diode-grids as frequency multipliers to verify the feasibility of us-

ing diode-grids for terahertz signal generations. It should be emphasized that these diode-grids are originally designed for sideband generators, therefore, some design features may not be optimal or proper for the use as multipliers. For example, flipping the diode polarity above and below the center row of the grid for IF input is inappropriate for multipliers because the cancellation of electric fields from the two halves in the far field creates an undesired null in the center of the output beam.

Organization of this chapter is in the following order:

Terahertz applications and achievements of terahertz sources are first mentioned to emphasize the importance of developing submillimeter-wave frequency multipliers. Then a review on conventional waveguide-multipliers and the achievements is presented. The concept and advantages of quasi-optical multipliers are examined. The idea of terahertz sideband generators is presented for the original motivation of developing planar Schottky diode grids. Then the structures, advantages and problems of planar Schottky diodes are introduced. A complete fabrication procedure of the planar Schottky diode grids is given along with an estimated equivalent circuit of the diode.

The design approach (linear part) is described. The unit-cell method and the calculations for embedding impedances of grid structures, developed by Robert Weikle and Jonathan Hacker, former students in the MMIC group at CalTech, are introduced and the results of linear analysis on the grid multipliers are shown.

The results of DC tests and RF measurements are shown in the order of DC I-V tests; low-frequency C-V tests; RF measurement arrangements; input pulses; time-domain responses; verification of second-harmonic generations; electric-field polarizations; frequency verifications; input power measurements; power dependences; and output patterns. The measured output pattern is verified by antenna-pattern calculations taking the antenna pattern of the bow-tie with contact fingers, the array factor and the finite acceptance-angle of the re-

ceiving horn into account. The verification of using the finite-element method to compute the antenna patterns is also given by comparing with analytic solutions on a pure bow-tie antenna. The nulls in the output beam, due to the improper diode orientations, are shown and verified. The attempt of using a dielectric lens to correct the output patterns shows it is necessary to fabricate a new array with proper diode orientations to increase the output powers. Then impedance tunings and biasing effects are shown as an endeavor to increase multiplication efficiencies.

The current saturation is discussed and an effort of measuring RF currents is made. The RF current measurements, though didn't provide enough information on diode behaviors, initiate the possibility to determine terahertz characteristics of diodes. Failure of diodes and possible approaches of preventing diodes from damage are discussed. Then conclusions on present works are given.

Future works include the improvements of the grid design, diode structures, and experimental setup. A new design of 12 × 12 arrays and estimated output patterns are shown. The possibility of using other devices rather than Schottky varistor diodes is also discussed including a new grid frequency tripler using InAs quantum-well devices.

2.1 TERAHERTZ APPLICATIONS

Microwave remote-sensing techniques and recent developments on submillimeter-wave heterodyne radiometric systems have made possible their use in limb sounders at submillimeter wavelengths to study the upper atmosphere of Earth [1-4]. The Antarctic ozone hole discovered in 1985 [5] shows that it is necessary and urgent to monitor the upper atmosphere in order to detect the change of the stratospheric ozone layer which shields life from solar ultraviolet radiation but is depleted by pollution from industrial activities. Observations in the terahertz region have been successful in determining the density of many species such as hydrogen chloride, hydrogen fluoride, and many radicals such

as atomic oxygen, chlorine monoxide and hydroxyl which enters in many atmospheric chemical reactions including the catalytic cycles of HO_x, NO_x and ClO_x which lead to the destruction of ozone [6]. NASA EOS (Earth Observing Systems) scheduled an enhanced MLS (Microwave Limb Sounder) to be launched in 2002 [7] for monitoring ozone depletion, climate change, tropospheric chemistry and volcanic effect. Technology needs include local oscillators for radiometers and mixers up to 2.5 THz.

Astronomers note that interstellar medium emit energy mostly in the sub-millimeter-wave spectral region [8] which is very important for the investigation of a wide range of astronomical topics including star-forming molecular cloud regions, the interstellar medium, the composition of planetary atmospheres, galaxies and cosmic background radiation [9]. Spaceborne observations will be required to study these subjects at submillimeter-wave ranges due to the interference with the terrestrial atmosphere while ground-based, airborne and balloon-borne observations continue [8]. NASA, ESA (Europe Space Agency) and some other national space administrations are planning several satellite missions for the time span of 1995-2010 including NASA's ISO (Infrared Space Observatory), SWAS (Submillimeter-wave Astronomy Satellite), SMMM (Submillimeter Moderate Mission), LDR (Large Deployable Reflector), LSI (Lunar Submillimeter Interferometer), SIRTF (Space Infrared Telescope Facility), ESA's FIRST (Far Infrared and Submillimeter Space Telescope), Japanese IRTS (Infrared Telescope in Space), and Swedish Space Center's ODIN MOSES [9-15]. These projects present severe technical challenges on submillimeter-wave local oscillators for space-borne heterodyne receivers and focal-plane arrays. For example, the frequency coverage of the NASA's SMMM is from 400 GHz to 1.2 THz and the minimum output power requirement of the local oscillator at 1 THz is 50 μW. The challenge is to provide a small, light-weight reliable device requiring low-voltage power supply but generating enough output powers.

The THz technologies are also used on plasma diagnostics [16] including thermal imaging, density probing and backscattering measurement. In fusion research, measurements of a plasma's electron density profile have been obtained by a submillimeter-wave imaging system, using a bow-tie antenna/bismuth microbolometer detector array [17]. Terahertz coherent systems were also used for plasma heating and high energy accelerators in fusion researches [18].

Some potential submillimeter-wave applications include nondestructive testing for high voltage cable manufacturing [19]; military radars [20]; high-density high-directivity communications and data transmission [18,21]; medical diagnostics [22,23] - early diseases detection, spectroscope of expiration, emission and reflection from tissue and skin; medical treatments [24]; bio-chemical researches [22,25] - spectroscopy of gas product, radiometry of plants and environmental early warning systems; security [22,26] - life detectors, detection of concealed drugs and bombs, and identity verification; short range information [18,22,27] - automatic systems and automotive collision avoidance; as well as material measurements and commercial process control [18].

2.2 SOURCES

The realization of a simple tunable local oscillator with adequate output powers at submillimeter wavelengths presents severe technical difficulties. Traditional choices such as free-electron lasers, gas lasers, vacuum-tube oscillators and reflex klystrons are not suitable for space applications due to their large sizes, high-voltage supplies, short lifetimes, requirement for coolers and small tuning ranges. High-frequency carcinotrons or back-wave oscillators have been successfully developed at frequencies up to 1 THz [28]. However, they both are mechanically cumbrous and require high-power supplies or complicated phase lock systems. Therefore, all-solid-state local-oscillator sources would be more appropriate for most of the applications. Several solid-state components theoretically capable of generating oscillations at submillimeter wavelengths have

been under development such as TUNNETT [29-31], the quantum well diodes (QWD) [12, 29] and resonant-tunneling diodes (RTD) [32, 33]. For example, an output power of $0.2\,\mu$W at 420 GHz and an oscillation at 712 GHz using RTDs were obtained by Brown *et al.* [34]. It was also indicated possible to achieve fundamental oscillation up to 1 THz. A recent developing competitive approach is to use a photo-mixer of low-temperature-grown GaAs to mix the lights from two visible IR lasers to generate radiations in the frequency ranges from 100 GHz to 3.8 THz [35]. At 1 THz, an output power of $0.8\,\mu$W was observed.

These devices, though are potential submillimeter-wave local-oscillator sources, are still unable to generate enough output power for use and the power falls off dramatically at higher frequencies. Therefore, frequency multipliers or upconverters like Schottky diode multipliers pumped by a high-power, lower-frequency tunable source provides an attractive alternative to generate the required terahertz frequencies.

At millimeter wavelengths, two most commonly used solid-state components are IMPATT and Gunn devices. Hirayama *et al.* [36] demonstrated a 2.2 mW output power at 412 GHz and Kuno [37] showed that it is feasible to produce 900 mW at 94 GHz and 12 mW at 255 GHz using IMPATT diodes. Commercial products are available from 30 GHz to 143 GHz. Millitech provides CW IMPATT power oscillators with an output power of 200 mW at 96 GHz with a DC power supply requirement of 24 V [38]. Hughes provides pulsed IMPATT power sources with a long-pulse (a pulse width of 0.5-1000 μs) output power of 2 mW or a short-pulse (a pulse width of 50-100 ns) output power of 1 W at 143 GHz and CW IMPATT power oscillators with an output power of 20 mW at 143 GHz [39].

The features of the Gunn diode oscillators include low AM and FM noise, modulation options and availability of electrical tuning. For the GaAs Gunn diodes, Kuno reported an output power of 40 mW at 100 GHz [37]. Commercial products are available at 95 GHz with an output power of 40 mW [40] and

Hughes provides tunable GaAs Gunn oscillators at 100 GHz with an output power of 30 mW and a tuning range of 1 GHz [39]. For InP Gunn diodes, Kamoua *et al.* [41] demonstrated an output power of 20 mW at 120 GHz and 10 mW at 136 GHz and later Eisele *et al.* [31] showed an output power of 100 mW at 132 GHz. Commercial products are available at 95 GHz and 110 GHz with output powers of 100 mW and 40 mW, respectively [40]. Millitech provides InP Gunn diode oscillators up to 140 GHz with an output power of 30 mW [38].

These millimeter-wave devices provide possible local oscillators to pump frequency multipliers or multiplier chains to generate the required terahertz frequencies. The advantages of using a combination of frequency multipliers and solid-state sources will result from the favorable features of low frequency sources like lower noise, larger tuning range, lower cost and higher reliability.

2.3 MULTIPLIERS

Current diode multipliers have mostly been single-diode structures typically consisting of a Schottky varactor diode placed in a crossed-waveguide mount with a whisker contact shown in Figure 2.1 [42]. The structure design requires matched terminations at the fundamental frequency and the desired harmonic frequency; open-circuited terminations at the higher harmonics; and optimum reactive terminations at the idler frequencies [15]. The input power is fed through the input waveguide, passed a low-pass filter, and coupled into the diode chip which is mounted on the surface of the output waveguide. One of the diodes on the surface of the chip is contacted by a very thin wire (whisker) which acts like an antenna coupling harmonic power into the output waveguide. Sliding back-shorts in the input and output waveguides allow impedance tuning at the input and output frequencies. The step transformer transform the impedance of the waveguide to match the diode impedance. A stripline bias filter is used to provide the diode DC bias.

Frequency multiplication results from the nonlinear impedance of diodes.

There are usually two types of diode frequency multipliers: the varistor multipliers utilize the nonlinear I-V relationship with a forward bias; and the varactor multipliers make use of the nonlinear C-V relationship with a reversed bias. Single varistor multipliers have been well developed with low conversion efficiencies. Bauer *et al.* demonstrated resistive diode doublers at 300 GHz with a conversion loss of 18 dB [43]. Page [44] showed that the frequency multiplication efficiency of a purely resistive multiplier is limited to $1/n^2$, where n is the harmonic number. However, the advantages of using varistors are that the impedance
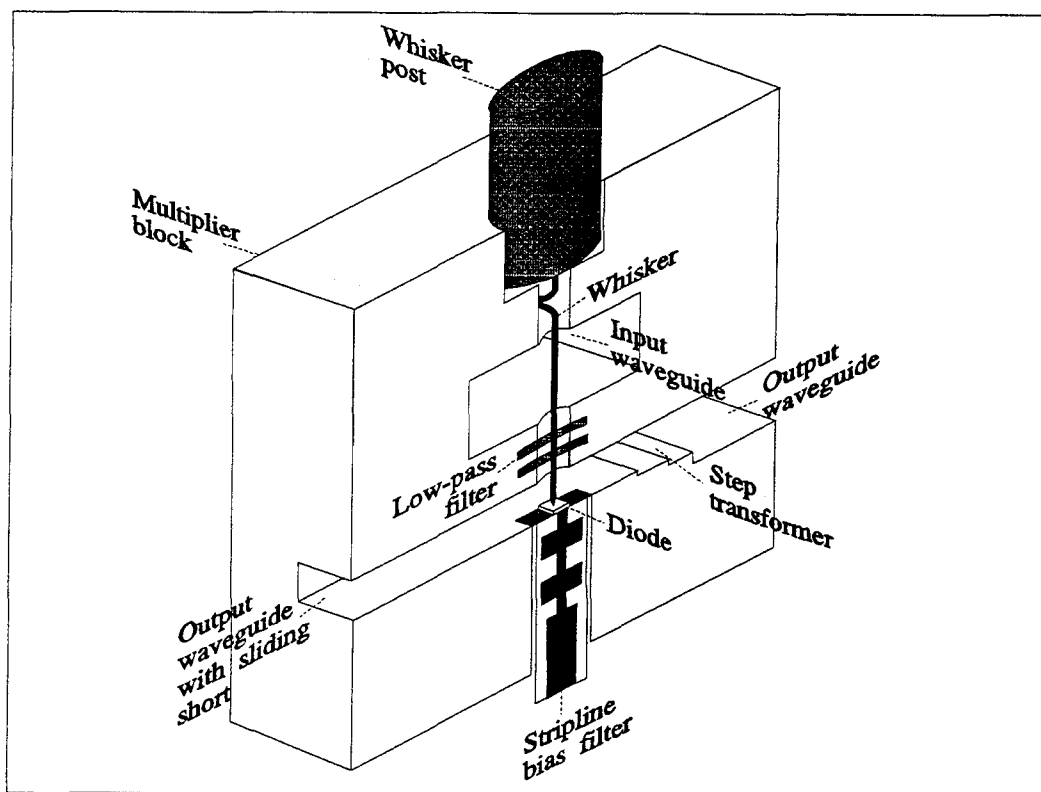
Fig. 2.1 A typical crossed-waveguide multiplier using one diode [42]. Only half of the structure is shown. The input power is fed through the input waveguide, passes a low-pass filter, and is coupled into the diode chip which is mounted on the surface of the output waveguide. One of the diodes on the surface of the chip is contacted by a very thin wire (whisker) which acts like an antenna coupling harmonic powers into the output waveguide. Sliding back-shorts in the input and output waveguides allow impedance tuning at the input and output frequencies. The step transformer transforms the impedance of the waveguide to match the input impedance of the diode. A stripline bias filter is used to provide the diode DC bias.

matching is easier as compared to varactors and the intermodulation distortion is smaller [45]. Therefore, a pair of two diodes in an antiparallel connection which provides negative differential resistivity to avoid the limitation associated with positive monotonic I-V characteristics can be more efficient [45], although the idea has not been demonstrated at millimeter or submillimeter wavelengths.

Manley and Rowe [46] first in 1956 showed that it is possible to approach 100% conversion efficiency with a purely nonlinear reactive device. Penfield and Rafuse [47] also predicted an ideal varactor will be able to convert all of the pump power to any higher harmonics with proper terminations, bias and pumping power. Therefore, varactors have been widely used for frequency multipliers. Up to date, multipliers using varactors in crossed-waveguides have achieved impressive conversion efficiencies. Archer [48] reported a doubler with 10% efficiency at any output frequency in the range 100-260 GHz. The maximum output power is 6 mW at 260 GHz. Faber *et al.* [49] demonstrated a doubler with 35% efficiency at 98 GHz which is close to the theoretical prediction. Erickson [50] demonstrated a doubler with a peak efficiency of 35% at 160 GHz using a balanced configuration of two series Schottky varactors.

At submillimeter wavelengths, considerable effort has been made to increase output power and output frequencies by using scaled-down versions of millimeterwave waveguide mounts but smaller active-area diodes. Takada *et al.* [51] reported a doubler with 5 mW output power at 300 GHz and a tripler with 500 μW at 450 GHz. Erickson [50] has built a doubler with a maximum output power of 4 mW at 330 GHz and a tripler with output powers of 700 μW and 550 μW at 474 GHz and 498 GHz, respectively. Zimmermann *et al.* [52-54] demonstrated triplers, quadruplers, quintuplers and sextuplers with output frequencies in the range of 450-750 GHz. A tripler with a 250 μW output power at 630 GHz [53], a quadrupler with a 30 μW output power at 750 GHz [53], and a chain of a doubler and a tripler with a 380 μW output power at 690 GHz [54] were reported.

Above 800 GHz, Rothermel *et al.* [55] reported an octupler producing 0.66 μW at 800 GHz when pumped by 20 mW at 100 GHz and a seventh harmonic with an output power of 1 μW at 805 GHz when pumped by 18 mW at 115 GHz. Rydberg *et al.* [56, 57] have demonstrated a Schottky varactor diode frequency tripler with a measured output power more than 120 μW at 803 GHz. Erickson *et al.* [58] presented a waveguide tripler with an output power of 110 μW at 800 GHz. Zimmermann *et al.* [59, 60] has demonstrated an output power of 60 μW at 1 THz by using a cascade of two whisker contacted Schottky varactor frequency triplers.

Figure 2.2 shows the state-of-art output power for frequency multipliers with output frequencies from 50 GHz to 1 THz. The number next to the data point indicates the reference number. Each data presents a maximum output power at an operating frequency in the references. Obviously the output power strongly depends on the pumping power, so some results do not have high output power due to the availability of pumping sources. Also some data shown may not have impressive output powers but have high efficiencies or being historic milestones. In most of the cases, the maximum output power is limited by the power saturation of the devices.

Though waveguide multipliers are highly developed and show to be promising to produce more output power at submillimeter wavelengths using two or more diodes in series, there are some limitations.

At frequencies above 200 GHz, the losses of waveguide components are too high for sensitive radiometers [54] and the machining for single-mode waveguides become more and more complicated and expensive as frequencies increase. Micromachining techniques provide possible solutions like micromachined slot waveguides on silicon to reduce losses and cost [100]; and quasi-planar integrated whisker/RF airline filters to replace the conventional whisker contacts [101,102]. These preliminary results are very impressive. However, these components are still under development and have not yet been integrated with other mounting

Fig. 2.2 State of the art of the output power of frequency multipliers from 50 GHz to 1 THz. The number next to the data point indicates the reference number. Each data presents a maximum output power at an operating frequency in the references.

components like sliding shorts and impedance transformers.

Besides mounting structure parameters (losses and the embedding imped-ances at the fundamental, idler, output and higher harmonic frequencies) the other important varactor parameter deciding the efficiency is the dynamic cutoff frequency f_c:

$$f_c = \frac{1}{2\pi R_s}\left(\frac{1}{C_{j,min}} - \frac{1}{C_{j,max}}\right) \tag{2.1}$$

where $R_s(f)$ is the series resistance of diodes, $C_{j,min}$ and $C_{j,max}$ are the mini-mum and maximum diode junction capacitances with different biases. A large capacitance ratio $C_{j,max}/C_{j,min}$ with a small $C_{j,min}$ will result a high cutoff fre-quency. However, a small $C_{j,min}$ is usually achieved by reducing the device active area which will also limit the saturation power. Therefore, increasing operating frequencies for a solid-state device inherently limits the output power.

Power combining technology then becomes essential to overcome this problem. Conventional power combining techniques utilizing waveguides and striplines have serious limitations at higher frequencies though they have reached high combining efficiencies at microwave and millimeterwave frequen-cies [103,104]. These structures have high losses at submillimeter wavelengths due to ohmic dissipation, are narrowband due to the resonant-cavities, are ex-pensive due to the small sizes, and usually require many hours of manual labor to assemble. Therefore, spatial power combining techniques have been applied to submillimeterwave frequency multipliers. Frerking *et al.* [63] used a quasi-optical Fabry-Perot interferometer to diplex the input and output frequencies and a varistor GaAs Schottky diode to make the frequency doubler produc-ing 50 μW at 600 GHz. Archer [64] used quasi-optical filtering and tuning ele-ments at the output on triplers and quadruplers to reduce losses and demon-strated a peak efficiency of 7.5% at 265 GHz and 5% at 340 GHz with 30 mW input power. Steup [98] demonstrated a 580 GHz quadrupler consisting of four whisker-contacted diodes and a quasi-optical antenna array in the output which

acts as a tunable power combiner to produce an output power of $29\,\mu$W with a pump power of $120\,$mW. A corner-cube doubler has been constructed by Lyons *et al.* [97] to generate $2\,\mu$W at $952\,$GHz with an input power of $22\,$mW. These methods demonstrated the low-loss feature of spatial power combining, however, didn't produce more power due to the power saturation of single or a small number of diodes. One approach to overcome the low power of solid-state devices in the submillimeter-wave band is to combine a large number of devices together.

2.4 Quasi-Optical Grid Multipliers

2.4.1 Advantages

A grid of many planar devices quasi-optically coupled in free space does not require the construction of single-mode waveguides and can potentially overcome the power limits of conventional single/dual-diode multipliers. Rutledge and Schwarz [105,106] first demonstrated the idea of integrating solid-state devices into a periodic grid as a multimode detector array. The approach of using quasi-optical grids to combine power provides many advantages and these advantages become more attractive when the frequencies increase:

(1) Higher power. By integrating a large number of devices together into the grid, very large powers can be achieved [108,118]. Because the input power is distributed onto the entire grid, each device only handles certain amount of input power which will increase the total saturation power and the dynamic range. To increase the power, we simply increase the number of devices and the size of the grid.

(2) Higher frequency. Quasi-optical system does not require the construction of single-mode waveguides or single-mode resonators, therefore, the limitation of operating wavelengths due to the machining difficulties is eliminated. Also there is no transmission line like microstrip or other planar waveguides

needed, the limitation of the roll-off frequencies or higher-mode cut-on frequencies then disappears.

(3) Less loss. Because the power is combined in free space, losses associated with waveguide walls and feed networks are eliminated. Conduction loss, dielectric loss and radiation loss which limit the operating frequencies using traditional planar-waveguide components will be reduced in a quasi-optical system.

(4) Easier tuning. Quasi-optical systems use mirrors, dielectric slabs, metal-patterned grids or Fabry-Perot interferometers for tuning the impedances, it is easier than for most of the power combiners based on microstrip lines or waveguides. The impedance tuning is independent of the active grid itself, there is no need to change the design or re-fabricate the active devices or lumped elements on the circuits when tuning the performance of the entire system. The tuning elements are easier to be replaced or redesigned without changing the active grids.

(5) Simpler analysis. Although quasi-optical circuits look more like optical devices, they can be modelled with reasonable accuracy using simple transmission-line and lumped-element components by assuming unit cells in a large array. This provides two major advantages. First, unit cells decide the performance of the whole grid. Design changes such as power requirements or operating frequencies can be done by simply changing the number of the unit cells or scaling of the unit cells, unlike microstrip circuits or waveguides which require a new iteration of analysis and layout. Second, simple transmission-line models allow the well-developed commercial computer-aided design tools for conventional microwave circuits such as Hewlett-Packard Microwave and RF Design Systems (*MDS*) and *Spice* to be applied to the design and modelling of quasi-optical circuits. Also the unit-cell feature makes it possible to use the EMF technique, which was

developed by Eisenhart and Khan [119] to derive the impedance of a wave-guide mounting structure and later extended by Weikle [120], to determine the characteristics of the grids. Conventional numerical techniques such as the finite-element methods or conjugate gradient methods which use an iterative approach require large amounts of computer time and memory. This method reduces the computing time and effort greatly.

(6) Monolithic. Either active or passive quasi-optical circuits are suitable for monolithic manufacture using planar photolithographic techniques and existing semiconductor fabrication technologies. Also no transmission lines or waveguides are used and that makes fabrication simpler and cost less.

(7) Failure tolerance. Intuitively, we expect a large number of devices in an array provides a better failure tolerance. Kim *et al.* [121] shows that a 10% failure of devices in a grid-amplifier only causes a 1-dB drop in output power. This means that grids could be more reliable than a single-device system.

2.4.2 CONCEPT

The multiplier concept is shown in Figure 2.3. The input beam at the fundamental frequency enters from the left. The first element is a pair of dielectric tuning slabs that act to transform the impedance of the input wave to one appropriate for the multiplier grid. Typically inductive reactance is needed to cancel capacitance of the diodes in the grid. In addition, the free-space wave impedance, $377\,\Omega$, is inconveniently high and needs to be reduced. Next the beam passes through a low-pass filter that passes the fundamental frequency, but reflects harmonics. Then the beam hits the diode-grid. A diode-grid is a periodic circuit loaded with diodes. The grid acts as a nonlinear surface which results from the nonlinearity of I-V or C-V characteristics of diodes and generates harmonics. This harmonic beam radiates both forward and backward, but the backward beam reflects off the low-pass filter. The forward beam passes through the high-pass filter, and then through another pair of tuning slabs. One impor-

tant feature is that the tuning slabs are outside the filters, so that the input and output can be tuned independently. The entire structure is quite compact, only a few wavelengths thick. The design is also suitable for cascading, so that even higher harmonics could be produced. The multiplication process preserves the beam shape. Therefore, a focused beam could be used so that different sizes of multiplier grids could be cascaded.

2.4.3 ACHIEVEMENTS

Lam *et al.* [109-111] first presented the idea using diode-grids designed for electronic beam steering as frequency multipliers and predicted a second-harmonic output power of 560 mW at 130 GHz with a conversion efficiency of 35%. Using this quasi-optical array approach on frequency multipliers, a second conversion efficiency of 9.5% and pulsed output powers of 0.5 W were achieved at 66 GHz by Jou *et al.* [112,113]. The diode-grid has 760 Schottky barrier varactor
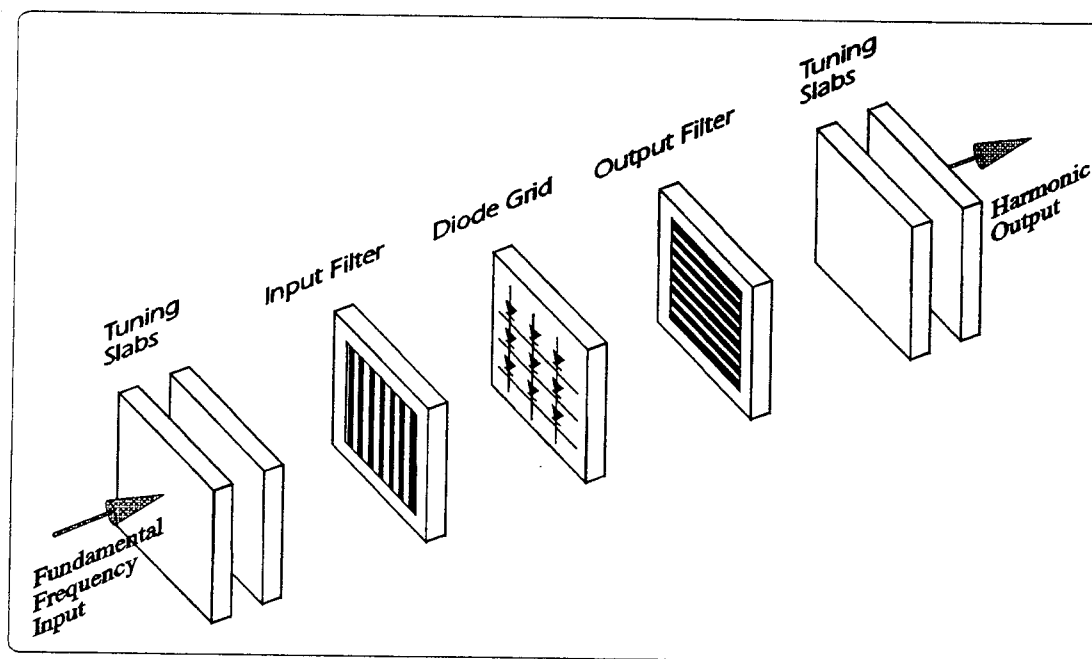

Fig. 2.3 The grid-multiplier concept. The fundamental wave enters on the left as a beam, passes through a filter, and is incident on the diode grid. The grid acts as a nonlinear surface and produces a beam at the harmonic frequencies, which passes through filters on the right.

diodes and was pumped by a 2.5 W input power with a pulse width of 2 μs. It is also shown that the experimental results agree well with the predictions using simple transmission-line models and unit cell methods. Hwu *et al.* [114] reported a frequency tripling efficiency of 24% at 99 GHz with an input power of 9 mW using a BIN (barrier-intrinsic-N^+) diode grid. Liu *et al.* [115,116] have recently demonstrated a frequency tripler consisting of 3,100 Schottky-quantum-barrier varactor diodes to produce 5 W pulsed output powers at 99 GHz and a tripler consisting of 3,000 multi-quantum-barrier varactor diodes to produce 1.25 W pulsed output powers at 99 GHz. The pulse width is 1 μs. A CW tripler which is currently being fabricated using superlattice Schottky-quantum-barrier varactor diodes is predicted to have an optimized efficiency of 28% at 300 GHz [117].

2.5 THz Sideband Generator

Applications of the diode-grids include frequency multipliers; electronic beam-steerers and phase shifters [109-111]; beam controllers [107]; mixers [122]; beam switches [123]; oscillators and resonators [124]; detectors and focal-plane imaging arrays [125,126]; phase-conjugation media [127]; and sideband generators. Hacker [108] proposed a terahertz sideband generator grid used as a grid mixer to upconvert a tunable low-frequency signal, the IF, to the terahertz region by mixing it with a single-frequency local oscillator such as a submillimeter-wave laser. Figure 2.4 shows the sideband generator grid concept. This terahertz sideband generator grid is a nonlinear surface to convert a variable 1-20 GHz IF signal onto a 1.6-THz local-oscillator (LO) signal. The LO beam incidents normally on the diode-grid and can be generated by a conventional gas laser or a multiplier. A mirror behind the grid is used to tune the impedance to match the free space for a better coupling efficiency. The IF signal is generated by a microwave sweeper and fed to the grid using a coplanar waveguide. The center row of the grid is connected to the center conductor of the coplanar waveguide and the edges of the grid are connected to the outer conductors. The diode orientation is flipped

over the central row to allow DC biasing.

This proposed project is a joint effort between the MMIC group at Caltech and the Semiconductor Devices Laboratory at the University of Virginia (UVA). Caltech is responsible for design and the University of Virginia is responsible for fabrication and testing of the sideband generators. This is the first attempt to use the state-of-the-art terahertz planar Schottky diodes developed successfully at UVA [128-132] on quasi-optical grids. These diode-grids have been fabricated and the testing for use as sideband generators is presently underway, nevertheless, we decided to test these diode-grids as frequency multipliers to verify the feasibility of using diode-grids for terahertz frequency multiplication. It should be emphasized that these diode-grids are originally designed for sideband generators, therefore, some design features may not be optimal or proper for use as multipliers. For example, flipping the diode polarity above and below the center row of the grid is inappropriate for multipliers because the cancellation of electric
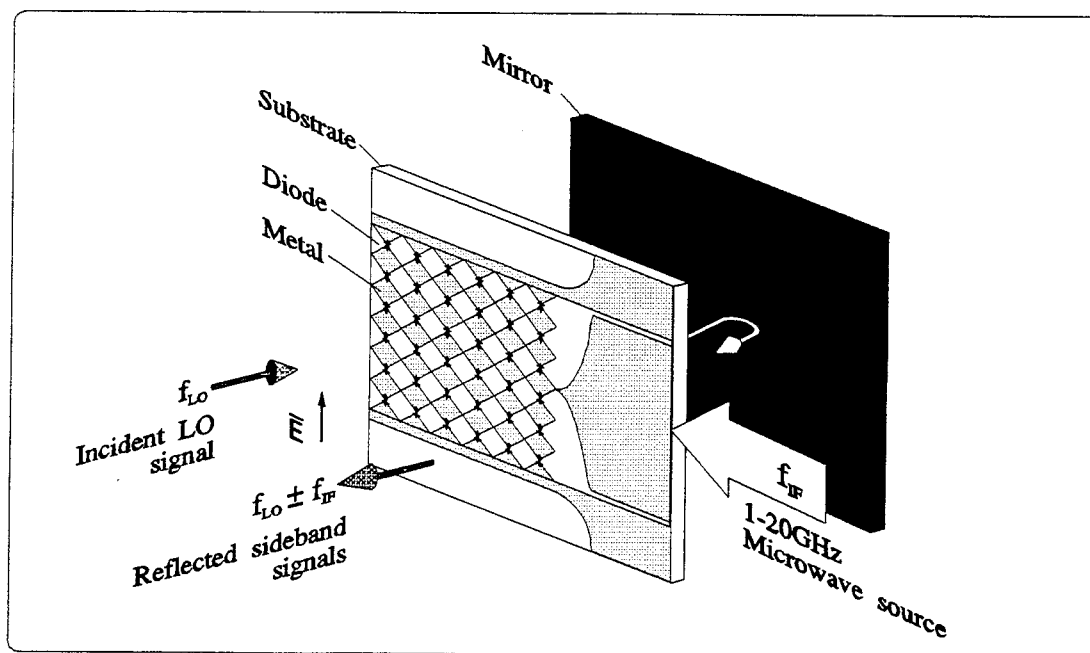

Fig. 2.4 The sideband generator grid [108]. The incident LO signal and reflected sideband signals couple to the diodes quasi-optically through the face of the grid. The mirror is used to tune out the capacitive reactance of the diodes for a better match to free space.

fields from the two halves in the far field creates an undesired null in the center of the output beam.
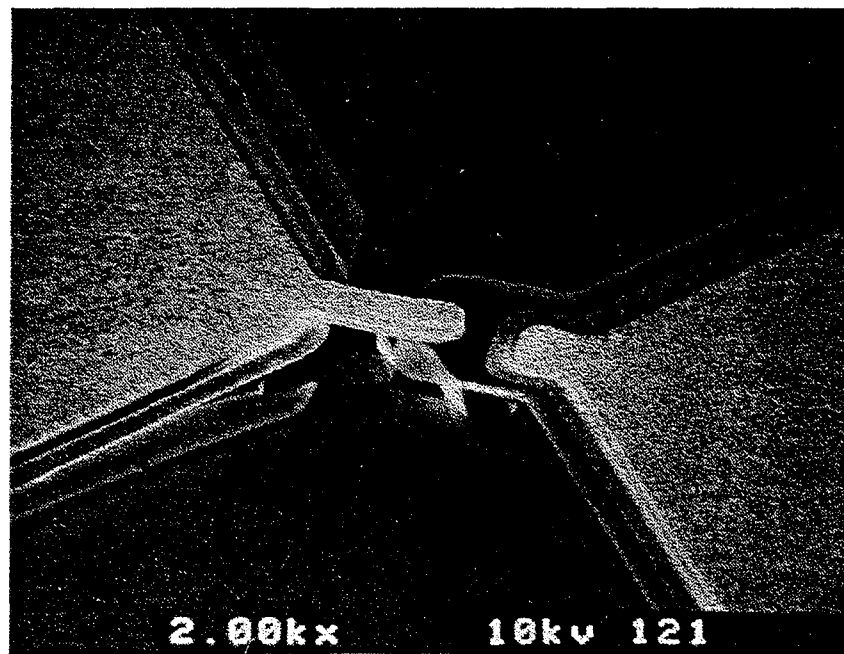
2.6 PLANAR SCHOTTKY DIODES

Schottky barrier diodes for submillimeterwave applications are typically fabricated as circular anode metallization on GaAs substrate with anode diameters from microns to submicrons for whisker contacts [129]. This type of structure provides benefits of simpler fabrication, less parasitic shunt capacitance with the whisker contact and higher efficiency for input power to be coupled into diodes. However, whisker-contacted diodes are costly to assemble and hard to combine power.

Planar Schottky barrier diodes have been developed by numerous laboratories over the past ten years [133-137]. These devices greatly simplify the system implementation, especially for space-based applications which require high reliability. The planar (whiskerless) Schottky diodes also allow integration of a large number of devices, easier fabrication for antiparallel diode pairs and integration with antenna structures or other devices such as filters, oscillators and amplifiers on the same chips.

However, three major issues need to be solved for using planar Schottky diodes [129].

First, the large shunt capacitance caused by the coplanar contact pads will reduce the cutoff frequencies and limit the operating frequencies below 100 GHz. Garfield, Mattauch and Bishop [133] developed a novel planar diode structure to overcome this problem. These devices have extremely low parasitic element values while still maintaining excellent current-voltage characteristics by etching a channel through the active GaAs layer.
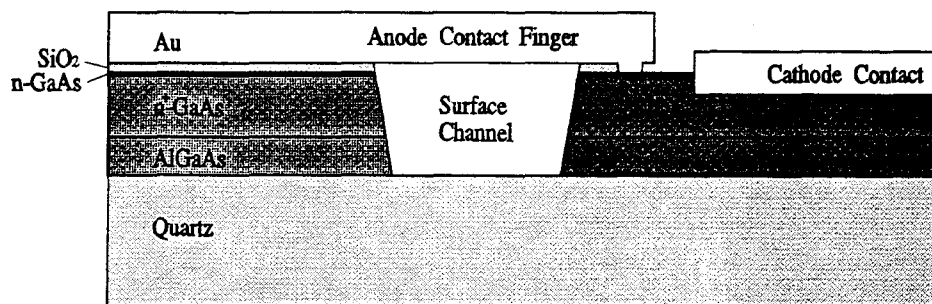
Second, the formation of submicron anodes on a planar diode is more difficult than a whisker-contacted diode. However, fabrication processes have been greatly improved by the Semiconductor Devices Laboratory at the University of

(a) SEM picture
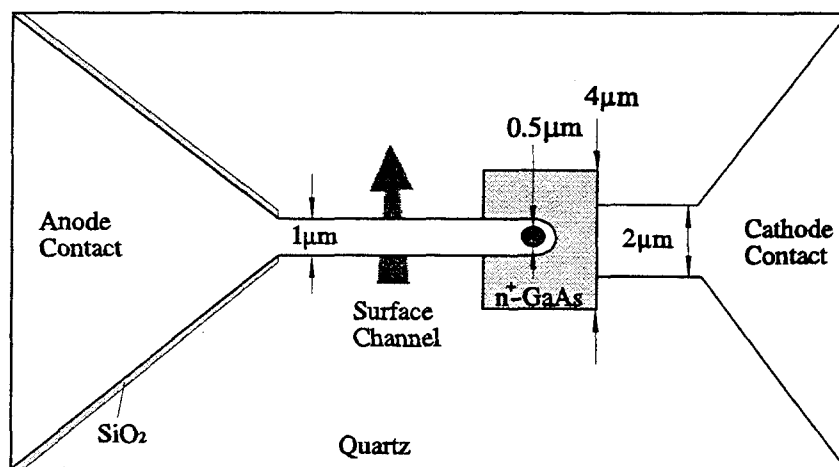
(b) Top View

(c) Cross Section

Fig. 2.5 (a) The SEM picture, (b) the top view and dimensions, and (c) the cross section of the planar Schottky diode.

Virginia [131]. The surface channel structure provides the benefit to form the anode on an essentially planar surface, therefore, makes it easier to define the anode formation and the anode-to-finger alignment. Also the structure avoids expensive and troublesome proton bombardment which is required for conventional planar structures.

Third, the LO coupling efficiency is low for a planar diode [129]. This problem can be solved by designing an integrated planar antenna structure and using outside impedance tuners to optimized the coupling efficiency. Quasi-optical grid is then a good candidate to use the planar diodes. Quoting Crowe's words in [129] "Solution of this problem will require close interaction between the diode fabrication experts and the RF circuit/antenna designers.....Thus, when the problems of shunt capacitance, large anodes and RF coupling are solved, planar diodes should outperform whiskered diodes at THz frequencies." Therefore, we believe the collaboration between UVA and Caltech will make an important contribution not only on realization of a higher-power THz LO source, but also on expansion of planar-diode applications.

2.7 FABRICATION

These planar Schottky diode-grids are fabricated by Yongjun Li in the Semiconductor Devices Laboratory at the University of Virginia. Figure 2.5(a) shows an SEM picture of the planar Schottky diode located between the metal fingers of the bow-tie structure. Figure 2.5 (b) and (c) show the top view and the cross section of the planar Schottky diode, respectively.

Fabrication procedures shown in Figure 2.6 are quite similar with the ones in [138]. To make a diode used in terahertz frequencies, series resistance R_s and zero-bias shunt capacitance C_{j0} should be greatly reduced by reducing anode diameter and choosing optimum active layer doping and thickness [155,156].

(1) The processes start with a highly Si-doped GaAs substrate with a layer of undoped AlGaAs on top. The AlGaAs layer has a thickness of 1.5 μm.
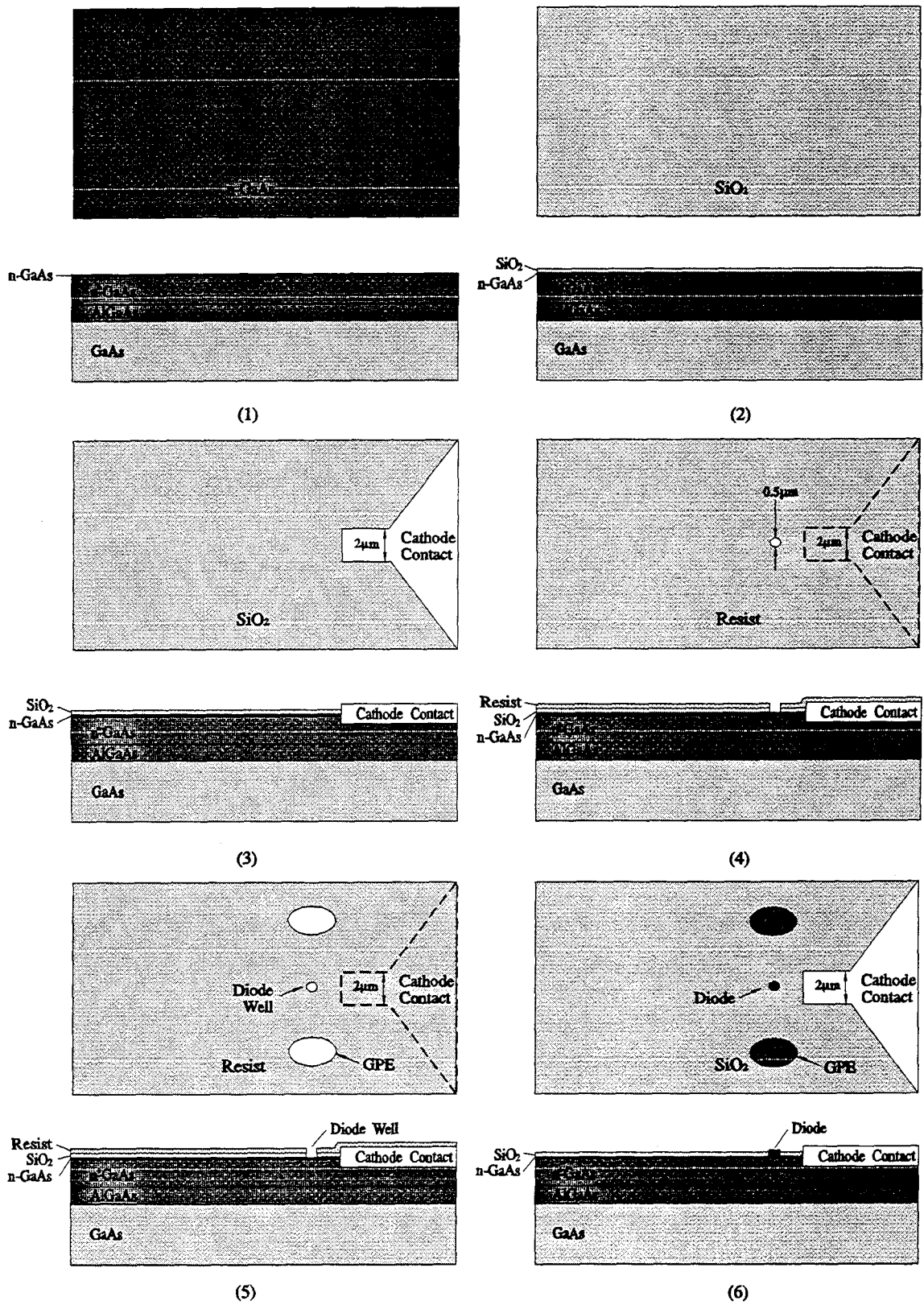
Fig. 2.6 Fabrication procedures for planar Schottky diodes.

Then a layer of Si-doped buffer GaAs and a layer of Si-doped active GaAs are deposited on the surface using MOCVD. The n-GaAs layer has a thickness of $0.1\,\mu$m and a doping concentration of 4×10^{17}cm^{-3}. The n$^+$-GaAs layer has a thickness of $3\,\mu$m and a doping concentration of 5×10^{18}cm^{-3}.

(2) A $(0.4\,\mu$m) layer of SiO$_2$ is deposited using chemical vapor deposition (CVD).

(3) Photoresist is applied to form the cathode contact pattern and then SiO$_2$ and n-GaAs are etched away. The ohmic contact metallization is deposited and alloyed.

(4) A thin layer of photoresist is applied to form the anode pattern using photolithographic techniques. The mask is made by *DuPont Photomas, Inc.*. SiO$_2$ then is etched away using the fluorine reactive ion etching (RIE) to form an anode well. A very thin (300-400$\overset{\circ}{A}$) layer of SiO$_2$ is left in the bottom of the well to protect the underlying GaAs from ion etching damage. The resist is removed by acetone.

(5) A layer of photoresist is spun on the whole wafer to cover SiO$_2$ and the anode well. Two circular patterns are exposed on each side of the anode. These two circular patterns are called the GPEs (Galvanic Protection Eyes).

Fabrication processes in previous experiences [138] result in two severe problems on planar Schottky diodes: high creep (a shift in forward knee voltage after applying reverse current) and low reverse breakdown voltage. These two problems will significantly degrade the diode performance. Possible cause is the galvanically accelerated etching (galvanic corrosion) which happens as applying anode-formation platinum plating. The galvanically accelerated etching is particularly stronger with small anode diameters. A formation of two protection wells around the anode contact to shunt the galvanic current away from the anode, prior to the anode plating, could reduce the excessive etching of GaAs epitaxial layer in the platinum plating solution. Experiments have been done by William Bishop and Yongjun Li at

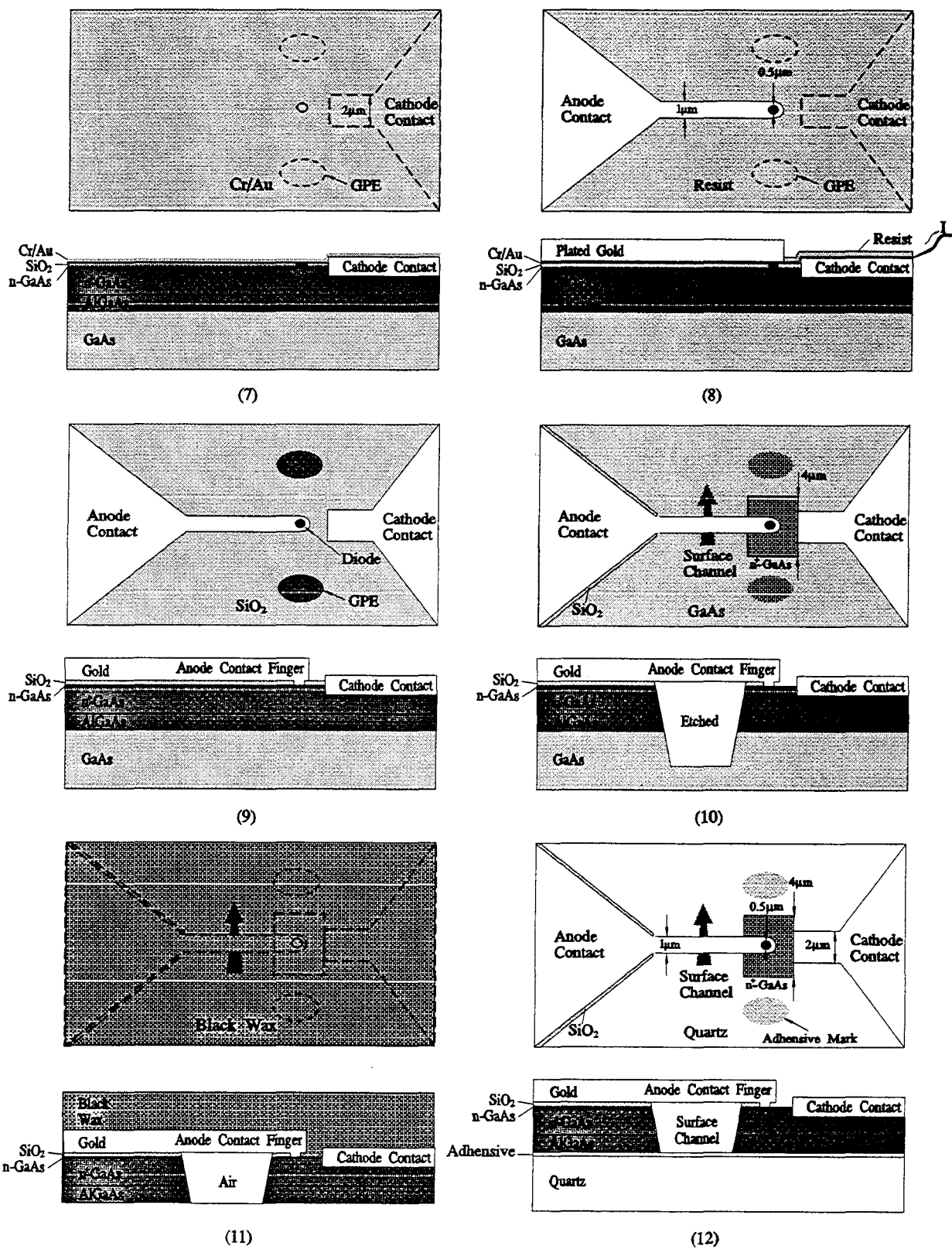(7)

(8)

(9)

(10)

(11)

(12)

Fig. 2.6 Fabrication procedures for planar Schottky diodes (continued).

UVA to show the assumption correct and the GPEs could greatly improve the I-V characteristics of the diodes.

The SiO_2 in the Galvanic Protection Eyes is completely etched away using the fluorine RIE. It is important to make sure that the epitaxial GaAs in the GPEs is also damaged by the RIE etching to keep away the galvanic current from entering the anode during plating. After the GPEs are formed, the resist is removed.

The thin layer in the bottom of the diode well is then etched by using buffered HF solution. The etching rate is another important parameter in this process. Insufficient etching may cause open-circuited or high resistance while overetching may result a larger diode.

(6) First platinum and then gold are electroplated to form the diode and fill the anode well. The anode has a diameter of $0.56\,\mu$m in the first batch and a diameter of $0.5\,\mu$m in the second batch. A very thin layer of Pt/Au will also be formed in the GPEs.

(7) A very thin layer of chromium and gold is deposited on the entire wafer for electroplating current to flow.

(8) Then photoresist is applied to form the anode contact-finger pattern and 2-μm thick gold is electroplated through the opening of photoresist.

(9) The resist is removed. The gold is sputtered away using turbo sputter system and the chromium layer is etched away using chromium etchant. The chromium etchant will also attack the Pt/Au layer in the GPEs and leave two holes on each side of the diode.

(10) Photoresist is applied again to form the surface channel pattern and SiO_2 and GaAs are etched away to form the isolating trench. The GaAs layers are first etched using Cl_2-RIE to thin the GaAs layers down to 10-20 μm, then etched using the (NaOH:H_2O_2:H_2O=1:1:10) selective etchant. This two-process GaAs etching is to avoid uneven etching for thick layers.

(11) A thick layer of black wax is applied on top as superstrate to protect the surface. Then the highly-doped GaAs substrate is etched away. The surface channel and the GPE holes are filled with wax during this process.

(12) The whole structure is glued on a 30-μm thick quartz substrate using a thin (2-3 μm) layer of optical adhesive. The GPE holes are molded by the adhesive and located on the quartz at each side of the anode finger. These circular GPE patterns can be seen in Figure 2.9 and 2.10. The black wax superstrate is then removed in acetone.

2.8 Equivalent Circuit for Planar Schottky Diode

Major circuit elements in a planar Schottky diode is shown in Figure 2.7(a). The surface channel eliminates the conducting path between the anode contact capacitance, C_{SC}, and the cathode contact. Therefore, instead of having a bigger capacitance, C_{SC}, it is replaced by the series combination of C_a and C_p which is the substrate capacitance. Because C_p is much less than C_a, the series capacitance is greatly reduced. The shunt C_{SC} contribution is not significant because it is now distributed across an air dielectric (ε_r=1) instead of GaAs (ε_r=13.1). C_p is also reduced by using quartz as substrate instead of semi-insulating GaAs. However, the poor thermal conductivity of fused quartz (1.4 W/(m·°K) at 273°K)
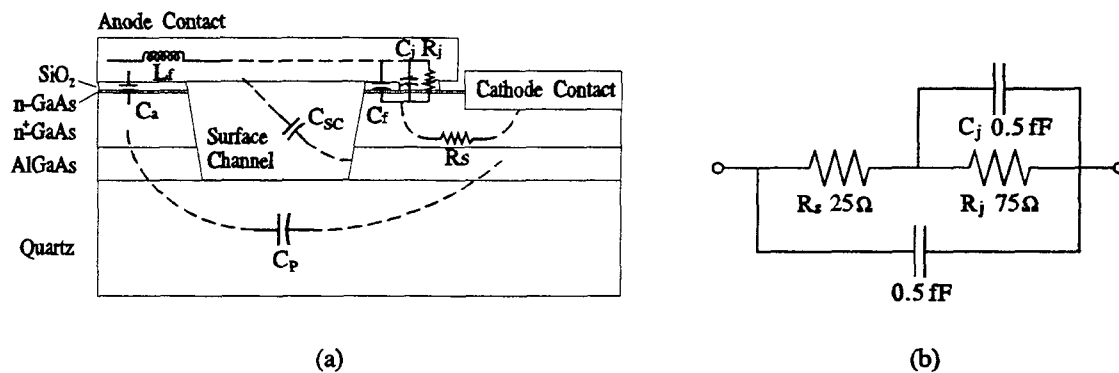

(a)   (b)

Fig. 2.7 (a) The cross section of the planar Schottky diode and equivalent-circuit elements; and (b) the equivalent circuit used for the sideband-generator design.

may cause more heating problems than GaAs (50 W/(m·°K) at 273°K for a doping concentration of $7 \times 10^{15} cm^{-3}$) [139]. Though the thermal properties of GaAs Schottky diodes on quartz substrate are still not well studied, experiments show heating effects more obvious for diodes on quartz substrate than the equivalent diodes on GaAs [128,149]. It is possible to improve the thermal properties of planar Schottky diodes by using c-axis crystalline quartz (thermal conductivity = 12 W/(m·°K) at 273°K) [139] as substrate or by cooling with liquid nitrogen [140,141].

Shunt capacitances from the contact finger, C_a and C_f, are further reduced by reducing the width of the finger and etching the surface channel as close as possible to the anode. The width of the finger is 1 μm and the distance between anode and channel is 2 μm. C_f can be further reduced by increasing the thickness of SiO_2, however, it will also increase the difficulties of anode formation. The finger inductance, L_f, can be calculated and helpful in tuning out the parasitic capacitances.

One of the distinct advantages in planar Schottky diodes is that the ohmic contacts are very close to the anodes, the electrical path length is greatly reduced. Therefore, the series resistance, R_s, and series inductance will be much less. McKinney et al. [142] reported a detailed analysis of series resistances for planar Schottky diodes. A thin layer of n-GaAs and a highly-doped n^+-GaAs layer should be to reduce the series resistances.

The resistive losses at ohmic contacts are further reduced when the planar Schottky diodes are used in a quasi-optical grid. Because the AC current paths are limited to the very small dimensions of the unit cells unlike the single-chip diode integrated with antenna or whisker contact which the AC current has to flow through the entire structure, the RF resistive losses can be reduced.

Figure 2.7 (b) shows the equivalent circuit used to model the planar Schottky diode. The element values shown are estimated and used in the design of sideband

generators [108]. Due to the experimental nature of the diode, this model can only approximate the actual diode impedance. Later on, the estimated series resistance, R_s=25 Ω, is replaced by a measured value, R_s=14 Ω, for analysis.

2.9 THE 6×6 DIODE-GRID ARRAYS

These grid multipliers are fabricated on a 30-μm thick fused-quartz substrate. It is a 6×6 array. Figure 2.8 shows the entire array. The active area is 420 μm×420 μm and the size of the entire chip is 700 μm×700 μm. Three diodes are in series from the top or bottom bias line to the center bias line. The adjacent bow-ties are not connected except the center row. The diodes in the top and bottom halves of the grid have opposite polarities. This is because the grid was originally designed as a sideband generator [108]. When the grid is used as a frequency multiplier, the polarity change causes an undesired null in the middle of the output beam. Figure 2.9 shows a closer look of the grid.

2.10 UNIT CELLS

Figure 2.10 shows the bow-tie-shaped metal pattern used for the unit cell. The Schottky diode junction is located at the center of the unit cell. The size of a unit cell is 70 μm×70 μm. The total length of the contact finger is 14 μm and the widths of the anode finger and the cathode finger are 1 μm and 2 μm, respectively. The relative dielectric constant of quartz is ε_r=3.78. The dark circular shadows located on each side of the contact-finger are the adhesive-molded GPE-holes as mentioned before.

2.11 DESIGN APPROACH

2.11.1 UNIT-CELL WAVEGUIDE APPROACH

These diode-grids are originally designed for sideband generators, therefore, before we analyze these grids as multipliers, it is necessary to mention the design
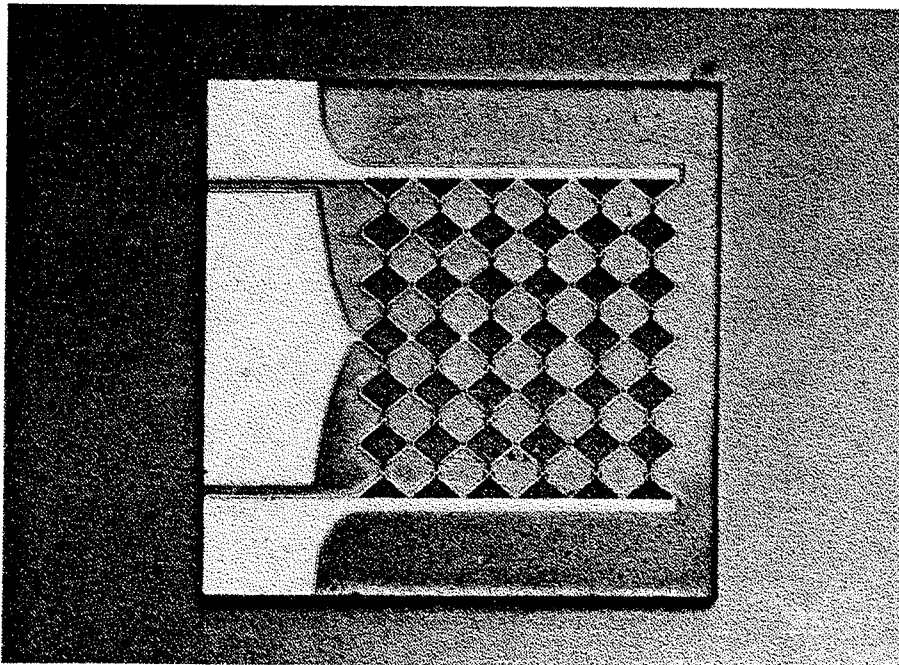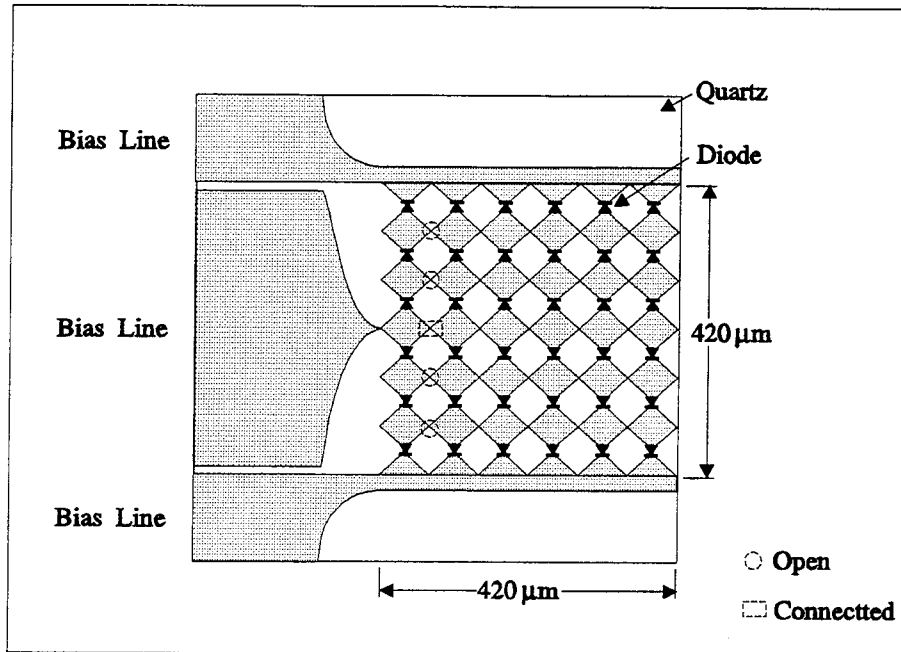
Fig. 2.8 The grid frequency doubler. It is a 6×6 array. The adjacent bow-ties are not connected except the center row. The diodes in the top and bottom halves of the grid have opposite orientations.
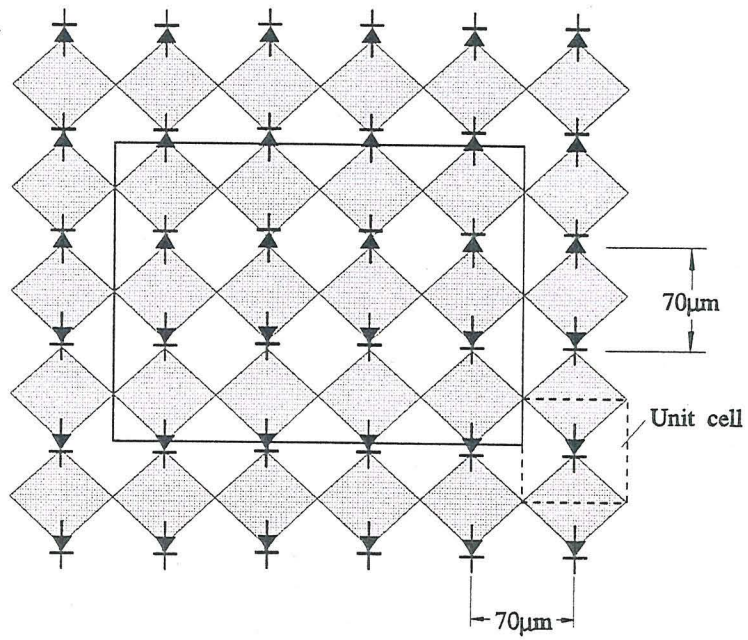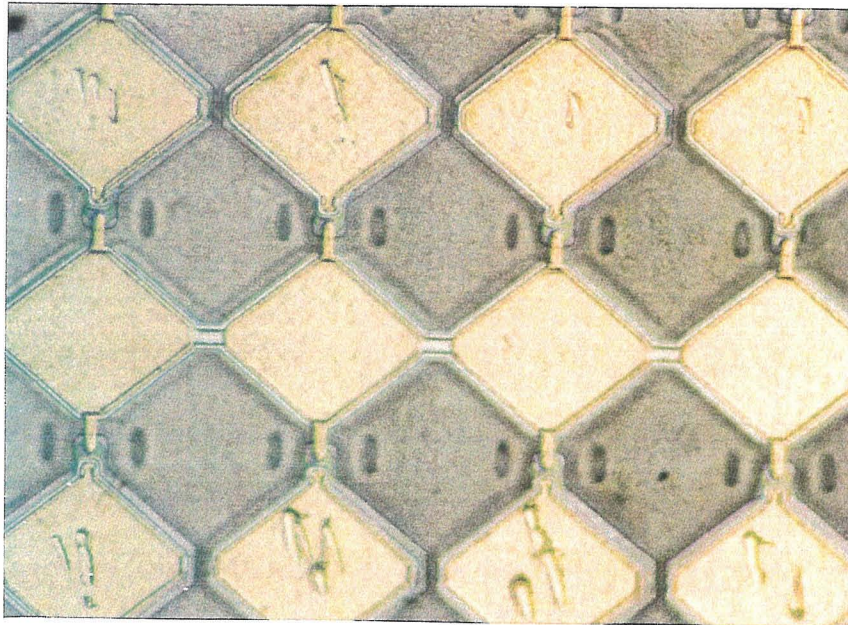
Fig. 2.9 A closer look of the grid frequency doubler. The rectangular area indicated in the drawing is shown in the picture. The dashed line indicates the unit cell used for design and analysis. The diodes in the top and bottom halves of the grid have opposite orientations.
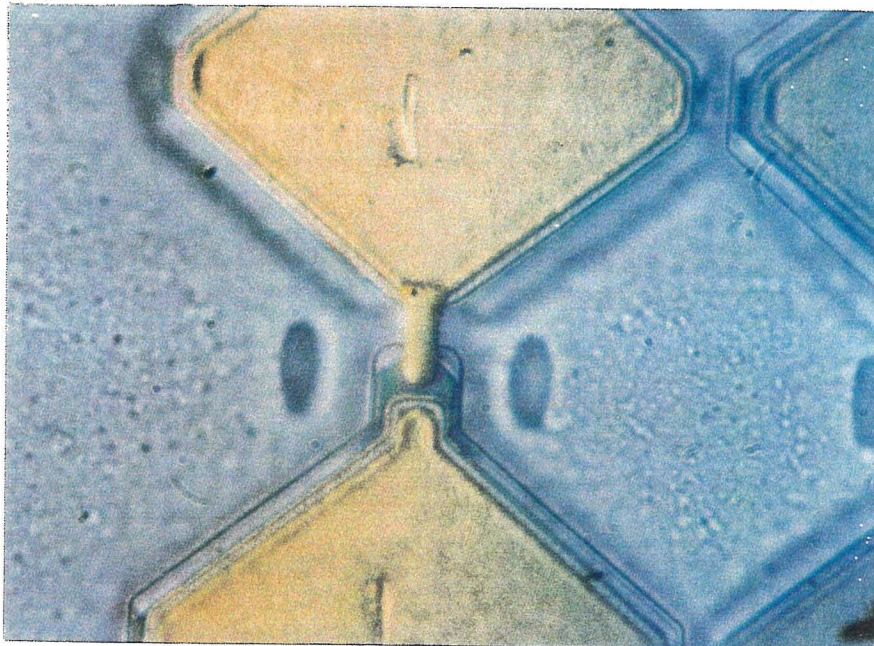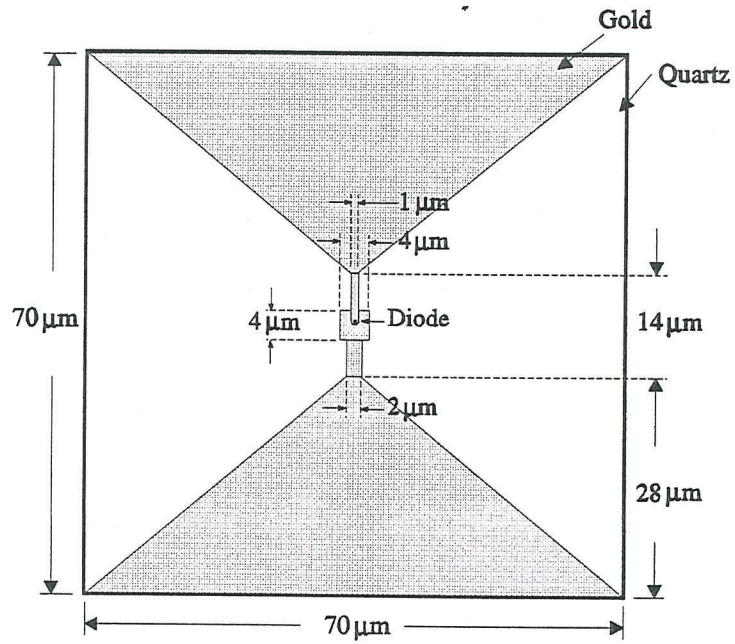
Fig. 2.10 The unit cell of the grid multiplier. The size of a unit cell is $70\,\mu m \times 70\,\mu m$.

methods used for these diode-grids. The design details are described in Hacker's thesis [108] and only the general ideas and final results will be mentioned here.

The configuration of sideband generators is shown in Figure 2.4. Diodes are loaded periodically in the grid and each diode defining a unit cell of the grid. There is a flat mirror behind the grid to act as a reactive tuning element. By optimizing the dimensions and the metal pattern of the unit cell as well as the dielectric constant and the thickness of the grid substrate, the reflection coefficient can be optimized for the incident signals at the operating frequencies.

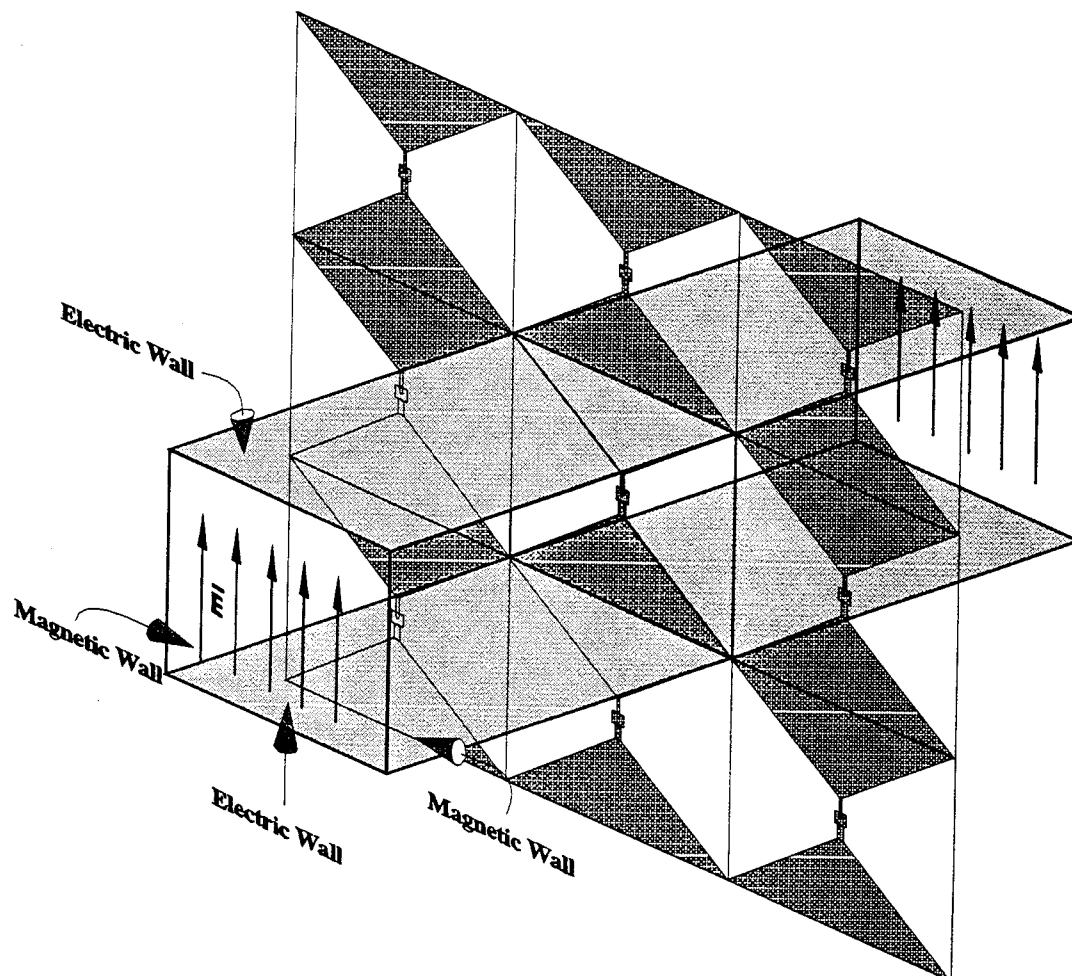Each diode in the array is presented with an embedding impedance which is

Fig. 2.11 The unit-cell waveguide. For a vertically-polarized electric field, the unit-cell waveguide has magnetic walls on the sides and electric walls on the top and bottom.

determined by the metal pattern repeated throughout each unit cell. By assuming an infinite grid with a uniform plane wave normally incident upon the grid, the symmetry allows us to replace the walls of the unit cell in the grid with electric and magnetic walls to form an equivalent unit-cell waveguide. Therefore, the analysis of the entire grid can be reduced to a simpler analysis of the equivalent unit-cell waveguide. For a TEM incident wave with vertically-polarized electric field, the unit-cell waveguide has magnetic walls ($H_{\text{tangential}} = 0$) on the sides and electric walls ($E_{\text{tangential}} = 0$) on the top and bottom, as shown in Figure 2.11. The propagating mode in the unit-cell waveguide is TEM and the evanescent modes couple to the currents flowing in the metal patterns. The AC current paths are limited in the unit cell by symmetry.

The equivalent unit-cell waveguide incorporated with a device can be presented as a simple transmission-line model to decide the performance of the entire grid, once we know the equivalent circuits for the device and the embedding impedance of the metal pattern. The embedding impedance of the metal pattern can be solved either by techniques developed for the analysis of structures placed inside waveguides, or by numerical three-dimensional finite-element methods. Because of the assumption of the grid to be infinite extended, the edge effects of the grid are ignored. From the past experiences, the unit cell solutions have been providing reasonable accuracy for a grid with sizes of 4×4 or bigger.

2.11.2 EMBEDDING IMPEDANCES - EMF ANALYSIS

For simple geometric metal patterns like strips or bow-ties, the embedding impedance presented to the terminals of the diode in the unit cell can be solved by the EMF analysis first described by Eisenhart and Kahn [119], and later developed by Weikle [120] and De Lisio at Caltech using Galerkin's moment method to find the current distribution on the metal patterns. Bundy *et al.* [143] used the same approach to develop a full-wave analysis to determine the driving impedances for any active devices embedded in the grid structure with more com-

plicated metal patterns.

For a unit cell with a vertical strip, the equivalent element in the transmission-line model is a shunt inductor, as shown in Figure 2.12, with reactance Z_L:

$$Z_L = \frac{2b}{a} \sum_{m=1}^{\infty} \cos^2\left(\frac{m\pi}{2}\right) \operatorname{sinc}^2\left(\frac{m\pi w}{2a}\right) \left(Z_{m0}^{TE+} \parallel Z_{m0}^{TE-}\right), \qquad (2.2)$$

where $Z_0^{TEM} = \sqrt{\mu/\epsilon}$, and $Z_{mn}^{TE} = \omega\mu/k_z$, and k_z is the propagation constant and is given by

$$k_z = \sqrt{\omega^2\mu\epsilon - \left(\frac{m\pi}{a}\right)^2 - \left(\frac{n\pi}{b}\right)^2}. \qquad (2.3)$$

For a bow-tie metal pattern in a unit cell, the embedding impedance resembles a shunt section of transmission line, as shown in Figure 2.13. The shunt transmission line has a characteristic impedance, Z_{BT}, and electrical length, θ_{BT} which are determined by [120]:

$$Z_{BT} = \sqrt{\frac{Z}{Y}}, \qquad (2.4)$$

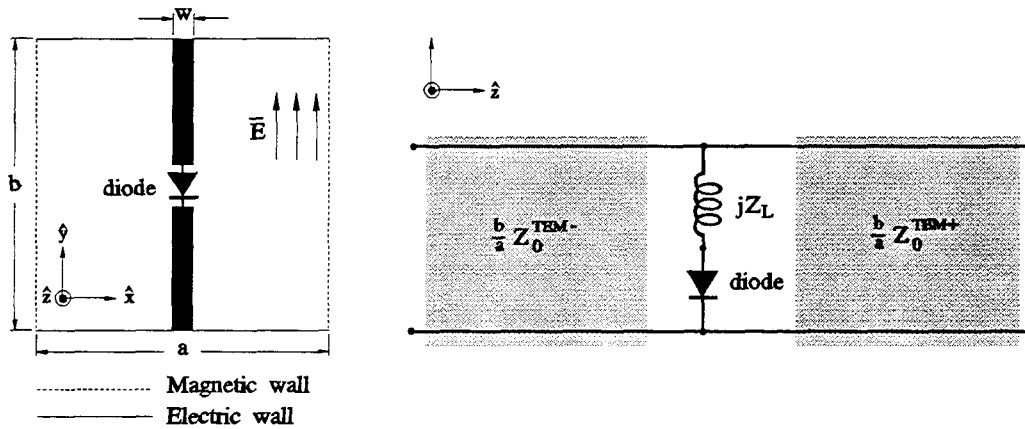$$\theta_{BT} = \sqrt{ZY}, \qquad (2.5)$$

Fig. 2.12 A unit cell with a vertical strip and the simplified equivalent-circuit elements for the unit-cell waveguide. The equivalent circuit of the diode can be incorporated.

where

$$Z = \frac{1}{ab} \sum_{\substack{m=1 \\ n=0}}^{\infty} 2\epsilon_{0n} \frac{k_c^2}{k_x^2} A_{mn}^2 \left(Z_{mn}^{TE+} \parallel Z_{mn}^{TE-} \right), \tag{2.6}$$

$$A_{mn} = \frac{\int_0^b \int_0^\phi \frac{\cos(k_x y \, \tan\psi)}{\sqrt{\sin^2\phi - \sin^2\psi}} \cos k_y y \, d\psi dy}{\int_0^\phi \frac{d\psi}{\sqrt{\sin^2\phi - \sin^2\psi}}}, \tag{2.7}$$

$$Y = \frac{1}{ab} \sum_{\substack{m=0 \\ n=1}}^{\infty} 2\epsilon_{m0} \frac{k_c^2}{k_y^2} B_{mn}^2 \left(Y_{mn}^{TM+} + Y_{mn}^{TM-} \right), \tag{2.8}$$

$$B_{mn} = \frac{\int_0^a \int_0^\theta \frac{\cos(k_y x \, \tan\xi)}{\sqrt{\sin^2\theta - \sin^2\xi}} \cos k_x x \, d\xi dx}{\int_0^\theta \frac{d\xi}{\sqrt{\sin^2\theta - \sin^2\xi}}}, \tag{2.9}$$

and $Y_{mn}^{TM} = \omega\epsilon/k_z$, $k_x = m\pi/a$, $k_y = n\pi/b$, $k_c^2 = k_x^2 + k_y^2$, and

$$\epsilon_{mn} = \begin{cases} 1, & \text{if } m = n; \\ 2, & \text{otherwise.} \end{cases} \tag{2.10}$$
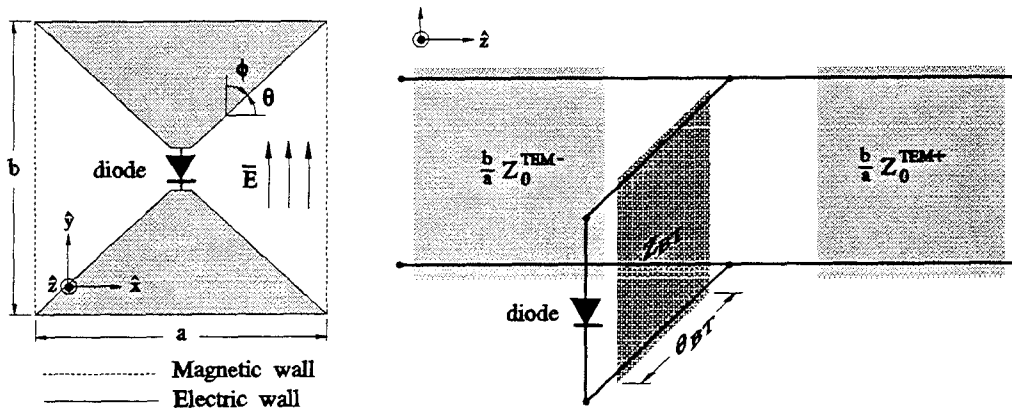

Fig. 2.13 A unit cell with a bow-tie pattern and the simplified equivalent-circuit elements for the unit-cell waveguide. The equivalent circuit of the diode can be incorporated.

In the sideband generators, the bow-tie metal pattern is chosen to achieve a broader-band operation. Because the embedding impedance of the bow-tie pattern resembles a shunt section of lower-impedance transmission line with an electrical length of a fraction of a wavelength, it has a broader bandwidth than a strip pattern if the junction capacitance is small. However, choosing the bow-tie will also degrade the reflection losses at the operating frequencies. A combination of a strip and a bow-tie pattern can be a tradeoff option for bandwidth and return losses. Due to the planar diode structure, the contact-fingers are required to reduce the parasitic capacitances. Therefore, we can use the innate contact-fingers as part of the strip patterns to help tuning out the diode capacitances along with the bow-tie to achieve a wider bandwidth with reasonable return losses.

2.11.3 EMBEDDING IMPEDANCES - THREE-PORT EXTRACTION

However, the EMF analysis can only provide a gross approximation to the actual impedance for a pattern with a combination of a short-strip and a short-ended bow-tie. Intuitively, it is expected the narrow strips of contact-fingers to add some inductance in series with the diode, and the short-ended bow-tie to have a shorter electrical length than that calculated by the EMF method in the shunt transmission line. To verify this assumption, the Hewlett-Packard High Frequency Structure Simulator (*HFSS*), a 3-D finite-element electromagnetic-wave solver, is used with the three-port embedding-impedance extraction technique developed by Hacker [108] to extract the embedding impedance of this complex geometry of the unit cell.

Figure 2.14 shows the quarter-piece structure used in *HFSS* for three-port embedding-impedance extraction. Port 1 and port 2 are the front- and the back-ports of the unit-cell waveguide, and port 3 which presents the driving point of the diode is connected to a short section of a rectangular coaxial waveguide. Because the symmetry between the left and right, the unit cell can be reduced to

a half piece by placing a vertical magnetic wall in the center of the unit cell. In order to simplify the analysis and shorten the computation time, the half-cell can be further reduced to a quarter piece by assuming the anode- and the cathode-finger widths the same. This symmetry allows us to place a horizontal electric wall in the center and the driving point of diode will be exposed at the edge of the quarter-piece unit-cell waveguide. The short section of the rectangular coaxial waveguide connected to the driving point is well-defined with a known propagation constant and a known waveguide impedance.

Simulations over the frequency range of interest are done in the 3-D structures to solve the s-parameters. Post-processing on the s-parameters is performed to remove the effect of adding the coaxial waveguide like de-embedding the phase shift and renormalizing s-parameter matrix to the free-space impedance. The final s-parameter matrix can be compared with the s-parameter matrix of our intuitive circuit model whose element values can be first approximated by the EMF analysis. Then the element values can be fine-tuned until the model s-
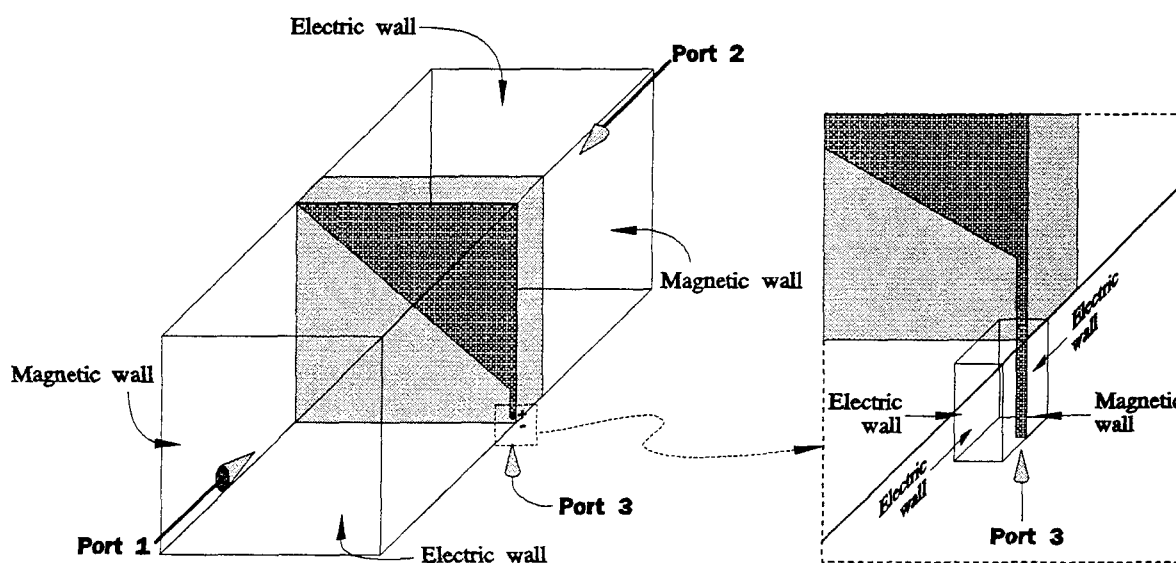

Fig. 2.14 The three-port quarter-piece waveguide with proper boundary conditions and the detail view of the rectangular coaxial waveguide connected to the driving point of the diode.

parameter matrices agree with the *HFSS* results.

A more convenient way to solve the embedding impedance is to utilize the calibration method used for a one-port network analyzer. A mirror is placed behind the grid which means short-circuited the port 2 in the circuit model and the structure becomes a two-port network with the *s*-parameter matrix **S**:

$$\mathbf{S} = \begin{pmatrix} s_{11} & s_{13} \\ s_{31} & s_{33} \end{pmatrix}. \tag{2.11}$$

We can now apply the calibration method for a one-port network analyzer. A series of three electrically distinct loads are placed across the port 3 connected to the driving point of the diode. This reduces the structure to a one-port with port 1 excited by a TEM incidence onto the grid. Typically these loads would be a short circuit, an open circuit, and a matched load. *HFSS* version 1 did not provide lossy material to be specified, so the matched load must be replaced by a delayed short which can be a shorted coaxial rectangular waveguide. Hacker [6] in his simulations used this method. *HFSS* version 2.0 and 3.0 permit resistive lossy materials or resistor-type boundary conditions, so a matched load can be applied across the port 3.

Simulations of the structure over the frequency range of interest are performed for each of the three loads solving three one-port *s*-parameter files, e_m, e_s, e_o corresponding to the matched termination, short-circuit, and open-circuit, respectively. These calibration *s*-parameters can then be used to find the two-port *s*-parameters of the grid using

$$s_{11} = e_m \tag{2.12}$$

$$s_{33} = \frac{e_o + e_s - 2e_m}{e_o - e_s} \tag{2.13}$$

$$s_{13}s_{31} = \frac{2(e_o - e_m)(e_s - e_m)}{e_s - e_o}, \tag{2.14}$$

and reciprocity ($s_{13} = s_{31}$) is applied to solve s_{13}. The **S** matrix then is compared with the intuitive circuit model to fine-tune the element values. Since the three-

port matrix (which has 4 variables when reciprocity and symmetry are applied: $s_{33}; s_{11} = s_{22}; s_{12} = s_{21};$ and $s_{13} = s_{31} = s_{23} = s_{32}$) now is replaced by a two-port matrix (with $s_{13} = s_{31}; s_{11};$ and s_{33}), the analysis becomes easier.

2.12 DESIGN FOR SIDEBAND GENERATORS (LINEAR)

Comparison of the s-parameters from the intuitive circuit model and the s-parameters from the *HFSS* shows our assumption correct. Figure 2.15(a) shows the fine-tuned values of the equivalent circuit in the frequency range from 1 THz to 2 THz, and (b) shows the comparison of the results from the equivalent circuit and the de-embedded s-parameters solved by *HFSS*. The values computed by the EMF method which assumes a bow-tie in the same size unit cell are shown in parentheses. As expected, the electric length of the bow-tie shunt transmission line is shortened corresponding to the physically shortened bow-tie and the total series inductance contributed by the contact-fingers is 2.9 pH.
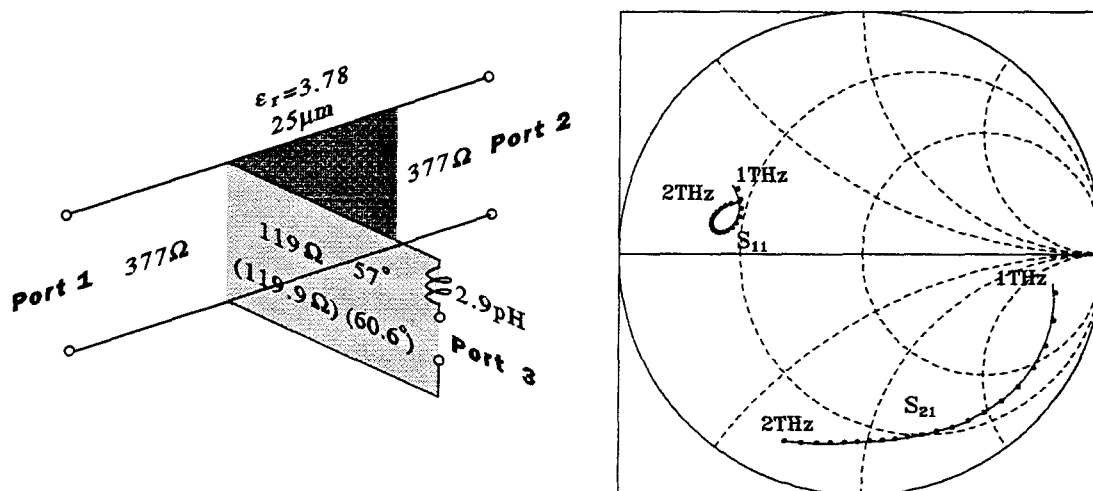

Fig. 2.15 (a) The equivalent circuit used to simulate the bow-tie grid with diode fingers for THz sideband generators. The total inductance contributed by the contact-fingers is 2.9 pH and the shunt section of the bow-tie transmission-line has an impedance of Z_{BT} =119 Ω and an electrical length of θ_{BT} =57° at 1.6 THz. (b) The s-parameters on a Smith Chart from *HFSS* simulations (•) and from the equivalent circuit of (a) (solid lines) with a short-circuit load at port 3.

The configuration of sideband generators, shown in Figure 2.4, has a flat mirror behind the grid to tune the reflection coefficient null to the desired frequency. The mirror provides a shunt short-circuited free-space transmission line in the equivalent circuit and the position of the mirror decides the electrical length. The equivalent circuit used for the planar diode is shown in Figure 2.7(b). The quartz substrate used in this design has a thickness of 25 μm and a relative dielectric constant of ε_r=3.78. By optimizing the dimensions and the metal pattern of the unit cell as well as the mirror position behind the diode-grid, the reflection coefficient can be optimized for the incident signals at the operating frequency. Figure 2.16 shows theoretical reflection coefficient from 1 THz to 2 THz. The null of the reflection coefficient can be tuned from 1.5 THz to 1.9 THz by adjusting the position of the mirror behind the grid. The electrical length between the grid and the mirror for the null at 1.6 THz is 23°. The total inductance contributed by the anode- and cathode-contact-fingers, which are assumed to have the same
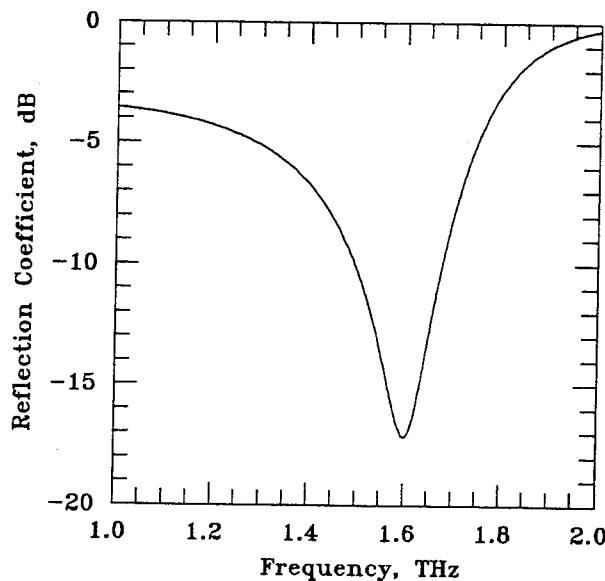

Fig. 2.16 Theoretical reflection coefficient for the diode-grid used as a sideband generator. The null can be tuned from 1.5 THz to 1.9 THz by adjusting the position of the mirror behind the grid. The electrical length between the grid and the mirror at 1.6 THz is 23°.

widths of $2\,\mu$m, with a total length of $14\,\mu$m is $2.9\,$pH. The bow-tie shunt transmission line has an impedance of Z_{BT} $=119\,\Omega$ and an electrical length of θ_{BT} $=$ $57°$.

2.13 LINEAR ANALYSIS FOR GRID MULTIPLIERS

We proposed to use these diode-grids as frequency doublers for the fundamental input in the frequency range from $500\,$GHz to $600\,$GHz considering measurement simplicity, equipment/component availability and past experiences. However, the sideband generator is designed for LO frequencies of $1.5878\,$THz $(190\,\mu$m$)$, $1.629\,$THz $(184\,\mu$m$)$ and $1.675\,$THz $(179\,\mu$m$)$ provided by gas lasers. Therefore, the *HFSS* simulations and the equivalent circuits in [108] performed are for the frequency range of 1-$2\,$THz. At lower frequencies (below $1.5\,$THz), the differences between the *HFSS* results and the equivalent circuit used the fine-tuned element values become noticeable. So it is necessary to re-examine the linear equivalent circuit for multiplier applications in the frequency ranges of interest. Also due to some changes made on the diode structure during fabrication, the equivalent circuit for the planar diode has been modified as shown in Figure 2.17. A 30-μm thick quartz substrate is used instead of $25\,\mu$m.

Simulations at frequencies from $200\,$GHz to $1.5\,$THz have been done and post-processes as well as the three-port extraction techniques are performed on the s-parameters to remove the effect of adding the rectangular coaxial waveguide
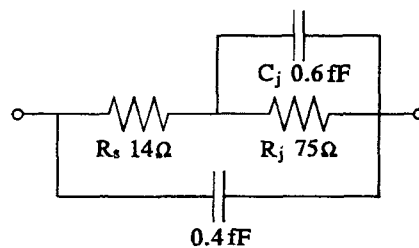

Fig. 2.17 The modified equivalent-circuit of the planar Schottky diode used in the multiplier diode-grids.

portion. The *HFSS* version 3.0 is used to provide the required loads - a short circuit, an open circuit, and a matched load. We used the resistor-type boundary condition at the port 3 as a matched load.

Two quarter-piece waveguides are used in *HFSS*, shown in Figure 2.18, to simulate the top half structure where the anode contact-finger has a width of 1 μm, and the bottom half where the cathode contact-finger has a width of 2 μm. The length of the anode finger is 7 μm and the cathode finger is shortened to 5 μm responding to the real physical length. The extra inductance contributed by the center conductor of the coaxial waveguide inserted into the unit-cell waveguide is deducted later. A piece of GaAs is placed behind the metal at the driving point to imitate the n-GaAs exposed around the diode. The GaAs piece has a relative dielectric constant of ε_r=13.1 and a thickness of 3 μm.

Figure 2.19 shows (a) the unit-cell structure and (b) the corresponding fine-tuned equivalent-circuit elements. The total inductance contributed by the contact-fingers is 4.9 pH and the shunt section of the bow-tie transmission line
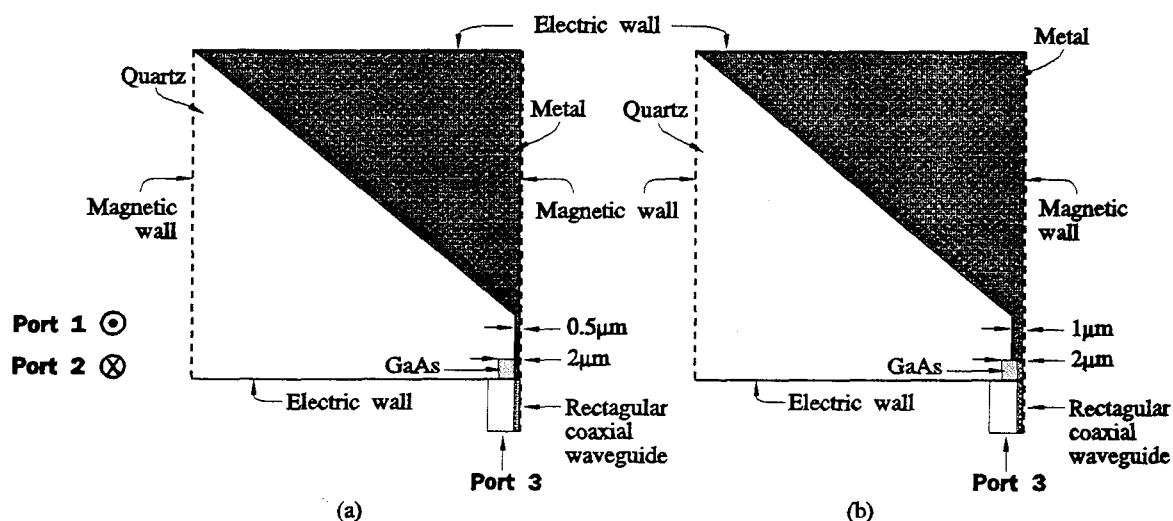
Fig. 2.18 Two quarter-piece unit-cells are used in *HFSS* to simulate (a) the top half structure where the anode contact-finger has a width of 1 μm, and (b) the bottom half where the cathode contact-finger has a width of 2 μm.
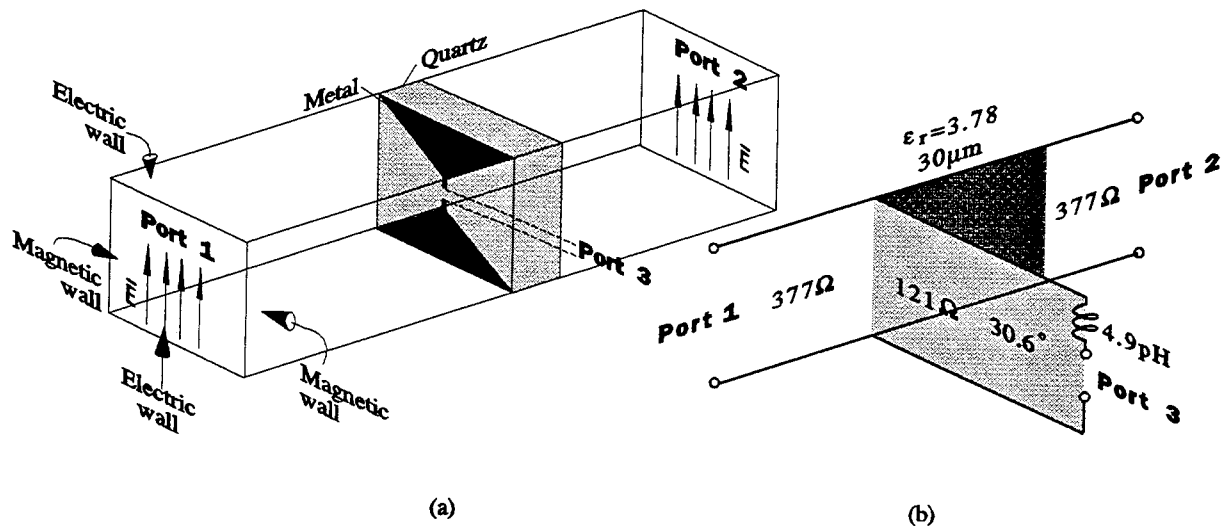
Fig. 2.19 (a) The unit-cell waveguide analysis for the diode grids, and (b) the equivalent circuit. The total inductance contributed by the contact-fingers is 4.9 pH and the shunt section of the bow-tie transmission line has an impedance of Z_{BT} =121 Ω and an electrical length of θ_{BT} =30.6° at 1 THz.

has an impedance of Z_{BT} =121 Ω and an electrical length of θ_{BT} =30.6° at 1 THz.

Figure 2.20 shows the s-parameters plotted on a Smith Chart from 200 GHz to 1.5 THz for *HFSS* simulation results and the results from the equivalent circuit of Figure 2.19(b) with a short-circuit load at port 3.

The equivalent circuit used for the planar Schottky diode, shown in Figure 2.17, is incorporated with the embedding impedance of the grid and the estimated reflectance and transmittance of the diode grids are shown in Figure 2.21. Although the junction-resistance in this equivalent circuit is estimated for 1 THz and it may vary from 300 GHz to 1.5 THz due to the skin effects, it is used before a more accurate theoretical model can be presented. The reflection for the input frequency, 500 GHz, is −3.1 dB and the transmission for the second-harmonic frequency, 1 THz, is −7 dB without impedance tuning or filters.
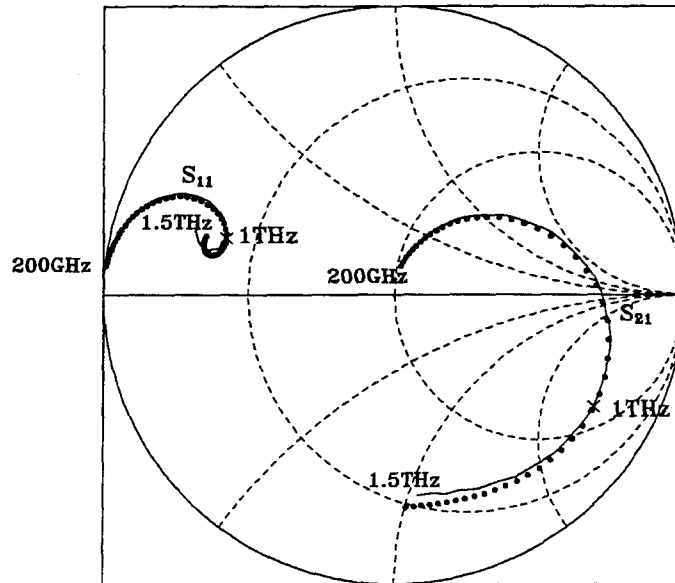
Fig. 2.20 The *s*-parameters plotted on a Smith Chart from 200 GHz to 1.5 THz for *HFSS* simulations (•) and the results from the equivalent circuit (solid lines) in Fig. 2.19(b), with a short-circuit load at port 3.
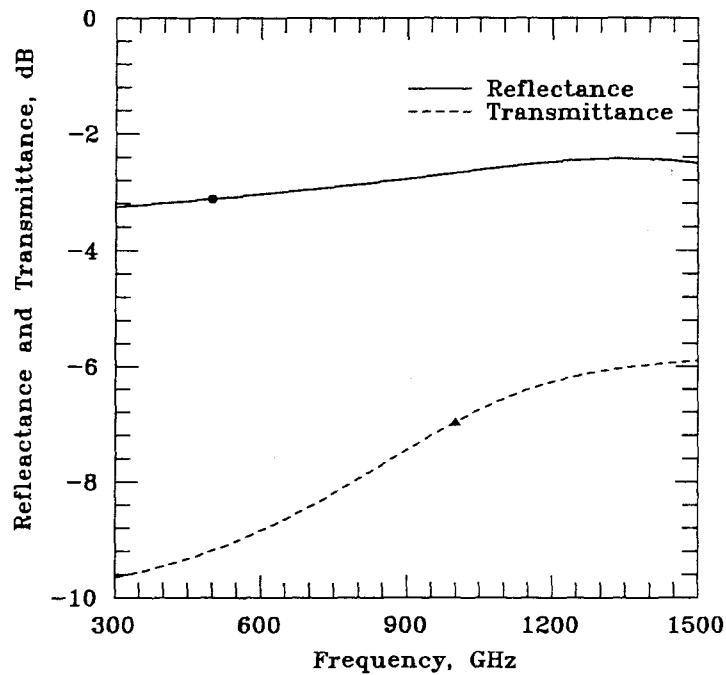

Fig. 2.21 The estimated reflectance and transmittance of the diode grids. The equivalent circuit used for the planar Schottky diode is in Fig. 2.17. The reflection at 500 GHz is −3.1 dB, and the transmission at 1 THz is −7 dB without impedance tuning or filters.

2.14 DC I-V Relationship

The RF equivalent-circuit element-values for the planar Schottky diodes strongly depend on the operating frequencies, pumping power, temperature and biasing conditions. Some models have been developed [133], however, can only provide limited information for the circuit elements which are decided without considering the parameters mentioned above. Due to the lack of information, DC element values are often used to allow us initiating the design and analysis for THz frequencies. These values used, of course, can only provide us an approximation and a feeling how the circuits will perform at RF and will vary significantly due to the skin effect, local temperature and the change of barrier heights with different bias or pumping power.

Figure 2.22(a) shows a typical I-V curve measured on one of the diodes with bias between −5.4 V and 1 V. Figure 2.22(b) shows the I-V relationship from

(a)   (b)

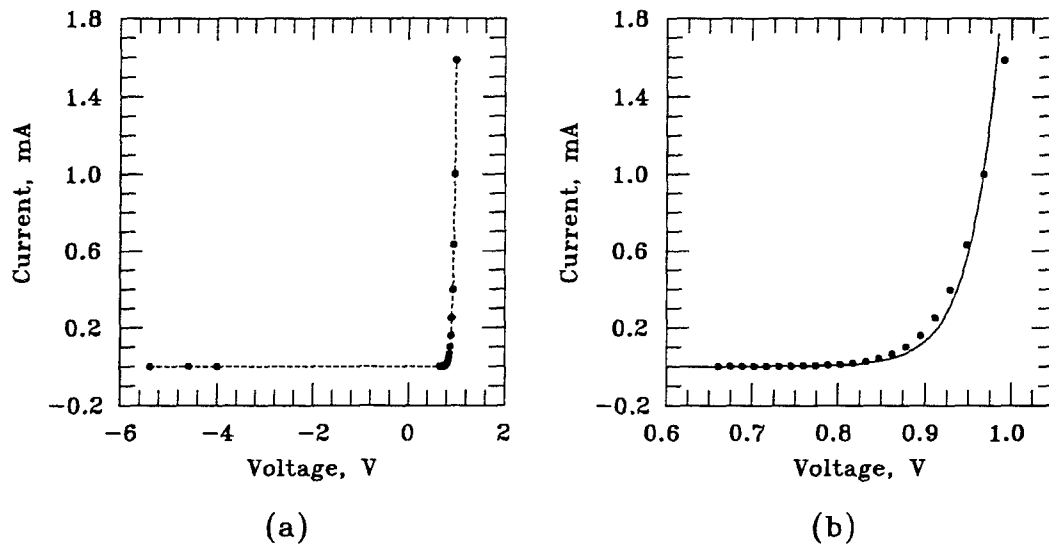**Fig. 2.22** (a) A typical measured DC I-V curve from -5.4 V to 1 V and (b) DC I-V relationship for forward bias. The measured data is shown by (•). The solid curve indicates a fitted I-V characteristic for diodes with an ideality factor η =1.1925 and a saturation current I_S = 1.3×10^{-16} A.

0.65 V to 1 V and the solid line indicates the fitted I-V characteristic for diodes:

$$I = I_S(e^{\frac{V}{\eta V_T}} - 1) \tag{2.15}$$

where I_S is the saturation current, V_T is the thermal voltage which is 25.2 mV at 20° C and η is the ideality factor for diodes. The ideality factor can be calculated by $\eta = \Delta V/(\ln(10)V_T)$ where ΔV is the voltage change for a decade change in current. The fitted I-V characteristic is plotted with the ideality factor $\eta = 1.1925$ ($\Delta V = 75$ mV for a change of current from $10\,\mu$A to $100\,\mu$A) and the saturation current $I_S = 1.3 \times 10^{-16}$ A.

The diode junction resistance can be expressed by

$$R_j = \frac{1}{\frac{\partial I}{\partial V}} \approx \frac{\eta V_T}{I} \tag{2.16}$$

assuming the diode is strongly forward-biased. For a forward current 0.4 mA with $V = 0.86$ V, the DC junction resistance is estimated to be 75 Ω, which is indicated in Figure 2.17.

The series resistance, R_s, can be derived from the DC I-V curves, given by

$$I = I_S(e^{\frac{V-IR_s}{\eta V_T}}) \tag{2.17}$$

where R_s may vary in different I-V regions. We measure the R_s with a current of 1.5 mA and use an average value, 14 Ω, in the equivalent circuit shown in Figure 2.17.

Table 2.1 shows the DC parameters for four different diode-grids. These parameters are obtained by probing each diode on the grids and averaged among the working diodes. In this table, R_s is the series resistance; V_o is the knee voltage with $1\,\mu$A current; ΔV is the voltage change for a decade change in current (I changes from $10\,\mu$A to $100\,\mu$A); and $V_{\text{Rev.}}$ is the reverse-biased breakdown voltage with $1\,\mu$A current.

Grid	Anode Diameter (μm)	Yield (%)	R_s (Ω)	V_o (mV)	ΔV (mV)	$V_{\text{Rev.}}$ (V)
1	0.56	100	13	725	75.5	5.6
2	0.5	100	15.2	730	75	5.42
3	0.5	94	16.1	732	76.2	5.92
4	0.5	83	10.8	699	81.6	2.77

Table 2.1 The DC parameters of diode-grids. R_s is the series resistance. V_o is the knee voltage with $1\,\mu$A current. ΔV is the voltage change for a decade change in current (I changes from $10\,\mu$A to $100\,\mu$A). $V_{\text{Rev.}}$ is the reverse-biased breakdown voltage with $1\,\mu$A current.

2.15 C-V RELATIONSHIP

In most of the cases, Schottky diode multipliers are reverse-biased to increase the frequency multiplying efficiencies since the diodes are designed as varactors. However, these diodes are originally planned for use as sideband generators and designed to be used under forward bias. Thus, these diodes have very thin epitaxial layer and the capacitance does not change significantly with reverse bias. Therefore, the frequency multiplication in these diode grids possibly comes from varistor multiplication, that is to say, from the nonlinear I-V relationship.

The junction capacitance at zero-bias, C_{j0}, can be calculated by

$$C_{j0} = \frac{\varepsilon_r \varepsilon_o \pi r^2}{d}\left(1 + \frac{bd}{r}\right) \tag{2.18}$$

where ε_r is the relative permittivity of GaAs; ε_o is the permittivity in vacuum; r is the diode radius; d is the depth of the depletion layer at zero-bias; and b is the edge-effect factor calculated numerically [144]. For GaAs, the edge-effect factor is 1.5.

Louhi [151] suggested an extra second-order correction term should be added to decide the junction capacitance for submillimeter wavelengths:

$$C_{j0} = \frac{\varepsilon_r \varepsilon_o \pi r^2}{d}\left(1 + b_1\frac{d}{r} + b_2\frac{d^2}{r^2}\right) \tag{2.19}$$

where $b_1 = 1.5$ and $b_2 = 0.3$.

The depletion depth, d, can be expressed as a function of bias as

$$d = \sqrt{\frac{2\varepsilon_r\varepsilon_o}{qN_e}(V_{\text{bi}} + V_r)} \qquad (2.20)$$

where q is the electronic charge; N_e is the doping density in the depletion region, which is 4×10^{17} cm^{-3}; V_{bi} is the built-in potential; and V_r is the reverse bias applied to the diode which is zero when calculating C_{j0}. The V_{bi} is defined as the potential difference between the top of the Schottky barrier and the edge of the depletion region where no bias is applied and can be determined by

$$V_{\text{bi}} = X_m - X_s \qquad (2.21)$$

where X_m and X_s are the work functions of the metal and the doped GaAs, respectively.

The junction capacitance of the diode at zero-bias, C_{j0}, is estimated to be 0.4 fF. There is a parasitic capacitance between the contact-finger and the active area, which is indicated as C_f in Figure 2.7, in parallel with the C_j. C_f can be decided by

$$C_f = \frac{\varepsilon_r\varepsilon_o A}{d} \qquad (2.22)$$

where ε_r is the relative dielectric constant of SiO$_2$; d is the height of the SiO$_2$ layer under the finger; and A is the contact area decided by the finger width and the distance between the diode and the edge of the surface channel. C_f is estimated to be 0.2 fF. Therefore, the total junction capacitance at zero bias is estimated to be 0.6 fF as shown in Figure 2.17.

C-V curves are measured by probing each diode in an array when other diodes are still connected with the one probed. The testing RF frequency is 1 MHz. The average capacitance of the diodes on the edge of the array stays the same (about 10 fF) when the bias changes from +0.4 V to −6 V. The average capacitance of the diodes in the center of the array varies from 19.2 fF to 18.4 fF

as the bias changes from +0.4 V to −6 V. These capacitances are much bigger than the estimated junction capacitance. The discrepancy is due to the fact that these diodes are still connected and therefore the measured capacitance is a result of all shunt capacitance in the array and the varactive capacitance is not significant to change it when the bias changes.

2.16 MEASUREMENTS

The measurements use the free-electron laser (FEL) as the input source in the Quantum Institute at the University of California , Santa Barbara. The free-electron laser is driven by high quality, relatively low energy electron beams from a recirculating electrostatic accelerators and capable of generating kilowatts of polarized radiation tunable from 120 GHz to 4.8 THz with a pulse width varied from 1 to 10's μs depending on the recirculation of the accelerator/electron beam line [145,146].

The measurement setup is shown in Figure 2.23. All of the components are aligned by a He-Ne laser. The spot size of the He-Ne laser at the focal point where the grid located is about 2 mm in diameter. The spot size of the He-Ne laser onto the bolometer is also about 2 mm in diameter which is smaller than the diameter of the waveguide-array filter window.

A certain fraction of the input power in the incident beam is split off into a reference detector. The beam splitter conserves the polarizations. A pyroelectric detector is used as the reference detector. The radiation from FEL then is focussed by an f/1.6 parabolic mirror at normal incidence on the grid. The distance between the focus of the mirror and the grid, L_a, is 15 cm. The input power is varied by inserting plexiglass attenuators before the beam splitter. The plexiglass attenuators also conserve the polarization.

The harmonic radiation from the grid is collimated by an f/1 parabolic mirror and propagates over 51 cm. The distance between the grid and the focus of the mirror, L_b, is 11 cm. A metallic-mesh Fabry-Perot interferometer in the

collimated beam is used to measure the frequency content of the radiation from the grid. The diameter of the interferometer is 15 cm which covers the entire collimated beam. Then the collimated beam is refocussed onto a liquid-helium-cooled Germanium bolometer by a parabolic mirror with an f number of 1. The distance between the mirror and the bolometer, L_c is 12.8 cm. All three parabolic
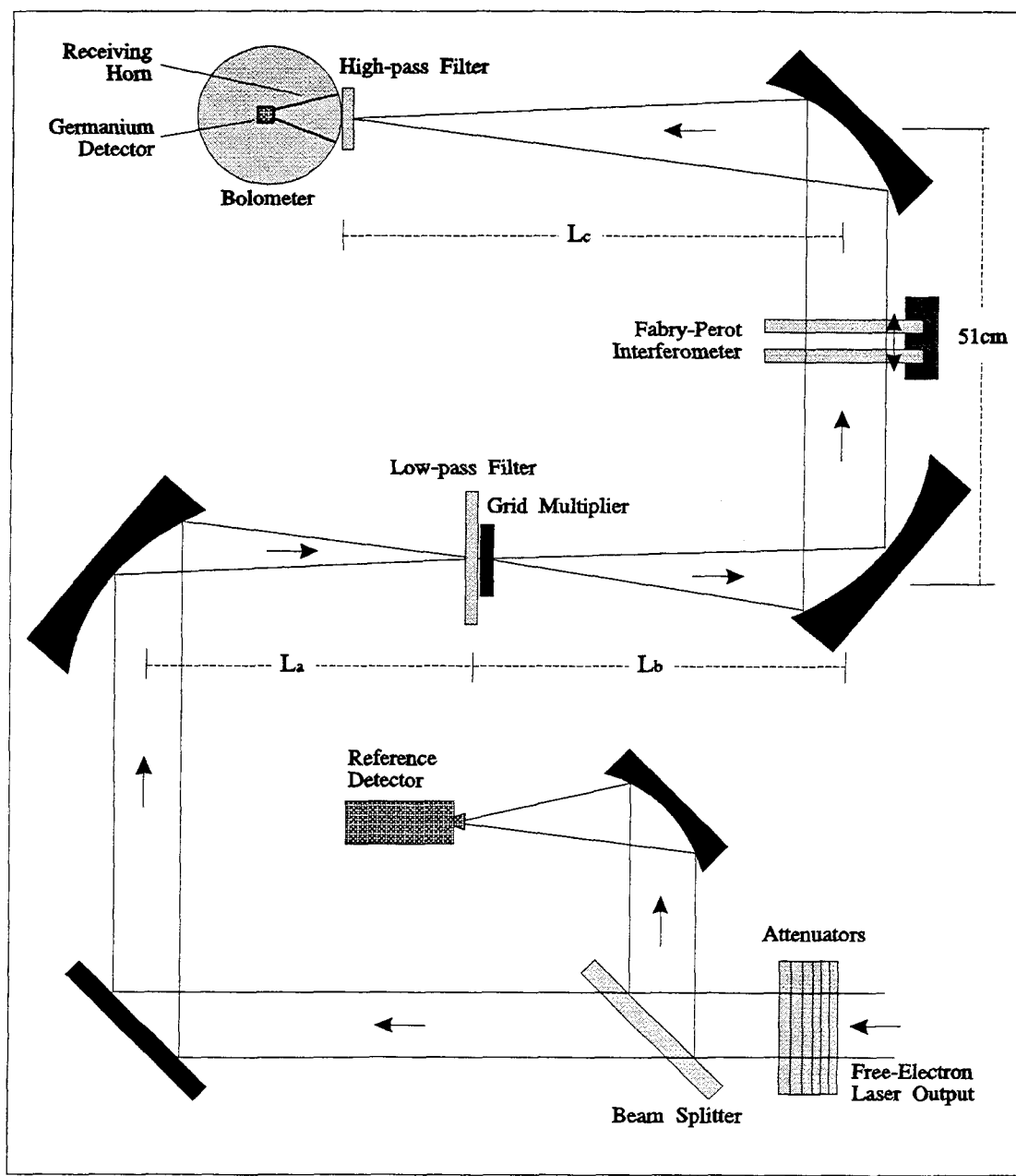

Fig. 2.23 Experimental arrangement.

mirrors are made of brass and polished down to 1-μm grit.

The bolometer has a theoretical responsivity of 10^5 V/W with a 200-μs response time. The transmittance of the input polypropylene window is 0.9 and that of the internal quartz scatter filter is 0.7. There is a winston cone placed as close as possible to the input window to collect the radiation and guide it to the small-area detector. The acceptance angle of the winston cone is $\pm 14°$ with an acceptance diameter of 17.2 mm. A waveguide-array cutoff filter is used as a high-pass filter and attached on the input window of the bolometer. The circular waveguides have a diameter of 200.7 μm and a length of 1.02 mm. The diameter of the array is 5.08 mm. Figure 2.24(a) shows the measured transmittances of the high-pass filter from 300 GHz to 1.5 THz. The transmittance at 1 THz is 0.76. The attenuation is more than 60 dB at 500 GHz which is measured separately by
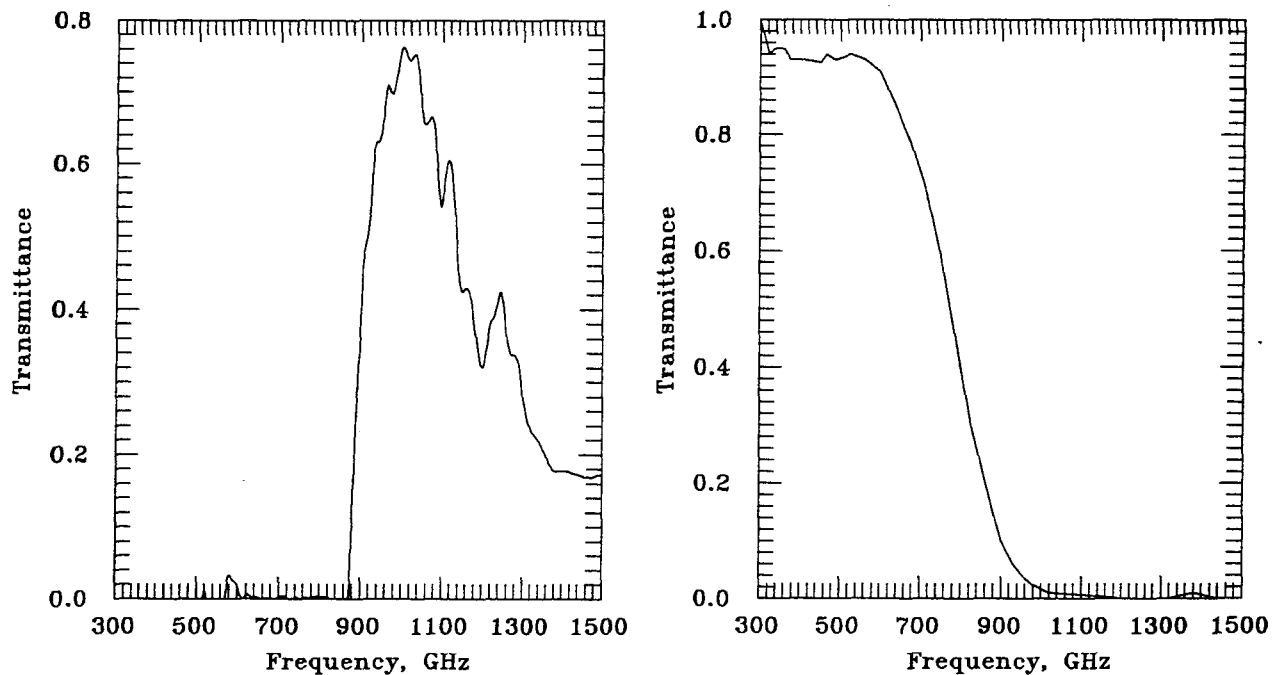

Fig. 2.24 Measured transmittances of (a) the waveguide-array filter and (b) the low-pass filter as a function of frequency. Courtesy of Andrea Markelz in the Department of Physics at the University of California, Santa Barbara.

tuning the FEL to 500 GHz.

An 8-layer metal-mesh filter is used as a low-pass filter on the input side. It has an attenuation more than 17 dB at 1 THz and a transmittance of 94% at 500 GHz. Figure 2.24(b) shows the measured transmittance of this low-pass filter. During the measurements, this filter was replaced by a better metal-mesh filter which has an attenuation more than 60 dB at 1 THz and a transmittance of 20% at 500 GHz. However, the transmittance curve as a function of frequency for the better low-pass filter is not available and the transmittances are only measured at 1 THz and 500 GHz.

Because of the strong attenuation caused by water absorption in the air, transmittance is measured by using FTIR techniques at room temperature in order to avoid waterlines and simplify the measurements. Figure 2.25 shows the measured transmittance in the fundamental frequency ranges, second harmonic frequency ranges and the third harmonic frequency ranges. At 500 GHz, 1 THz and 1.5 THz, the transmittances are 1, 0.96 and 1, respectively. Preliminary measurements were done at room temperature with humidity of 60%. Later the entire chamber was dehumidified to verify that the measurements are not suffered from water absorptions.

2.17 INPUT PULSES

The input pulses are first measured by switching the Pyroelectric detector to the fast setting (Figure 2.26). The average pulse-width at the fundamental frequency is 2.42 μs with a repeating rate of 0.75 Hz. The variance of pulse-widths is within 0.1 μs.

The Pyroelectric detector then is switched to the slow setting in order to increase the sensitivity. First, the FEL is tuned to the fundamental frequency, f_0, to measure the total incident energy on the focal plane with an electrically calibrated photoacoustic detector, which an absolute calibration of energy exists, manufactured by Thomas Keating Ltd.. Then the responsivities of the second
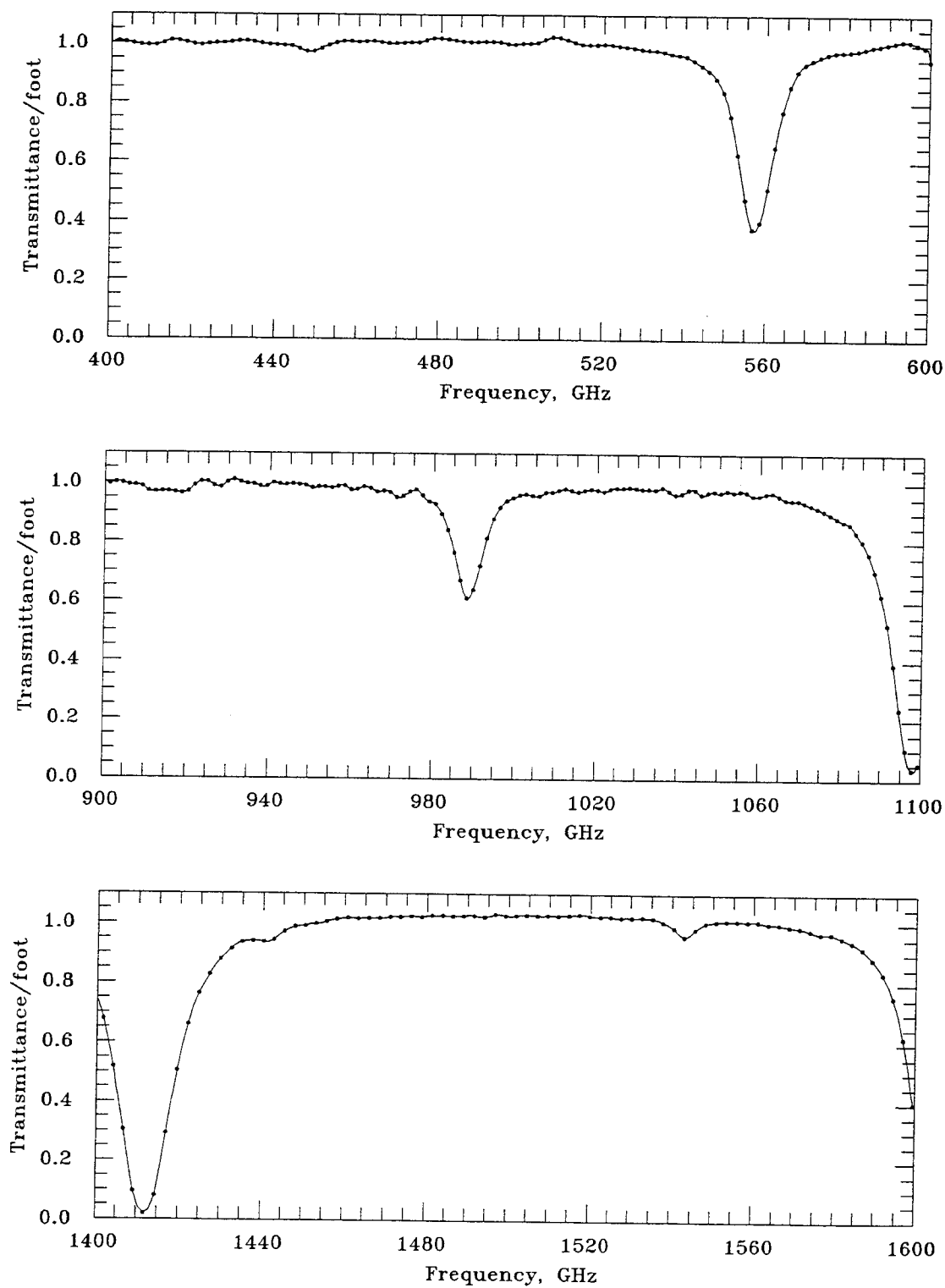
Fig. 2.25 Measured transmittances of air at room temperature. Courtesy of Andrea Markelz in the Department of Physics at the University of California, Santa Barbara.
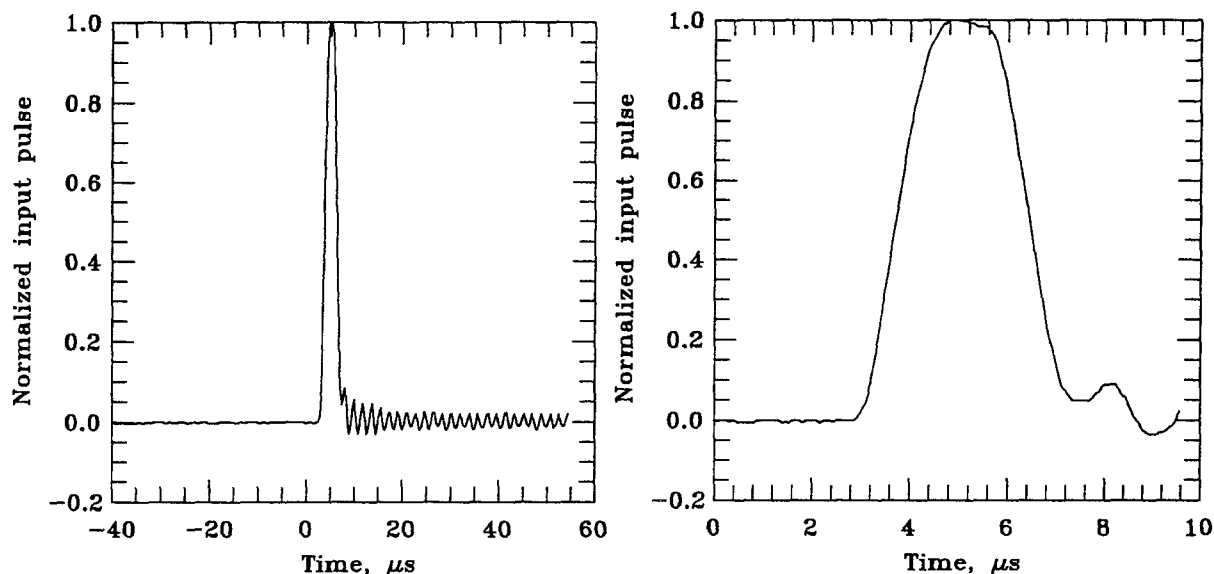
Fig. 2.26 A typical input-pulse shape in time domain: (a) in $100\,\mu s$ span, and (b) in $10\,\mu s$ span. The average pulse-width is $2.42\,\mu s$.

harmonic and the third harmonic energy are decided by tuning the FEL to $2\,f_0$ and $3\,f_0$ and measuring the bolometer responses through the high-pass filter, relative to the responses of the photoacoustic detector. Because the response time of the Germanium bolometer is much longer than the pulse width, the output voltage response of the bolometer is actually corresponding to the detected energy. Therefore, an absolute calibration of the peak energy responsivity is established. Unfortunately, the Pyroelectric detector is not sensitive enough to detect the higher harmonic pulses generated by the multiplier grids when it is switched to the fast setting, we are not able to decide the output pulse widths. Therefore, we use the input pulse-width, $2.42\,\mu s$, to calculate the input peak power and output peak power by dividing the detected peak energy by this pulse width.

It should be emphasized that all the powers mentioned in our measurements are "peak powers" calculated by dividing the measured peak energies with the input pulse-widths. If the output pulse-widths were known, the output peak

powers should be obtained using the output pulse-widths. It is expected that the higher harmonics generated by the multipliers should have pulse-widths narrower than the input pulses. However, we choose to be more conservative.

A liquid-helium-cooled silicon composite bolometer [35] or a liquid-helium-cooled InSb bolometer is suggested for future works because they might be sensitive and fast enough to measure the output pulse-shapes to determine the output power directly.

2.18 TIME-DOMAIN RESPONSES

Four different diode grids have been tested. These diode grids are glued on the edges of microscope glass slides with evaporated-gold bias-lines and suspended in the air as shown in Figure 2.27. The glass slides have a thickness of 160 μm.

Time responses of the harmonic signals from the grid are first measured. Figure 2.28 shows the output voltage of the bolometer as a function of time. Each curve is an average of 4 pulses. The solid lines indicate the output signals with the grid in the path pumped by four different input power levels - 0 dB, 3.8 dB, 5.8 dB and 7 dB attenuations. The dashed line is measured without the multiplier in the path and 0-dB input power attenuation. This measurement shows the harmonics are radiated from the multiplier grid instead of the harmonic leakage from the free-electron laser. The free-electron laser normally contaminate
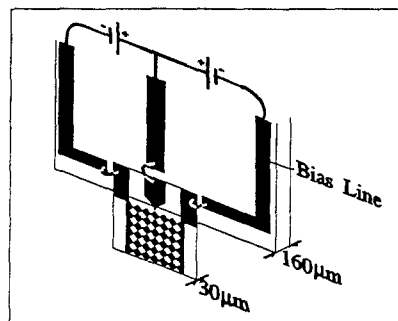

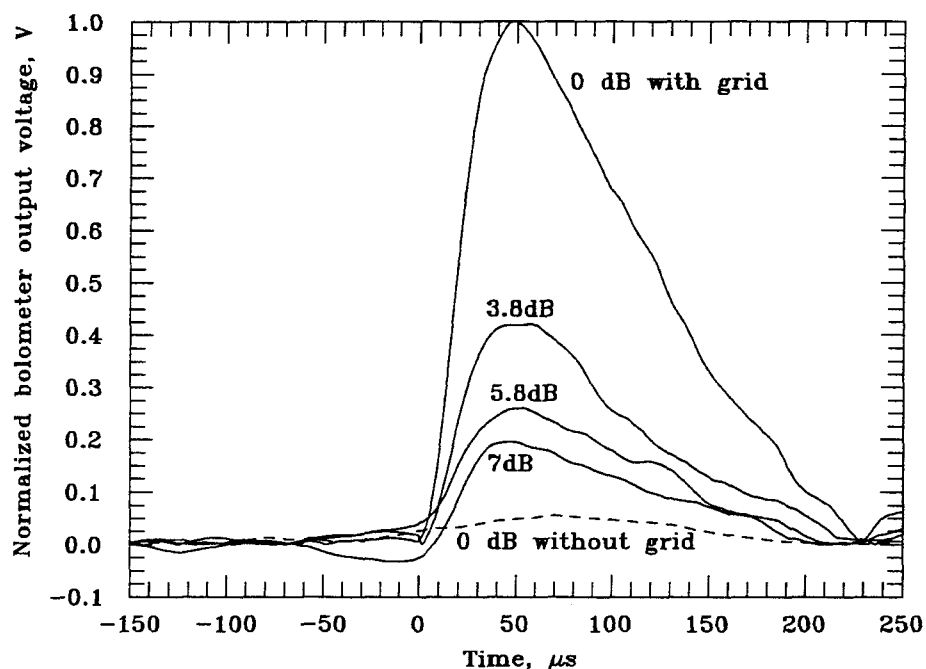**Fig. 2.27** Details of the mounting structure.

Fig. 2.28 Normalized output voltage of the bolometer as a function of time.

with higher harmonics. However, the plexiglass attenuators behave like low-pass filters which attenuate the higher harmonics much faster than the fundamental signal. The 0-dB attenuation reference here is actually set with enough plexiglass in front of the beam splitter so that there is no output signal detected by the bolometer when the multiplier is removed from the path. Then extra attenuations are added to measure the time responses with different input signal levels.

2.19 POLARIZATIONS

Another way to show that the THz radiation comes from the multiplier rather than the FEL is to rotate the grid by 90° and measure the cross-polarized signal. Figure 2.29 shows the time responses. The solid line is measured with the electric field parallel to the diodes and the dashed line is measured with the electric field perpendicular to the diodes. This result shows that

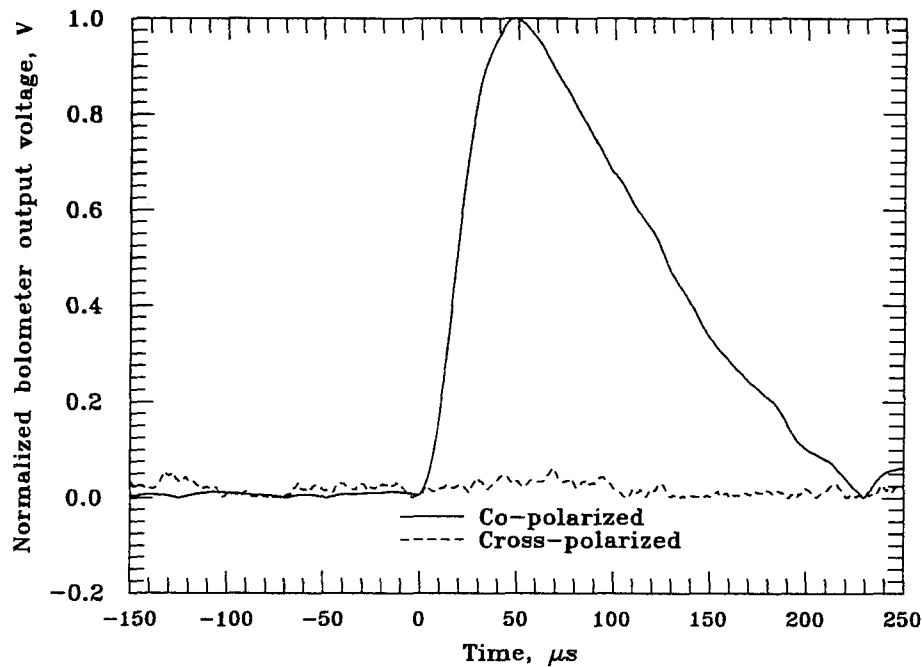1. The signals from the FEL and the grid are linearly-polarized.

Fig. 2.29 Normalized output voltage of the bolometer as a function of time with co-polarized and cross-polarized inputs.

2. The bow-tie metal structures on the grid work as linearly-polarized antennas and couple signal into the diodes. The harmonic signals are not generated by just pumping high energy on GaAs in the device.

3. The harmonic signals are not the harmonic contaminations from the FEL.

2.20 FREQUENCIES

A Fabry-Perot interferometer is used to verify the signal frequencies. The metal-mesh plates can be positioned in 0.7-μm increments. Figure 2.30 shows the fundamental frequency from the free-electron laser after passing the low-pass filter but without the high-pass filter; and Figure 2.31 shows the output frequency from the grid after passing the high-pass filter. These figures only show parts of the measured curves. The average distance between two peaks in the output-frequency measurement is $301\,\mu$m over 14 peaks. This indicates

the output frequency is 1.00 THz. No higher harmonics have been detected. The average distance between two peaks in the input-frequency measurement is 603 μm over 9 peaks. This indicates the input frequency is 500 GHz.

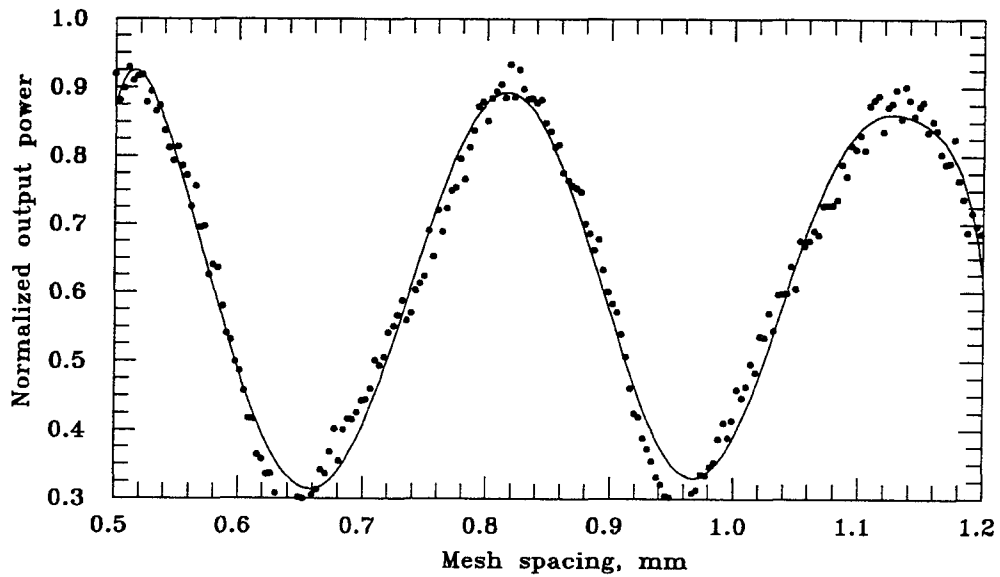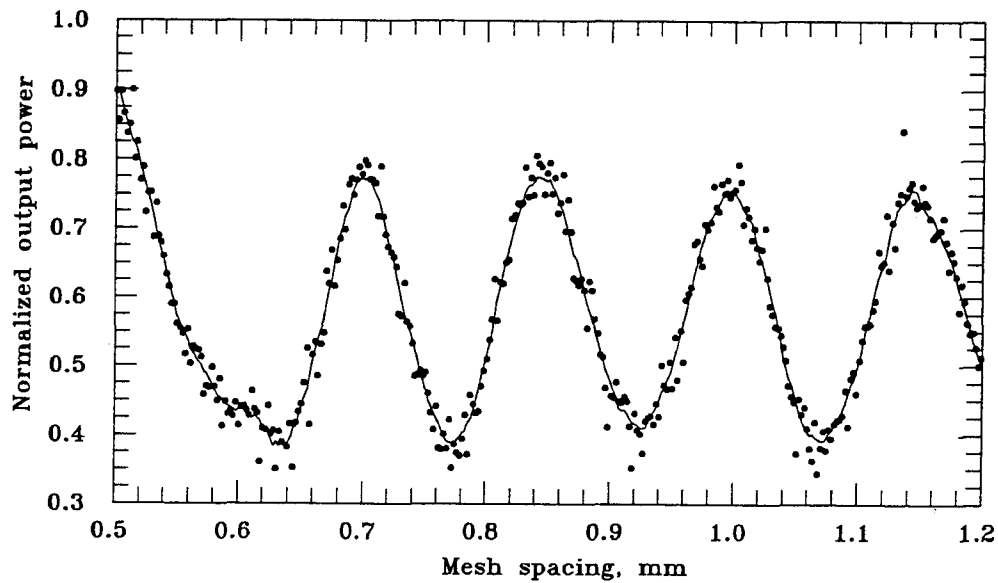**Fig. 2.30** Input frequency verification.

Fig. 2.31 Output frequency verification.

2.21 INPUT POWERS

To decide the input power on the grid at the focal plane, the multiplier is used as a detector to measure the spot size of the focussed laser beam. Figure 2.32 shows the normalized power contour in the focal plane. The second harmonic signal is measured by moving the multiplier in $\hat{x}$ and $\hat{y}$ directions. Then the input power at the fundamental frequency is derived from the square-power relationship which is verified by the power-dependence measurements later. Each data point in this figure is an average value of ten pulses. The input power on the grid, when the grid is well focussed, then is determined by:

$$\frac{\text{Active area } (420\mu\text{m} \times 420\mu\text{m})}{\dfrac{\int_x P(x,y)dx}{P_{m_{\hat{x}}}} \quad \dfrac{\int_y P(x,y)dy}{P_{m_{\hat{y}}}}} \times P_{\text{in}} \tag{2.23}$$

where the P_{in} is the total fundamental power detected by the reference detector, $P_{m_{\hat{x}}}$ and $P_{m_{\hat{y}}}$ are the maximum peak input powers in $\hat{x}$ and $\hat{y}$, respectively.
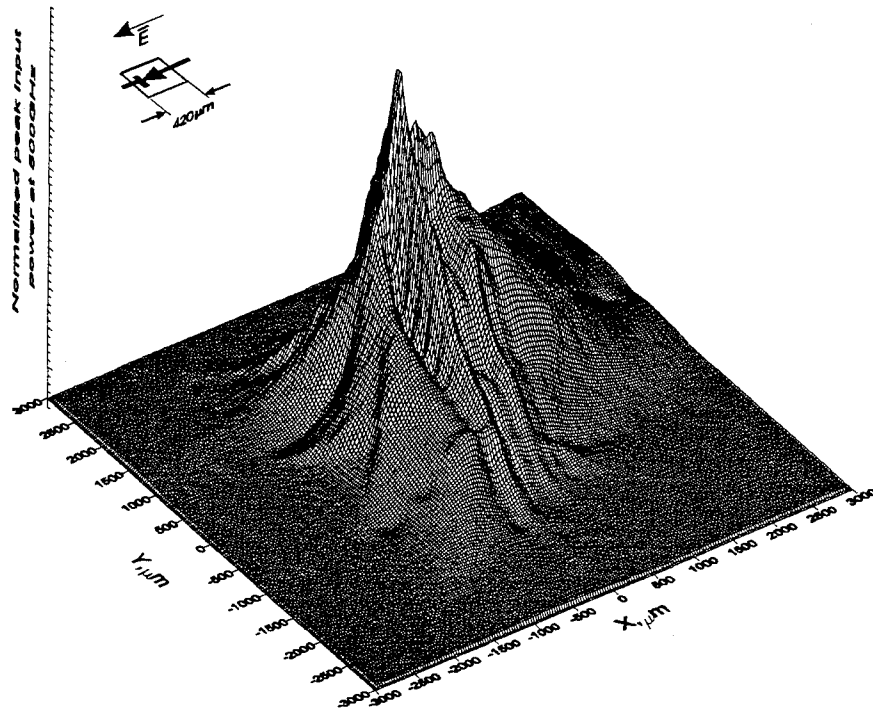

Fig. 2.32 Input spot-size measurement at the focal plane using the multiplier as a detector.

2.22 OUTPUT POWERS

Figure 2.33(a) shows the power dependence of multiplier #1 with normal incidence. This diode grid has diodes with an anode diameter of 0.56 µm and 100% yield. The dashed line indicates a square-power relationship. A peak output power of 330 µW at 1 THz is achieved when the diode grid is pumped with an input power of 3.3 W at 500 GHz. Figure 2.33(b) shows the power dependence of multiplier #4 with normal incidence. This diode grid has diodes with an anode diameter of 0.5 µm and 83% yield. The failed diodes are open-circuited, verified by an I-V curve tracer. The dashed line indicates a square-power relationship. With low input power, the data do not follow the square-power relationship, possibly due to measurement noise. It should be noticed that these diodes have not yet saturated. We tried to increase the input power in order to investigate the saturation conditions. However, some of the diodes are damaged when the input power reached 13 W. These damaged diodes are open-circuited, verified by a curve tracer too.
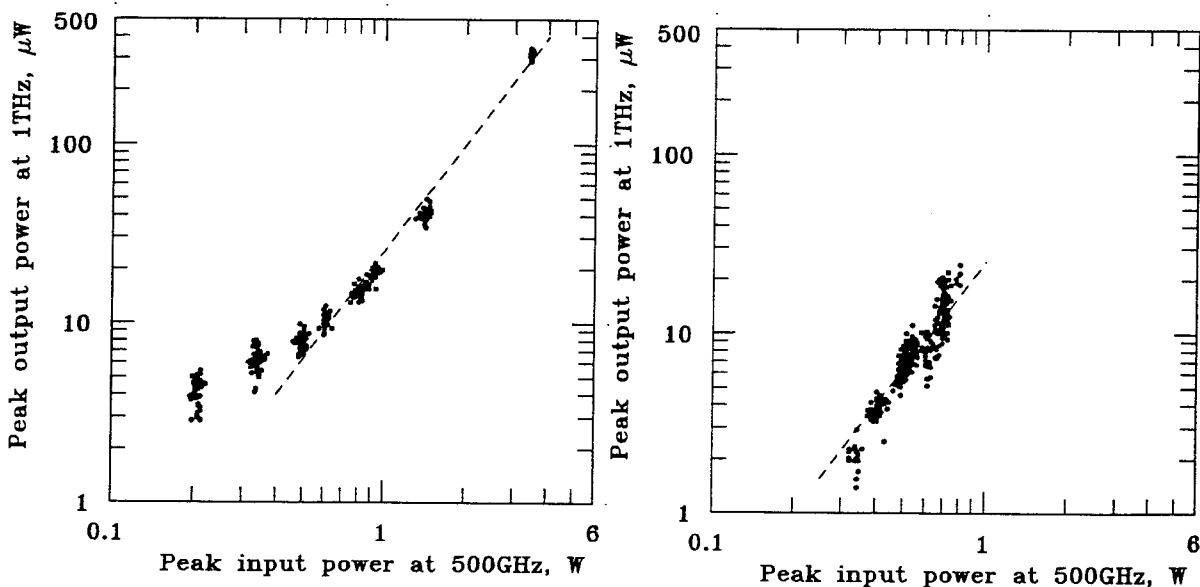

Fig. 2.33 (a) Measured power dependence of multiplier #1, and (b) multiplier #4. The diodes are not biased. The dashed lines indicate a square-power relationship.

We improved the data acquisition method to investigate the power dependence with low input power. Each pulse is integrated to reduce noise effect. The output voltages from the bolometer and the pyroelectric detector are synchronized with the FEL trigger signals. The noise offset is first obtained by integrating the output signal of the bolometer over 50 μs before the trigger signal comes in. The peak output power with noise effect is obtained by integrating the output signal of the bolometer from the instant that trigger signal comes in to the instant that the output signal reached the maximum and then dividing the integrated signal by the integrating period. The peak output power then is obtained by subtracting the peak output power with noise effect by the noise offset. This same procedure is done for each pulse.

Because some of the diodes got damaged in these grids, we used new devices. Figure 2.34 shows the power dependence with normal incidence in a linear scale. These grids have diodes with an anode diameter of 0.5 μm. The solid line indicates a square-power relationship. Figure 2.34(a) shows the power dependence of multiplier #3 which has 2 open-circuited diodes in two different columns. Fig-
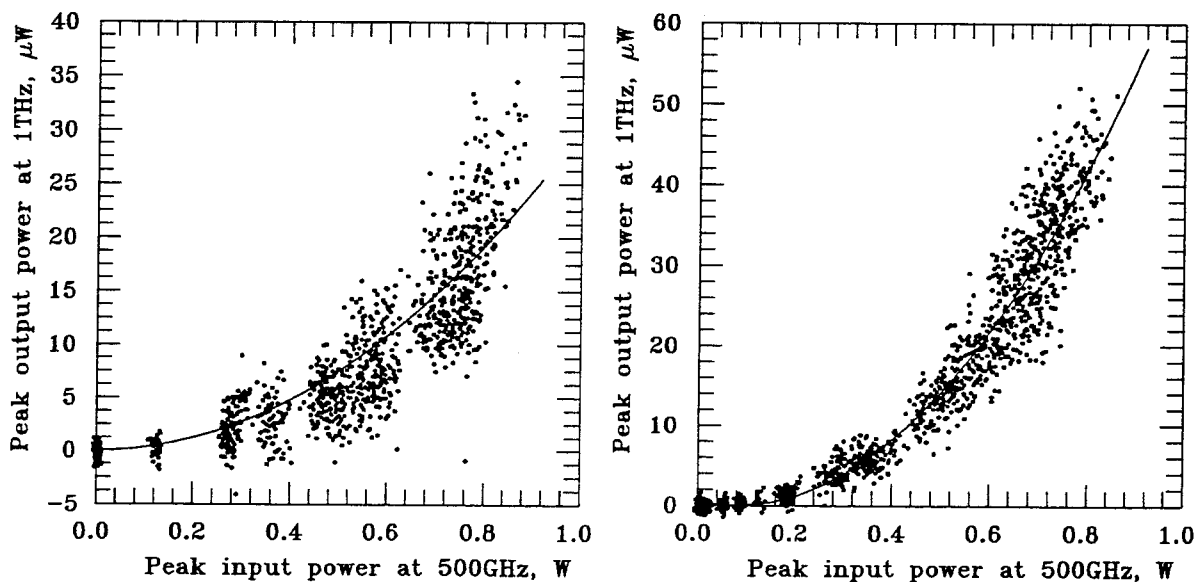

Fig. 2.34 (a) Measured power dependence of multiplier #3, and (b) multiplier #2.

ure 2.34(b) shows the power dependence of multiplier #2. This diode-grid is 100% yield. With an input power of 800 mW, this multiplier generated a peak output power of 45 μW while multiplier #3 generated an output power of 20 μW. It should be noticed that two open-circuited diodes in multiplier #3 cause two open-circuited columns which result in 83% yields and the maximum output power is degraded by 56%. These diodes have not saturated yet and some of the diodes are damaged when the input power is increased to 4 W. It should be noticed that the data with low input power follows the square-power relationship after reducing the noise effect.

2.23 PATTERNS

2.23.1 MEASURED PATTERNS

The diodes in the top and bottom halves of the grid have opposite polarities because the grid was originally designed for a sideband generator. When the grid is used as a frequency doubler, this causes an undesired null in the middle of the output beam. Output pattern is measured to verify the existence of the null in the center of the far field pattern. The measurements are done by rotating the multiplier itself, as shown in Figure 2.35(a).

Figure 2.35(b) and Figure 2.36 show the measured output patterns of multiplier #1 and #2, respectively. The peak input power is 300 mW. Peaks appear at 42° and 26° from the center with a power of 3.2 times and 2.3 times bigger than the power in the null, respectively. The accuracy of this measurement is limited by the uncertainty in the position of the rotating axis. The error of mounting the grids on center of the rotating axis is about 200 μm through a microscope. The asymmetry of the output pattern may be caused by the off-axis rotating effect or by the fact that the diodes in one array are not completely identical. The bolometer has a receiving horn with an acceptance angle ($\pm 14°$) and only 10% of the total radiated power is accepted at normal incidence.

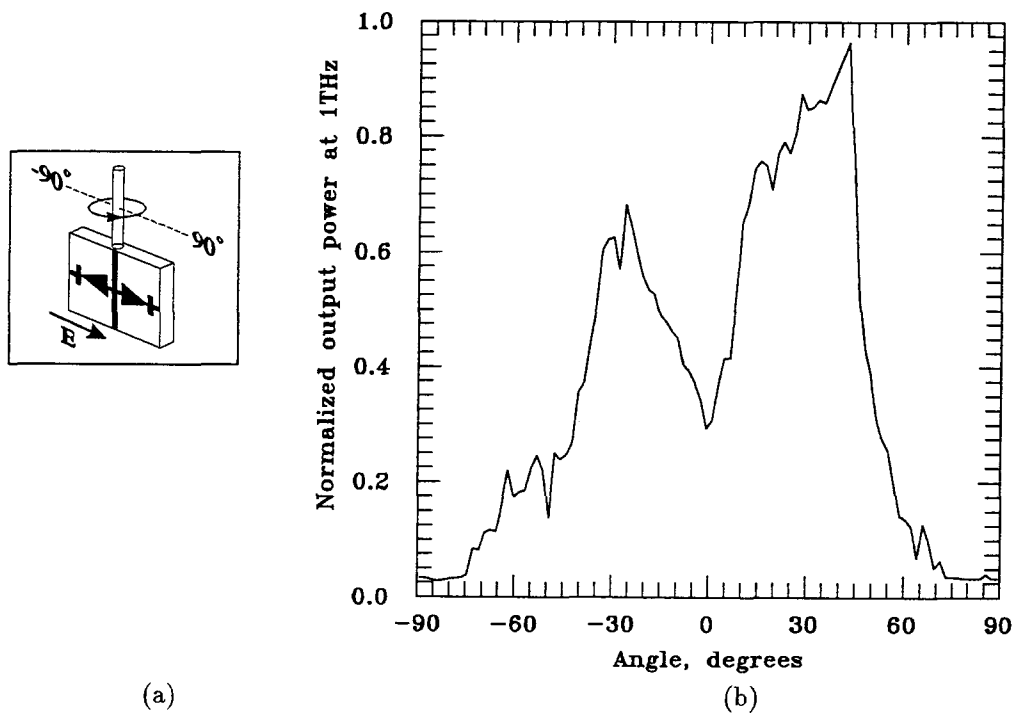(a)   (b)

Fig. 2.35 (a) Measurement of the output pattern by rotating the grid itself, and (b) the measured output pattern of multiplier #1.
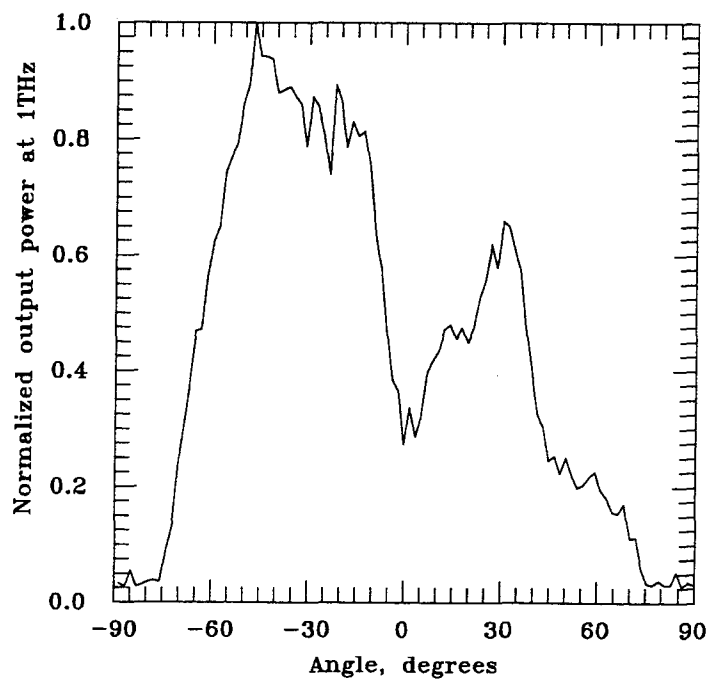

Fig. 2.36 The measured output pattern of multiplier #2.

2.23.2 THEORETICAL PATTERNS

There are three main factors to decide the output patterns: the antenna pattern of the bow-tie with contact-fingers; the effect of flipping the diode orientations across the center row; and the finite angle of the receiving horn at the bolometer.

2.23.2.1 UNIT-CELL PATTERN

The radiation patterns of a bow-tie with finite length and infinitesimal thickness on a lossless half-space dielectric substrate has been discussed by Compton *et al.* [147]. This method, although a rigorous analysis using the method of
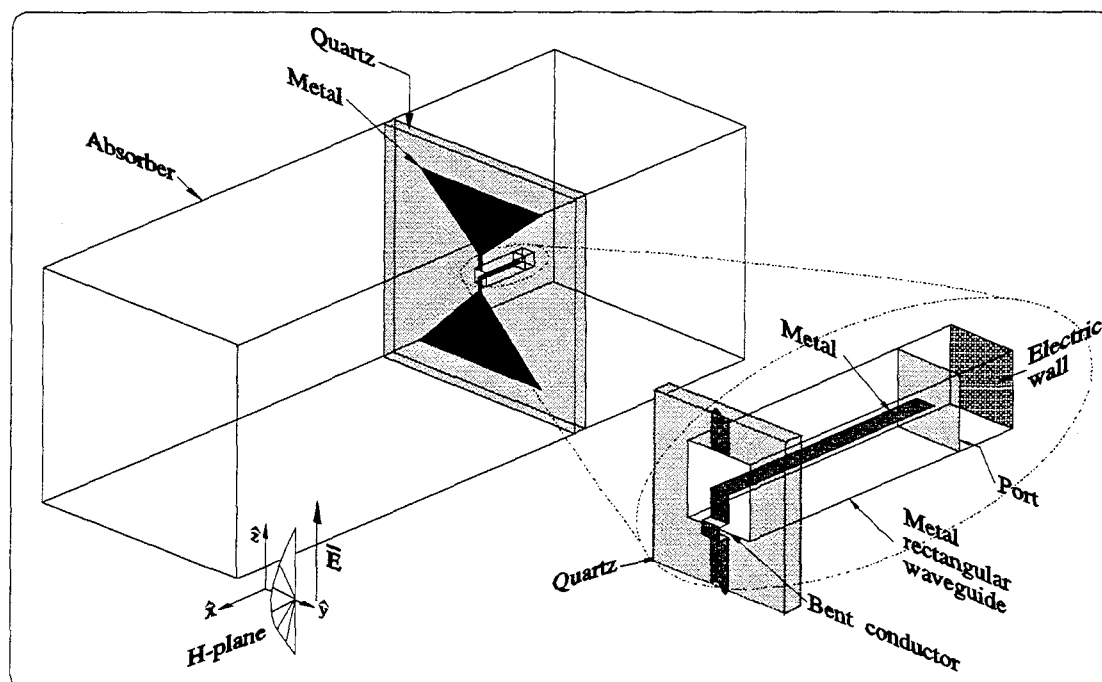

Fig. 2.37 The simulation structure of the bow-tie with contact-fingers for the antenna far-field patterns using *HFSS* version 3. The antenna driving points are fed by a coaxial rectangular waveguide. The center conductor connecting to the bottom part of the bow-tie is bent to avoid the contact of the center conductor on the outer conductor of the coaxial waveguide. The modes in the coaxial waveguide are excited by the port in the end of the center conductor in the waveguide. There is a short section of a rectangular cavity (with electric wall in the end) attached to the coaxial waveguide to terminate the waveguide.

moments, does not need to apply in our cases. First, the bow-ties have contact-fingers connected to the driving points and the lengths of the fingers are not very small compared to the bow-ties. The approximation using bow-ties antenna patterns may not be accurate in this case. Second, the quartz substrate is very thin compared to the wavelengths ($30\,\mu$m$=0.1\lambda_{air}=0.19\lambda_{quartz}$), so the effect of the substrate will not be significant. Therefore, exploring the use of *HFSS* version 3 to calculate the far-field patterns may be a quick and simple option. With Release 3.0 of *HFSS*, a new radiation boundary type is available on defining boundary conditions to model radiating structures characterized by outgoing and propagating waves and eliminates the need for a spherical-shaped outer boundary closure. Then the radiation pattern is calculated from a near-field to far-field transformation.

Figure 2.37 shows the structure of the bow-tie with contact-fingers for far-field pattern simulations. The antenna driving points are fed by a coaxial rectangular waveguide with the center and the outer conductors connecting to two fingers. The center conductor connecting to the finger in the bottom is bent to avoid the contact of the center conductor on the outer conductor of the coaxial waveguide. The modes in the coaxial waveguide are excited by the port by the end of the center conductor in the waveguide. There is a short section of a rectangular cavity (with electric wall in the end) attached to the coaxial waveguide to force the port fields radiating only into the coaxial waveguide, but not the free space. There is a small opening in the substrate to allow the connection of the coax to the antenna. We can specify the impedance of the coaxial waveguide by adjusting the permittivity or the permeability of the material filled in the waveguide to match the antenna impedance. The big rectangular enclosure of the entire structure is specified as absorbing boundary to allow the wave propagating into free space.

This is our first attempt to use the finite-element method for far-field pattern

calculations, to verify the accuracy of the *HFSS* solutions, a simple test is done by comparing the solutions from the finite-element method and the solutions from a far-field analysis for a free-standing bow-tie antenna. Figure 2.38 shows (a) the simulation structures in *HFSS* and (b) the analytic far-field calculations.

To find the radiating pattern for the bow-tie, we assume an impressed electric current flows on the bow and the current density can be expressed as [147]

$$\mathbf{J}(r, \psi) = \frac{\mathrm{I}_0/r}{\sqrt{\sin^2\phi - \sin^2\psi}} \, \hat{r} \qquad (2.24)$$

where I_0 is the total current; ϕ is the angle of the bow which is 45°; r and ψ are the distance and the angle from the current element to the apex, respectively; and $0 \leq \psi \leq \phi$. The vector potential $\mathbf{A}$ then can be solved as

$$\mathbf{A} = \frac{\mu}{4\pi} \iint_S \mathbf{J}(r, \psi) \frac{e^{-jk \cdot R}}{R} dr \, d\psi \qquad (2.25)$$

where R is the distance from any point in the metal to the observation point. Far-field conditions are applied and the electric fields can be approximated by
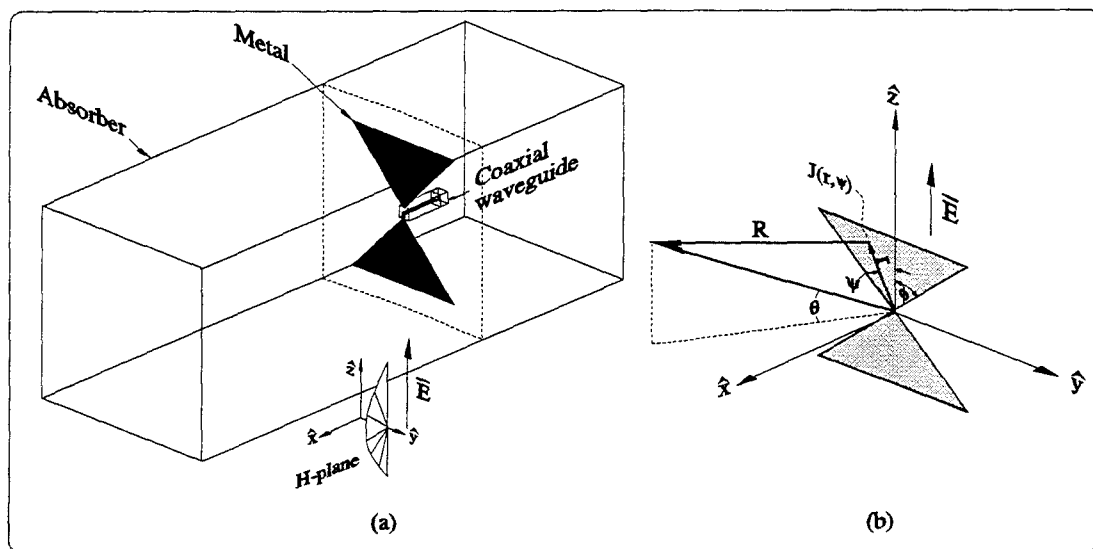

(a)   (b)

Fig. 2.38 (a) *HFSS* structure for radiation-pattern calculation and (b) notation for far-field analysis.

$E_\perp \approx -j\omega A$ and $E_{\hat{R}} \approx 0$ which lead to the radiating pattern on the H-plane:

$$| E |^2 \approx C \cos^2 \theta \qquad (2.26)$$

where θ is the angle from the $\hat{x}$-axis on the $\hat{x} - \hat{z}$ plane and C is a constant.

Both results of using the *HFSS* pattern simulation and the far-field analysis are shown in Figure 2.39. The agreement is excellent except some discrepancies from $+60°$ to $+90°$ which might be caused by the bent connection from the center conductor of the coaxial waveguide to the bottom part of the bow-tie.

The results for a free-standing bow-tie convince us to compute the radiation patterns for bow-ties with contact-fingers using the finite-element method. Figure 2.40(a) shows the radiation patterns of the bow-tie with contact-fingers in two different absorbing boundary enclosures. The quartz substrates are assumed to be zero in these cases. The smaller enclosure has a dimension of $210 \times 210 \times 210 \,\mu m^3$ (the unit-cell size of the grid is $70 \,\mu m \times 70 \,\mu m$) and the bigger one has a dimension of $900 \times 900 \times 900 \,\mu m^3$ (the wavelength of $1\,THz$ in free space is $300 \,\mu m$). The patterns are almost the same which allows us to reduce
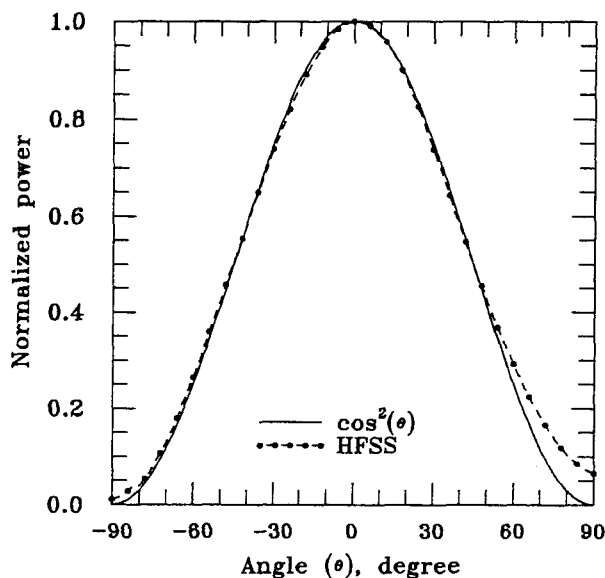
Fig. 2.39 The radiation patterns for a free-standing bow-tie antenna calculated by *HFSS* and an analytic form.

the size of the structure to shorten computation time and reach a better convergence. Figure 2.40(b) shows the antenna patterns on the metal side with four different substrate thickness's. The antenna patterns on the metal side do not change significantly when the substrate thickness changes from $0\,\mu$m to $500\,\mu$m, but change dramatically from $500\,\mu$m to $5\,$mm. The pattern are almost identical for the one without substrate and the one with 30-μm thick substrate. These calculations are to confirm the pattern calculation for the 30-μm case. Because it is very thin compared to the wavelength and some dimensions in the structure, it creates much more finer-meshes as applying the finite-element method and takes much more computation time but results in a poor convergent condition. The calculations for the one without substrate and the one with 500-μm thick substrate, however, reaches good convergence. Therefore, we can conclude that the radiation pattern for the 30-μm thick quartz substrate should be accurate enough to estimate the antenna pattern of the bow-tie with contact-fingers on our grids.

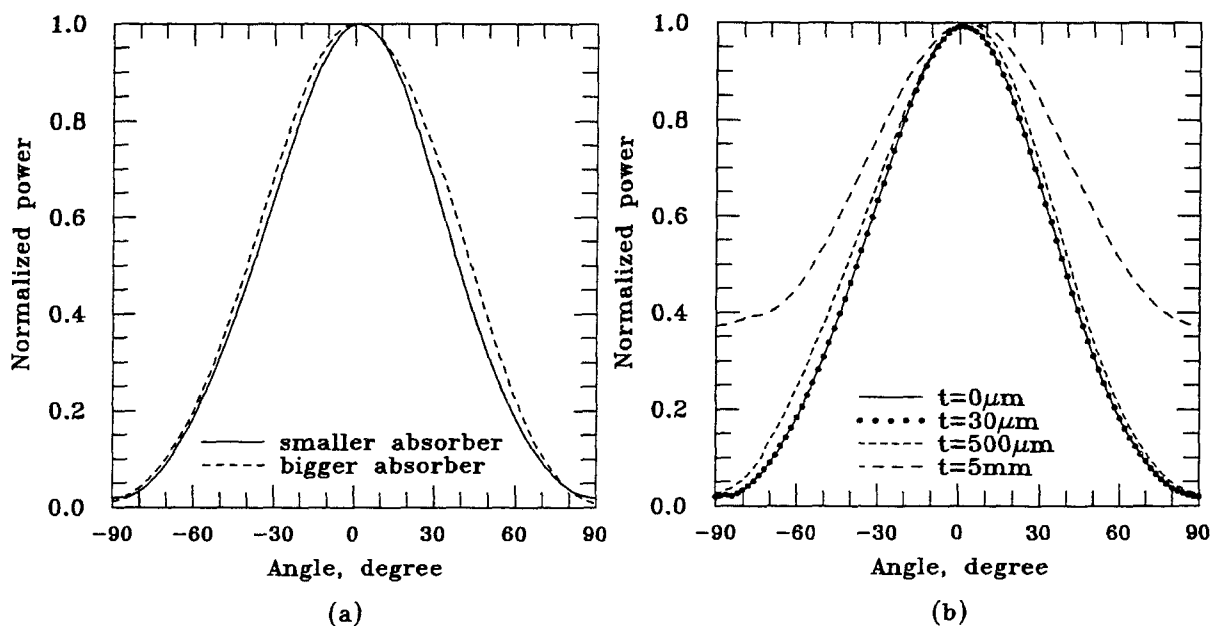(a)   (b)

Fig. 2.40 (a) The theoretical antenna patterns of the bow-tie with contact-fingers in two different sizes of *HFSS* absorber-boundaries. (b) The theoretical antenna patterns of the bow-tie with contact-fingers on different quartz substrates with thickness's of $t = 0\,\mu$m, $30\,\mu$m, $500\,\mu$m and $5\,$mm.

2.23.2.2 Array Factor Pattern

Three infinitesimal current elements on one side are assumed to have an opposite phase from the other three elements on the other side of a linear array to calculate the array factor as shown in Figure 2.41(a). The spacing between
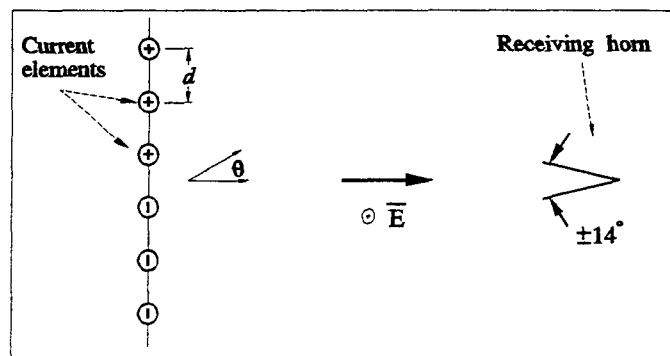
(a)
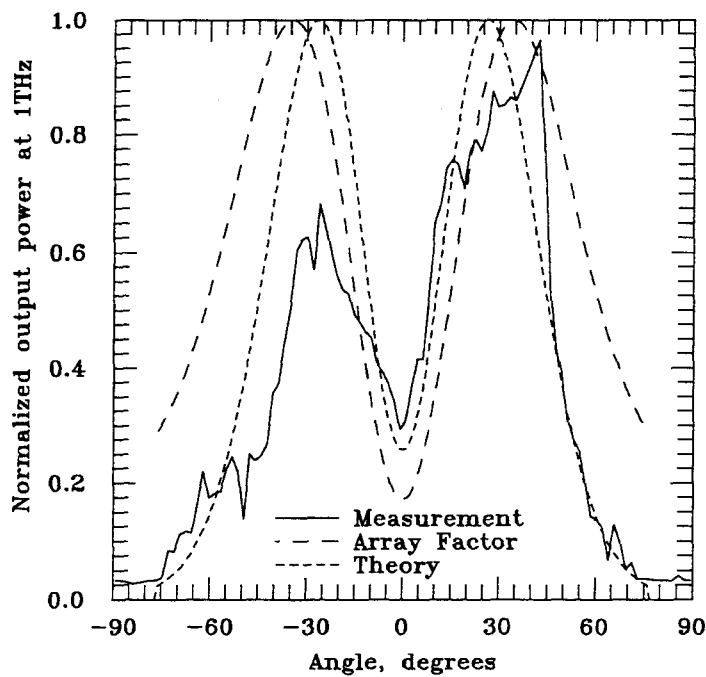
(b)

Fig. 2.41 The theoretical and measured output patterns of multiplier #1. The array factor with the effect of the limited receiving angle is also shown in the double-dashed line.

elements is $70\,\mu$m. The normalized array factor is determined by [148]

$$A(\theta) = \left[\frac{\sin(\frac{3k_0 d}{2}\sin\theta)}{\sin(\frac{k_0 d}{2}\sin\theta)}\right]^2 \cdot \left[\sin(\frac{3k_0 d}{2}\sin\theta)\right]^2 \qquad (2.27)$$

where θ is the angle, d is the spacing and the propagation constant $k_0 = 2\pi / \lambda_0$ where λ_0 is the wavelength, $300\,\mu$m.

The receiving horn in the bolometer has an acceptance angle of $\pm 14°$. Therefore, taking both the antenna array factor and the finite acceptance-angle effect into account, the array-factor pattern is calculated by

$$P(\phi) = \int_{\phi - 14°}^{\phi + 14°} A(\theta)d\theta. \qquad (2.28)$$

2.23.2.3 THEORETICAL OUTPUT PATTERN FOR THE GRID

The double-dashed line in Figure 2.41(b) shows the calculated one-dimensional array-factor pattern from Eq. (2.27) and (2.28). Combining both
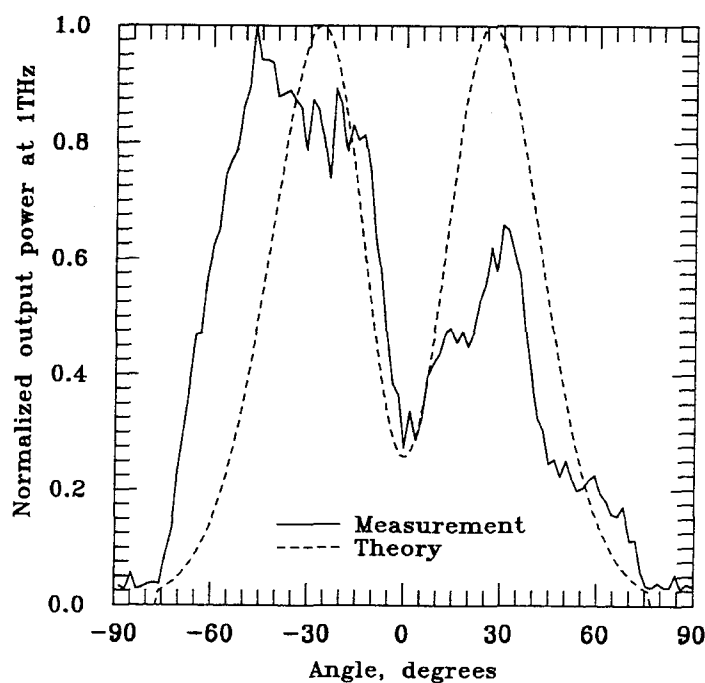

Fig. 2.42 The theoretical and measured output patterns of multiplier #2.

the antenna pattern for the bow-tie with fingers and the array factor with the effect of finite receiving angle, the calculated output patterns and the measured patterns are shown in Figure 2.41(b) for the multiplier #1 and Figure 2.42 for the multiplier #2, respectively.

2.24 LENS

Several focussing lenses are used trying to correct the output patterns in order to collect more output powers. These lens are placed between the output side of the multiplier and the second parabolic mirror. These measurements are rough due to the availability of the lenses, however, done to verify the possibility of using lens to correct the output patterns.

Lens #1 is a plano-convex fused silica lens with a center thickness of 1.6 cm and a diameter of 2.5 cm. Figure 2.43(a) shows the average (over 4 pulse) time-responses of the bolometer output voltage with the lens placed as close as possible to the grid; with the lens as close as possible to the mirror; and without the lens

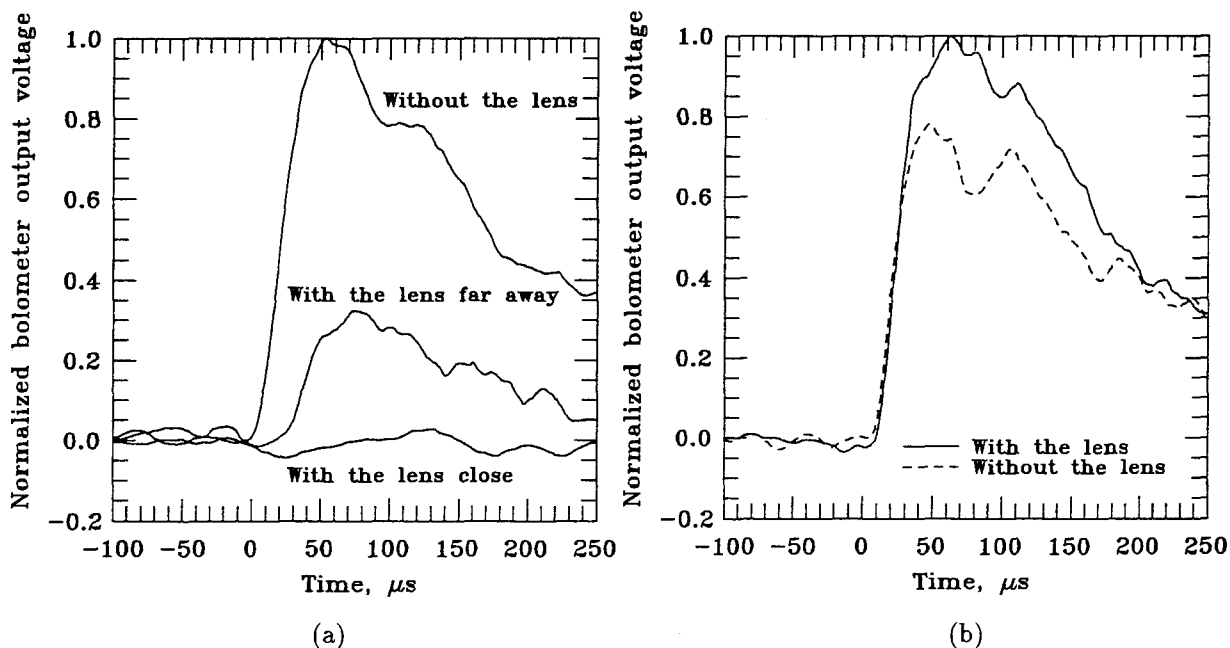(a)   (b)

Fig. 2.43 (a) The time responses of the bolometer output voltage with and without lens #1. (b) The time responses of the bolometer output voltage with and without lens #2.

in the path. The lens is moved between the grid and the mirror, but the output signal is always smaller than that without lens.

Lens #2 is a plano-convex x-cut quartz lens with a center thickness of 5 mm and a diameter of 1.1 cm. Figure 2.43(b) shows the average (over 4 pulse) time responses of the bolometer output voltage with the lens placed 6 cm away from the grid which gives the maximum output, and without the lens in the path. The average peak-voltage over 64 pluses is 36.56 mV with the lens and 25.5 mV without the lens.

Lens #3 is a symmetric-convex fused quartz lens with a center thickness of 7.5 mm, a focal length of 10 mm and a diameter of 5 mm. The average output voltage over 8 pluses is 13.8 mV with the lens placed at the optimized position to collect maximum output power at the bolometer and 28.4 mV without the lens.

Lens #4 is a symmetric-convex fused quartz lens with a center thickness of 3 mm, a focal length of 15 mm and a diameter 7.5 mm. The average output-voltage over 8 pluses is 18 mV with the lens placed at the optimized position to collect maximum output power at the bolometer and 35 mV without the lens.

Lens #5 is a symmetric-convex TPX (poly-4-methyl-pentene-1) lens with a thickness of 5 mm and a diameter of 2.5 mm. The relative dielectric constant of TPX is about 2.7. The transmittance of a 0.5 mm thick TPX slab is 93% at 1 THz and 93% at 500 GHz [150]. To compare, the transmittance of a 0.56 mm thick fused-quartz slab is 66% at 1 THz and 81% at 500 GHz. The average output-voltage over 64 pluses is 68.8 mV with the lens placed at the optimized position to collect maximum output power and 42.8 mV without the lens. This lens clearly changes the output power pattern, however, we are not able to measure the output pattern due to the current experimental arrangement.

2.25 TUNING

In previous measurements, the input or output tuners are not used so that neither the input nor output impedances are matched to achieve the optimal har-

monic generations. It is concluded from the past experiences that the impedance tuners are essential to achieve high efficiency [108,113,116]. A pair of dielectric slabs (fused quartz slabs) were used as impedance tuners in Jou's multipliers [113] and in Liu's multipliers [116] which are similar to the tuner in Archer's quasi-optical waveguide multiplier design [64]. The slabs behave in a similar manner to the double stub tuner in a coaxial line or a waveguide. The slab thickness should be a quarter-wavelength at the fundamental frequency for the input tuner and a quarter-wavelength at the second harmonic frequency for the output tuner. However, neither fused-quartz slabs with a thickness of $38.1\,\mu$m $(1/4\lambda_{1THz})$ nor low-doping silicon slabs with a thickness of $21.6\,\mu$m were available as output tuners during the measurements, we used a variety of fused-quartz slabs and low-doping silicon slabs with different thickness's instead.

2.25.1 INPUT-SIDE TUNING

The low-pass filter is moved away from the grid to leave a spacing of about 1 cm between the grid and the filter for the tuning slab. The tuning slabs are mounted on a micrometer and placed as close as possible to the grid. A He-Ne laser is used to examine the closeness of the tuner to the grid and avoid them touching. Because the grid is suspended on the edge of the glass slide, the motion from the motor attached to the micrometer might vibrate the grid if the slab touches it.

A low-doping silicon slab with an average thickness of $290\,\mu$m is used. The resistivity is more than $2500\,\Omega\cdot$ cm. Peak output power is measured as a function of relative spacing between the grid and the slab as shown in Figure 2.44. The input power is about 600 mW assuming the slab doesn't change the input spot size. There are ten pulses at each position and the solid line indicates the average values over 10 pulses. The dashed line indicates the average peak output power of $23\,\mu$W over 60 pluses which is measured without the tuning slab and with the low-pass filter 1 cm away from the grid. The highest output power is $30.5\,\mu$W

Fig. 2.44 Measured output power as a function of the relative spacing between the grid and the silicon slab. The average thickness of the silicon slab is 290 μm.

which is 1.3 times bigger than that without the tuning slab.

Another low-doping silicon slab with an average thickness of 338 μm is used. Peak output power is measured as a function of relative spacing between the grid and the slab as shown in Figure 2.45. The solid line indicates the average values over 10 pulses. The dashed line indicates the average peak output power of 11.8 μW over 55 pluses which is measured without the tuning slab and with the low-pass filter 1 cm away from the grid.

It should be noticed that the average period for the output power peaks over the last four major periods is 310 μm, which is about half the wavelength of
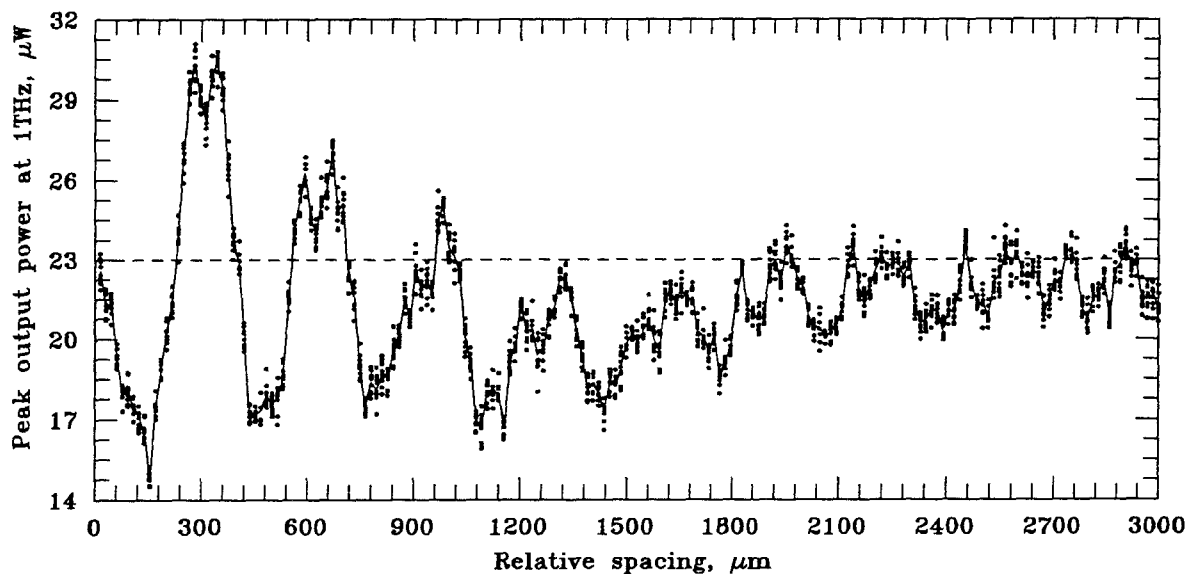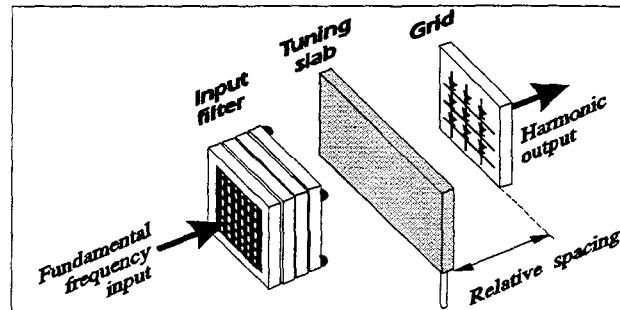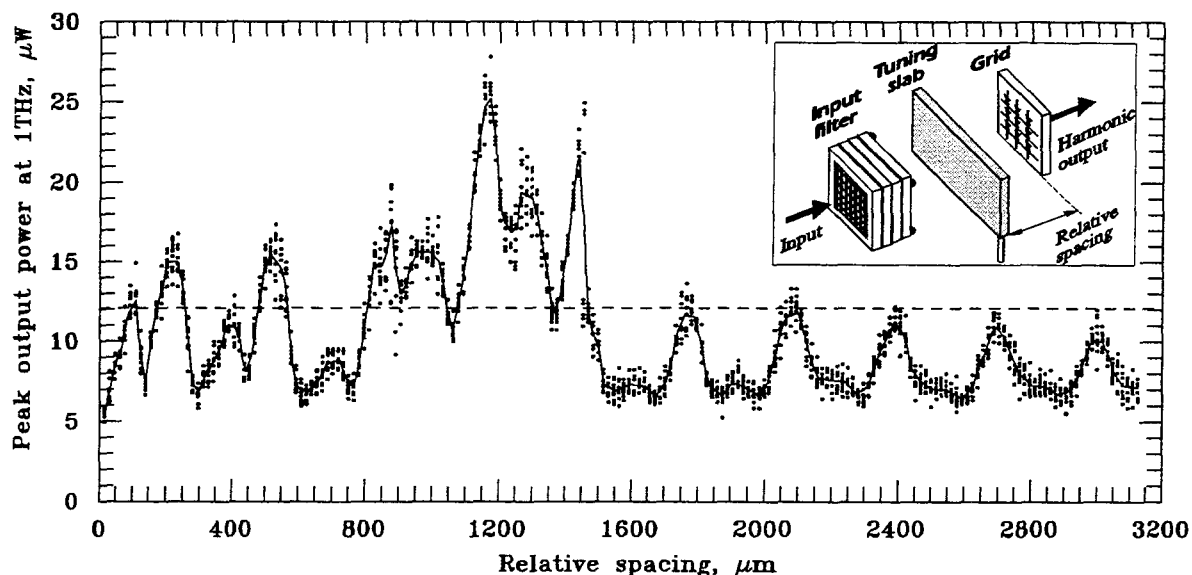
Fig. 2.45 Measured output power as a function of the relative spacing between the grid and the silicon slab. The average thickness of the silicon slab is $338\,\mu$m.

the fundamental frequency. The tuning curves show a combination of two effects because the input filter is part of the matching circuit for the output signal. The Fabry-Perot etalon effect between the tuning slab and the low-pass filter interferes with the etalon effect between the tuning slab and the grid. When the slab moves away from the grid, the etalon effect between the slab and the filter dominates and shows periods of half the wavelength of the fundamental frequency. When the slab moves closer to the grid, the etalon effect caused by the backward-propagating 1-THz signal from the grid starts to interfere. Within the relative spacing of $1500\,\mu$m, the average spacing between two peaks over the first 9 periods (regardless the heights of the peaks) is $150\,\mu$m which is half the wavelength of the second harmonic frequency. The tuning curves also show that the diffraction effects need to be considered as we design a multiplier system with tuning elements. A more compact and flexible arrangement will help to reduce the diffraction losses.

A fused quartz slab with an average thickness of $135\,\mu$m is used too. Peak

output power is measured as a function of relative spacing between the grid and the slab as shown in Figure 2.46. The solid line indicates the average values over 40 pulses. The dashed line indicates the average peak output power of 13.6 μm over 60 pluses which is measured without the tuning slab and with the low-pass filter 1 cm away from the grid. The average period for the output peaks over the last four major periods is 310 μm, which is about half the wavelength of the fundamental frequency. This curve also shows the combination of the etalon effect between the tuning slab and the low-pass filter, and the etalon effect between the tuning slab and the grid. However, the etalon effect between the tuning slab and the grid is not obvious in this measurement because the dielectric constant of the fused quartz slab is much smaller than that of the silicon slab.

The low-pass filter which is a reflective filter can also be used as a tuning element by changing the spacing between the filter and the grid. Figure 2.47 shows the measured output power of the second harmonic signal as a function of the relative spacing between the grid and the low-pass filter. Each point in
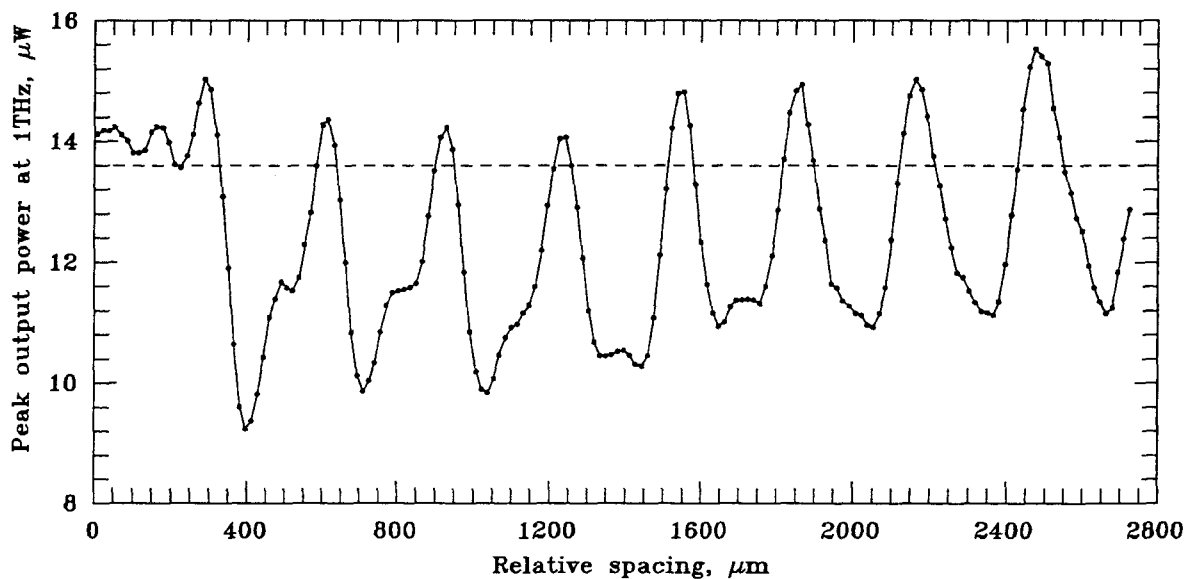

Fig. 2.46 Measured output power as a function of the relative spacing between the grid and the quartz slab. The average thickness of the quartz slab is 135 μm.

this curve is an average of ten pulses. Unfortunately, there are four screws on the frame of the filter so that the closest spacing between the grid and the filter is 2 mm ($\approx 7\lambda_{1THz}$). These screws couldn't be removed due to the calibration for the filter transmittance. Therefore the origin of the relative filter position is actually $7\lambda_{1THz}$ away from the grid. The first two maxima indicate the output power could be increased from 12 μW to 40 μW by moving the filter closer to the grid by 400 μm. The signal decays quite quickly when the filter moves away from the grid. The explanation is relatively straightforward. The size of the multiplier is only 420 μm which is only 1.4 times the wavelength of the second harmonic signal and 70% of the wavelength of the fundamental signal. As a result, beam diffraction is very serious in the present configuration. A more compact setup or a bigger array is essential to reduce the diffraction losses.
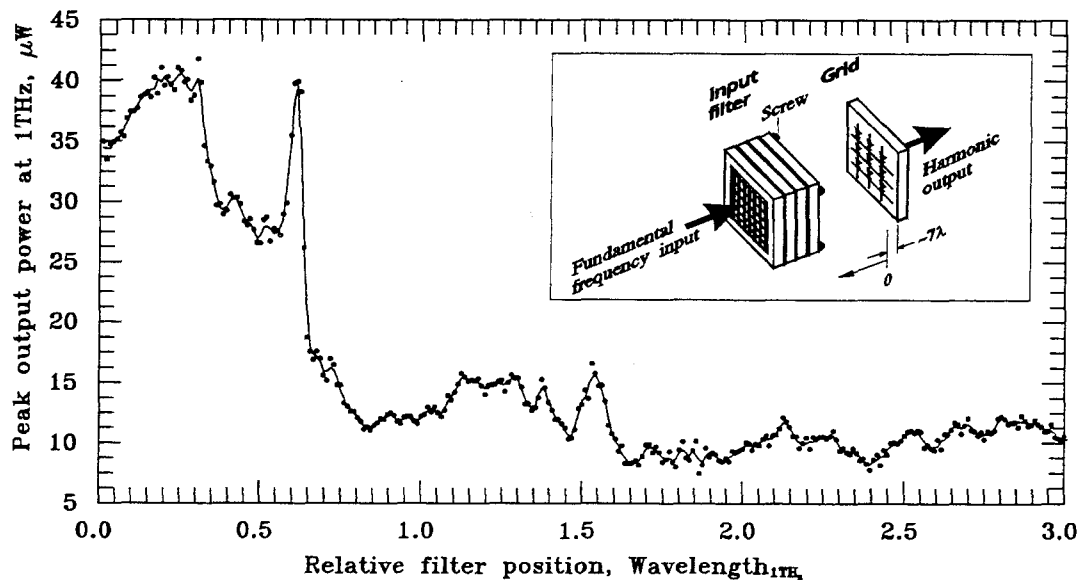

Fig. 2.47 Measured output power as a function of the relative filter position of the input filter.

2.25.2 OUTPUT-SIDE TUNING

Impedance tuning at the output side has also been investigated. Several silicon slabs and fused quartz slabs are used to tune the impedance by placing them close to the grid and then moving them away from the grid in the output side. Similar Fabry-Perot etalon effect is observed. However, the output power levels are always lower than that without tuning slabs. A possible reason is that the dielectric loss in these slabs cancels out the effect of matching impedance. Another possible reason is that the extra diffraction effects by adding the slabs scatter out the output power from being collected by the parabolic mirror. Therefore, a TPX lens is used as a tuning element because a flat, thin TPX slab is not available at the time. Figure 2.48 shows the measured peak output power as a function of the relative spacing between the lens and the multiplier. The lens is placed as closed as possible in the origin of the relative spacing verified by a He-Ne laser. The solid line is composed of data points which are averaged over
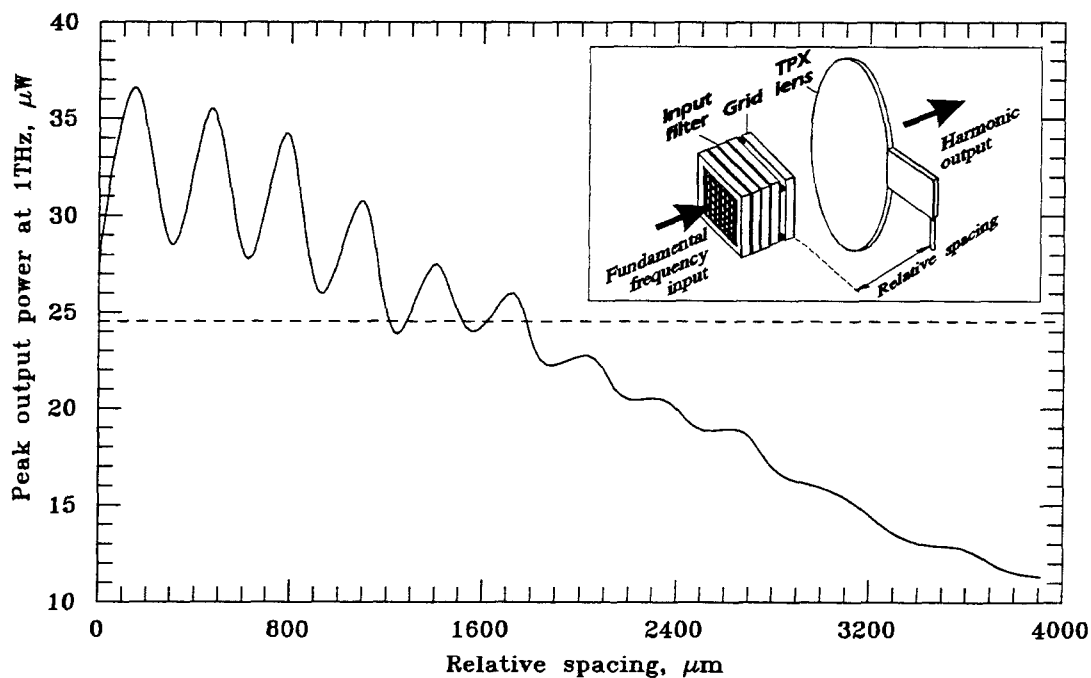

Fig. 2.48 Measured output power as a function of the relative spacing between the lens and the multiplier.

40 pulses at each position. The dashed line indicates the average peak output power of 24.6 μW over 230 pulses without the tuner in the path. The maximum peak output power is 35.5 μW and the power maximum repeated itself with a period of 300 μm which is half the wavelength of the input fundamental signal. It is also observed that the closer the lens is placed to the array, the larger the second harmonic power is. This is possibly caused by diffraction effect which is also observed in [116] and the focussing effect of the lens.

2.26 BIASING

As mentioned before, in most of the cases, Schottky diode multipliers are reverse-biased to increase the frequency multiplying efficiencies since the diodes are designed as varactors. However, these diodes are originally planned for use as sideband generators and designed to be used under forward bias. Therefore, the frequency multiplication in these diode grids possibly comes from varistor multiplication, that is to say, from the nonlinear I-V relationship. C-V measurements show that the harmonic generations from the nonlinearity of C-V relationship will not be significant. Biasing tests are done to verify this assumption and try to increase the doubling efficiency.

The grid is rotated to the angle where the maximum output appears. The maximum point of the output pattern should be more sensitive to the bias than the null in the center (with normal incidence) due to that the null is caused by a cancellation of electric fields from the two halves of the diodes.

Peak output power is measured as a function of bias with a peak input power of 400 mW (Figure 2.49). The maximum peak output power is 17 μW with a bias of 0.375 V. Comparing with a peak output power of 13 μW which is measured with the open-circuited bias line, it seems biasing only makes a small improvement in the output power. One possible reason is that these diodes are self-biased when the bias lines are open-circuited.

Power dependences are measured under different biasing conditions. Fig-

ure 2.50 shows the measured peak power dependence of the multiplier #1 with bias $-0.1\,$V and $0.234\,$V. Each data point is an average of 30 pulses. The frequency doubling efficiency at $14.2\,\mu$W output power is increased from 1.51×10^{-5} with a bias of $-0.1\,$V to 3.6×10^{-5} with $0.234\,$V bias It should be noticed that
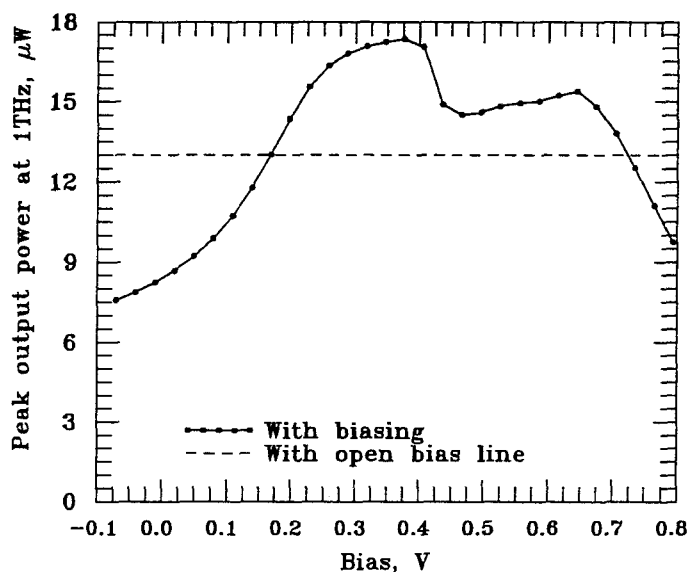

Fig. 2.49 Measured peak output power as a function of bias. The peak input power is 400 mW. The dashed line is measured with open-circuited bias lines.
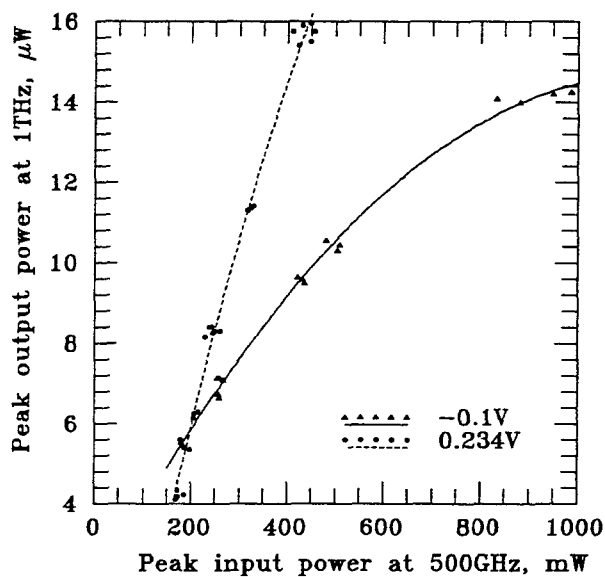

Fig. 2.50 Measured power dependence of multiplier #1 with bias $-0.1\,$V and $0.234\,$V.

these diodes become saturated with high input power when they are reverse-biased.

Power dependence is also measured under different biasing conditions on multiplier #2. Figure 2.51 shows the measured peak-power dependences with bias 0 V, 0.136 V, 0.5 V and 0.665 V. Each data point is an average of 60 pulses. The frequency doubling efficiency at 14 μW output power is increased 2.6 times when the bias increases from 0 V to 0.5 V. The power saturations are also observed when the diodes are biased at zero bias and 0.136 V.

The peak output power contour as a function of peak input power with different biases from -0.07 V to 0.79 V is measured and shown in Figure 2.52. The input power is carefully varied by tilting the plexiglass in front of the beam splitter in order to achieve higher resolution of the input power levels. Each data point is an average of 30 pulses. The frequency doubling efficiency increases significantly as the bias changes from 0.2 V to 0.3 V.

2.27 Current Saturation

Current saturation, which is the maximum current can flow through the device, is an important factor that strongly affects the multiplier performance because the diode cross-section is very small for the planar Schottky diodes on our grids. In our power-dependance measurements with open-circuited bias lines, the diodes are not saturated. This provides a possibility of increasing output power. The saturation of output power is mainly determined by the electron velocity saturation which happens with high electric fields.

In a DC electric field, the maximum electron velocity in GaAs is about 2.2×10^5 m/s with an electric field of 3.2 kV/cm [152]. The electron conduction current is determined by

$$i_e = q(\pi r^2) N_e v_e \tag{2.29}$$

where N_e is the doping density and v_e is the electron velocity. The saturation
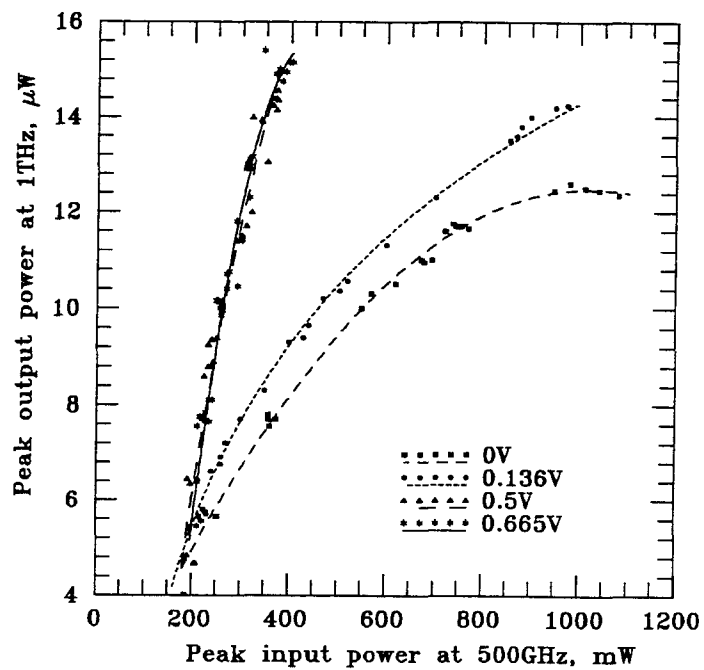
Fig. 2.51 Measured power dependence of multiplier #2 with bias 0 V, 0.136 V, 0.5 V and 0.665 V.
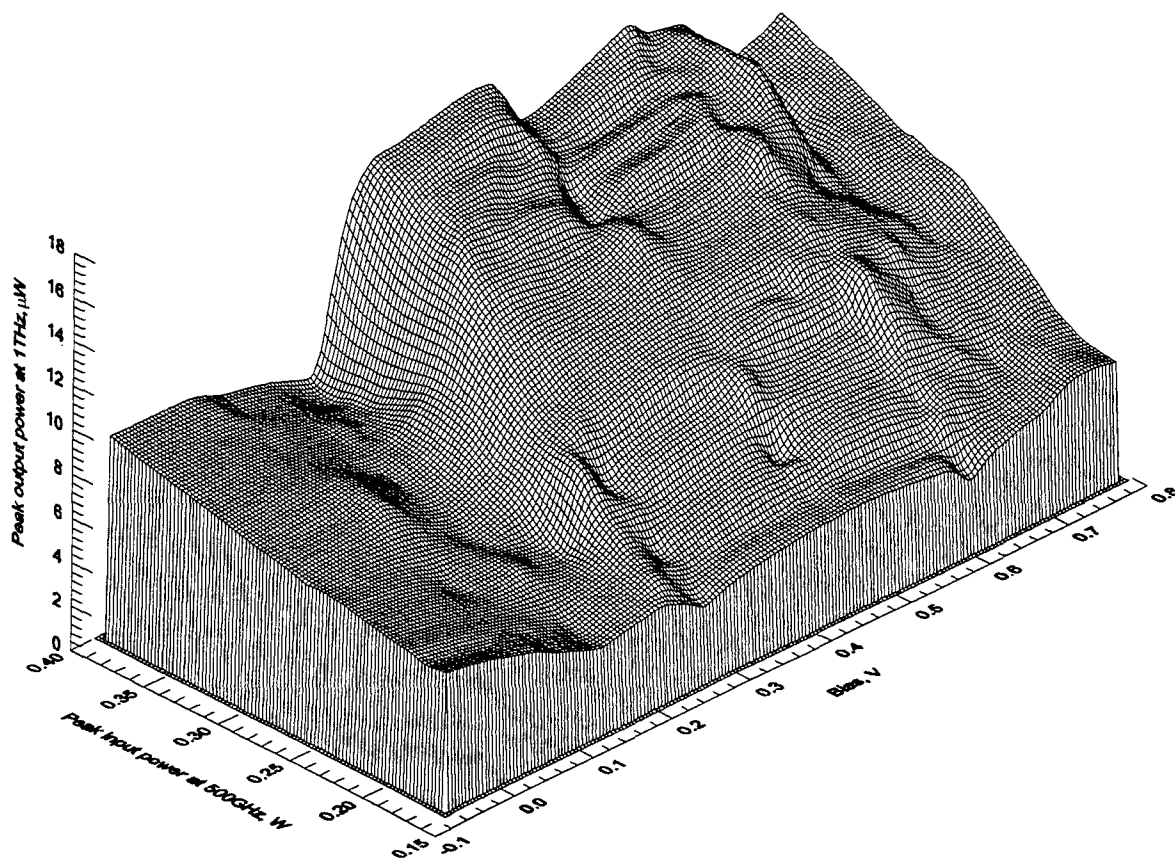

Fig. 2.52 Measured power dependence with different biases from −0.07 V to +0.79 V.

happens when the current in diode, I, reaches the maximum electron conduction current, $i_{e,\max.}$. In our diodes, the estimated saturation current is 2.76 mA.

Louhi *et al.* [153] and Kollberg *et al.* [154] modelled the current saturation on varactor diodes considering the edge effect of the junction capacitance [144] and the effective series resistances. The models give excellent agreement between the theoretical results and the measurements on varactor diodes. The saturation current with the correction factor, γ_C, is given by [153]

$$i_{e,\max.} = q\left(\pi r^2\right) N_e v_{e,\max.} \gamma_C \qquad (2.30)$$

where γ_C =1.5 is decided by the edge effect which means that the maximum current of the diodes depends on the actual transition area between the depleted and undepleted layers. Using this model, the estimated saturation current is 4.14 mA.

2.28 RF CURRENTS

There are three motivations for attempts to measure the RF currents on the diode grids. First, due to the fairly new developments of the THz surface-channel planar Schottky diodes, not enough information on the RF behaviors is available to analyze the RF equivalent-circuits of the multiplier grids. We can only use DC values such as I-V curves and series resistance, low-frequency values such as C-V relationship and estimated values such as junction impedances for the simulation parameters. Second, during the experiments, we noticed that the thermal effects strongly influence the results and possibly cause damages of diodes which degrade the output powers. Understanding how much heat dissipates from the diodes because of the RF currents could help us to avoid the damages. Third, the knowledge of terahertz dynamics on the devices will benefit us using harmonic-balance techniques to predict the output powers and efficiencies in order to optimize the performance.

RF current measurement arrangement is shown in Figure 2.53. The multiplier grid is mounted on and one of the diodes is electrically probed by a conventional probe station. The 500-GHz signal is obliquely incident on the grid due to the equipment limitation. Both the bow-tie and the probe, which behaves like an antenna, couple the RF radiations into the diode. The diode behaves like a video detector and rectifies the RF currents to provide a total DC current as a function of DC bias. The 500-GHz input power is varied by changing the attenuators and monitored by a reference detector. However, due to the oblique incidence, the reading from the reference detector can only give a relative value instead of an absolute incident power. The bias is modulated with a period of 2.22 μs and synchronized with the trigger signal of the free-electron laser so that the bias varies from -0.5 V to $+0.5$ V within the 500-GHz pulse widths.

Figure 2.54 shows the results. The input powers are varied with attenuations of 0 dB, 3.8 dB, 5 dB and 8 dB. The curve without RF radiation is also shown.
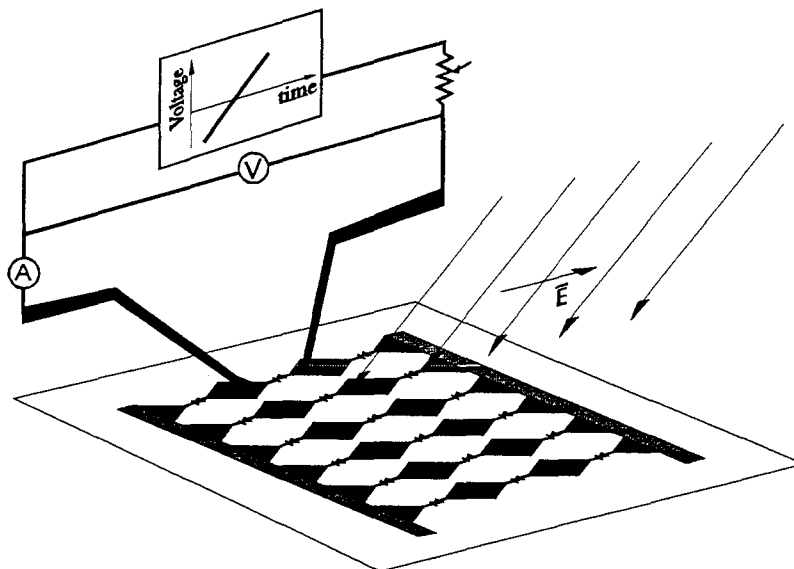

Fig. 2.53 RF current measurement. The 500-GHz signal is obliquely incident on the grid due to the equipment limitation. One diode is probed with a 450-kHz modulated bias. The trigger signal of the free-electron laser is synchronized with the modulated bias so that the bias varies from -0.5 V to $+0.5$ V within the 500-GHz pulse widths.

Although we couldn't decide the absolute absorbed powers due to the oblique incidence and the coupling structures, we expect the absorbed powers be in a "large signal" range. The extra DC currents with negative biases should mostly come from the 500-GHz input signal and the ones with positive biases should be combinations of the 500-GHz fundamental signal and higher harmonics. This explains why the I-V slopes change. The peak RF currents, which should be $\sqrt{2} \times I_{DC}$, added by the RF radiations, are less than 2.7 mA and have not reached the saturation yet.

This measurement didn't allow us to determine the exact amounts of RF currents flowing through the diode due to the present experiment arrangement, more works should be done in the future with proper experimental setup. Ideally we would like to measure the RF I-V relationship at THz frequencies to determine the high-frequency behavior of the diodes. However, it seems not practical. One approach to understand the RF non-linear behavior is to measure the second
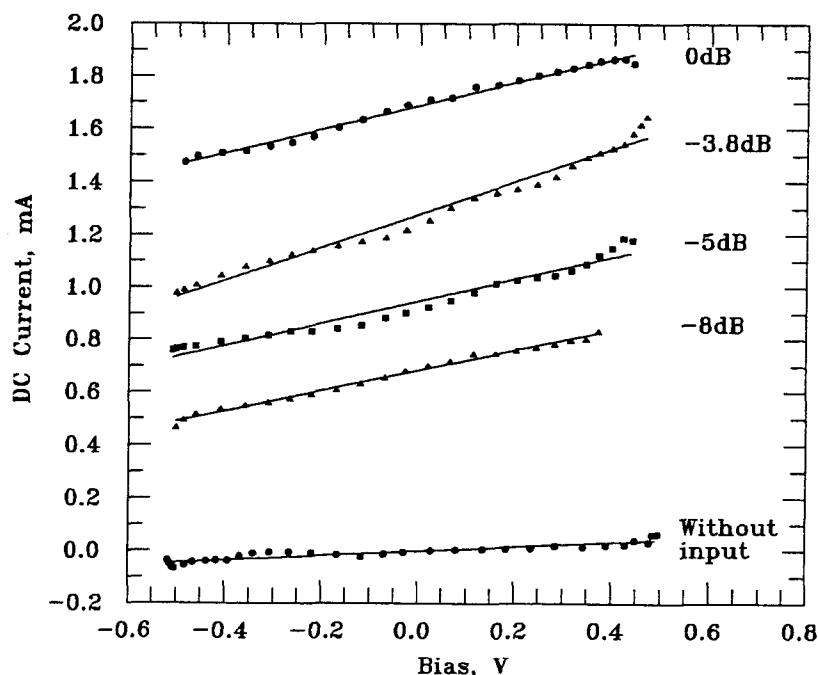

Fig. 2.54 Total DC current as a function of bias with different attenuations of the 500-GHz input powers.
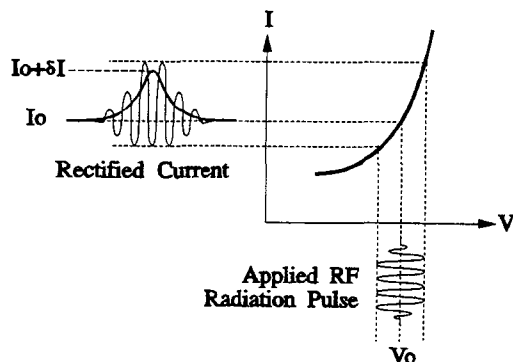
Fig. 2.55 Measurement of RF I-V relationship with small-signal inputs.

derivative of the I-V curves treating the diode as a detector irradiated with a "small signal" input as shown in Figure 2.55.

The non-linear I-V relationship can be expressed as

$$i = f(V_0 + v),$$

$$= I_0 + \frac{\partial f(v)}{\partial v} \Big|_{V=V_0} v + \frac{1}{2} \frac{\partial^2 f(v)}{\partial v^2} \Big|_{V=V_0} v^2 + \frac{1}{6} \frac{\partial^3 f(v)}{\partial v^3} \Big|_{V=V_0} v^3 + \dots$$

$$(2.31)$$

where the small-signal voltage, v, is a time-dependent function. Applying a small-signal $v(t) = v_o \cos(\omega t)$, the changes of DC currents will be proportional to the second derivative of the I-V, $\delta i \propto (\partial^2 f(v)/\partial v^2)$, at RF frequencies.

2.29 DIODE FAILURE

During the measurements, some diodes got damaged when the grid was pumped with high powers. For example, the output power degraded from 330 μW to 200 μW when the pumping power was increased from 3.3 W to 13 W. It is not due to the power saturation because when we reduced the pumping power back to 3.3 W, the multiplier only generated 110 μW. The entire power-dependance curve shifts down after the diodes got damaged. The damaged diodes are open-circuited, verified by an I-V curve tracer. Figure 2.56 shows a photo of a damaged

diode and a working diode. The contact finger of the damaged diode has been stripped off from the device, possibly due to the large currents flowing through the active layer. We also notice that the damaged diodes are mostly located on the top and bottom boundaries of the array. A possible reason is that the unit cells on the boundaries do not satisfy the electric-wall boundary conditions and result in larger RF currents flowing through the diodes. This condition can be improved by introducing quarter-wavelength horizontal metal-strips as bias lines to preserve the symmetries assumed in the unit-cell model. The quarter-wavelength width would transform an open boundary condition into a short one which satisfies the electric-wall assumptions.

Some changes of I-V curves have also been observed on the diodes which are not open-circuited. The saturation current is reduced from 1.3×10^{-16} A to $10^{-18} - 10^{-19}$ A and the DC series resistances are increased. This degradation may
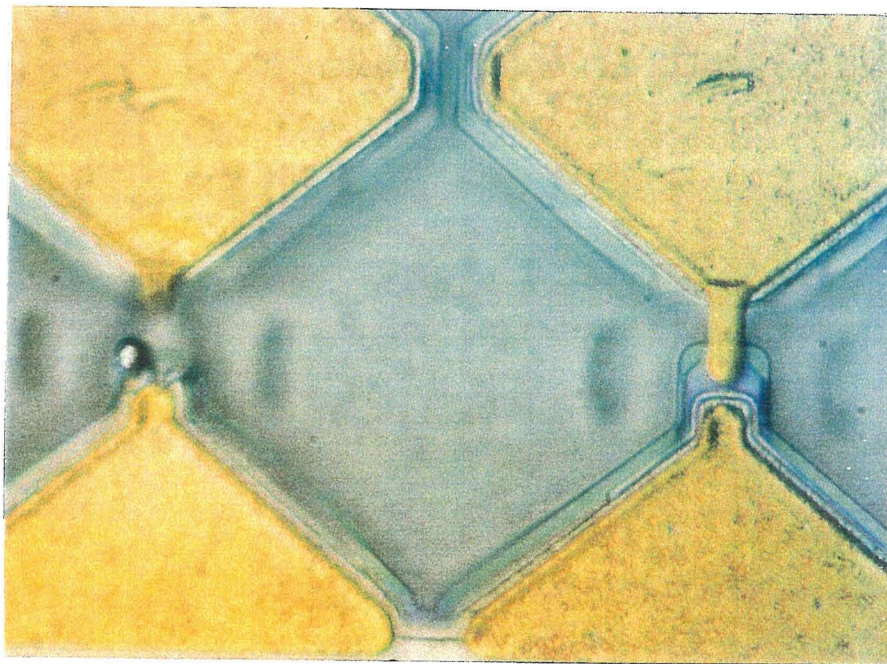

Fig. 2.56 A damaged diode (left) and a working diode (right). The contact finger of the damaged diode has been lifted off.

be caused by the formation of a high-resistance layer between the ohmic metal and GaAs crystal due to the diffusion reaction of the big RF currents [157].

Another possibility for the damage of the diodes is thermal effect. The poor thermal conductivity of fused quartz substrate $(1.4\,W/(m\cdot°K)$ at $273°K)$ may cause heating problems. Cooling the multipliers to $77°$ K with liquid nitrogen or to $150°$ K by passive cooling may solve the problems and offer some other advantages [140,141]. The increased mobilities of the free carriers and the decreased series resistances by cooling the diodes can increase the multiplication efficiencies. The cooled diode can also reach a higher current saturation which will increase the maximum output power. Louhi *et al.* [141] shows that the maximum output power can be improved by 10 dB for a cooled Schottky varactor diode operated at 1 THz.

2.30 HARMONIC-BALANCE ANALYSIS (NONLINEAR ANALYSIS)

The classic theory for nonlinear analysis of frequency multipliers and mixers was studied by Penfield and Rafuse [47] based on ideal varactors at microwave frequencies. Burckhardt [163] further discussed the cases which the varactors have series resistances and nonideal characteristics. However, for complicated cases at millimeter or submillimeter wavelengths, where the harmonics are terminated with different embedding impedances, the simple analysis fails to predict the performances. For arbitrary nonlinearity, the most convenient analysis method would be numerical. The equivalent circuit is divided into linear and nonlinear subcircuits, as shown in Figure 2.57, to perform harmonic-balance analysis. The linear subcircuit is analyzed in the frequency domain to reach the frequency-domain solutions that satisfy the external circuit equations, and the nonlinear subcircuit is analyzed in the time domain to reach time-domain current and voltage solutions that satisfy the diode conditions. Fourier transform is used between these two domains and iterations are performed until both domains reach reasonable convergence. One popular form of the harmonic-balance analysis is

the multiple-reflection technique introduced by Kerr [164]. In his technique, the multiplier circuit is divided into linear and nonlinear subcircuits separated by an inserted transmission line with an arbitrary characteristic impedance. By choosing the length of the transmission line to be an integral number of wavelength at the fundamental frequency, which would also be integral numbers of harmonic wavelengths, the steady-state responses will be the same as without the transmission line. The separation allows to treat the frequency domain and the time domain separately and the conditions of the transmission line should be satisfied in both domains.

Using this technique, Siegel and Kerr [42,165] developed a computer program to perform a full nonlinear large-signal analysis of Schottky diodes, used in multipliers or mixers, with frequency-dependent series-resistances and arbitrary C-V and I-V characteristics. This program calculates current and voltage waveforms based on given diode parameters and embedding impedances at the fundamental and harmonic frequencies, and derives theoretical efficiency and input impedance at a given operating point where the input power and bias are specified. This program and modified versions have been widely used in many research groups. The version we used in this analysis is based on two modified versions written by Tolmunen [158, 166] and by Choudhury [82,88]. The program is modified to
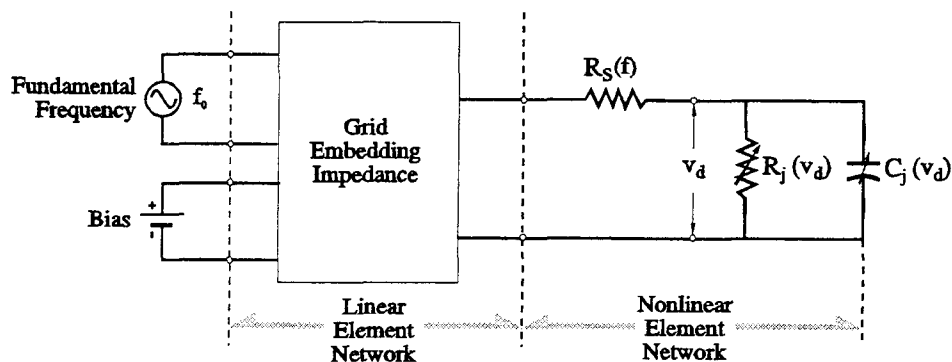

Fig. 2.57 Equivalent circuit of a diode frequency multiplier using harmonic-balance analysis [42].

incorporate the grid embedding impedances and the estimated parameters of the planar Schottky diode used in our multipliers.

Commercial software is also available to perform the harmonic-balance analysis. The Hewlett-Packard *HP85150B* Microwave and RF Design Systems (*MDS 6.0*) package is also used to perform the nonlinear analysis, with the help of Dr. Moonil Kim at JPL. The software provides a complete list of symbolically-defined devices, database-defined devices and nonlinear models of diodes which allows to perform the harmonic-balance analysis more accurately.

Figure 2.58 shows the equivalent circuit of the grid frequency doubler used in the harmonic-balance analysis. The diode is specified as a varistor and the measured DC I-V curve is used due to the fact that the RF I-V is not available. The measured DC value ($14\,\Omega$) is used for the series-resistance of the diode and specified as frequency-independent. This may not be true in real cases. The forward saturation current is assumed to be $4.14\,\text{mA}$ per diode according to
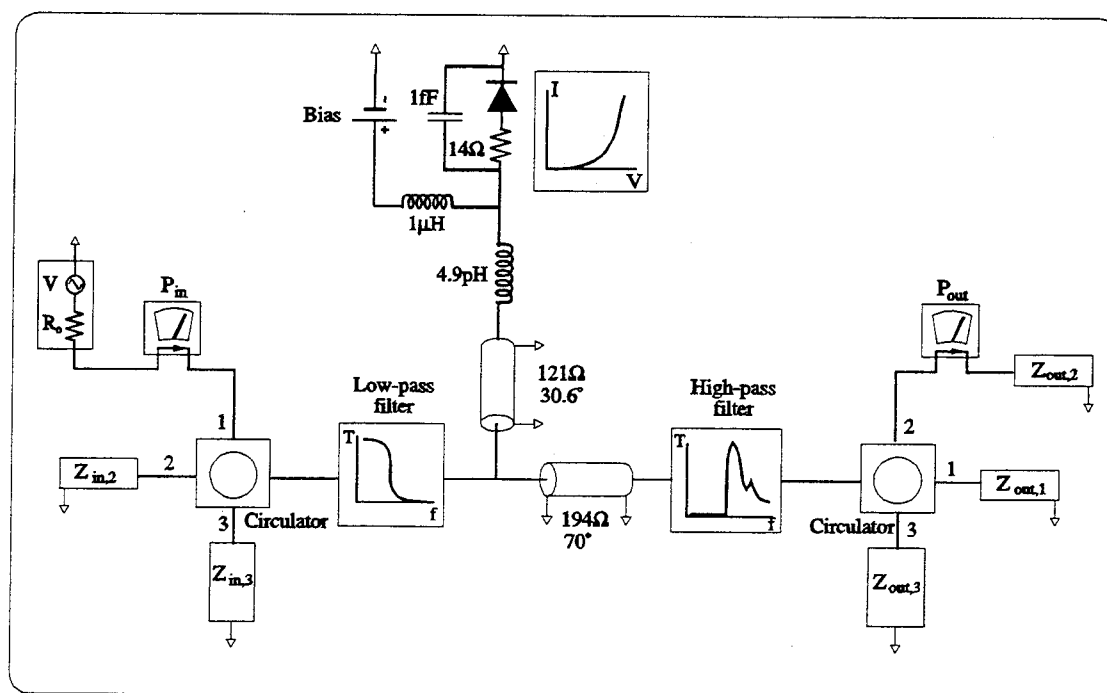

Fig. 2.58 Equivalent circuit of the grid frequency doubler using the harmonic-balance method.

Louhi's model [153]. The reverse breakdown voltage is assumed to be 5 V with 1 μA current. A large (1 μH) series inductor is added to isolate the DC bias. The shunt transmission-line with an impedance of 121 Ω and an electrical length of 30.6° at 1 THz resembles the bow-tie antenna and the inductance of 4.9 pH is contributed by the contact fingers. The quartz substrate is presented by a transmission line with an impedance of 194 Ω and an electrical length of 70° at 1 THz. The input and output filters are incorporated using the measured transmittances of the filters. Two circulators are used to isolate the fundamental and harmonic frequencies. The number of harmonics included in the calculations is six.

Both harmonic-balance methods are used. The modified program based on Siegel's method [42] calculates the optimal performance of the multiplier assuming that the parasitic elements of the diodes are properly tuned-out by outside impedance-tuners and the harmonic impedances are properly terminated. Cal-
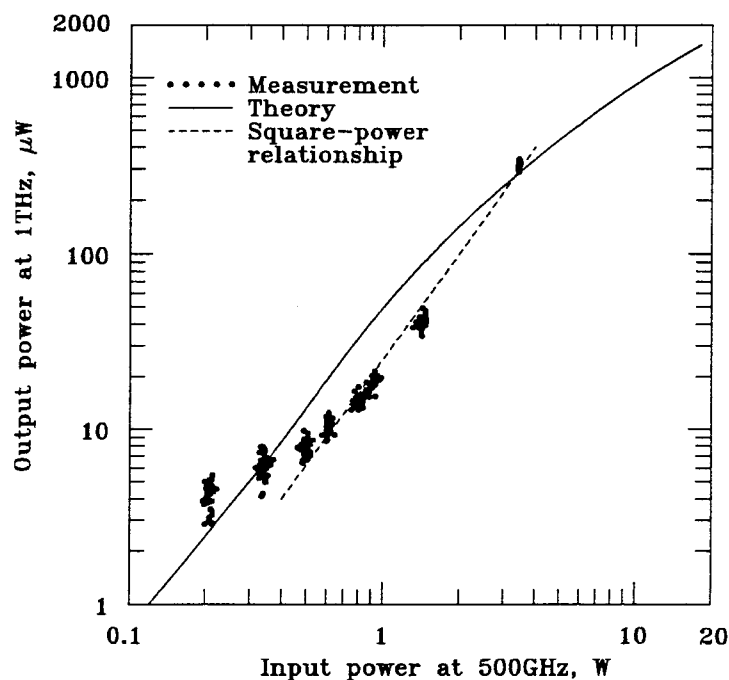
Fig. 2.59 Comparison of theoretical and measured power dependence for multiplier #1.

culations are carried out with bias varied between $-0.3\,\mathrm{V}$ and $+0.7\,\mathrm{V}$, and a maximum efficiency is found to be 2.72% with a bias of 0.5 V and an input power of 1 W for a 6×6 grid with proper diode-orientation. This means, with optimal impedance tunings, the multiplier should be able to generate 27.2-mW output power at 1 THz with an input power of 1 W at 500 GHz.

Figure 2.59 shows the comparison of measurements and calculations on multiplier #1. The calculations are performed by *MDS 6.0* taking the parasitic elements, the transmission curves of the filters and the transmittance of the bolometer window into account The improper diode-orientation factor is also considered by reducing the output powers to 10% of their calculated values, because from measurements, we found that only 10% of the output power is collected by the detector due to the improper output pattern. A bias of 0.3 V is assumed because, from the biasing power-dependence measurements, the diodes seem to be self-biased at around 0.3 V. With an input power of 1 W, the calculated output power is $50\,\mu\mathrm{W}$ and the measured power is about $20\,\mu\mathrm{W}$. It should be emphasized that the measured peak output power is actually calculated from the measured peak output energy using the input pulse width. We expect the output pulses to be narrower than the input pulses so that the actual output powers should be higher than what we presented. The calculated output powers start to become saturated with input powers more than 2 W. This is not observed in our measurements and the discrepancy is possibly due to the estimated forward saturation currents.

2.31 CONCLUSION

Terahertz quasi-optical grid frequency doublers have been investigated by using Schottky diode-grids which are originally designed as sideband generators. This is the first experimental result of quasi-optical grid frequency multipliers in the terahertz frequency range. A peak output power of $330\,\mu\mathrm{W}$ is measured at 1 THz for 2.42-μs 500-GHz input pulses with a peak power of 3.3 W without any

impedance tuning. The relationship between the input power at 500 GHz and the output power at 1 THz follows a square-power relationship. The polarity of the diodes designed for sideband-generator applications results in a null in the center of the output beam for multiplier applications. Measurements show that only 10% of the total radiated power is received by the detector due to the null in the output beam. Theoretical output patterns are calculated to verify the measurements. Results show the attempt of using a lens to correct the output patterns disappointing. Therefore, changing the diode orientations for multiplier applications would be the proper way to improve the output patterns. Biasing tests verify that the frequency multiplication results from varistors. It should be possible to increase the output powers and the conversion efficiencies since these diodes are not saturated yet. Biasing tests also show that these planar Schottky diodes may be self-biasing when no bias is applied. Impedance-tuning tests also indicate that the frequency multiplication results from varistors and, therefore, reactive tuning will not improve the output powers significantly.

2.32 FUTURE WORK

2.32.1 IMPROVEMENT

The diode-orientation designed for sideband-generator applications results in a null in the center of the output beam when used as frequency multipliers. A grid with diode-orientation appropriate for a multiplier application should improve the output pattern and increase the output power without changing the grid design or the planar diode structures. A new batch is being fabricated now by Yongjun Li and Thomas Crowe at the University of Virginia.

The new diode grids will be 12×12 arrays with the same unit-cell design as before. The active area is $840\,\mu m \times 840\,\mu m$ ($2.8\lambda_{1THz} \times 2.8\lambda_{1THz}$) and the entire grid will be 1 mm×1 mm, as shown in Figure 2.60. Each column has 12 diodes in series and the adjacent bow-ties are not connected to avoid possible

short-circuited problems. The planar Schottky diodes face the same direction and have the same structures as before. The top and bottom horizontal metal strips are bias lines. To preserve the symmetries assumed in the unit-cell model, the width of the metal strips extends a quarter-wavelength above and below the top and bottom rows. The quarter-wavelength width would transform an open boundary condition into a short one which satisfies the electric-wall assumptions.
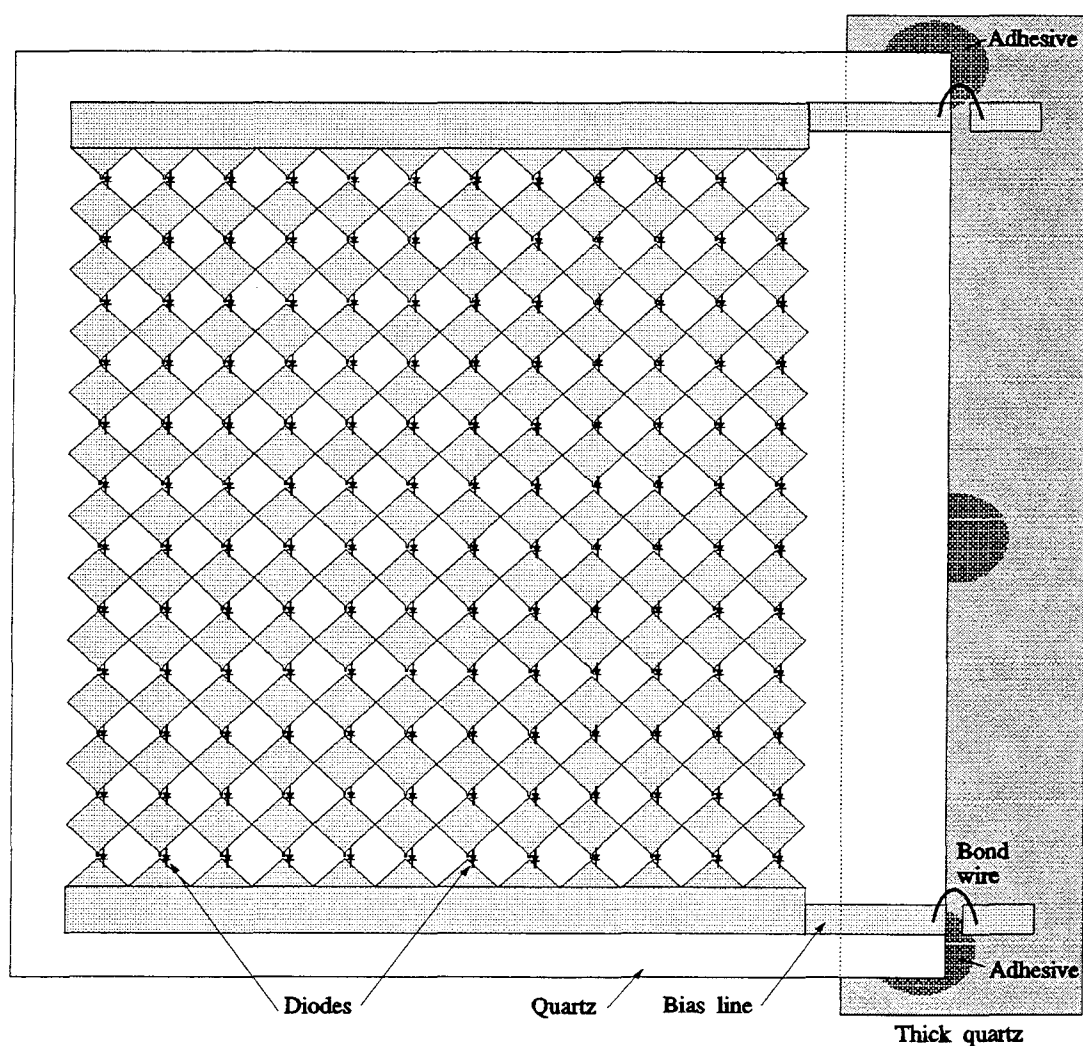

Fig. 2.60 The 12×12 grid multiplier. The unit-cells stay the same as before. Each column has 12 diodes in series and the adjacent bow-ties are not connected. The diodes face the same direction and this diode-orientation will improve the output beam and increase the output powers.

In choosing the quarter-wavelength width, $\lambda_g/4$, the mean dielectric constant of the substrate and the free space is used:

$$\lambda_g = \frac{\lambda_0}{\sqrt{\varepsilon_{\mathrm{mean}}}} = \frac{\lambda_0}{\sqrt{\frac{\varepsilon_r + 1}{2}}} \qquad (2.32)$$

where λ_0 is the free-space wavelength and ε_r is the relative dielectric constant of the substrate. The grid will be glued using optical adhesive on the edge of a thicker quartz and suspended in the air. Bonding wires are used to bring the DC bias in from the side.

The estimated output pattern for the new 12×12 grid multipliers with correct diode-orientation is shown in Figure 2.61. The output patterns for a 6×6 grid with correct diode-orientation and the old 6×6 grid with opposite diode-
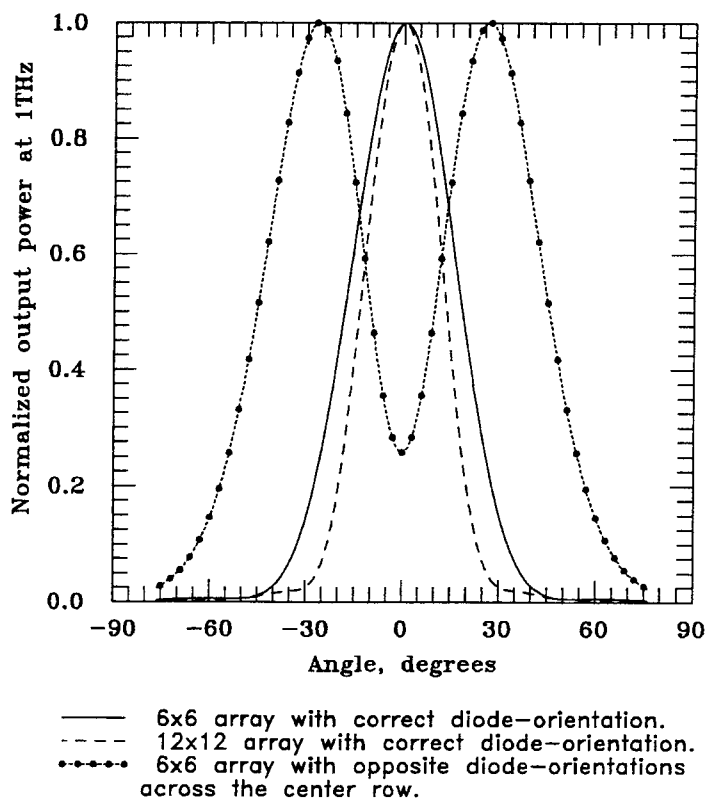

Fig. 2.61 The calculated output pattern for the new 12×12 grid multipliers with correct diode-orientation. The output patterns for a 6×6 grid with correct diode-orientation and the old 6×6 grid with opposite diode-orientations across the center row, are also shown.

orientations across the center row, are also shown. These patterns are calculated taking into consideration of array factors, finite acceptance-angle ($\pm 14°$) of the receiving horn and the antenna pattern of the bow-tie with contact-fingers. Instead of only 10% (measured value) of total radiating power been received by the bolometer in the tested multipliers, 42.5% of total output power will be received for the 6×6 array with correct diode-orientation, using a $\pm 14°$ receiving horn. Increasing the array size also narrows the output beam. 63.5% of total output power will be received by the bolometer for the 12×12 array with correct diode-orientation using the same receiving horn. A calculated 2-D output-beam contour is shown in Figure 2.62. The 2-D array factor is decided by

$$
A(\theta, \psi) = \left[\frac{\sin\left(\frac{12}{2}\phi_y\right)}{\sin\left(\frac{\phi_y}{2}\right)} \right]^2 \left[\frac{\sin\left(\frac{12}{2}\phi_z\right)}{\sin\left(\frac{\phi_z}{2}\right)} \right]^2 \tag{2.33}
$$

where θ and ψ are shown in the notations of Figure 2.38(b) and

$$
\phi_y = k_0 d_y \sin(\theta)\cos(\psi), \qquad \phi_z = k_0 d_z \sin(\theta)\sin(\psi)
$$

with $k_0 = 2\pi/\lambda_0$ and $d_y = d_z = 70\,\mu$m. The 2-D antenna pattern of the bow-tie with contact-fingers is computed by *HFSS*.

Increasing the size of grid does not only increase the output powers, but also reduces the diffraction losses in the matching circuits and filters, especially the low-pass filter. The low-pass filter reflects the second harmonic signal back to the output side and a narrower beam by a larger array will reduce the diffraction losses. A more compact setup for the entire system to bring the tuning slabs as close as possible to the grid will also reduce the diffraction losses. Since the diodes act as varistors, single-slab reactive tuning will not be sufficient for matching impedances. Double-slab tuning circuits are needed. Two quarter-wavelength thick TPX slabs with adjustable distances between the slabs are a suitable option considering the low-loss feature of TPX material. An ideal setup
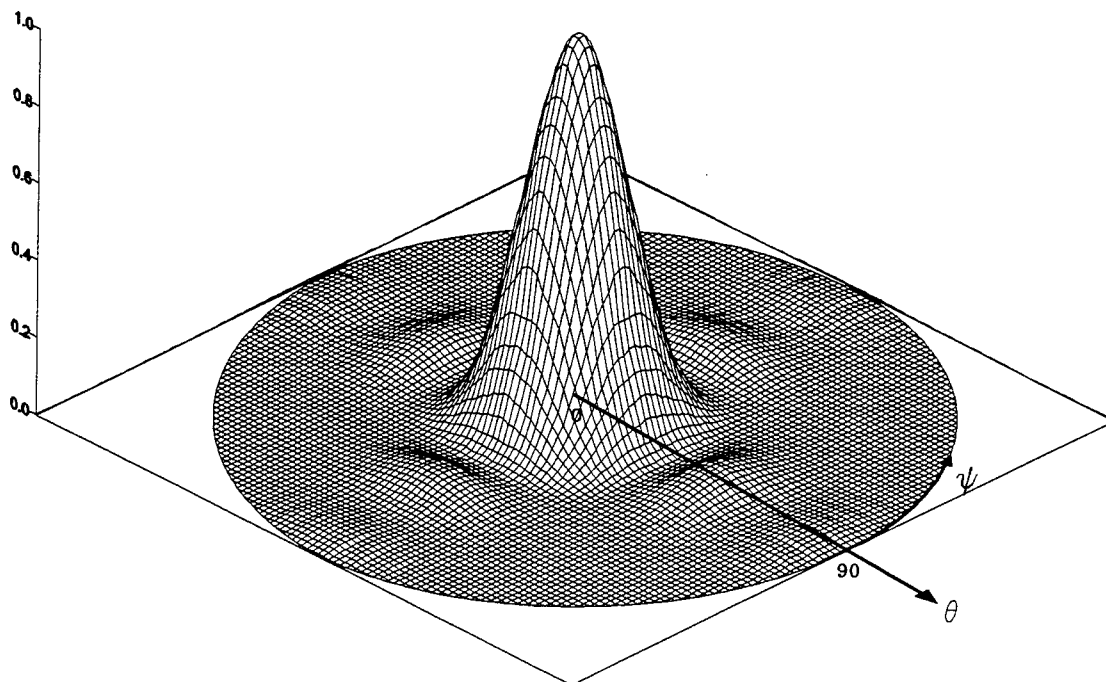
Fig. 2.62 The calculated 2-D output-beam contour for a 12×12 grid multiplier with correct diode-orientation.

would have all the elements mounted on a stage with $\hat{x}$, $\hat{y}$ and $\hat{z}$ movements, two-degree rotations, and relative spacing adjustments of all the elements on the stage.

Predictions of output powers by the harmonic-balance analysis should also be improved by more accurate modelling of the Schottky diodes. The method of using hydrodynamic device simulations combined with the harmonic-balance analysis is recommended. Jones *et al.* [167,168] demonstrated the idea and reported calculation results which are in good agreement with previously-published measurement results. A computer program employing the same method to simulate Schottky diodes has been ready to be tested at the time this thesis was written, unfortunately, due to the time constraint, we are not able to test it.

2.32.2 OTHER DEVICES

Frequency multiplication results from a nonlinear impedance driven by a periodic source. There are three choices using diodes as the nonlinear devices: varistors, varactors and combinations of these two kinds. The varistor utilizes the nonlinear I-V relationship of a forward-biased diode while the varactor utilizes the nonlinear C-V relationship of a reverse-biased diode. The advantages of using varistors are that they inherently have real impedances and high cutoff frequencies, so the impedance tuning will not be very critical. The disadvantage is that the maximum conversion efficiencies are 25% for a doubler and 11% for a tripler [44]. The varactors rely on variable capacitance, and therefore can, in principle, have higher efficiency (ideally, the efficiency will reach 100%) [46] and higher power-handling ability [158]. However, the cutoff frequencies of varactors are lower because the variable junction capacitances unavoidably increase the parasitic capacitances.

Both planar varactor and varistor diodes have now been made to roughly 1-THz applications at University of Virginia. Our next attempt will be using planar varactor diodes on the diode-grids to increase conversion efficiencies. Both planar varistors and varactors potentially suffer from the current saturation problem due to the small size of device area. The estimated saturation current in our device is 2.74 mA or 4.14 mA, depending on the models [153, 158]. To compare, a whisker-contacted diode with a doping concentration of $N_d = 10^{17}$ cm^{-3} and a nominal device area of 5 μm^2 made at UVA (UVA2T2-diode) will have a saturation current of 20 mA [158]. Performance can be improved by increasing doping concentration, increasing the cross section of the diode or using semiconductor materials with higher saturation electron velocity such as InAs. Increasing doping concentration will decrease the reverse breakdown voltage and increasing the diode area will increase the parasitic capacitance that reduces the roll-off frequency. Therefore seeking for a better device structure or material such as

InP-based planar varactors [159] or superlattice barrier varactors [160] for the planar Schottky diode grid will be an important direction in the future in order to increase conversion efficiencies and powers.

As mentioned before, the main purpose of this project is to integrate the expertise of Dr. Tom Crowe's group on planar Schottky diodes at University of Virginia and the experience of quasi-optical grid methods developed in Dr. David Rutledge's group at Caltech to develop submillimeter-wave frequency multipliers. The similar situation happened when the measurements took place in the Quantum Institute at University of California, Santa Barbara (UCSB). In the Center for Free-Electron Laser Studies, Dr. Jim Allen's group has been using the free-electron laser to study nonlinear electron dynamics at terahertz frequencies. One of the impressive results is the discovery of the giant third-order nonlinear susceptibilities of single InAs quantum wells [161, 162]. Third-order, free-carrier nonlinear susceptibilities, $\chi^{(3)}$, have been measured for InAs/AlSb quantum wells from 570 GHz to 690 GHz. The peak value of $\chi^{(3)}$ reaches 1 esu at 600 GHz which is several orders of magnitude larger than n-GaAs ($\sim 10^{-4}$ esu) or polyacetylene ($\sim 10^{-7}$ esu). This makes the InAs/AlSb an attractive candi-
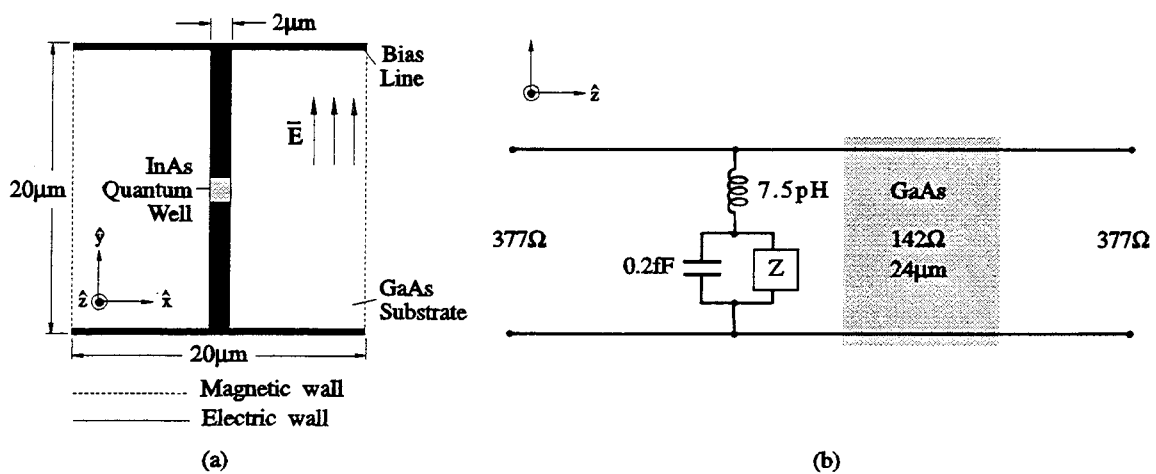

Fig. 2.63 (a) The unit cell for an InAs quantum-well frequency tripler and (b) the equivalent circuit.

date for third-harmonic radiation generations. So far, all the measurements for InAs/AlSb quantum-well device are done with a single device on GaAs wafer at normal incidence of fundamental signal. Quasi-optical grid combining lots of devices could efficiently increase the output powers and provide means for impedance matching.

The unit-cell for a 1.8-THz InAs quantum-well tripler is shown in Figure 2.63(a). The fundamental frequency is 600 GHz and the unit-cell size is $20\,\mu m \times 20\,\mu m$. The device is located in the center of the unit cell connected by two metal strips which act as a dipole antenna to couple the electric fields into the device. The size of the device is $2\,\mu m \times 2\,\mu m$. Figure 2.63(b) shows the equivalent circuit. The shunt inductance contributed by the metal strip is 7.5 pH. The GaAs substrate has a thickness of $24\,\mu m$ and a relative dielectric constant of 13.1. The impedance of the device is estimated to be $Z = 62\,\Omega + 28\,pH$ at 1.8 THz and the calculated shunt capacitance is 0.2 fF for a device-height of $2\,\mu m$. Calculated reflectance of the InAs quantum-well grid tripler is shown in Figure 2.64.
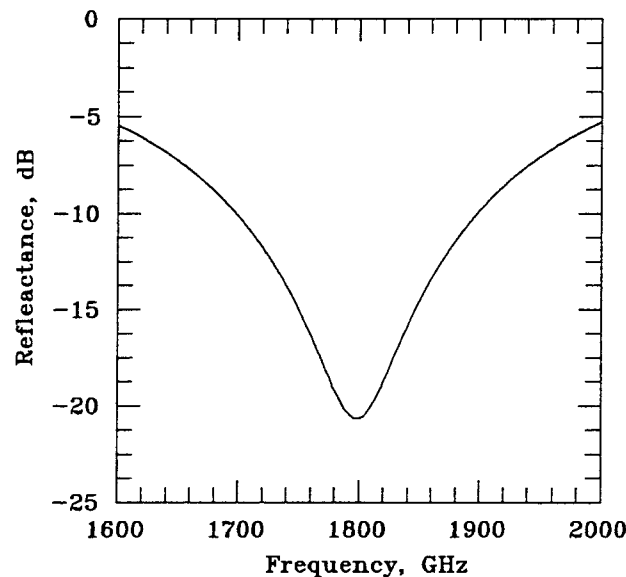

Fig. 2.64 Calculated reflectances as a function of frequency for the design in Figure 2.63, without impedance-tuning elements.

The reflectance has a null of $-21\,$dB at $1.8\,$THz.

Unfortunately, the fabrication of the InAs quantum-well tripler grids were still underway at UCSB at the time this thesis was written, no experimental results can be presented. The measurements will be using the free-electron laser at UCSB with the similar experiment arrangement we used. From the past experiences [162], output powers at $1.8\,$THz are expected to be in the range of $10\,\mu$W-$100\,\mu$W for a 10×10 array pumped by a watt-level 600-GHz signal.

2.33 ACKNOWLEDGEMENTS

I would like to give my sincere gratitude to the following friends for helping me with this project:

Dr. Jonathan Hacker at Bellcore for his foresight on this project and a terrific job on designing these diode grids. Andrea Markelz at University of California, Santa Barbara (UCSB) for helping me with measurements, providing me a lot of information and sharing with me her experimental data. Without her help, these measurements would take $20\,$dB more time and effort. Yongjun Frank Li at University of Virginia (UVA) for fabricating diode grids and providing information of fabrications. The fabrication is the most difficult part of this project. Jeffrey Hesler at UVA for designing the first batch and original discussions on the sideband generator grids. Dr. Tom Crowe at UVA for his generosity for offering me these devices and his expertise on design, fabrication as well as analysis on planar Schottky diodes. Dr. Jim Allen at UCSB for using the free-electron laser and valuable suggestions on THz measurements; and David Enyeart as well as the staff of the Center for Free-Electron Laser Studies for their help on operating the laser. Kent Potter at CalTech for helping me build the measurement components. Michael De Lisio at CalTech for valuable discussion on pattern calculations. Dr. Timo Tolmunen at Turku Institute of Technology, Finland; Dr. Debabani Choudhury at Millitech; and Dr. Moonil Kim at Jet Propulsion Laboratory (JPL) for their help on the harmonic-balance analysis. Dr. Peter

REFERENCES

[1] J.W. Waters et al., "Aircraft Search for Millimeter-Wavelength Emission by Stratospheric ClO," *Journal of Geophysical Research*, 84, C11, pp. 7034-7040, Nov. 1979.

[2] D. Robbins, J. Waters, P. Zimmermann, R. Jarnot, J. Hardy, H. Pickett, S. Pollitt, W. Traub, K. Chance, N. Louisnard, W. Evans and J. Kerr, "Ozone Measurements from the Balloon Intercomparison Campaign," *Journal of Atmospheric Chemistry*, 10, pp. 181-218, 1990.

[3] J.W. Waters, "Submillimeter Heterodyne Remote Sensing of Upper Atmosphric Gases," *Microwave and Optical Technology Letter*, Vol. 4, No. 1, pp. 2-6, Jan. 1991.

[4] J.W. Waters and P.H. Siegel, "Applications of Millimeter and Submillimeter Technology to Earth's Upper Atmosphere: Results To Date and Potential for the Future," *The 4th International Symposium on Space Terahertz Technology*, Los Angeles, CA, March 1993.

[5] J. Farman, B. Gardiner and J. Shanklin, "Large Losses of Total Ozone in Antarctica Reveal Seasonal ClO_x/NO_x Interaction," *Nature*, Vol. 315, pp. 207, 1985.

[6] P.B. Hays and H.E. Snell, "Atmospheric Remote Sensing in the Terahertz Region," *The Proceeding of the 1st International Symposium on Space Terahertz Technology*, pp. 482, 1990.

[7] "NASA/OACT Submillimeter Sensor Program Local Oscillator Review," Jan. 27, 1994.

[8] T.G. Phillips, "Developments in Submillimeterwave Astronomy," *The 19th International Conference on Infrared and Millimeter Waves in Sendai, Japan*, 1994.

[9] S. Gulkis, "Submillimeter Wavelength Astronomy Missions for the 1990s," *The Proceeding of the 1st International Symposium on Space Terahertz Technology*, pp. 454-457, 1990.

[10] J.A. Cutts, "STROTECH 21: Terahertz Technology for Space Astronomy in the 21st Century," *The Proceeding of the 1st International Symposium on Space Terahertz Technology*, pp. 69-73, 1990.

[11] M.Sokoloski and C.A. Kukkonen, "NASA's Terahertz Technology Program," *The Proceeding of the 1st International Symposium on Space Terahertz Technology*, pp. 33-68, 1990.

[12] M.A. Frerking, "The Submillimeter Mission Heterodyne Instrument," *The Proceeding of the 2nd International Symposium on Space Terahertz Technology*, pp. 17-31, 1991.

[13] "FIRST. Far Infrared and Submillimeter Space Telescope. Assessment Study," *ESA document*, No. SCI(83)1, Sep. 1983.

[14] G.J. Melnick, "On the Road to the Large Deployable Reflector (LDR): The Utility of the Ballon-Borne Platforms for Far-Infrared and Submillimeter Spectroscopy," *Int. J. Infrared Millimeter Waves*, Vol. 9, No. 9, pp. 781-812, 1988.

[15] A. Räisänen, "Frequency Multipliers for Millimeter and Submillimeter Wavelengths," *Proceedings of the IEEE*, Vol. 80, No. 11, pp. 1842-1852, Nov. 1992.

[16] N.C. Luhmann. Jr., "Instrumentation and Techniques for Plasma Diagnostics: An Overview.," *Infrared and Millimeter Waves*, Vol. 2, K.J. Button, ed., Academic Press, Inc., New York, 1979.

[17] P.E. Young, D.F. Neikirk, P.P. Tong and N.C. Luhmann. Jr., "Multi-Channel Far-Infrared Phase Imaging For Fusion Plasma," *Rev. Sci. Instrum.*, 56, pp. 91-89, 1985.

[18] P.F. Goldsmith "Coherent Systems in the Terahertz Frequency Range: Elements, Operation and Examples," *The Proceeding of the 3rd International Symposium on Space Terahertz Technology*, pp. 1-23, 1992.

[19] P.K. Cheo, "An Inductrial Qualified FIR Laser Scanner for High-Voltage Cable Inspection," *7th Int'l Conf. on Infrared and Millimeter Wave, Marseille, France*, pp. W3-1, 1983.

[20] E.K. Reedy and W. Emell, "Millimeter Radar," *Infrared and Millimeter Waves*, Vol. 4, Chap. 2, K.J. Button, ed., Academic Press, Inc., New York, 1982.

[21] K. Miyanchi, "Millimeter-Wave Communications," *Infrared and Millimeter Waves*, Vol. 9, Chap. 1, K.J. Button, ed., Academic Press, Inc., New York, 1983.

[22] H.H. Brand, J. Brune, A.J. Harth, R.H. Janker, M.G. März, S.L. Martius, D.P. Steup and B.G. Stöckel "Terahertz-Research at Erlangen University Laboratories for High Frequency Technology," *The Proceeding of the 5th International Symposium on Space Terahertz Technology*, pp. 1-26, 1994.

[23] B. Stec and M. Zurawski, "Compensated Microwave Thermometer for Biomedical Measurements," *Proceedings of the 23rd European Microwave Conference, Madrid, Spain*, pp. 269-270, Sept. 1993.

[24] R.S. Avakian and A.L. Taube, "Devices for Microwave Resonance Therapy," *Proceedings of the 23rd European Microwave Conference, Madrid, Spain*, pp. 52-57, Sept. 1993.

[25] M.M.Z. Kharadly and A.Y. Chan, "Proposed Microwave Technique for On-Line Measurement of Moisture Content in Green Lumber," *Proceedings of the 23rd European Microwave Conference, Madrid, Spain*, pp. 271, Sept. 1993.

[26] J. Bel Hadj Tahar, J. Ch. Bolomey and M. Cauterman, "Microwave Life Detector for Buried Victims," *Proceedings of the 23rd European Microwave Conference, Madrid, Spain*, pp. 263-264, Sept. 1993.

[27] M. Guttenberger, K.H. Mierzwiak and W. Sturm, "Microstrip Array Antenna for an Automatic Road Pricing System," *Proceedings of the 23rd European Microwave Conference, Madrid, Spain*, pp. 351-353, Sept. 1993.

[28] G. Kantorowicz and P. Palluel, "Backward Wave Oscillator," *Infrared and Millimeter Waves*, Vol. 1, Chap. 4, K.J. Button, ed., Academic Press, Inc., New York, 1983.

[29] F.T. Ulaby, "Overview of the University of Michigan Space Terahertz Technology Program," *The Proceeding of the 1st International Symposium on Space Terahertz Technology*, pp. 5-32, 1990.

[30] G.I. Haddad and J.R. East, "Tunnel Transit-time (TUNNETT) Devices for Terahertz Sources," *The Proceeding of the 1st International Symposium on Space Terahertz Technology*, pp. 104-126, 1990.

[31] H. Eisele and G.I. Haddad, "InP Gunn Devices and GaAs TUNNETT Diodes as Low-Noise High-Performance Local Oscillators in Fundamental Mode," *The Abstracts of the 6th International Symposium on Space Terahertz Technology*, 1995.

[32] E.R. Brown, "Submillimeter-wave Resonant-Tunneling Oscillators," *The Proceeding of the 1st International Symposium on Space Terahertz Technology*, pp. 74-83, 1990.

[33] D.P. Steenson, R.D. Pollard, R.E. Miles and J.M. Chamberlain, "Power-Combining of Resonant Tunnelling Diode Oscillators at W-band," *The 19th International Conference on Infrared and Millimeter Waves in Sendai, Japan*, 1994.

[34] E.R. Brown, C.D. Parker, A.R. Calawa, M.J. Manfra, C.L. Chen, L.J. Mahoney, W.D. Goodhue, J.R. Söderströmt and T.C. McGill, "High Frequency Resonant-tunneling Oscillators," *Microwave and Optical Technology Letters*, pp. 19, Vol. 4, No. 1, Jan. 5,1991.

[35] E.R. Brown, K.A. McIntosh, K.B. Nichols and C.L. Dennis, "Photomixing up to 3.8 THz in Low-Temperature-Grown GaAs," *Applied Physics Letters*, 66(3), pp. 285-287, 16 Jan. 1995.

[36] M. Hirayama, T. Takada, T. Ishibashi and M. Ohmori, "Submillimeter Wave Frequency Multipliers and Impatt Oscillators," *IEEE, MTT-S Int. Microwave Symposium Digest*, pp. 435-437, 1978.

[37] H.J. Kuno, "Solid-state Millimeter-wave Power Sources and Combiners," *Microwave Journal*, Vol. 24, No. 6, pp. 21, 1981.

[38] "Millitech Millimeter Wave and Submillimeter Wave Components Catalog," 1992.

[39] "HUGHES Millimeter-wave Product Catalog," June 1989.

[40] M. Ohmori, "Millimeter-wave InP Gunn Diodes," *US-Japan Workshop on Development of Millimeter- and Submillimeter-wave Technology for Diagnostic Applications for Large Plasma Devices*, 8-1, March 1994.

[41] R. Kamoua, H. Eisele and G.I. Haddad, "D-Band (110-170 GHz) InP Gunn Devices," *Solid-State Electronics*, pp. 1547-1555, Vol. 36, No. 11, 1993.

[42] Peter H. Siegel, "Topics in the Optimization of Millimeter-Wave Mixers," *Ph.D. Dissertation*, Columbia University, 1984.

[43] A. Mardon, "Nonlinear Resistance and Nonlinear Reactance Devices for Harmonic Generation," *Millimetre and Submillimetre Waves*, pp. 179-191, 1969.

[44] C.H. Page, "Frequency Conversion with Positive Nonlinear Resistors," *Journal of the National Bureau of Standards*, pp. 179-182, Vol. 56, April 1956.

[45] M.V. Schneider, "Metal-Semiconductor Junctions as Frequency Converters," *Infrared and Millimeter Waves*, Chapter 4, Vol. 6, 1982.

[46] J.M. Manley and H.E. Rowe, "Some General Properties of Nonlinear Elements - Part I. General Energy Relations," *Proceedings of IRE*, pp. 904-913, Vol. 44, No. 7, July 1956.

[47] P. Penfield Jr. and R.P. Rafuse "Varactor Applications," *Cambridge, MA, MIT Press*, 1962.

[48] J.W. Archer, "Millimeter Wavelength Frequency Multipliers," *IEEE Trans. on Microwave Theory and Tech.*, Vol. MTT-29, No. 6, pp. 552-557, June 1981.

[49] M.T. Faber, J.W. Archer and R.J. Mattauch, "A High Efficiency Frequency Doubler for 100GHz," *IEEE, MTT-S Int. Microwave Symposium Digest*, pp. 363-366, 1985.

[50] N. Erickson, "High Efficiency Submillimeter Frequency Multipliers," *IEEE, MTT-S Int. Microwave Symposium Digest*, pp. 1301-1304, 1990.

[51] T. Takada, T. Makimura and M. Ohmori, "Hybrid Integrated Frequency Doublers and Triplers to 300 and 450 GHz," *IEEE Trans. on Microwave Theory and Tech.*, Vol. MTT-28, pp. 966-973, Sep. 1980.

[52] R. Zimmermann, R. Zimmermann and P. Zimmermann, "490 GHz Solid State Source with Varactor Quadrupler," *The 13th International Conference on Infrared and Millimeter Waves Digest*, pp. 77-78, 1988.

[53] R. Zimmermann, R. Zimmermann and P. Zimmermann, "All Solid-State Radiometer at 557 GHz," *Proceedings of the 21st European Microwave Conference*, Stuttgart, pp. 253-256, Sept. 1991.

[54] R. Zimmermann, R. Zimmermann and P. Zimmermann, "All-Solid-State Radiometers for Environmental Studies to 700 GHz," *The Proceeding of the 3rd International Symposium on Space Terahertz Technology*, pp. 706-723, 1992.

[55] H. Rothermel, T.G. Phillips and J. Keene, "A Solid-State Frequency Source for Radio Astronomy in the 100 to 1000 GHz Range," *The International Journal of Infrared and Millimeter Waves*, pp. 83-100, 1989.

[56] B.L.A. Rydberg, B.N. Lyons and U.S. Lidholm, "Multipliers for THz Heterodyne Systems," *The Proceeding of the 2nd International Symposium on Space Terahertz Technology,* pp. 212-224, 1991.

[57] A. Rydberg, B.N. Lyons and S.U. Lidholm, "On the Development of a High Efficiency 750 GHz Frequency Tripler for THz Heterodyne Systems," *IEEE Trans. on Microwave Theory and Tech.,* Vol. 40, No. 5, pp. 827-830, May 1992.

[58] N. Erickson and J. Tuovinen, "A Waveguide Tripler for 800-900 GHz," *The 6th International Symposium on Space Terahertz Technology,* Pasadena, CA, March 1995.

[59] A. Räisänen, "Recent Advances in the Studies of Frequency Multipliers at Millimeter and Submillimeter Wavelengths," *The Proceedings of the 24th European Microwave Conference,* pp. 133-143, Cannes, France, Sept. 1994.

[60] R. Zimmermann, T. Rose and T. Crowe, "An All Solid-State 1 THz Radiometer for Space Applications," *The 6th International Symposium on Space Terahertz Technology,* Pasadena, CA, March 1995.

[61] N.R. Erickson, "A High Efficiency Frequency Tripler for 230 GHz," *Proc. 12th Eur. Microwave Conf., Helsinki, Finland,* pp. 288-292, Sep. 1982.

[62] N.R. Erickson, "High Efficiency Millimeter and Submillimeter Frequency Multipliers," *The 8th International Conference on Infrared and Millimeter Waves in Miami,* M3.2, Dec. 1983.

[63] M.A. Frerking, H.M. Pickett and J. Farhoomand, "A Submillimeter Wave Quasi-Optical Frequency Doubler," *IEEE MTT-S Int. Microwave Symposium Digest,* pp. 108-109, 1983.

[64] J.W. Archer, "A Novel Quasi-Optical Multiplier Design for Millimeter and Submillimeter Wavelengths," *IEEE Trans. on Microwave Theory and Tech.,* Vol. MTT-32, No. 4, pp. 421-427, April 1984.

[65] J.W. Archer, "An Efficient 200-290 GHz Frequency Tripler Incorporating a Novel Stripline Structure," *IEEE Trans. on Microwave Theory and Tech.,* Vol. MTT-32, No. 4, pp. 416-420, April 1984.

[66] J.W. Archer and M.T. Faber, "High-Output, Single- and Dual-Diode, Millimeter-Wave Frequency Doublers," *IEEE Trans. on Microwave Theory and Tech.,* Vol. MTT-33, No. 6, pp. 533-538, June 1985.

[67] P.D. Batelaan and M. A. Frerking, "Quantum Well Multipliers," *Twelfth International Conference on Infrared and Millimeter Waves Digest,* pp. 14-15, 1987.

[68] A. Räisänen and M. Sironen, "Capability of Schottky-Diode Multipliers as Local Oscillators at 1 THz," *The Proceeding of the 1st International Symposium on Space Terahertz Technology,* pp. 293-302, 1990.

[69] M. A. Frerking, "Quantum Well Multipliers: Triplers and Quintuplers," *The Proceeding of the 1st International Symposium on Space Terahertz Technology*, pp. 319-342, 1990.

[70] A. Räisänen and M. Sironen, "Capability of Schottky-Diode Multipliers as Local Oscillators at 1 THz," *Microwave and Optical Technology Letter*, Vol. 4, No. 1, pp. 29-33, Jan. 1991.

[71] Y. Kwon and D. Pavlidis, "Diode Multipliers for Submillimeter-Wave InAlAs/InGaAs Heterostructure Monolithic Integrated Circuits," *Microwave and Optical Technology Letter*, Vol. 4, No. 1, pp. 38-43, Jan. 1991.

[72] Y. Kwon, D. Pavlidis,P. March, M. Tutt, G.I. Ng and T. Brock, "90-180 GHz Heterostructure Monolithic Integrated Doubler," *The Proceeding of the 2nd International Symposium on Space Terahertz Technology*, pp. 238-254, 1991.

[73] T.W. Crowe, W.C.B. Peatman and E. Winkler, "GaAs Schottky Barrier Varactor Diodes for Submillimeter Wavelength Power Generation," *Microwave and Optical Technology Letter*, Vol. 4, No. 1, pp. 49-53, Jan. 1991.

[74] H. Grönqvist, E. Kollberg and A. Rydberg , "Quantum-Well and Quantum-Barrier Diodes for Generating Submillimetre Wave Power," *Microwave and Optical Technology Letters*, Vol. 4, No. 1, pp. 33-38, Jan. 5 1991.

[75] W.C.B. Peatman T.W. Crowe and M. Shur, "A Novel Schottky/2-DEG Diode for Millimeter- and Submillimeter-Wave Multiplier Application," *IEEE Electron Device Letters*, Vol. 13, No. 1, pp. 11-13, Jan. 1992.

[76] W.C.B. Peatman T.W. Crowe, M. Shur and B. Gelmont, "A Schottky/2-DEG Varactor Diode for Millimeter- and Submillimeter-Wave Multiplier Applications," *The Proceeding of the 3rd International Symposium on Space Terahertz Technology*, pp. 93-109, 1992.

[77] N.R. Erickson, B.J. Rizzi and T.W. Crowe, "A High Power Doubler for 174 GHz Using a Planar Diode Array," *The Proceeding of the 4th International Symposium on Space Terahertz Technology*, pp. 287-296, 1993.

[78] D. Choudhury, A. Räisänen, R.P. Smith and M.A. Frerking, "A Back-to-back Barrier-N-N$^+$ (bbBNN) Diode Tripler at 200 GHz," *The Proceeding of the 4th International Symposium on Space Terahertz Technology*, pp. 274-286, 1993.

[79] B.N. Lyons, D.R. Vizard and U.S. Lidholm, "A High Efficiency Tripler for Use in a Far Infrared Solid State Source," *The 19th International Conference on Infrared and Millimeter Waves in Sendai, Japan*, 1994.

[80] O. Tanguy, D. Lippens, J. Bruston, J.C. Pernot, G. Beaudin, J. Nagle and B. Vinter, "Frequency Conversion to 368GHz Using Resonant Tunneling Diodes," *The Proceeding of the 5th International Symposium on Space Terahertz Technology*, pp. 524-530, 1994.

[81] T.Tolmunen, A. Räisänen, E. Brown, H. Grönqvist and S. Nilsen, "Experiments with Single Barrier Varactor Tripler and Quintupler at Millimeter Wavelengths," *The Proceeding of the 5th International Symposium on Space Terahertz Technology*, pp. 486-496, 1994.

[82] D. Choudhury, P. Siegel, A. Räisänen, S. Martin and P. Smith, "A Tripler to 220GHz Using Back-to-back Barrier-N-N$^+$ Varactor Diode," *The Proceeding of the 5th International Symposium on Space Terahertz Technology*, pp. 475-485, 1994.

[83] D. Choudhury, A.V. Räisänen, R.P. Smith, M.A. Frerking, S.C. Martin and J.K. Liu, "Experimental Performance of a Back-to-back Barrier-N-N$^+$ Varactor Tripler at 200 GHz," *IEEE Trans. on Microwave Theory and Tech.*, Vol. 42, No. 4, pp. 755-758, 1994.

[84] P.A. Jaminet, "Solid-State Local Oscillator Sources for 600-900GHz," *The Proceeding of the 5th International Symposium on Space Terahertz Technology*, pp. 448-459, 1994.

[85] B.J. Rizzi and T.W. Crowe, "Planar Balanced Doubler Chip to 320GHz," *The Proceeding of the 5th International Symposium on Space Terahertz Technology*, pp. 414-425, 1994.

[86] N.R. Erickson, J. Tuovinen, B.J. Rizzi and T.W. Crowe, "A Balanced Doubler Using a Planar Diode Array for 270GHz," *The Proceeding of the 5th International Symposium on Space Terahertz Technology*, pp. 409-413, 1994.

[87] M. Cohn, R.G. Freitag, H.G. Henry, J.E. Degenford and D.A. Blackwell, "A 94 GHz MMIC Tripler Using Anti-Parallel Diode Arrays for Idler Separation," *IEEE MTT-S Int. Microwave Symposium Digest*, pp. 763-766, 1994.

[88] D. Choudhury, A.V. Räisänen, R.P. Smith, S.C. Martin, J.E. Oswald, R.J. Dengler, M.A. Frerking and P.H. Siegel, "Frequency Tripler with Integrated Back-to-Back Barrier-N-N$^+$ (bbBNN) Varactor Diodes in A Novel Split-Waveguide Block at 220 GHz," *IEEE MTT-S Int. Microwave Symposium Digest*, pp. 771-774, 1994.

[89] H. Zirath, I. Angelov, N. Rorsman, C. Karlsson and E. Kollberg, "A Balanced W-Band HFET Doubler," *Proceedings of the 23rd European Microwave Conference*, Madrid, Spain, pp. 837-839, Sept. 1993.

[90] A. Rydberg and E. Kollberg, "Wideband Tunable 140 GHz Second-Harmonic InP-TED Oscillator," *Electronics Letters*, Vol. 22, No. 15, pp. 770-771, 17th July 1986.

[91] A. Rydberg and H. Grönqvist, "Quantum-Well High-Efficiency Millimetre-Wave Frequency Tripler," *Electronics Letters*, Vol. 25, No. 5, pp. 348-349, 2 March 1989.

[92] A. Rydberg and H. Grönqvist, "Millimeter- and Submillimeter-Wave Multipliers Using Quantum-Barrier-Varactor (QBV) Diodes," *IEEE Electron Device Letters*, Vol. 11, No. 9, pp. 373-375, Sept. 1990.

[93] A. Rydberg, "High Efficiency and Output Power from Second- and Third-Harmonic Millimeter-Wave InP-TED Oscillators at Frequencies Above 170 GHz," *IEEE Electron Device Letters*, Vol. 11, No. 10, pp. 439-441, Oct. 1990.

[94] T.C.L.G. Sollner, E.R. Brown, W.D. Goodhue and C.A. Correa, "Harmonic Multiplication Using Resonant Tunneling," *Journal of Applied Physics*, Vol. 64, No. 8, pp. 4248-4250, 15 Oct. 1988.

[95] A. Rydberg, "A Contribution to the Design of Wideband Tunable Second Harmonic Mode Millimeter-Wave InP-TED Oscillators Above 110 GHz," *Int. Journal of Infrared and Millimeter Waves*, Vol. 11, No. 3, pp. 383-404, 1990.

[96] K. Krishnamurthi, R.G. Harrison, C. Rogers, J. Ovey, S.N. Nilsen and M. Missous, "Stacked Heterostructure Barrier Varactors on InP for Millimeter Wave Triplers," *The Proceedings of the 24th European Microwave Conference*, pp. 758-763, Cannes, France, Sept. 1994.

[97] B.N. Lyons, I. Sheridan, W.M. Kelly, U.S. Lidholm and A. Räisänen, "Experimental and Theoretical Evaluation of a Quasi-Optical Submillimeter-Wave Multiplier," *Proceeding of MIOP'90*, Stuttgart, pp. 369-374, April 1990.

[98] D. Steup, "Whisker-Contacted Diode-Multipliers as Quasioptical SMMW-Arrays," *Int. Journal of Infrared and Millimeter Waves*, Vol. 14, No. 12, pp. 2519-2532, 1993.

[99] D. Steup and A. Weber, "Quasioptical Multiplier Array with Separate Waveguide Feed," *The Proceeding of the 5th International Symposium on Space Terahertz Technology*, pp. 531-547, 1994.

[100] W.R. McGrath, C. Walker, M Yap and Y.-C. Tai, "Silicon Micromachined Waveguides for Millimeter-wave and Submillimeter-wave Frequencies," *IEEE Microwave and Guided Wave Letters*, pp. 61-63, Vol. 3, No. 3, March 1993.

[101] C.M. Mann, B.J. Maddison, M.L. Oldfield, D.N. Matheson, A. Jones and B.N. Ellison, "A Novel Quasi-planar Independently Biased Double Diode 560 GHz Subharmonic Mixer," *The 19th International Conference on Infrared and Millimeter Waves in Sendai, Japan*, M3.5, 1994.

[102] B.J. Maddison, C.M. Mann, M.L. Oldfield, D.N. Matheson, A. Jones and B.N. Ellison, "A Novel Quasi-planar Integrated Whisker/RF Airline Filter Circuit for the Terahertz Region," *The 19th International Conference on Infrared and Millimeter Waves in Sendai, Japan*, M3.6, 1994.

[103] K.J. Russell, "Microwave Power Combining Techniques," *IEEE Trans. on Microwave Theory and Tech.*, Vol. MTT-27, No. 5, pp. 472-478, May 1979.

[104] K. Chang and C. Sun, "Millimeter-wave Power Combining Techniques," *IEEE Trans. on Microwave Theory and Tech.*, Vol. MTT-31, No. 2, pp. 91-107, Feb. 1983.

[105] David B. Rutledge, "Submillimeter Integrated-Circuit Antennas and Detectors," *Ph.D. Dissertation*, University of Califonia, Berkeley, 1980.

[106] D.B. Rutledge and S.E. Schwarz, "Planar Multimode Detector Arrays for Infrared and Millimeter-wave Applications," *IEEE J. Quantum Electronics*, Vol. QE-17, pp. 407-414, 1981.

[107] L.B. Sjogren, H.-X. L. Liu, F. Wang, T. Liu, X.-H. Qin, W. Wu, E. Chung, C.W. Domier, N.C. Luhmann, Jr., "A Monolithic Diode Array Millimeter-wave Beam Transmittance Controller," *IEEE Trans.Microwave Theory Tech.*, Vol. 41, no. 10, pp. 1782-1790, Oct. 1993.

[108] Jonathan B. Hacker, "Grid Mixers and Power Grid Oscillators," *Ph.D. Dissertation*, California Institute of Technology, 1994.

[109] W.W. Lam, C.F. Jou, N.C. Luhmann, Jr. and D.B. Rutledge, "Diode Grids for Electronic Beam Steering and Frequency Multiplication," *Int. Journal of Infrared and Millimeter Waves*, 7, pp. 27-41, 1986.

[110] Wayne W. Lam, "Millimeter-Wave Monolithic Schottky Diode-Grid Phase Shifter," *Ph.D. Dissertation*, California Institute of Technology, 1987.

[111] W.W. Lam, C.F. Jou, N.C. Luhmann, Jr. and D.B. Rutledge, "Millimeter-wave Diode-Grid Phase Shifters," *IEEE Trans. on Microwave Theory and Tech.*, Vol. MTT-36, pp. 902-907, No. 5, May 1988.

[112] C.F. Jou, W.W. Lam, H.Z. Chen, K.S. Stolt, N.C. Luhmann, Jr. and D.B. Rutledge, "Millimeter-Wave Diode-Grid Frequency Doubler," *IEEE Trans. on Microwave Theory and Tech.*, Vol. 36, No. 11, pp. 1507-1514, Nov. 1988.

[113] Christina Jou, "Millimeter-Wave Monolithic Schottky Diode-Grid Frequency Doublers," *Ph.D. Dissertation*, University of California, Los Angeles, 1987.

[114] R.J. Hwu, N.C. Luhmann Jr., L. Sjogren, X. H. Qin, W. Wu, D.B. Rutledge, B. Hancock, J. Maserjian, U. Lieneweg, W. Lam, and C. Jou, "Watt-Level Quasi-Optical Monolithic Frequency Multiplier Development," *The Proceeding of the 1st International Symposium on Space Terahertz Technology*, pp. 126-149, 1990.

[115] H-X.L. Liu, L.B. Sjogren, C.W. Domier, N.C. Luhmann, Jr., D.L. Sivco and A.Y. Cho, "Monolithic Quasi-Optical Frequency Tripler Array with 5-W Output Power at 99 GHz," *IEEE Electron Device Letters*, Vol. 14, No. 7, pp. 329-331, July 1993.

[116] Hong-Xia Liantz Liu, "Monolithic Schottky Barrier and Quantum Barrier Device Arrays for Millimeter Wave Frequency Multiplication," *Ph.D. Dissertation*, University of California, Los Angeles, 1993.

[117] J.Y. Liao, X. Qin, W-M. Zhang, C.W. Domier and N.C. Luhmann, Jr., "High Power Submillimeter Wave CW Frequency Multipliers," *The 19th International Conference on Infrared and Millimeter Waves in Sendai, Japan*, 1994.

[118] J. Hacker, M.P. DeLisio, M. Kim, C.-M. Liu, S.-J. Li, S.W. Wedge and D.B. Rutledge, "A 10-Watt X-Band Grid Oscillator," *IEEE MTT-S Int. Microwave Symposium Digest*, pp. 823-826, 1994.

[119] R.L. Eisenhart and P.J. Khan, "Theoretical and Experimental Analysis of a Waveguide Mounting Structure," *IEEE Trans. Microwave Theory Tech.*, Vol. 19, No. 8, pp. 706-719, Aug. 1971.

[120] Robert M. Weikle, II, "Quasi-Optical Planar Grids for Microwave and Millimeter-wave Power Combining," *Ph.D. Dissertation*, California Institute of Technology, 1992.

[121] M. Kim, E.A. Sovero, J.B. Hacker, M.P. De Lisio, J.-C. Chiao, S.-J. Li, D.R. Gagnon, J.J. Rosenberg and D.B. Rutledge, "A 100-Element HBT Grid Amplifier," *IEEE Trans. Microwave Theory Tech.*, Vol. 41, No. 10, pp. 1762-1771, Oct. 1993.

[122] J.B. Hacker, R.M. Weikle II, M. Kim, M.P. De Lisio, D.B. Rutledge, "A 100-Element Planar Schottky Diode Grid Mixer," *IEEE Trans. Microwave Theory Tech.*, Vol. 40, No. 3, pp. 557-562, March 1992.

[123] K.D. Stephan, F. H. Spooner and P.F. Goldsmith, "Quasioptical Millimeter-wave Hybrid and Monolithic PIN Diode Switches," *IEEE Trans. Microwave Theory Tech.*, Vol. 41, No. 10, pp. 1791-1798, Oct. 1993.

[124] J. Bae, Y. Aburakawa, H. Kondo, T. Tanaka and K. Mizuno, "Millimeter and Submillimeter Wave Quasi-Optical Oscillator with Gunn Diodes," *IEEE Trans. Microwave Theory Tech.*, Vol. 41, No. 10, pp. 1851-1855, Oct. 1993.

[125] D.P. Neikirk, D.B. Rutledge, M.S. Muha, H. Park and C.X. Yu, "Far-Infrared Imaging Antenna Arrays," *Applied Physics Letters*, Vol. 40, pp. 203-205, 1982.

[126] C. Zah, D. Kasilingam, J.S. Smith, D.B. Rutledge, T. Wang and S.E. Schwarz, "Millimeter-wave Monolithic Schottky Diode Imaging Arrays," *Int. Journal of Infrared and Millimeter Waves*, Vol. 6, pp. 981-997, 1985.

[127] B.Y. Zel'dovish, N.F. Pilipetsky and V.V. Shkunow, "Introduction to Optical Phase Conjugation," *Principles of Phase Conjugation*, Springer-Verlag, New York, 1984.

[128] B.J. Rizzi, J.L. Hesler, H. Dossal and T.W. Crowe, "Varactor Diodes for Millimeter Sub-millimeter Wavelengths," *The Proceeding of the 3rd International Symposium on Space Terahertz Technology*, pp. 73-92, 1992.

[129] T.W. Crowe, R.J. Mattauch, H.P. Röser, W.L. Bishop, W.C.B. Peatman and X. Liu, "GaAs Schottky Diodes for THz Mixing Applications," *Proceedings of the IEEE*, Vol. 80, No. 11, pp. 1827-1841, Nov. 1992.

[130] B.J. Rizzi, K.K. Rausch, T.W. Crowe, P.J. Koh, W.C.B. Peatman, J.R. Jones, S.H. Jones adn G. Tait, "Planar Varactor Diodes for Submillimeter Applications," *The Proceeding of the 4th International Symposium on Space Terahertz Technology*, pp. 297-311, 1993.

[131] W. L. Bishop, T.W. Crowe and R.J. Mattauch, "Planar GaAs Schottky Diode Fabrication: Progress and Challenges," *The Proceeding of the 4th International Symposium on Space Terahertz Technology*, pp. 415-429, 1993.

[132] W.L. Bishop, T.W. Crowe, R.J. Mattauch and P.H. Ostdiek, "Planar Schottky Barrier Mixer Diodes for Space Applications at Submillimeter Wavelengths," *Microwave and Optical Technology Letter*, Vol. 4, No. 1, pp. 44-49, Jan. 1991.

[133] D. G. Garfield, R.J. Mattauch and W.L. Bishop, "Design, Fabrication and Testing of a Novel Planar Schottky Barrier Diode for Millimeter and Submillimeter Wavelengths," *Proceedings of IEEE Southeastcon '88 in Knoxville, TN*, pp. 154-160, April 1988.

[134] J.A. Calviello, S. Nussbaum and P.R. Bie, "High Performance GaAs Beam-Lead Mixer Diodes for Millimeter and Submillimeter Applications," *Proceedings of International Electron Device Meeting*, Dec. 1981.

[135] N.J. Cronin and V.J. Law, "Planar Millimeter-wave Diode Mixer," *IEEE Trans. Microwave Theory Tech.*, Vol. 33, No. 9, pp. 827–830, Sept. 1985.

[136] W.L. Bishop, K. McKinney, R.J. Mattauch, T.W. Crowe and G. Green, "A Novel Whisker-less Schottky Diode for Millimeter and Submillimeter Wave Applications," *IEEE MTT-S Int. Microwave Symposium Digest*, pp. 607-610, 1987.

[137] J.W. Archer, R.A. Batchelor and C.J. Smith, "Low-Parasitic, Planar Schottky Diodes for Millimeter-wave Integrated Circuits," *IEEE Trans. Microwave Theory Tech.*, Vol. 38, No. 1, pp. 15-25, Jan. 1990.

[138] W.L. Bishop, T.W. Crowe, R.J. Mattauch and H. Dossal, "Planar GaAs Diodes for THz Frequency Mixing Applications," *The Proceeding of the 3rd International Symposium on Space Terahertz Technology*, pp. 600-615, 1992.

[139] American Institute of Physics Handbook, pp. 4-156 and 4-158, 3rd ed., McGraw-Hill Com., 1972.

[140] J. Louhi, A. Räisänen and N.R. Erickson, "Effect of Cooling on the Efficiency of Schottky Varactor Frequency Multipliers at Millimeter Waves," *The Proceeding of the 3rd International Symposium on Space Terahertz Technology*, pp. 134-145, 1992.

[141] J. Louhi, A. Räisänen and N.R. Erickson, "Cooled Schottky Varactor Frequency Multipliers at Submillimeter Wavelengths," *IEEE Trans. on Microwave Theory and Tech.*, Vol. 41, No. 4, pp. 565-571, April 1993.

[142] K. McKinney, R.J. Mattauch and W.L. Bishop, "Design, Fabrication and Performance of a Whiskerless Schottky Diode for Millimeter and Submillimeter Wave Applications," *Proceedings of IEEE Southeastcon '85*, pp. 111-115, April 1988.

[143] S.C. Bundy and Z.B. Popović, "Analysis of Planar Grid Oscillators," *IEEE MTT-S Int. Microwave Symposium Digest*, pp. 827-830, 1994.

[144] J.A. Copeland, "Diode Edge Effect on Doping-Profile Measurements," *IEEE Trans. on Electron Devices*, Vol. ED-17, No. 5, pp. 404-407, May 1970.

[145] S.J. Allen, K. Craig, B. Galdrikian, J.N. Heyman, J.P. Kaminski, K. Campman, P.F. Hopkins, A.C. Gossard, D.H. Chow, M. Lui and T.K. Liu, "Materials Science in the Far-IR with Electrostatic Based FELs," presented at *FEL 94*, Stanford, CA, August 1994. to be published *Nucl. Instrum. Methods Phys. Res. A*

[146] S.J. Allen, K. Craig, C.L. Felix, P. Guimarães, J.N. Heyman, J.P. Kaminski, B.J. Keay, A.G. Markelz, G. Ramian, J.S. Scott, M.S. Sherwin, K.L. Campman, P.F. Hopkins, A.C. Gossard, D. Chow, M. Lui and T.K. Liu, "Probing Terahertz Dynamics in Semiconductor Nanostructures with the UCSB Free-Electron Lasers," *Journal of Luminescence*, 60&61, pp. 250-255, 1994.

[147] R.C. Compton, R.C. McPhedran, Z. Popović, G.M. Rebeiz, P.P.Tong and D.B. Rutledge, "Bow-Tie Antennas on a Dielectric Half-Space: Theory and Experiment," *IEEE Trans. Microwave Theory Tech.*, Vol. 35, No. 6, pp. 622-631, June 1987.

[148] D. Cheng, *Field and Wave Electromagnetics*, Addison-Wesley Pub. Co., Chap. 11, 1983.

[149] W.L. Bishop, E. R. Meiburg, R.J. Mattauch T.W. Crowe and L. Poli, "A Micro-Thickness, Planr Schottky Diode Chip for Terahertz Applications with Theoretical Minimum Parasitic Capacitance," *IEEE MTT-S Int. Microwave Symposium Digest*, pp. 1305-1308, 1990.

[150] W.L. Wolfe and G.J. Zissis, "The Infrared Handbook," *Environmental research Institute of Michigan, Infrared Information and Analysis Center*, 1985.

[151] J.T. Louhi, "The Capacitance of a Small Circular Schottky Diode for Submillimeter Wavelengths," *IEEE Microwave and Guided Wave Letters*, Vol. 4, No. 4, 1994.

[152] S.M. Sze, *Physics of Semiconductor Devices*, Wiley, New York, 1981.

[153] J.T. Louhi and A. Räisänen, "On the Modelling of the Millimeter Wave Schottky Varactor," *The Proceeding of the 5th International Symposium on Space Terahertz Technology*, pp. 426-436, 1994.

[154] E. Kollberg, T. Tolmunen, M. Frerking and J. East, "Current Saturation in Submillimeter Wave Varactors," *The Proceeding of the 2nd International Symposium on Space Terahertz Technology*, pp. 306-322, 1991.

[155] A. Simon, A. Grüb, V. Krozer, K. Beilenhoff and H.L. Hartnagel, "Planar THz Schottky Diode Based on a Quasi Vertical Diode Structure," *The Proceeding of the 4th International Symposium on Space Terahertz Technology*, pp. 392-403, 1993.

[156] A.Grüb, V. Krozer, A. Simon and H.L. Hartnagel, "Design Optimization of Schottky Barrier Diodes at THz," *The Proceeding of the 5th International Symposium on Space Terahertz Technology*, pp. 394-403, 1994.

[157] K. Mizuishi, H. Kurono, H. Sato and H. Kodera, "Degradation Mechanism of GaAs MESFET's," *IEEE Trans. on Electron Devices*, Vol. 26, No. 7, July, 1979.

[158] T.J. Tolmunen and M.A. Frerking, "Theoretical Efficiency of Multiplier Devices," *The Proceeding of the 2nd International Symposium on Space Terahertz Technology*, pp. 197-211, 1991.

[159] P. Marsh, D. Pavlidis and K. Hong, "Planar Varactor and Mixer Diodes Fabricated Using InP-Based Materials," *The Proceeding of the 5th International Symposium on Space Terahertz Technology*, pp. 514-523, 1994.

[160] C. Raman, J.P. Sun, W.L. Chen, G. Munns, J. East and G. Haddad, "Superlattice Barrier Varactor," *The Proceeding of the 3rd International Symposium on Space Terahertz Technology*, pp. 146, 1992.

[161] A.G. Markelz, N.G. Asmar, E.G. Gwinn, M.S. Sherwin, C. Nguyen and H. Kroemer, "Subcubic Power Dependence of Third-Harmonic Generation for In-Plane, Far-Infrared Excitation of InAs Quantum Wells," *Semiconductor Science and Technology*, 9(5), pp. 634-637, 1994.

[162] A.G. Markelz, E.G. Gwinn, M.S. Sherwin, C. Nguyen and H. Kroemer, "Giant Third-Order Nonlinear Susceptibilities for In-Plane, Far-Infrared Excitation of Single InAs Quantum Wells," *Solid-State Electronics*, Vol. 37, No. 4-6, pp. 1243-1245, 1994.

[163] C.B. Burckhardt, "Analysis of Varactor Frequency Multipliers for Arbitrary Capacitance Variation and Drive Level," *Bell System Technical Journal*, Vol. 44, No. 4, pp. 675-692, 1965.

[164] A.R. Kerr, "A Technique for Determining the Local Oscillator Waveforms in a Microwave Mixer," *IEEE Trans. on Microwave Theory and Tech.*, pp. 828-831, Oct. 1975.

[165] P.H. Siegel and A.R. Kerr, "The Measured and Computed Performance of a 140-220 GHz Schottky Diode Mixer," *IEEE Trans. on Microwave Theory and Tech.*, Vol. MTT-32, No. 12, pp. 1579-1590, Dec. 1984.

[166] T.J. Tolmunen and M.A. Frerking, "Theoretical Performance of Novel Multipliers at Millimeter and Submillimeter Wavelengths," *Int. Journal of Infrared and Millimeter Waves*, Vol. 12, No. 10, pp. 1111-1133, 1991.

[167] M.F. Zybura, S.H. Jones, G.B. Tait and J.R. Jones, "100-300 GHz Gunn Oscillator Simulation Through Harmonic Balance Circuit Analysis Linked to a Hydrodynamic Device Simulator," *IEEE Microwave and Guided Wave Letters*, Vol. 4, No. 8, pp. 282-284, August 1994.

[168] J.R. Jones, S.H. Jones, G.B. Tait and M.F. Zybura, "Heterostructure Barrier Varactor Simulation Using an Integrated Hydrodynamic Device/Harmonic-Balance Circuit Analysis Technique," *IEEE Microwave and Guided Wave Letters*, Vol. 4, No. 12, pp. 411-413, Dec. 1994.

Chapter 3

Microswitch Beam-Steering Grids

Quasi-optical power combining techniques offer a promising approach to realize compact, reliable, lightweight, higher-power and economical systems at millimeter and submillimeter wavelengths. A complete structure of quasi-optical transmitter or receiver requires electronic beam-controllers for beam steering, focussing and switching in the applications such as radars for aircraft-guiding and missile-seeking; automobile radars for collision avoidance systems; and millimeterwave imaging cameras which allow to see through fog. Electronic-scanning systems are more reliable, flexible and have higher scanning speeds than mechanical scanning systems. The high-speed capability of electronic-scanning devices allows the beam to shift rapidly, so it can track or image more targets simultaneously. Conventional waveguide beam-steering systems are heavy, bulky and usually require complicated control circuits. Previous efforts of using quasi-optical monolithic diode-grids as electronic beam-controllers at millimeter wavelengths show impressive results and the advantages of lower losses and high-speed control.

Extending the quasi-optical diode-grid method for beam-control to higher frequencies faces technical challenge to reduce the losses caused by the series resistances of the diodes. Past experiences show that it is extremely important to keep series resistances of diodes as low as possible to reduce losses. However, the series resistances of Schottky diodes increase when the operating frequencies increase and the series resistances will cause more serious loss problems at submillimeter wavelengths. Therefore, exploring the possibility of a novel method

using passive elements instead of diodes is the main purpose of this work.

Micromechanical membrane-switches offer the advantages of very low series resistances and simple control circuits. We proposed to utilize the binary changes of reactance by switching the microswitches to establish a discrete phase shifter. A multi-layer structure provides higher resolutions of phase-shifts with lower losses which can be minimized by adjusting the spacing between layers and the unit-cell patterns. Simulations predict that a 4-bit controlled 10-layer microswitch beam-steering grid can have a phase-shift resolution of 22.5° over 360° with a loss of 1.6 dB at 240 GHz.

The organization of this chapter is in the following order:

A review on quasi-optical diode-grid beam-controllers is first given. Then the structures of micromechanical membrane-switches and the approach of using these microswitches on beam-steering grids are discussed. A general system and the modelling method are shown. Two designs including practical considerations of using $\langle 110 \rangle$ and $\langle 100 \rangle$ orientation silicon wafers are presented.

Because of the smaller wavelengths, submillimeter-wave beam-steering grids should have TE_{10}-waves guided in etched vertical-wall rhombic waveguides with microswitches inside to provide the required shunt reactances for phase-shifting. The dimensions and spacings of rhombic waveguides in the grid have been calculated to minimize the losses. Performance prediction, simulations and design principles are discussed for a 240-GHz beam-steering grid.

For longer wavelengths, thin $\langle 100 \rangle$ silicon wafers are used for supporting the microswitches and the free space between layers is used for providing the proper electrical lengths. Performance prediction, simulations and design principles are discussed for a 44-GHz beam-steering grid.

Micromechanical SiO_xN_y-membrane switches are fabricated on $\langle 100 \rangle$ orientation silicon wafers to demonstrate the feasibility of fabricating long (longer than 500 μm) electrostatically-controlled binary switches on silicon. Rhombic-

waveguide arrays are also made by using ⟨110⟩ orientation silicon wafers and anisotropic etching techniques to show that it is feasible to fabricate vertical-wall waveguides on silicon.

Finally, measurements are done for the designs of 44-GHz beam-steering grids to verify the simulations.

3.1 MOTIVATION

Recent developments in millimeter and submillimeter-wave technologies offer new and exciting solutions to problems that have plagued rival systems. For example, compared to microwave systems, millimeter-wave systems have broader bandwidths, better spatial resolutions, and smaller equipment and antenna sizes. At the same time, millimeter-wave radiations are capable of penetrating fog, clouds, dust and dark of night - unlike optical and infrared radiations. Unfortunately, using millimeter-waves to their full advantages has been impeded by the lack of inexpensive, high-resolution and reliable electronic beam-steering devices.

The advantages of the electronic-scanning system over its mechanical counterpart are well known. Mechanical-scanning devices are slow to scan an area and therefore limit the resolution. It is expensive to build a mechanical-scanning system and usually it is heavy and bulky. Electronic-scanning systems have more reliability, flexibility and higher scanning-speeds. The high-speed capability of electronic-scanning devices allows the beam to shift rapidly, so it can track or image more targets simultaneously. This provides choices for the demands of a high-resolution radar in terminal homing for missiles and aircraft.

A conventional electronic-scanning system consists of phase-shifters mounted in waveguides in the juxtaposed wave-paths. A large number of elements in the array is usually required to steer the beams. The small size of millimeter-wave or submillimeterwave waveguides requires very close manufacturing tolerance and a lossless material. Using many phase-shifters and other controller circuits could be expensive and requires complicated interconnecting when the wavelengths

become smaller.

Phased antenna array provides an attractive option for electronic beam-steering. Many phased antenna arrays involve the use of antenna elements such as dipoles, patches or slots fed by waveguides or microstrips [1-3] and the use of solid-state circuits as phase-shifting controllers such as liquid crystals [4]; superconducting thin films [5]; optical-controlled devices like PIN diodes, IMPATT diodes, MESFET and HEMT irradiated by lasers [6]; optoelectronic integrated circuits (OEICs) [7]; modulation-doped charge-coupled devices (MD-CCDs) [8]; and varactor diodes [9]. Such designs limit versatility of antenna arrays and still require routing of RF signals through guiding structures such as microstrips or striplines which suffer from the losses at millimeter and submillimeter wavelengths, as mentioned in the previous chapter. Furthermore, it is difficult to integrate a large size of phased antennas in an array without generating grating-sidelobes. Recently, Liao and York [10] demonstrated a linear antenna array using antenna-coupled oscillators to eliminate the need of phase-shifters. By adjusting the frequencies of the end oscillators in the chain, the radiation pattern could be continuously steered over a range from $-15°$ to $+12.5°$. This idea opens a new door for beam-steering methods, however, still needs more studies on the tradeoff between scanning-ranges and bandwidths, the oscillating-frequency issues and the possibility of two-dimensional scanning.

3.2 Quasi-Optical Diode-Grid Methods

Quasi-optical methods provide many advantages, as mentioned in the previous chapter, at millimeter and submillimeter wavelengths. The low-loss features make a quasi-optical electronic beam-steering very attractive. Quasi-optical monolithic active reflectors become more possible when solid-state devices are added to periodic structures. Lee and Fong made a pioneering study of the effect of embedding negative-resistance diodes in a corrugated grating [11]. Later, Alexopoulos *et al.* proposed using these active surfaces for scanning a beam elec-

tronically [12], and Chekroun *et al.* proposed RADANT®, a three-dimensional grid of diodes for steering a beam [13]. Rutledge and Schwarz demonstrated a multimode microbolometer array [14], and Lam *et al.* used the similar idea to demonstrate a monolithic design of a periodic grid loaded with diodes for electronic beam steering and frequency multiplication [15-17].

Monolithic diode grids were fabricated on $2\,cm \times 3\,cm$ GaAs wafers, mounted on a metal mirror, with 1600 Schottky-barrier varactor diodes, as shown in Figure 3.1. The unit-cell size is $500\,\mu m \times 500\,\mu m$. Vertical inductive leads with a width of $20\,\mu m$ connect diodes in series while the horizontal lines bias the diodes in the same rows. The incident beam reflects off the diode-grid surface, where changing the DC biases on the diodes changes the reactances, with a controlled reflected phase. The bias lines are programmable and a linear variation of phase across the aperture sets the direction of the reflected beam. A quadratic variation of the reflected phase across the surface focusses the beam. This quasi-optical
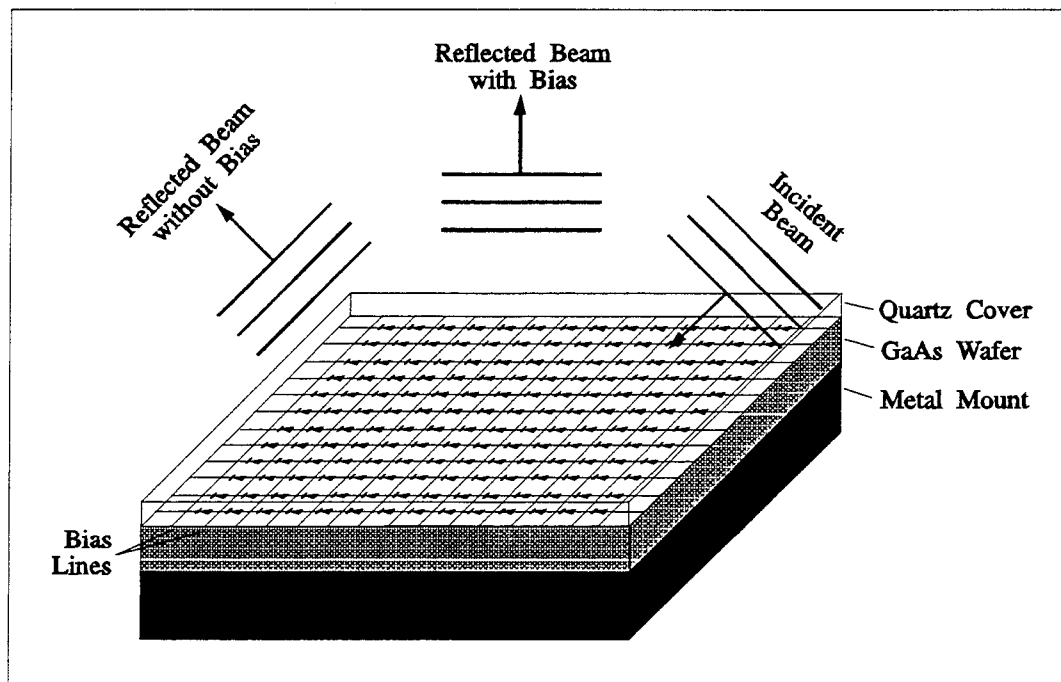
Fig. 3.1 Electronically programmable beam-steering array using Schottky diode grids.

beam-steering method eliminates the needs for waveguides or microstrips. Furthermore, the power is distributed among all the diodes, the power handling capability can be increased by increasing the size of the grids, as mentioned in Chapter 2. A phase shift of 70° with a 6.5-dB loss was obtained at 93 GHz when the bias on the diode grid was changed from -3 V to $+1$ V.

Using the same approach, Sjogren et $al.$ [18, 19] demonstrated electronic beam-steering and focussing on a Schottky diode-grid loaded with 7168 diodes. A phase shift of 70° is achieved with a reflection loss of 3.5 dB at 120 GHz. Qin et $al.$ [20, 21] reported a 130° reflection phase-shift with a 2.7 dB loss at 60 GHz. The diode grids can also be used in a transmission system, instead of a reflection system, as beam controllers such as beam modulation and beam switching, without the reflection mirror. Transmission controls over the range of 20% to 50% at 99 GHz and 20% to 70% at 165 GHz were demonstrated by Sjogren et $al.$ [19,22] using the similar diode grids (8640 diodes). Qin et $al.$ [20,21] also demonstrated a 24 dB ON/OFF ratio with a minimum transmission loss of 2.2 dB using a single diode-grid and a 42 dB ON/OFF ratio with a minimum transmission loss of 4 dB using two stacked layers at 60 GHz.

These results are very impressive and promising for the use of diode-grids as beam controllers at millimeter wavelengths. However, there are several drawbacks which prevent diode-grids to be used at higher frequencies as phase-shifters. First, the series resistances of Schottky diodes increase when the operating frequencies increase. Previous experiences show that it is extremely important to keep series resistances of diodes as low as possible to reduce losses. The series resistances will cause more serious loss problems at submillimeter wavelengths. Second, thermal effects induced by large currents on diodes increase the noise and influence the stability of devices. Third, diode-grid devices require complicated fabrication processes for diodes such as molecular beam epitaxy (MBE) which increase the cost. Therefore, exploring the use of passive elements instead of active

elements to provide phase-shifts with less losses at submillimeter wavelengths is the main purpose of this work.

3.3 MICROMECHANICAL SWITCHES

We propose a novel beam-steering method which only includes passive elements instead of diodes or other active devices. The microswitch beam-steering arrays can be fabricated monolithically on silicon wafers using conventional photolithographic techniques and provide discrete phase-shifts.

In 1978, Peterson successfully built micromechanical SiO_2-membrane switches on $\langle 100 \rangle$ orientation silicon wafers [23-25]. These switches are electrostatically deflectable devices, shown in Figure 3.2. They are batch fabricated on silicon using conventional photolithographic and integrated-circuit processing techniques. These devices are basically small, typically 100 μm long, and used as electrostatically controlled mechanical relays. They are cantilever beams composed of thin (0.35 μm), metal-coated insulating SiO_2-membranes attached to the silicon substrate at one end and suspended over a shallow rectangular pit with pyramid-shaped sidewalls. This pit is produced by etching the silicon out
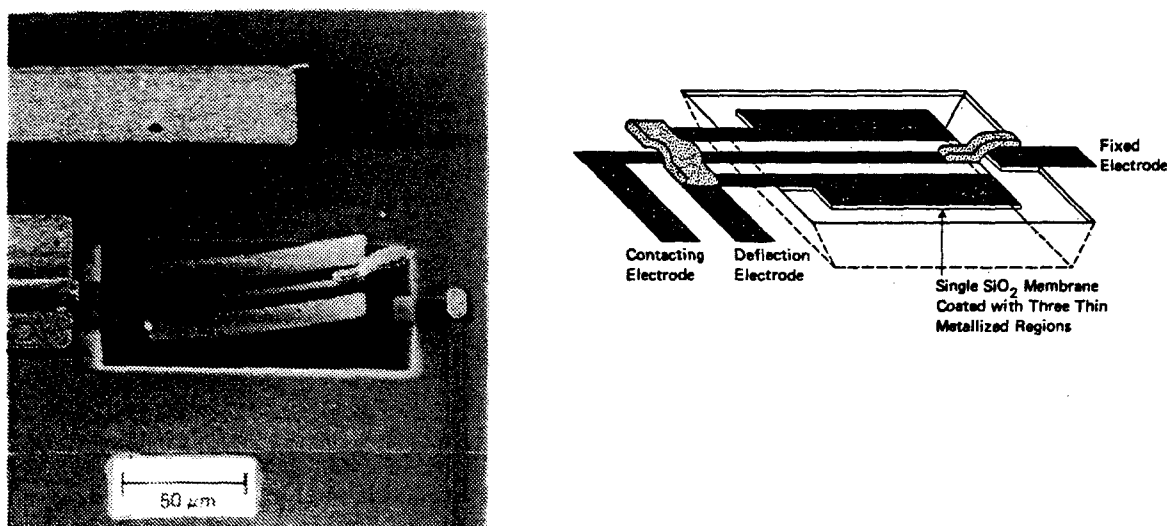
Fig. 3.2 A micromechanical SiO_2-membrane switch on $\langle 100 \rangle$ silicon. Work of K.E. Petersen at IBM in 1978 [23-25].

from under the deposited insulating film in silicon etchant (EDP). First, several layers of photoresist are applied on the membranes to form a cantilever bridge structure. Gold is plated over the bridge structure and forms a contact on the membrane tip. Finally, the photoresist layers and excessive plating-gold base are stripped and silicon is etched to form the cantilever beam. The fabrication details will be discussed later.

When a voltage is applied between the highly-doped silicon in the bottom of the pit and the deflection electrode metallization on the membrane surface, the cantilever bridge will experience an electrostatic force to pull the membrane downward until two electrodes contact. When the bias is removed, the stress of the thermally grown SiO_2 membrane separates two electrodes.

The experiments show that the series resistance is very low because of the pure metal-to-metal contacts in the devices. The switching and sustaining powers are very low which make control circuits simpler. The device density can be very high since the size of the device is very small. The fabrication processes only include mask fabrication, wet chemical etching, metal evaporation and electroplating but exclude complicated processes such as MBE.

The advantages of using microswitches on a beam-steering grid are:

1. The microswitches should have much lower series resistances over a frequency range from gigahertz to terahertz compared to GaAs Schottky diodes because the RF conduction losses of metal should be lower than GaAs.

2. The ON-/OFF-state impedance ratios are extremely high which provides a good binary separation.

3. It is fully monolithic and needs simpler fabrication processes compared with Schottky diode-grid reflectors.

4. It requires simple low-frequency control circuits and the control signal can be digitalized.

5. Power handling capability can be greatly improved since there are no break-

down voltages to be concerned with.

3.4 APPROACHES

Using the microswitches to change the phases of propagating waves, we utilize the two states of the switches. Shown in Figure 3.3 are the equivalent-circuit elements for two different metal patterns in waveguides. For vertically polarized electric fields, a gap between two horizontal metal strips is presented as a capacitor while a vertical strip is presented as an inductor in a transmission-line model. The waveguides can be either commonly-used all-metal waveguides or unit-cell waveguides, which are used in the analysis of quasi-optical grids for TEM-wave incidence, with electric walls on the top and bottom and magnetic walls on the sides. We proposed to use the ON/OFF-states of the microswitches to achieve these two circuit-elements in order to change the reactances for the propagating waves.

Figure 3.4 shows the concept for transmission-type beam-steering. The incident wave enters the grid from the left side, passes through several layers of microswitch and waveguide arrays, and re-radiates from the waveguide-array surface in the right side into free space. The microswitches are built inside the waveguides and designed as binary switches to change the shunt reactances in
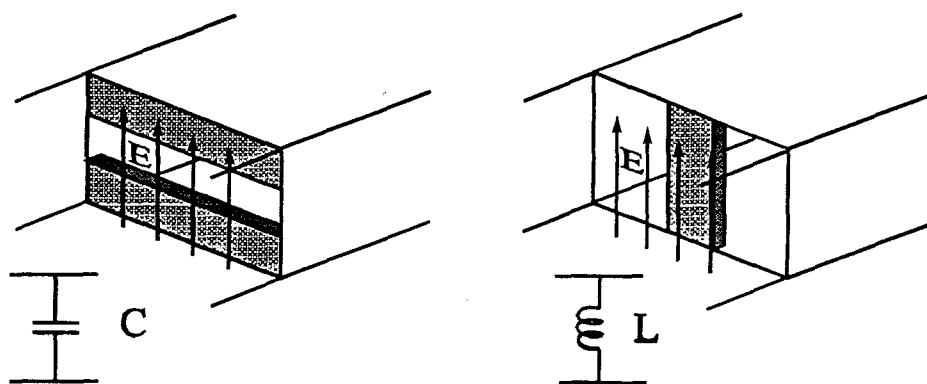
Fig. 3.3 Equivalent circuits for metal patterns in waveguides.

the transmission lines. When the switches close by biasing on the two electrodes, inductive reactances would be presented to the propagating wave, and when the switches open, capacitive reactances would be presented to the propagating waves. In each waveguide-path, by changing the settings of switches in different layers to reach different reactances, different phase-shifts can be achieved. A linear phase variation across the transmitting aperture sets the direction of the deflected beam and a quadratic variation focusses the beam in far field.

Using one layer of microswitches can provide a binary phase-shift. Stacking several layers together allows to shift more phases in order to achieve higher
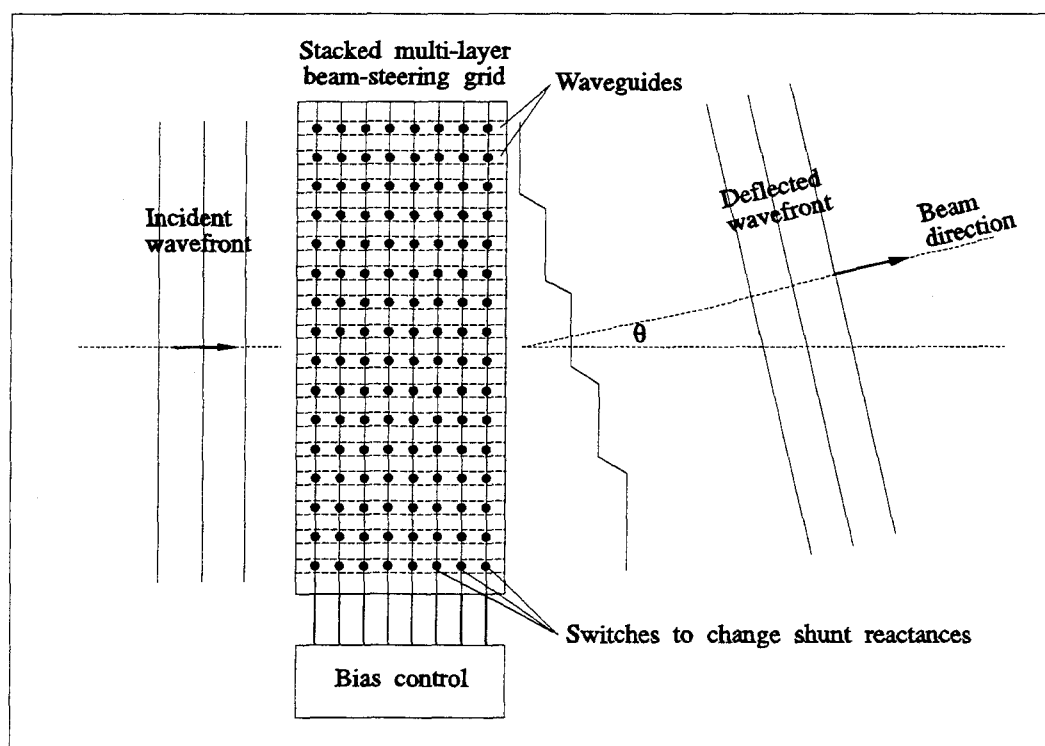
Fig. 3.4 Schematic concept for transmission-type beam-steering. The incident wave enters the grid from the left side, passes through several layers of microswitches and waveguides, and re-radiates from the right side into free space. By changing the settings of switches to change the reactances in the wave-paths, different phase-shifts can be added. A linear phase variation across the transmitting aperture sets the direction of the deflected beam.

resolutions of steering. If we use $\langle 100 \rangle$ orientation silicon wafers to form the waveguides, as previous works by Petersen, after etching, holes with pyramid-shaped sidewalls will be formed instead of vertical walls. This will introduce reflection loss problems and excite higher modes in the waveguides.

This problem can be solved by using $\langle 110 \rangle$ orientation silicon wafers.

Silicon belongs to the diamond cubic crystal structure. In the cubic structure, the crystalographic directions are perpendicular to the crystal planes. There are several low-index planes that we can apply wet-chemical anisotropic etching to form cavities on silicon [26]. Figure 3.5 illustrates $\langle 100 \rangle$ plane and $\langle 111 \rangle$ planes in the cube. If we use $\langle 100 \rangle$ orientation silicon wafers and anisotropic etchant EDP (ethylenediamine-pyrocatechol and water) to form the waveguides, since the etching rate of EDP for $\langle 100 \rangle$ planes is 35 times faster than for $\langle 111 \rangle$ planes (at $110°$ C), after etching, we will get a pyramid-shaped cavity with an angle of $70.6°$ between two $\langle 111 \rangle$ planes.
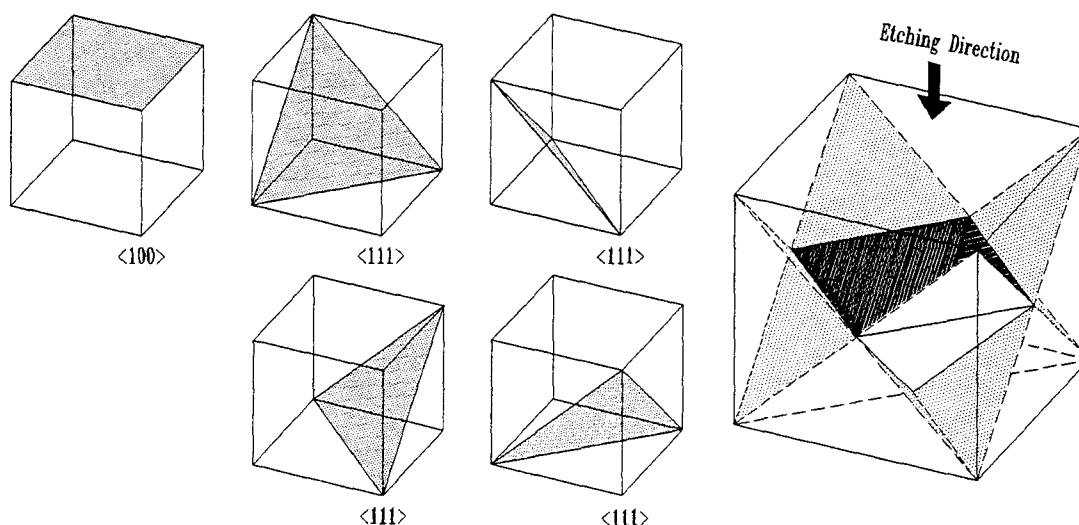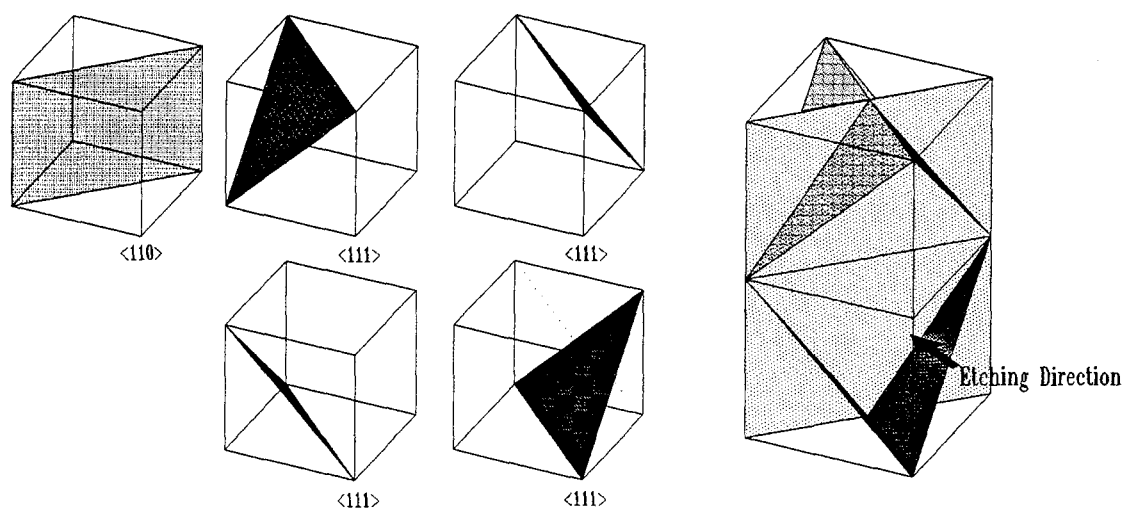

Fig. 3.5 Illustration of the $\langle 100 \rangle$ crystal plane and the $\langle 111 \rangle$ crystal planes in the cubes. The anisotropic etching direction is shown by the arrow when the etchant EDP is used on a $\langle 100 \rangle$ orientation silicon wafer.

However, four ⟨111⟩ planes in two cubes form vertical walls perpendicular to the ⟨110⟩ planes, as shown in Figure 3.6. By using anisotropic etchant KOH solution on a ⟨110⟩ orientation silicon wafer, the ⟨110⟩ plane silicon particles can be etched out to form vertical-wall rhombus-shaped waveguides since the etching rate of KOH for ⟨110⟩ planes is 160 times (at 85° C) faster than for ⟨111⟩ planes [27]. The inside angles of the rhombic holes define by the ⟨111⟩ planes are 109.4° and 70.6°.

The microswitches can be fabricated on ⟨110⟩ orientation silicon wafers and the vertical-sidewall holes allow us to stack many layers together for shifting more phases. Figure 3.7 shows one microswitch sandwiched by two waveguides in one wave-path. When the switch opens, a shunt capacitance is presented. When the switch closes by applying a bias, a shunt inductance is presented if the susceptance of the central conductor is twice as much as the capacitive susceptance at the operating frequency. The rhombic waveguide is designed to be single-mode waveguide with electric-field polarization parallel to the microswitch.

Fig. 3.6 Illustration of the ⟨110⟩ crystal plane and the ⟨111⟩ crystal planes in two cubes. The anisotropic etching direction is shown by the arrow when the etchant KOH solution is used on a ⟨110⟩ orientation silicon wafer.
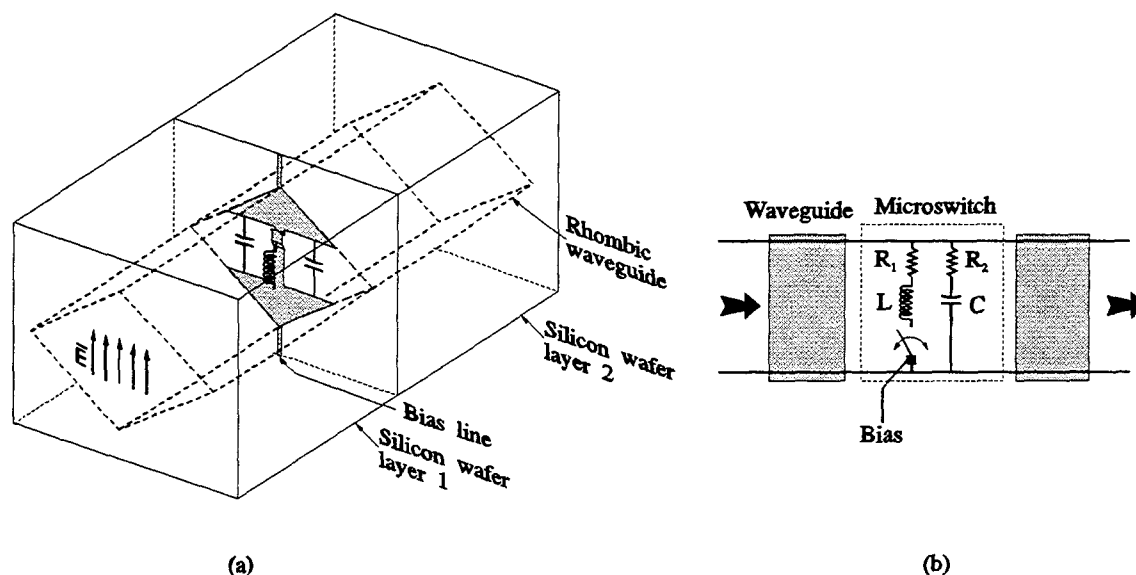
Fig. 3.7 (a) One microswitch sandwiched by two waveguides in one wave-path and (b) the equivalent circuit. The resistors, R_1 and R_2, represent the RF conduction losses.

We plan to fabricate microswitches on $\langle 110 \rangle$ orientation silicon wafers for higher frequencies and on thin $\langle 100 \rangle$ wafers for lower frequencies because the sidewall reflections will not be significant for longer wavelengths. A design for lower frequencies (44 GHz) will be discussed later. Figure 3.8 shows the entire structure using $\langle 110 \rangle$ silicon wafers. It has 10 stacked layers which allow to shift more phase. Each column is controlled by parallel bias lines, which will provide the elements in the same column with the same phase shifts. By changing the settings of switches in different layers, different phase shifts can be achieved in different paths. The layer #0 provides an impedance matching to the free-space impedance to reduce the reflection losses. The surfaces of the first layer (layer #0) and the last layer (layer #10) as well as the sidewalls of the rhombic waveguides will be plated with metal to reduce losses. Here only shows one-dimensional beam steering, however, two-dimensional beam-steering is also possible if we add more bias lines between waveguides to control each microswitch individually.
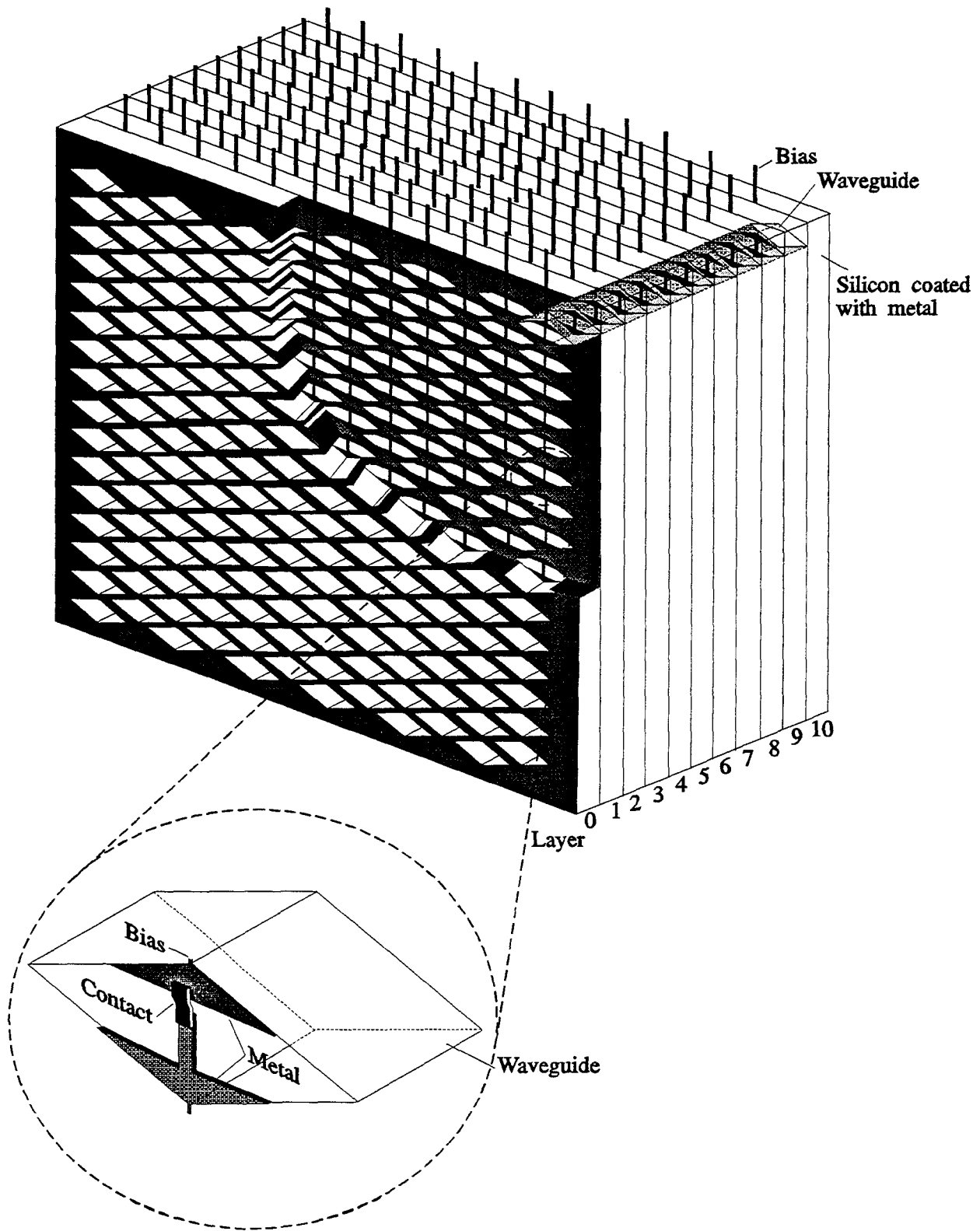
Fig. 3.8 The entire microswitch beam-steering grid.

3.5 240-GHz Design

3.5.1 Equivalent-Circuit Model

Several designs are made for 240 GHz for different possible applications. A 7-layer 3-bit controlled structure with identical layers provides simpler fabrications and less cost. An 8-layer 3-bit controlled or a 10-layer 4-bit controlled structure with different designs of switches on different layers provides more control flexibility or a higher-resolution of phase-shifts.

A 7-layer structure is designed and the equivalent circuit is shown in Figure 3.9. Each layer has the same metal patterns to provide the desired shunt reactances of $\pm j1.317Z_0$ where Z_0 is the characteristic impedance of the rhombic waveguide. 2-Ω series resistance is added on each switch for imitating RF conduction losses. By changing the switch-setting combinations and adjusting the electrical lengths of the waveguide sections, a phase-shift increment of 45° over 360° is achieved. Calculated performance for this 3-bit controlled design is shown in Figure 3.10. The electrical length is 86° at 240 GHz. The dashed lines indicate the desired phase-shift resolution (45° over 360°) and the distances from the outer circle to the markers indicate losses. The maximum phase error is 9° and the maximum loss is 1.63 dB.

The 7-layer structure has identical layers which make the fabrication simpler, however, provides less flexibility of increasing phase-shift resolutions. To demonstrate the idea of adding flexibility of stacking more layers and to reduce the phase-shift error, an 8-layer structure is designed. The 8-layer structure is designed to have six identical layers and two extra layers with different switch-design. The equivalent circuit is shown in Figure 3.11. The first six layers have the same metal patterns to provide shunt reactances of $\pm j1.317Z_0$ and the last two layers have metal patterns to provide shunt reactances of $\pm j2.624Z_0$ by narrowing the capacitive gaps between the horizontal metal strips and the vertical

inductive strips. The switches are controlled by pairs. 2-Ω series resistance is added on each switch for conduction losses. By changing the switch-setting combinations and adjusting the electrical lengths of the waveguide sections, a phase-shift resolution of 45° over 360° is also achieved. Changing the position of the $(2Z_{C,L} - 2Z_{C,L})$-pair in the equivalent circuit will also change the performance
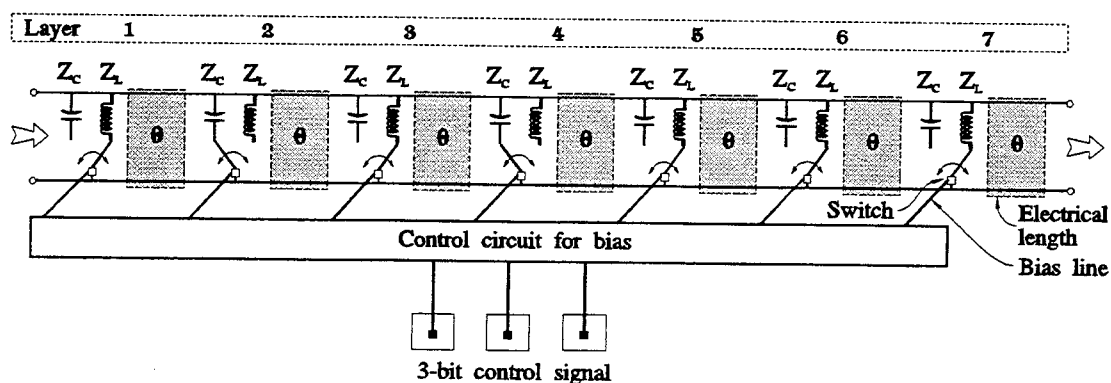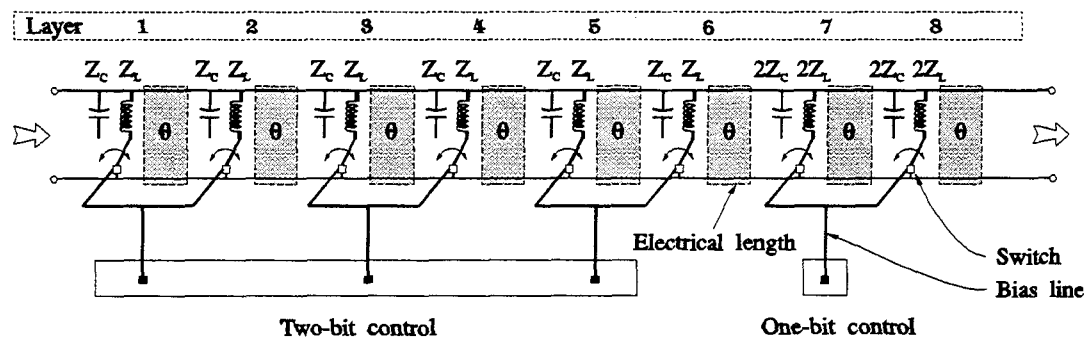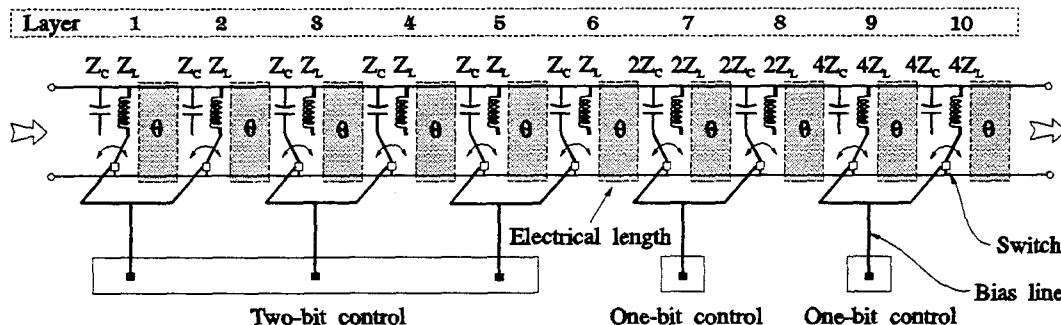

Fig. 3.9 Circuit model for a 7-layer 3-bit controlled beam-steering grid. 2-Ω series resistance is added on each switch for conduction losses.
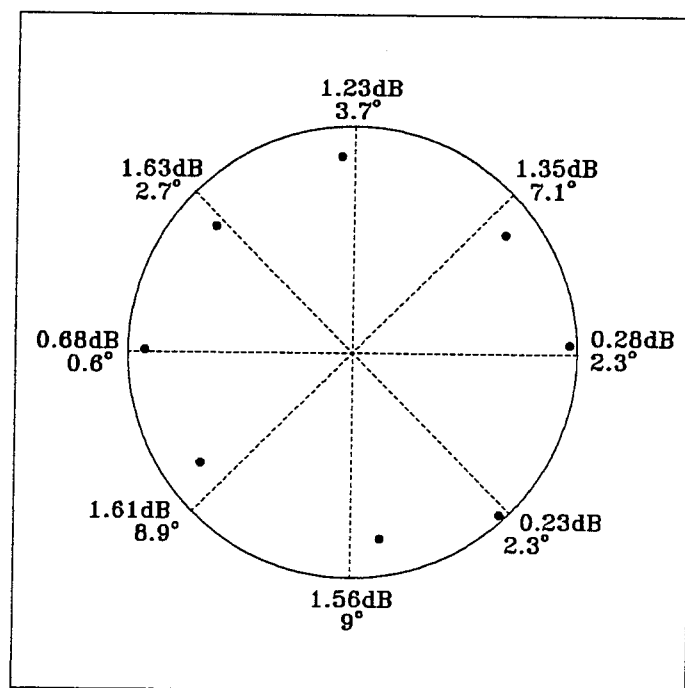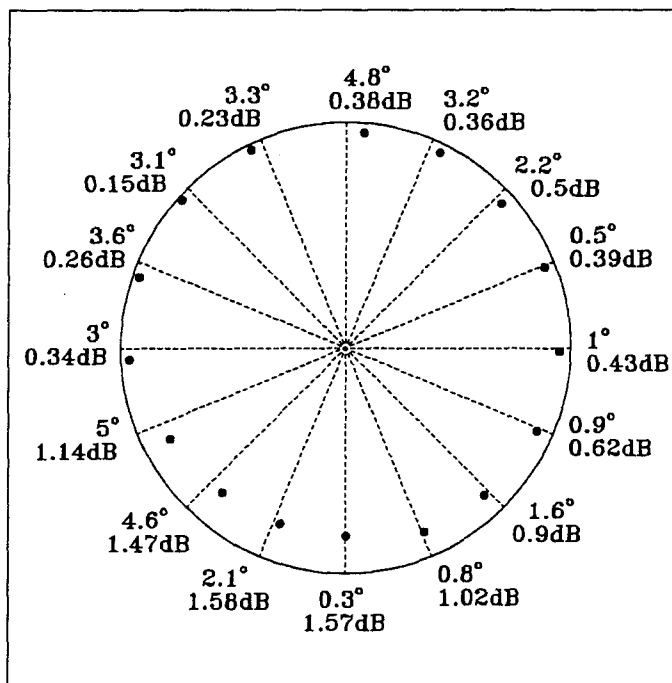

Fig. 3.10 Calculated performance for a 7-layer 3-bit controlled beam-steering grid. The dashed lines indicate the desired phase-shift resolution (45° over 360°) and the distances from the outer circle to the markers indicate losses.

(will be discussed later). The layer arrangement shown in Figure 3.11 gives the best result and the calculated performance for this 3-bit controlled design is shown in Figure 3.12. The electrical length is 102° at 240 GHz. The dashed lines indicate the desired phase-shift resolution (45° over 360°) and the distances from the outer circle to the markers indicate losses. The maximum phase error is 5.3° and the maximum loss is 1.71 dB.

Fig. 3.11 Circuit model for an 8-layer 3-bit controlled beam-steering grid. 2-Ω series resistance is added on each switch for conduction losses.
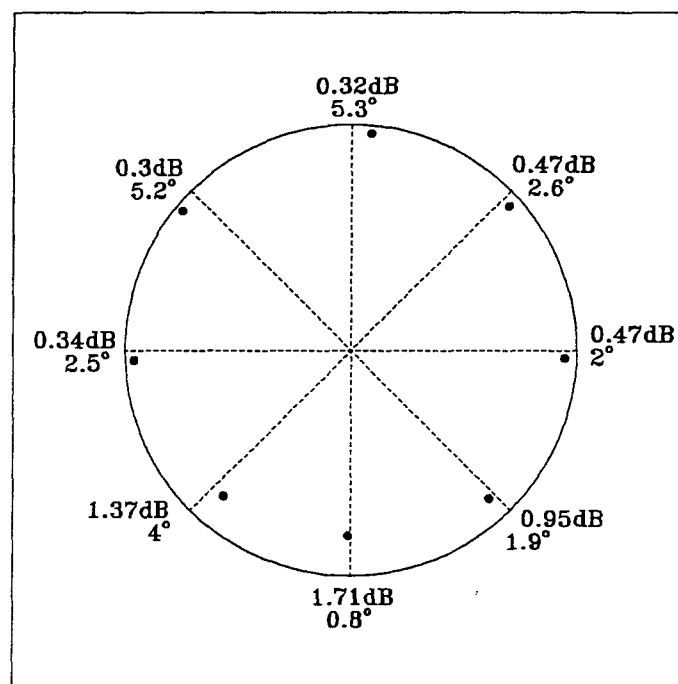
Fig. 3.12 Calculated performance for an 8-layer 3-bit controlled beam-steering grid. The dashed lines indicate the desired phase-shift resolution (45° over 360°) and the distances from the outer circle to the markers indicate losses.

Using the same idea, a 10-layer 4-bit controlled beam-steering grid is also designed with a desired phase-shift resolution of 22.5° over 360°. The circuit model is shown in Figure 3.13 and the calculated optimal performance is shown in Figure 3.14. The maximum phase error is 5° and the maximum loss is 1.58 dB.

Fig. 3.13 Circuit model for a 10-layer 4-bit controlled beam-steering grid. 2- Ω series resistance is added on each switch for conduction losses.

Fig. 3.14 Calculated performance for a 10-layer 4-bit controlled beam-steering grid. The dashed lines indicate the desired phase-shift resolution (22.5° over 360°) and the distances from the outer circle to the markers indicate losses. The electrical length is 102° at 240 GHz and the designed reactances are $Z_L = +j1.317Z_0$ and $Z_C = -j1.317Z_0$.

3.5.2 DESIGN

3.5.2.1 SPACINGS

The first layer of the stacked multi-layer beam-steering grid (the layer #0 in Figure 3.8) serves as an impedance-matching transition between the free space and the rhombic-waveguide array. The design goal is to minimize the reflection loss by adjusting the waveguide dimensions and the spacings. There are three parameters in simulations (Figure 3.15) - the horizontal and vertical spacings, $2x$ and $2y$, and the width of the rhombic waveguide, w. Since the inside-angles are determined by the $\langle 111 \rangle$ planes of silicon, the height of the waveguide, l, is equal to $w/\sqrt{2}$.

The unit-cell waveguide method is used to simulate a TEM-wave incidence by Hewlett-Packard High Frequency Structure Simulator ($HFSS$), a finite-element solver for calculating wave distributions in a 3-D passive structure. Figure 3.15 shows (a) the front view and (b) the 3-D structure used in the simulations. For a TEM-wave incidence, the unit cell has magnetic walls on the sides and electric walls on the top and bottom. Symmetry allows to further reduce the unit cell to a quarter piece with magnetic walls on the sides and electric walls
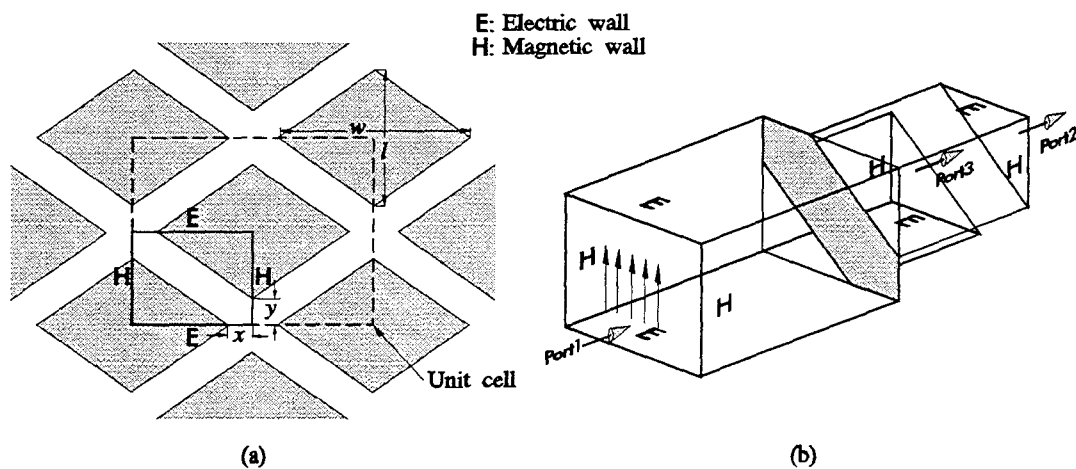
Fig. 3.15 (a) The front view and (b) the 3-D simulation structure.

on the top and bottom. Port 1 is the front quarter-piece unit-cell waveguide. Port 2 and 3 are the back quarter-piece rhombic waveguides. In *HFSS* version 1 and 2, the ports cannot be set on the same planes, so these two waveguides have slightly different lengths. In version 3, these two ports can be set individually. The s-parameters are de-embedded to the incident surface and renormalized after they are solved.

There are several design considerations. The rhombic waveguides have to be small enough to be single-mode waveguides, but big enough to minimize the reflections. The spacings also have to be in a reasonable range for integration of bias lines. Figure 3.16 shows the results for one design. The width, w, and height, l, of the rhombic waveguides are $0.76\lambda_0$ and $0.54\lambda_0$, respectively, where λ_0 is the free-space wavelength at 240 GHz. The spacing parameters are $x = y = 0.246\lambda_0$.

(a)   (b)
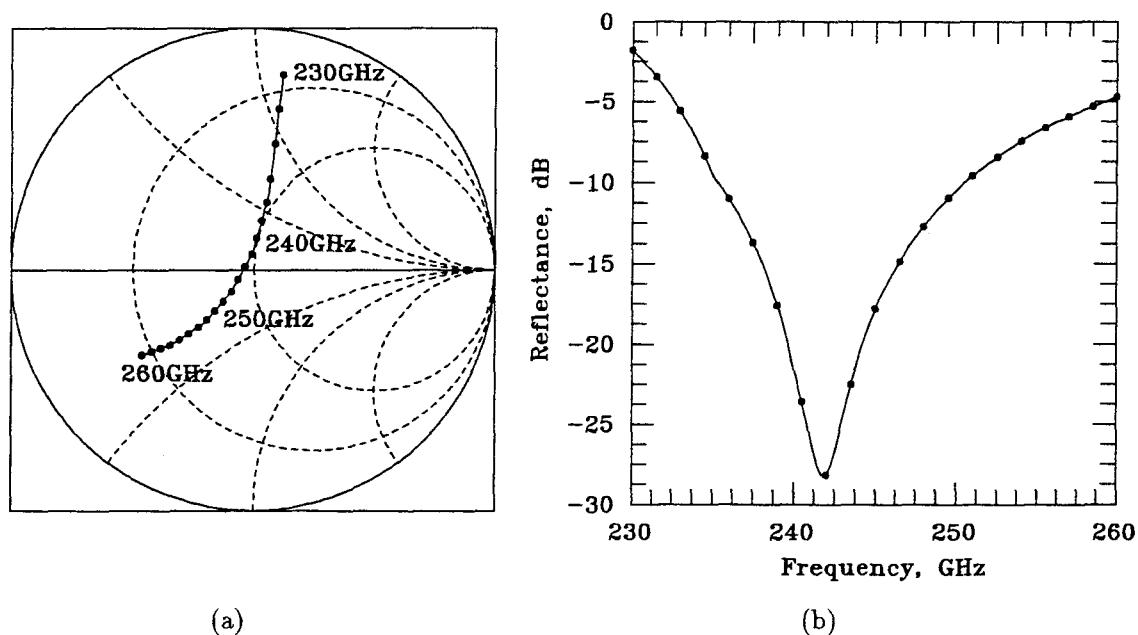
Fig. 3.16 (a) The reflection coefficient, s_{11}, plotted on a Smith Chart and (b) the reflectance as a function of frequency. The rhombic waveguides have a width of $0.76\lambda_0$ and a height of $0.54\lambda_0$. The spacing parameters, shown in Figure 3.15, are $x = y = 0.246\lambda_0$ where λ_0 is the free-space wavelength at 240 GHz.

For 240 GHz, $x = y = 307\,\mu$m which leaves enough space between rhombic holes for bias lines. Figure 3.16 shows (a) the reflection coefficient, s_{11}, plotted on a Smith Chart and (b) the reflectance from 230 GHz to 260 GHz. The resonant frequency is 242 GHz and the respective reflectances are -28 dB at 242 GHz and -24 dB at 240 GHz.
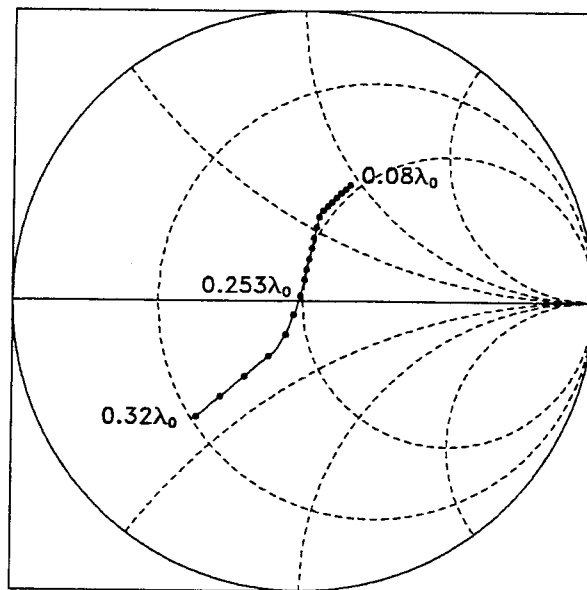
Figure 3.17 shows the reflection coefficient, s_{11}, plotted on a Smith Chart as a function of the spacing parameters, $x = y$, at 240 GHz. The minimum reflection happens at $x = y = 0.253\lambda_0$, where λ_0 is the free-space wavelength at 240 GHz. The minimum reflectance is -38 dB.

Fig. 3.17 The reflection coefficient, s_{11}, plotted on a Smith Chart as a function of the spacing parameters, $x = y$, shown in Figure 3.15. The rhombic waveguides have a width of $0.76\lambda_0$ and a height of $0.54\lambda_0$. The minimum reflection happens at $x = y = 0.253\lambda_0$ where λ_0 is the free-space wavelength at 240 GHz.

3.5.2.2 Rhombic Waveguides

Characterization of rhombic waveguides with inside-angles of 60° and 120° have been demonstrated by Overfelt [28]. Conformal mapping and eigenfunctions of the waveguide are used to solve the cutoff frequencies and eigenvalues. However, there are discrepancies between the analytic solutions and the results from finite-element or finite-difference methods. According to Laura and Ercoli's comments [29], there are no analytical solutions available in the rhombic domains using the conformal mapping approach. Overfelt suggested to use an infinite series of solutions to the Helmholtz equation to generate the lowest-order eigenfunction of the rhombic waveguide in analytic form and calculate the eigenvalue [28]. This method will provide an exact solution for the fundamental mode, however, won't work for higher modes. Therefore, we decide to use *HFSS* to characterize the rhombic waveguides.

Since the two lowest-order eigenfunctions are always TE modes for any con-
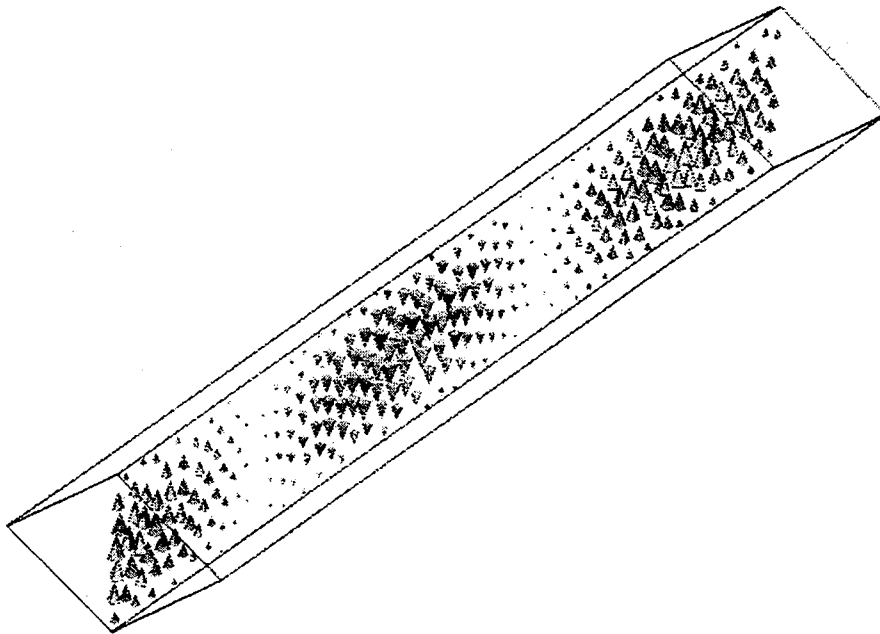
Fig. 3.18 Plot of magnitudes and polarizations of electric fields on the longitudinal plane inside the rhombic waveguide. The sizes and the tips of pyramids indicate the magnitudes and the directions of the electric fields, respectively.

vex domain [30], we will not be concerned with the TM modes for our applications. For TE modes, $\vec{E}_z = 0$, where z is the propagating direction, and $\vec{H}_z$ needs to satisfy

$$(\nabla_T{}^2 + k^2)\vec{H}_z = 0 \tag{3.1}$$

and

$$\frac{\partial \vec{H}_{\hat{z}}}{\partial \hat{n}} = 0 \tag{3.2}$$

where $\hat{n}$ is the outward normal to the walls. The relationship between the propagation constant, β, and the eigenvalue of the i-th mode, k_i, is

$$k_i{}^2 = k_0{}^2 - \beta^2 \tag{3.3}$$

where $k_0{}^2 = \omega^2 \mu_0 \varepsilon_0$. The eigenvalue of the ith mode, k_i, decides the cutoff wavelength of the i-th mode:

$$k_i = \frac{2\pi}{\lambda_{c,i}}. \tag{3.4}$$

Overfelt used $\lambda_{c,1} = w$, where w is the width of the rhombic waveguide, to solve the eigenvalues and found the discrepancies. We define $\lambda_{c,1} = \chi w$, where χ is a correction factor, and solve the cutoff wavelength using *HFSS*.

Figure 3.18 and 3.19 show the simulation structures. The waveguide has a length of $3.5\lambda_0$, a width of $0.76\lambda_0$ and a height of $0.54\lambda_0$, where λ_0 is the free-space wavelength at 240 GHz. Figure 3.18 shows the plot of magnitudes and polarizations of electric fields on the longitudinal plane inside the rhombic waveguide. Figure 3.19 shows the electric-field distributions on two longitudinal planes inside the rhombic waveguide. The correction factor, χ, is found to be 0.724 which agrees with the discrepancy-numbers in [28]. The propagation constants for the first three modes are plotted in Figure 3.20. The cut-off frequencies for the fundamental mode, TE_{10}, is 229 GHz and for the next higher mode, TE_{01}, is 305 GHz. The phase constant, β, is 1.5×10^3 rad./m at 240 GHz in this single-mode waveguide.
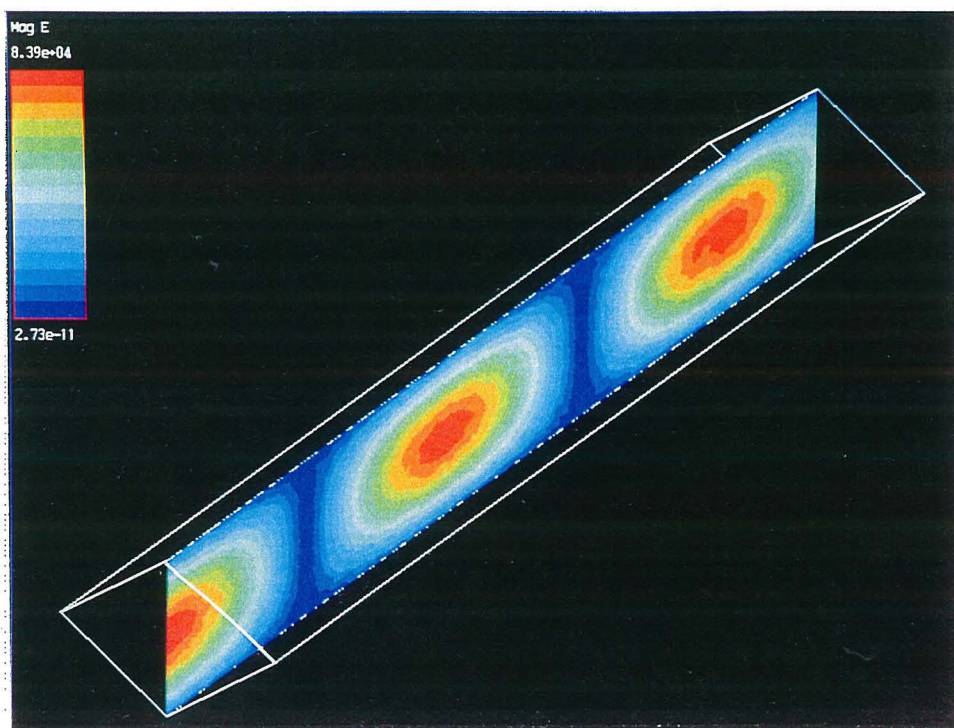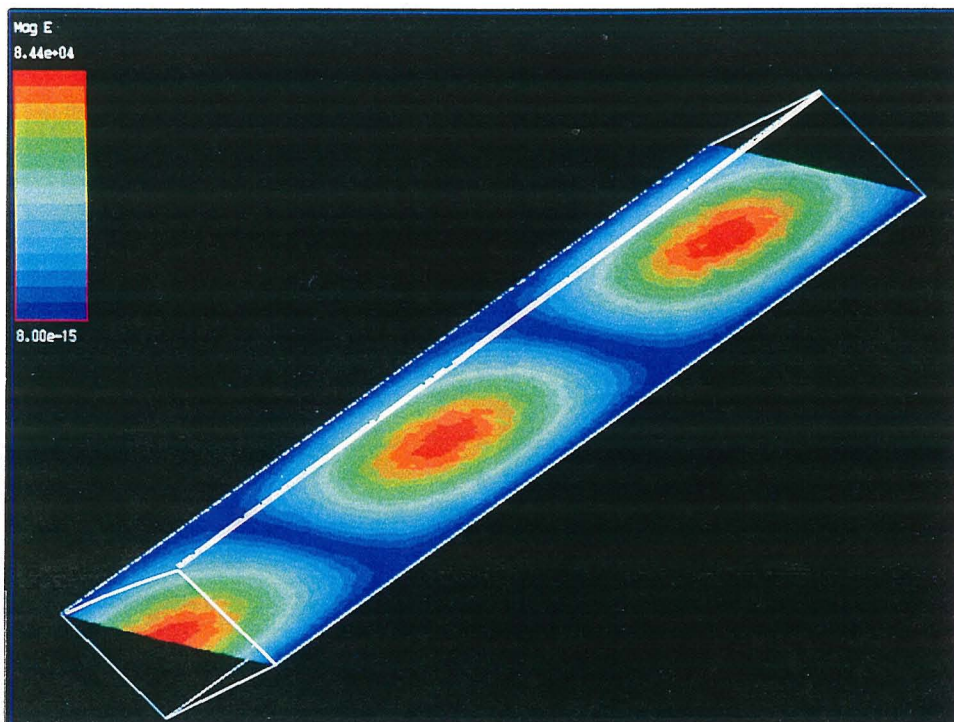
Fig. 3.19 Electric-field distributions on two longitudinal planes inside the rhombic waveguide.
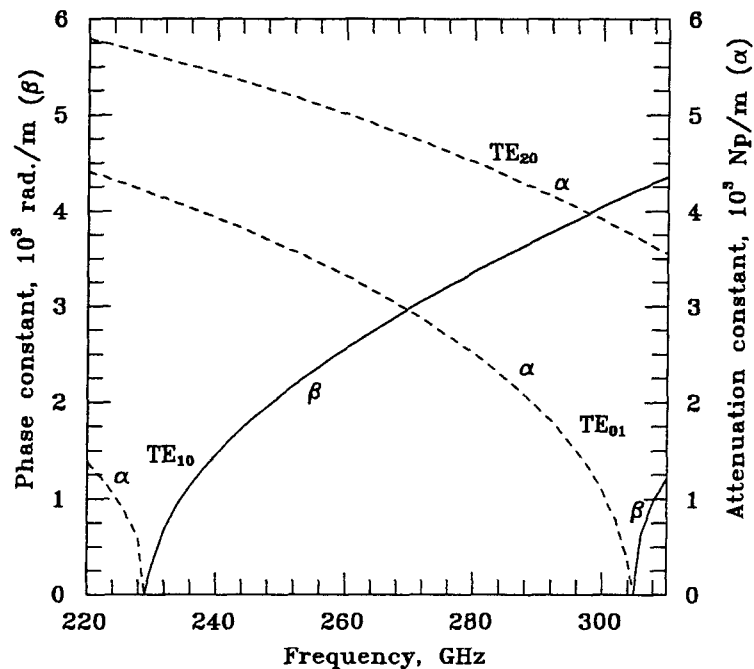
Fig. 3.20 The propagation constants of the rhombic waveguide with a width of $0.76\lambda_0$ and a height of $0.54\lambda_0$, where λ_0 is the free-space wavelength at 240 GHz. The cut-off frequencies for the fundamental mode, TE_{10}, is 229 GHz and for the next higher mode, TE_{01}, is 305 GHz.

The power handling capability of a single-mode waveguide can be defined as [31]

$$\eta = \frac{P_{\text{peak}}}{A \cdot P_D} \tag{3.5}$$

where P_{peak} is the peak transmitted power inside the waveguide, A is the cross section of the waveguide and P_D is the power density in free space. P_D can be normalized as

$$P_D = \frac{|\vec{E}_T|^2}{Z_0} \tag{3.6}$$

where $|\vec{E}_T|$ is the maximum electric-field magnitude in the waveguide cross section and Z_0 is the free-space impedance. The peak transmitted power is determined by

$$P_{\text{peak}} = \iint_A (\vec{E} \times \vec{H}^*) \cdot \hat{z} dA \tag{3.7}$$

where $\vec{E}$ and $\vec{H}^*$ can be obtained from the calculated field distributions. The power handling capability is 0.425 for the rhombic waveguides with inside-angles of 70.6° and 109.4°, defined by the $\langle 111 \rangle$ planes of silicon. By optimizing the shapes of rhombus, the maximum power handling capability is found to be 0.434 for a 60°-120° rhombic cross section [28]. To compare, a rectangular waveguide with a cross section which has a ratio (width to height) of 2:1 will have a power handling capability of 0.465. The power handling efficiency of the rhombic waveguides in our design is only slightly less than that of a rectangular waveguide.

To find the attenuation constant due to the losses in the imperfectly conducting sidewalls of the waveguide, the law of conservation of energy is used. The rate of decrease of propagating power, $P(z)$, with distance along the waveguide equals the time-average power loss, $P_L(z)$, per unit length. The attenuation constant, α_c, is determined by

$$\alpha_c = \frac{P_L(z)}{2P(z)} \tag{3.8}$$

where $P(z)$ is the time-average power flowing through a cross section of the waveguide and $P_L(z)$ is the time-average power lost on the walls. They can be decided by

$$P(z) = \iint_A \frac{1}{2}\mathrm{Re}(\vec{E} \times \vec{H}^*)dA \tag{3.9}$$

and

$$P_L(z) = \iint_S \frac{1}{2}|\vec{J_s}|^2 R_s ds \tag{3.10}$$

where R_s is the surface resistivity, $\vec{J_s}$ is the surface current density, S is the sidewalls of the waveguide and A is the cross section. The surface current density can be calculated by $\vec{J_s} = \vec{a}_n \times \vec{H}$, where $\vec{a}_n$ is the normal of the sidewall. The $\vec{E}$, $\vec{H}$ and $\vec{H}^*$ can be obtained from the calculated field distributions. The calculated attenuation constant is $\alpha_c = 1.8 \times 10^{-9}$ Np/m by assuming the surface resistivity of gold $R_s = 2.96 \times 10^{-7}\sqrt{f}$ $\Omega\cdot\mathrm{m}^{-2}$, where $f = 240$ GHz [32].

3.5.2.3 REACTIVE METAL PATTERNS

After the spacings and dimensions of the rhombic waveguides are decided, metal patterns are placed inside the waveguides to achieve the desired reactances. Figure 3.21 (a) shows the simulation structure for an open switch. The rhombic waveguide has a width of $0.76\lambda_0$ and a height of $0.54\lambda_0$, where λ_0 is the free-space wavelength at 240 GHz. The propagating mode is TE_{10} and the gap between two horizontal metal strips, g, decides the shunt capacitive reactance. Figure 3.21 (b) shows the de-embedded s-parameters as a function of the distance between the horizontal metal strips. The desired shunt reactance, $-j1.317Z_0$, is achieved with $g = 0.254\lambda_0$.

Inductive metal pattern is added on the capacitive pattern to imitate a closed switch. Figure 3.22(a) shows the pattern. With a fixed gap, g, the vertical

(a)   (b)
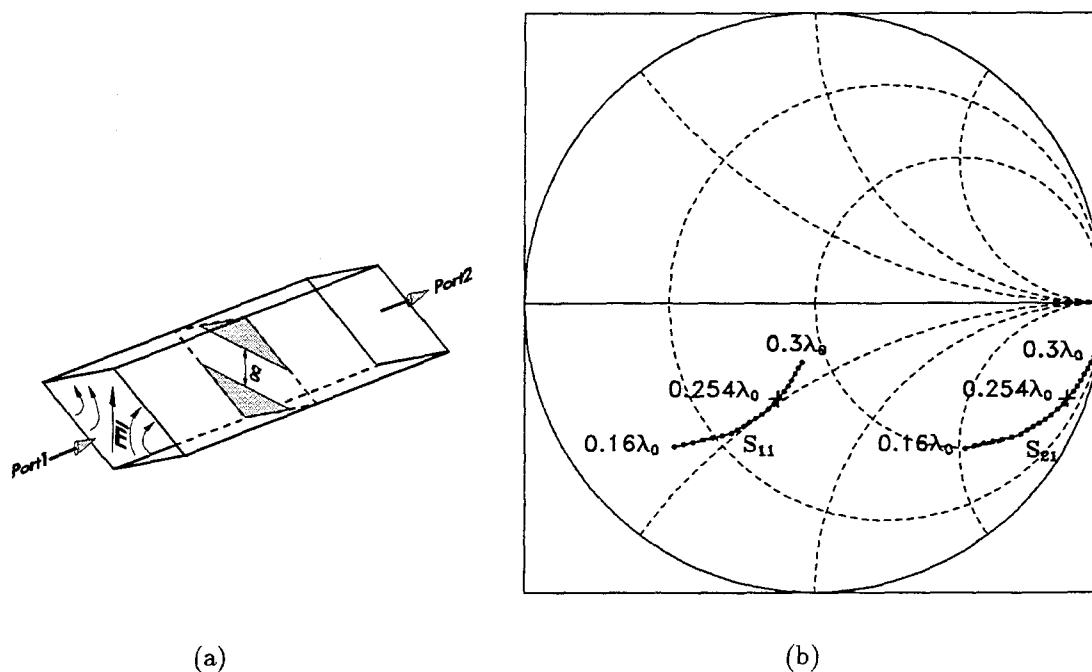
Fig. 3.21 (a) Simulation for an open switch and (b) the de-embedded s-parameters as a function of the distance between the horizontal metal strips. The desired shunt reactance is $-j1.317Z_0$, where Z_0 is the rhombic-waveguide impedance at 240 GHz.

metal strip adds a shunt inductance which is mainly determined by the width, k, and the length, t, of the vertical metal strip. However, a simple strip connecting the top and bottom horizontal metal strips ($t = g$) doesn't contribute enough inductance. So instead of reducing the width to reach the desired shunt inductance, we increase the length. The top and bottom horizontal strips in the center are scooped out leaving a rectangular area to allow increasing the length of the vertical strip. This will not reduce the shunt capacitance of an open switch when the width of the scooped-out area ($2r + k$) is small.

Figure 3.22(b) shows the de-embedded s-parameters as a function of the length of the vertical metal strip. The desired shunt reactance, $+j1.317Z_0$, is achieved with $r = 1.5 \times 10^{-2}\lambda_0$, $k = 8 \times 10^{-4}\lambda_0$ and $t = 0.534\lambda_0$.

(a)   (b)
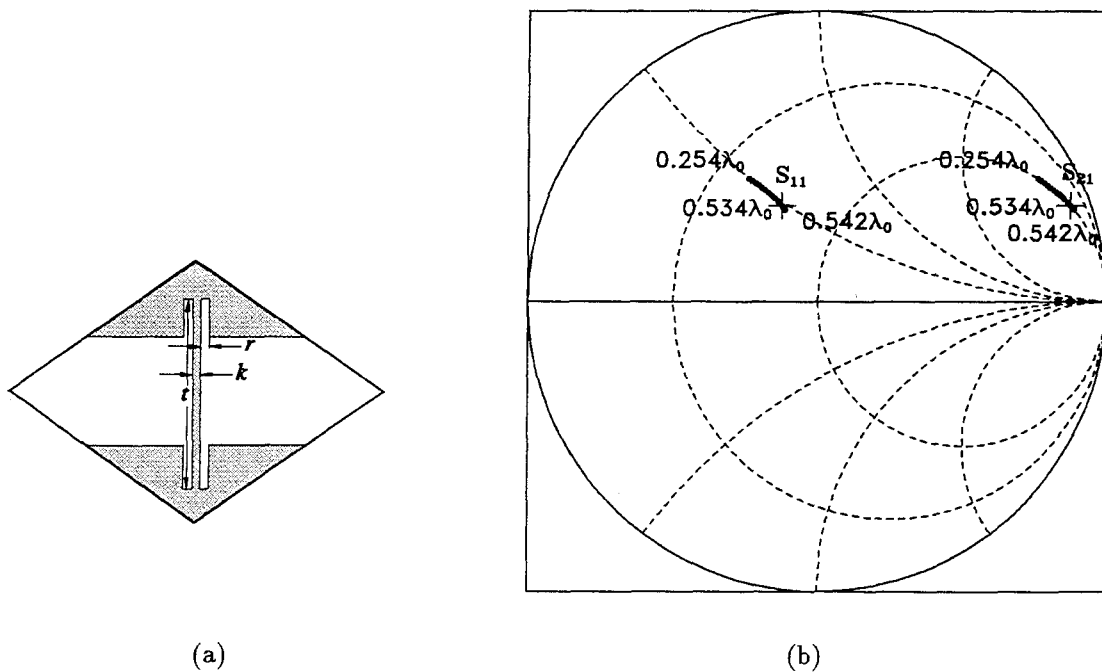
Fig. 3.22 (a) Simulation for a closed switch and (b) the de-embedded s-parameters as a function of the length of the vertical metal strip which has a width of $8 \times 10^{-4}\lambda_0$.

3.6 44-GHz Design

3.6.1 Motivation

With the increasing attentions on developing sensors for automobile controls and crash-avoidance systems [33,34], the needs for electronic beam-control devices in the frequency ranges from 40 to 130 GHz are urgent. After all, a mechanical scanning system in vehicles is not an attractive idea for automobile manufactures. Quasi-optical transmitter with electronic beam-controllers providing advantages of low losses, high speeds and small sizes would be a competent candidate.

Efforts are underway to develop 44 GHz monolithic quasi-optical grid-amplifiers using HBT devices at Rockwell Science Center [35]. Also a f/0.2 binary lens made of rexolite for beam shaping has been demonstrated to be used in a 44 GHz quasi-optical transmission system [36]. The key element to complete this quasi-optical transmitter system is a low-loss beam-steerer. Conventional waveguide-methods are bulkier and have more losses. Quasi-optical diode-grid beam-controller is an attractive option. However, power-handling and loss problems due to the diode structures and the series resistances may become major issues for a watt-level system. Microswitch beam-steering grids should certainly be able to handle more power than diode-grids. The losses can be minimized by adjusting grid-layouts and the spacings between layers because the series resistance of the micromechanical switch should be much smaller than that of diode, which is the main source of losses, at millimeter wavelengths.

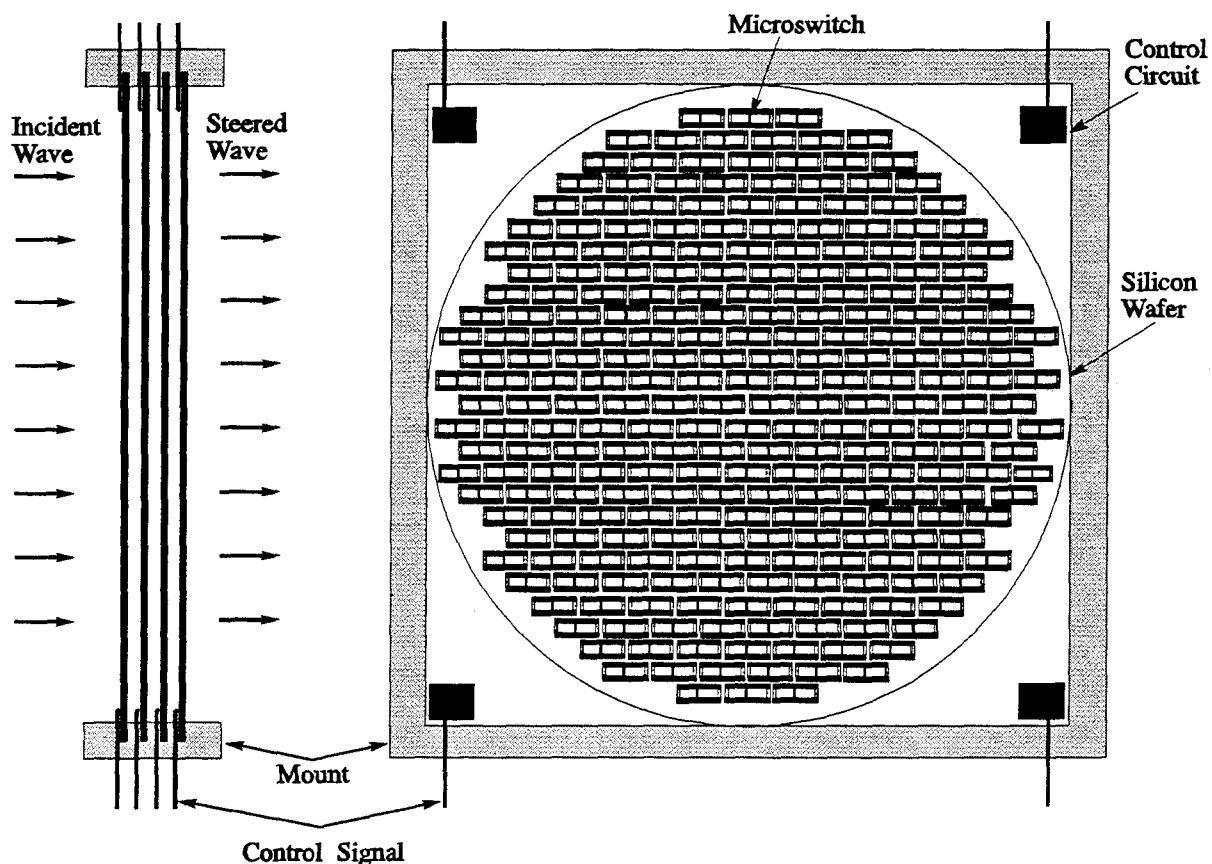Figure 3.23 shows a monolithic microswitch beam-steering grid design for 44 GHz. The microswitches will be fabricated on thin ⟨100⟩ silicon wafers with pyramidal cavities underneath. The thickness ($300 \mu m$) of silicon wafers is much smaller than the wavelength (6.8 cm), so the reflection losses from the sidewalls of the pyramidal cavities can be minimized by adjusting the unit-cell layouts. Free

space is used to provide proper electrical lengths between switches. The electrical lengths are adjusted to reach a minimum loss and an optimal phase-shift resolution. Generally speaking, the electrical lengths should be in the neighborhood of $\lambda_0/4$ (1.7 mm). Using the free space eliminates the needs of thick wafers, the needs of accurate thickness for wafers, and the waveguide-wall losses. It also provides tuning capability. Bias lines are integrated between cavities to control each switch. The biases are controlled by IC control circuits which can be fabricated

Fig. 3.23 Monolithic microswitch beam-steering grid design for 44 GHz. The microswitches will be fabricated on thin ⟨100⟩ silicon wafers with pyramidal cavities underneath. Bias lines are integrated between cavities to control each switch. Integrated-circuit control devices can be fabricated on the same wafer to decode the control signals into bias signals in order to reduce the numbers of control wires coming out of the grids. Spacings between layers are adjusted to minimize the reflection losses.

on the same wafer to decode the control signals into biasing signals in order to reduce the numbers of wires coming out of the grid.

3.6.2 DESIGN

The unit-cell waveguide method is used for simulations. Port 1 and 2 are respectively the front and back of the grid. The unit cell has electric walls on the top and bottom, and magnetic walls on the sides for TEM-wave incidence. Symmetry allows us to further reduce the unit-cell to a quarter-piece, as shown in Figure 3.24. The quarter-piece waveguide also has electric walls on the top and bottom, and magnetic walls on the sides. Structure parameters include the thickness of the wafer, h; the horizontal and vertical spacings between holes, a and b; the sizes of the front windows, l and w; and the skewed angle of the lattice, α, which decides the arrangements of odd and even rows. For fabrication reasons, the thickness is chosen to be $300\,\mu$m. The simulations are performed using *HFSS*.

First, a structure without capacitive or inductive metal patterns is used to find the structure parameters, l, w, α, a and b, in order to reach a minimum reflection loss. Then either a capacitive metal pattern, which imitates an open switch, or an inductive metal pattern, which imitates a closed switch, is added on the opening window of the pyramidal holes to calculate the added shunt reactances in the unit cell. The equivalent circuit for a structure without reactive elements can be approximately presented as a resonant circuit with a resonant frequency of 44 GHz. The shunt reactances in the first layer of a 10-layer system, which gives a phase-shift resolution of 22.5° over 360° (will be described later), should provide ±20.8° phase shifts, as shown in Figure 3.25.

A structure without reactive metal patterns is first used in *HFSS* to find the proper parameters, l, w, α, a and b, to reach a minimum reflection loss. The pyramidal holes should have a height less than a half-wavelength and a width more than a half-wavelength in order to avoid the propagation of cross-
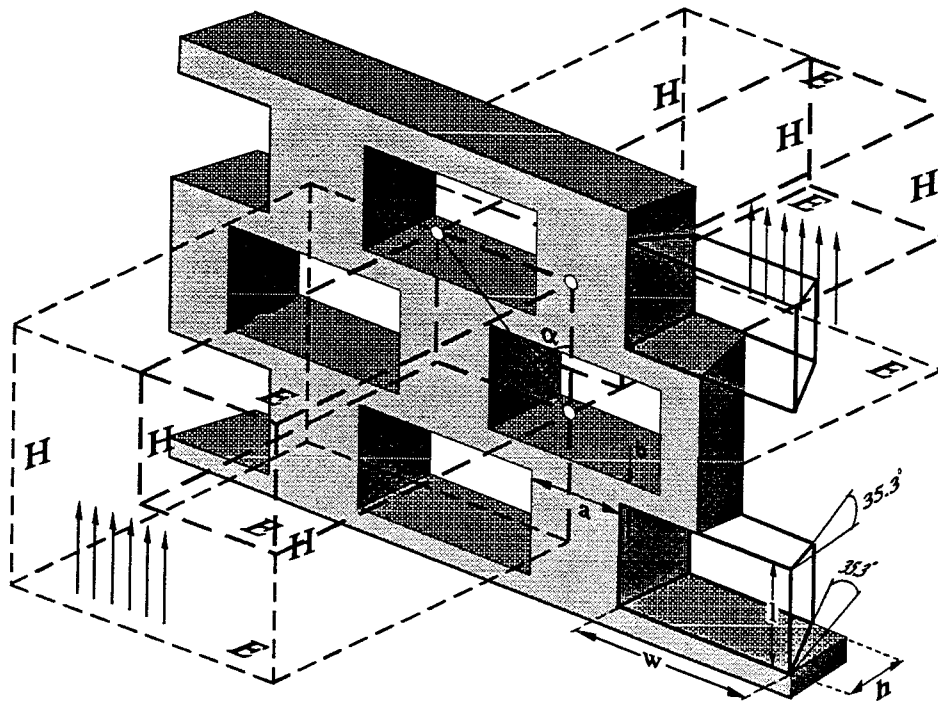
Fig. 3.24 Simulation structure. The inside-angles are 35.3° defined by ⟨111⟩ planes of silicon. Symmetry allows to further reduce the unit-cell waveguide to a quarter-piece waveguide with electric walls on the top and bottom and magnetic walls on the sides. Structure parameters include the thickness of the wafer, h, the horizontal and vertical spacings between holes, a and b, the sizes of the front windows, l and w, and the angle of the lattice, α.
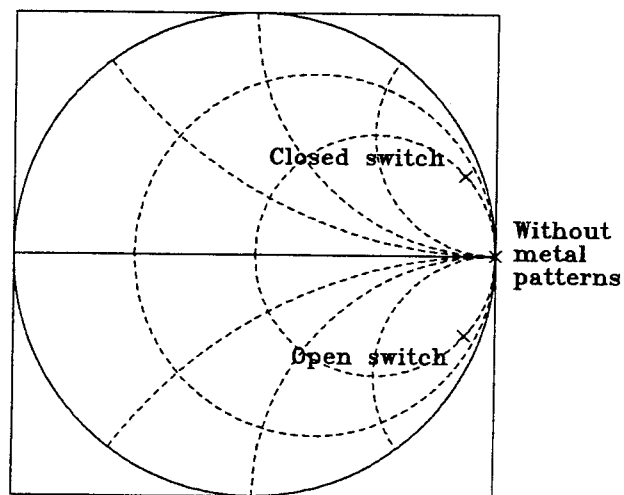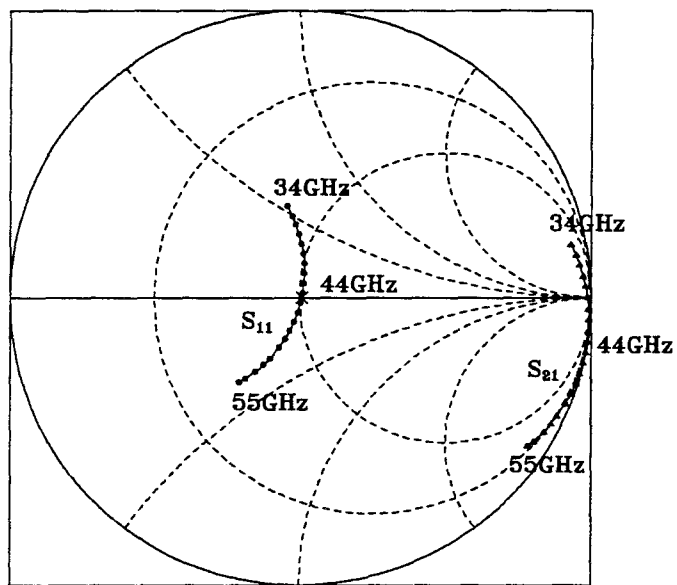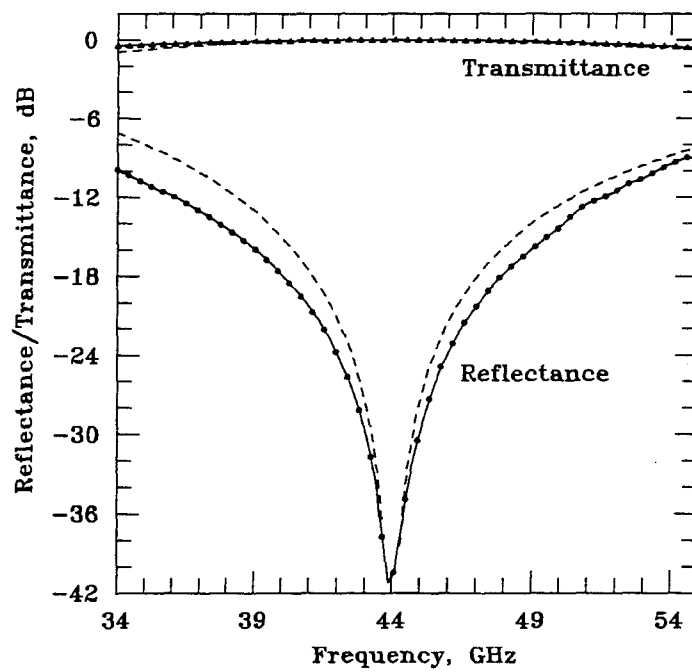

Fig. 3.25 Desired transmission coefficients, s_{21}, for closed- and open-switch configurations on the first layer of a 10-layer structure.

(a)

(b)

Fig. 3.26 (a) The reflection and transmission coefficients as a function of frequency, and (b) the reflectance and transmittance as a function of frequency. The dashed lines show the resonant-circuit results.

polarizations excited by the sidewalls. The spacings between holes need to be big enough for the integration of bias lines and feasible fabrication. Both square-lattice arrangements, $\alpha = 0°$, and equilateral-triangular-lattice arrangements, $\alpha = \tan^{-1}((w + a)/2(l + b))$, are calculated to find the minimum reflection. Simulations over the frequency range of interest are carried out to verify the resonant points since the finite-element method does not converge well at the resonant point.

The final design is an equilateral-triangular-lattice arrangement of rectangular windows with l=2.47 mm $(0.36\lambda_0)$, w=5.2 mm $(0.76\lambda_0)$, a=500 μm $(0.073\lambda_0)$, b=600 μm $(0.088\lambda_0)$, and $\alpha = 42.9°$, where λ_0 is the free-space wavelength at 44 GHz. For square-lattice arrangements, $\alpha = 0°$, we are not able to reach resonances at 44 GHz with design-parameters feasible for fabrications.

Figure 3.26 shows (a) the reflection and transmission coefficients, s_{11} and s_{21}, and (b) the reflectance and transmittance as a function of frequency. The dashed lines indicate the calculations from the equivalent circuit shown in Figure 3.27. As one can expect, the equivalent circuit of the unit cell with an equilateral-triangular-lattice arrangement of the rectangular holes should be more complicated than the one shown in Figure 3.27 and the disagreements in Figure 3.26(b) also verify that. However, this simplified equivalent-circuit allows us easily to decide the equivalent circuits for closed and open switches.

As mentioned before, the finite-element method does not converge well around resonant points. One way to verify the resonant point is to sweep the frequencies, as shown in Figure 3.26(a). Another way to verify is to vary the
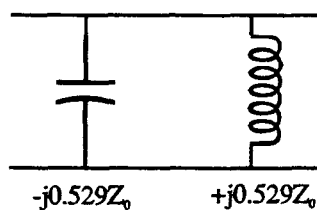

-j0.529Z_0　　+j0.529Z_0

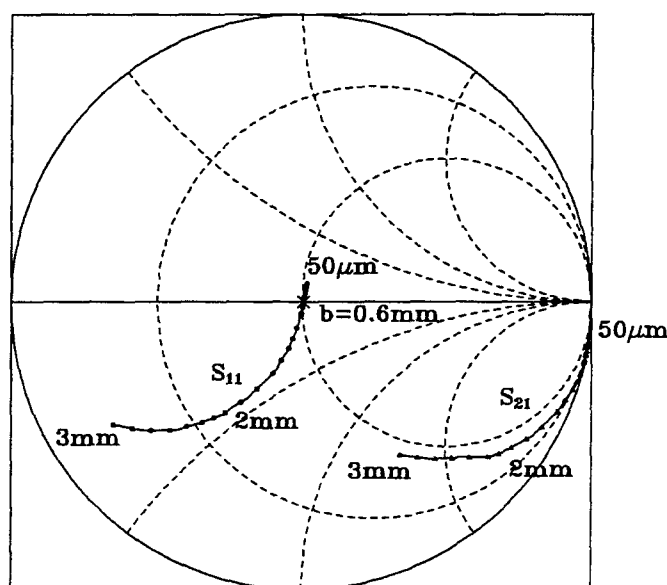Fig. 3.27 The simplified resonant circuit. Z_0 is the free-space impedance.

Fig. 3.28 The reflection and transmission coefficients as a function of the vertical spacing, b, between rows. × indicates the resonant point.

design parameters. Figure 3.28 shows the s_{11} and s_{21} as a function of the vertical spacing between rows, b. The spacings are varied from $50\,\mu$m to $3\,$mm and the resonance happens with a spacing of $b = 600\,\mu$m.

Capacitive metal patterns are added on the windows of the pyramidal cavities to imitate open switches. Figure 3.29 shows the simulation structure. The gap, g, between the horizontal metal strips is varied to obtain the desired shunt capacitive reactance. Figure 3.30 shows the calculated reflectances from $30\,$GHz to $60\,$GHz and the equivalent circuit for a gap of $1.11\,$mm. A shunt capacitive reactance of $-j1.312Z_0$ is added to the resonant impedance by the metal-strip gap.

Inductive metal patterns are added on the windows of the pyramidal cavities to imitate closed switches. Figure 3.31 shows the simulation structure. With a fixed gap, g, the vertical metal strip adds a shunt inductance to the impedance of an open-switch configuration. The inductance is mainly determined by the
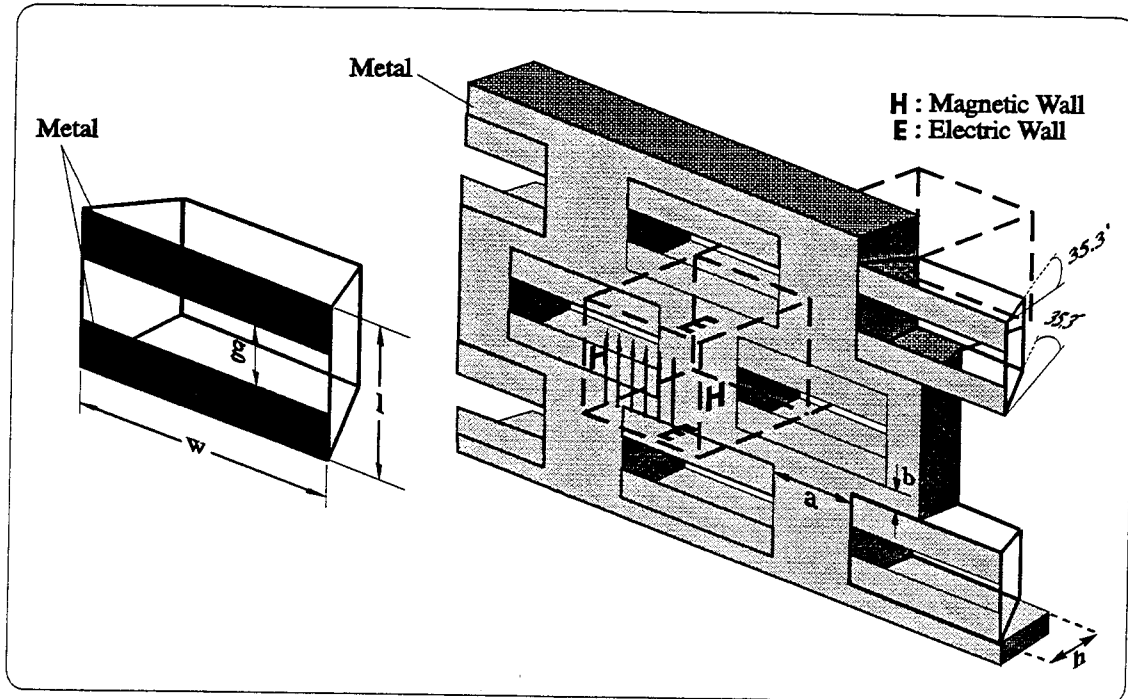
Fig. 3.29 Capacitive metal patterns on the windows of the pyramidal cavities to imitate open switches. The shunt capacitance is determined by the gap, g.
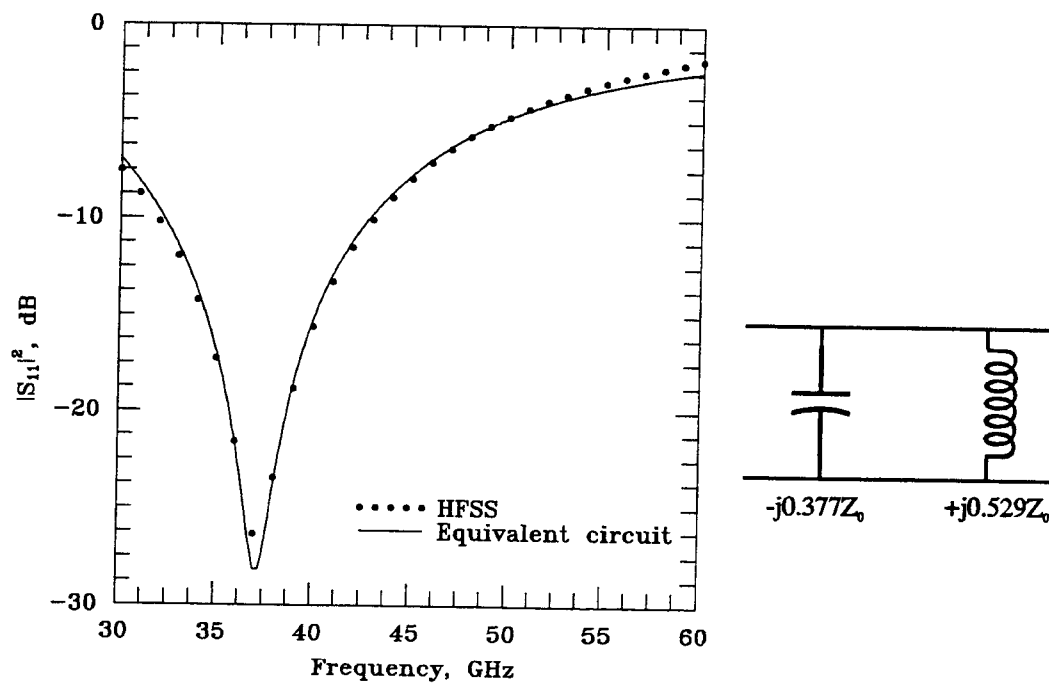

Fig. 3.30 Calculated reflectances as a function of frequency and the equivalent circuit for an open switch.
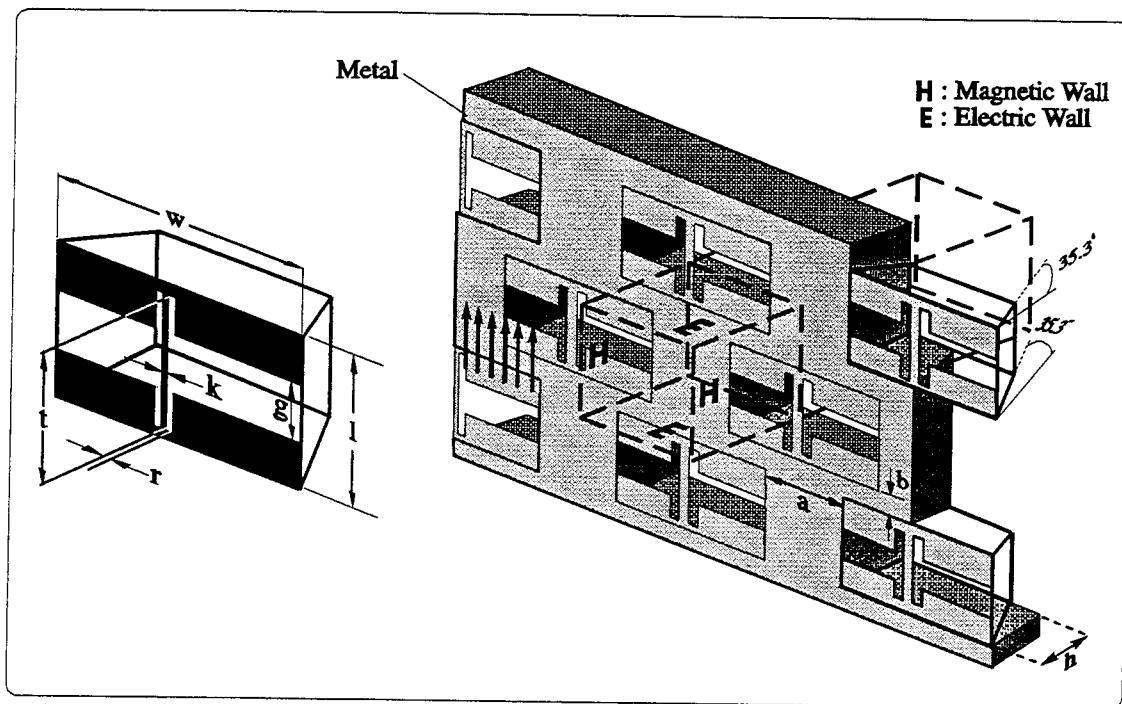
Fig. 3.31 Inductive metal patterns on the windows of the pyramidal cavities to imitate closed switches. The shunt inductive reactance is mainly determined by the length, t, and the width, k, of the vertical metal strip.
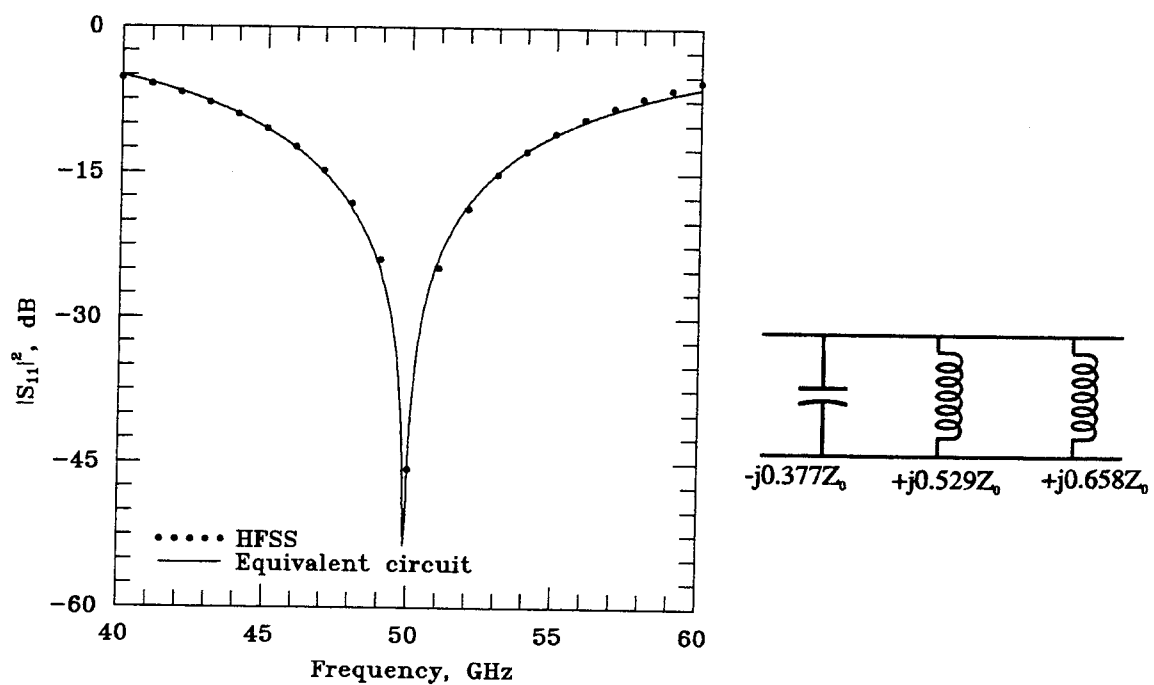

Fig. 3.32 Calculated reflectances as a function of frequency and the equivalent circuit for a closed switch.

width, k, and the length, t, of the vertical metal strip. However, for the desired inductive reactance, a simple strip connecting the top and bottom horizontal metal strips ($t = g$) needs to have a width of less than $0.5\,\mu$m which is very difficult to fabricate. So instead of reducing the width to reach the desired shunt inductance, we increase the length. The top and bottom horizontal strips in the center are scooped out leaving a rectangular area to allow increasing the length of the vertical strip. This will not add extra shunt capacitance in the unit cell when the electric field is vertically polarized or reduce the shunt capacitance of an open switch when the width of the scooped-out area ($2r + k$) is small.

Figure 3.32 shows the calculated reflectances from 40 GHz to 60 GHz and the equivalent circuit. For a 20-μm wide vertical strip, the design dimensions are $t = 1.94$ mm and $r = 20\,\mu$m. A shunt inductive reactance of $+j0.658Z_0$ is added to the impedance of an open-switch configuration by the vertical metal-strip.

3.6.3 CALCULATED PERFORMANCE

The desired shunt reactances, $\pm j1.317Z_0$, in the first layer of a 10-layer system should provide $\pm 20.8°$ phase shifts, as shown in Figure 3.25. It may seem not particularly useful. However, a 10-layer system with proper spacers can provide phase-shifts with a resolution of 22.5° over 360° by a 4-bit control signal. Figure 3.33 shows the idea. Each layer includes a microswitch and a free-space electrical length, θ. Two adjacent layers will be controlled by the same bias lines which can switch the microswitches by pairs. The first six layers have the same metal patterns which provide a shunt inductance of 1.8 pH with a closed switch or a shunt capacitance of 7.3 fF with an open switch. These six layers (three pairs) are controlled by a 2-bit signal. The seventh and eighth layers controlled by a 1-bit signal have the metal patterns which provide a shunt inductance of 3.6 pH with a closed switch or a shunt capacitance of 3.6 fF with an open switch. The ninth and tenth layers also controlled by a 1-bit signal have the metal patterns which provide a shunt inductance of 7.2 pH with a closed switch or a shunt

capacitance of 1.8 fF with an open switch.

2- Ω series resistance is added on each switch for imitating RF conduction losses. The real series-resistance is expected to be smaller than 2 Ω at 44 GHz. By adjusting the electrical length, θ, and different switching configurations, losses
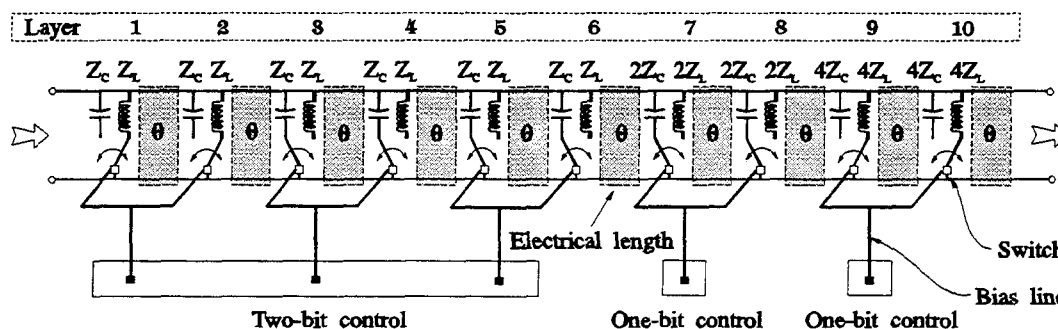

Fig. 3.33 Circuit model for a 10-layer 4-bit controlled microswitch beam-steering grid. 2- Ω series resistance is added on each switch for imitating RF conduction losses.
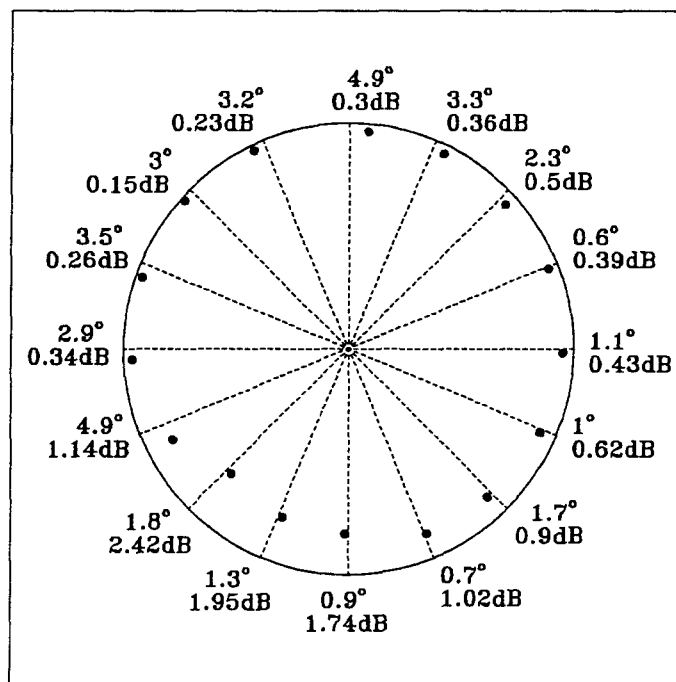

Fig. 3.34 Phase-shifts and losses at 44 GHz for a 10-layer system. The dashed lines indicate the desired phase-shift resolution (22.5° over 360°) and the distances from the outer circle to the markers indicate losses.

and phase-shifts can be calculated. Figure 3.34 shows the transmission coefficients on a polar plot. The dashed lines indicate the desired phase-shift resolution (22.5° over 360°) and the distances from the outer circle to the markers indicate losses. Two considerations are taken into account in the calculations. First, some different combinations of switch-settings will have different phase-shifts and losses for the same desired phase-shifts. For example, for layers #1−#6, a combination of ⟨(open-open)–(close-close)–(open-open)⟩ generates different phase-shift and loss from the combinations of ⟨(close-close)–(open-open)–(open-open)⟩ or ⟨(open-open)–(open-open)–(close-close)⟩, although the projected phase-shift is the same. A tradeoff between phase-shift error and loss needs to be made in this kind of case. Basically we chose minimum losses over minimum phase-shift errors unless the phase-shift errors are more than 11° (a half of the resolution angle) where the observed point will be mixed up with the adjacent points.

Second, different layer-arrangements will have different performances. For example, an arrangement of

$$(Z_{C,L}\text{--}Z_{C,L}) - (Z_{C,L}\text{--}Z_{C,L}) - (Z_{C,L}\text{--}Z_{C,L}) - (2Z_{C,L}\text{--}2Z_{C,L}) - (4Z_{C,L}\text{--}4Z_{C,L})$$

will have a different performance from the arrangement of

$$(2Z_{C,L}\text{--}2Z_{C,L}) - (Z_{C,L}\text{--}Z_{C,L}) - (Z_{C,L}\text{--}Z_{C,L}) - (Z_{C,L}\text{--}Z_{C,L}) - (4Z_{C,L}\text{--}4Z_{C,L}).$$

Taking both considerations into account and adjusting the electrical length, the optimal performance is shown in Figure 3.34. The layer-arrangement for this optimal result is shown in Figure 3.33. The maximum phase-shift error is 4.9° and the maximum loss is 2.42 dB for this 4-bit controlled, 10-layer beam-steering grid.

In radar applications, the Doppler frequency-shift effect needs to be considered. Figure 3.35 shows the transmission coefficients at different frequencies. The switch settings and layer-arrangement are based on the optimal design for 44 GHz. Using the same configurations, 40 GHz and 48 GHz results are calculated. The losses and shifted-phases are listed in Table 3.1.

	40 GHz	40 GHz	44 GHz	44 GHz	48 GHz	48 GHz
Target	Loss (dB)	Phase shift	Loss (dB)	Phase shift	Loss (dB)	Phase shift
0°	0.39	-2.2°	0.43	-1.1°	0.16	-2.9°
-22.5°	0.38	-24.3°	0.62	-23.5°	0.19	-26°
-45°	0.55	-47.7°	0.9	-46.7°	0.28	-49.7°
-67.5°	0.58	-69.7°	1.02	-66.8°	0.28	-69.9°
-90°	2.28	-93.4°	1.74	-90.9°	1.96	-98.1°
-112.5°	1.7	-118.3°	1.95	-111.2°	1.57	-121.8°
-135°	2.06	-140.9°	2.42	-133.2°	0.63	-141.3°
-157.5°	2.14	-157.5°	1.14	-152.6°	0.77	-162.3°
-180°	1.92	-173.1°	0.34	-177.1°	0.18	169°
157.5°	1.7	169.6°	0.26	161°	0.1	147.4°
135°	1.37	146°	0.15	138°	0.5	125.8°
112.5°	1.31	123.9°	0.23	115.7°	0.27	105.2°
90°	0.27	95.2°	0.3	85.1°	1.8	81.5°
67.5°	0.26	73.4°	0.36	64.2°	1.26	57.3°
45°	0.17	49.9°	0.5	42.7°	0.55	39.3°
22.5°	0.15	27.9°	0.39	21.9°	0.7	14.9°

Table 3.1 The shifted-phases and losses of the 4-bit controlled, 10-layer beam-steering grid at 40 GHz, 44 GHz and 48 GHz.
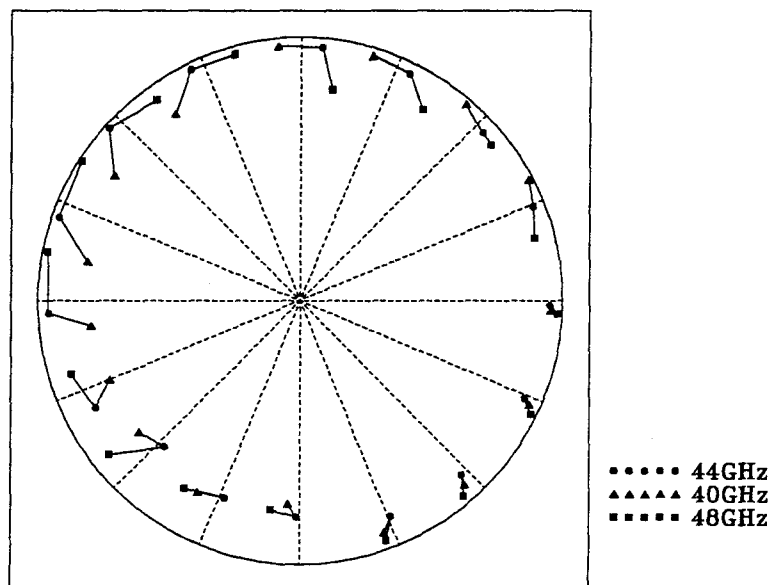

Fig. 3.35 Transmission coefficients at 40 GHz, 44 GHz and 48 GHz on a polar plot. The dashed lines indicate the desired phase-shifts and the distances from the outer circle to the markers indicate losses. The data are listed in Table 3.1.

3.7 FABRICATION

Fabrication for micromechanical switches have been described by Petersen in [23,24]. However, the switch structures made by Petersen are different from our designs and can not be used directly in our grids.

First, the micromechanical switches that have been demonstrated are four-terminal devices, shown schematically in Figure 3.2. The thin metallization covering the membrane is divided into three segments: the two outer, large-area deflection electrodes and the contacting electrode in the center of the membrane. The two deflection electrodes are connected together by a plated metal bridge on the wafer surface. The membrane is deflected by applying a voltage between the deflection electrodes and the bottom of the etched well. The deflected membrane takes the contacting tip down and makes the electrical contact with the fixed electrode.

In our case, the silicon underneath the switches must be etched through to form a waveguide to allow electromagnetic waves to transmit. This eliminates the possibility of establishing static charges between the metallization and the wafer. The deflection electrodes have to be combined with the contact electrodes. The larger membrane covered by metallization now is replaced by a single strip of metal-coated membrane. The width of the strip is usually narrow (less than 20 μm) in order to reach the required shunt inductance. Furthermore, the waveguides underneath the switches have to be big enough to have the cutoff frequency of the propagating mode below the operating frequencies. This means the length of the strip has to be long enough. The longest membrane-switches demonstrated [25] is 118 μm, however, for applications at millimeter wavelengths, it has to be much longer. Fabricating narrower but longer membrane-switches makes the stress-control and the quality of the membrane much more important than before.

Second, because the silicon has to be etched through the wafer, a long period

of silicon etching is required. Previous membrane-switches only require 20-minute EDP etching at 118° C and it is sufficient to create a pit underneath the switches. For our case, the EDP etching and the KOH etching take 10-12 hours and 4 hours to etch through a 300-μm thick silicon wafer, respectively. This again emphasizes the importance of quality control of the membranes.

Third, low-resistivity highly-doped n-type silicon wafers with surface polished are used to reduce the RF losses instead of low-doped silicon wafers which were used in Petersen's experiments. However, the highly-doped feature with a dielectric thin-film cover creates a highly-reflective surface on the wafer for photolithography and causes trouble to define etching or lift-off patterns on our wafers using the same type of photoresist used before. Problems are solved by using other types of photosensitive materials, however, the fabrication processes also have to be changed such as spinning speeds; baking times and temperatures; curing times and temperatures; and stripping methods.

Finally, the attempt to repeat the fabrication processes in [23,24] to make microswitches results in disappointing failures. After the final step of gold plating, the entire metallization along with the bridge structure would be stripped off from the surface when the photoresist sacrificial-layer was removed in acetone. We suspect that it might be caused by the improper undercuts in the edges of the photoresist mesa. However, it seems impossible to create a photoresist mesa without undercut on one edge but with undercuts on the other three edges. This is not described in [23,24] and seems that it didn't cause any problems to fabricate micromechanical switches. We solved this problem by using an oblique evaporation technique to eliminate the requirement of impractical undercuts in the bridge-structure mesa.

3.7.1 FABRICATION PROCEDURES

(1) Fabrication processes start with a highly-doped n-type silicon wafer. A 1-μm thick layer of silicon-oxynitride (SiO_xN_y) is deposited on both sides of
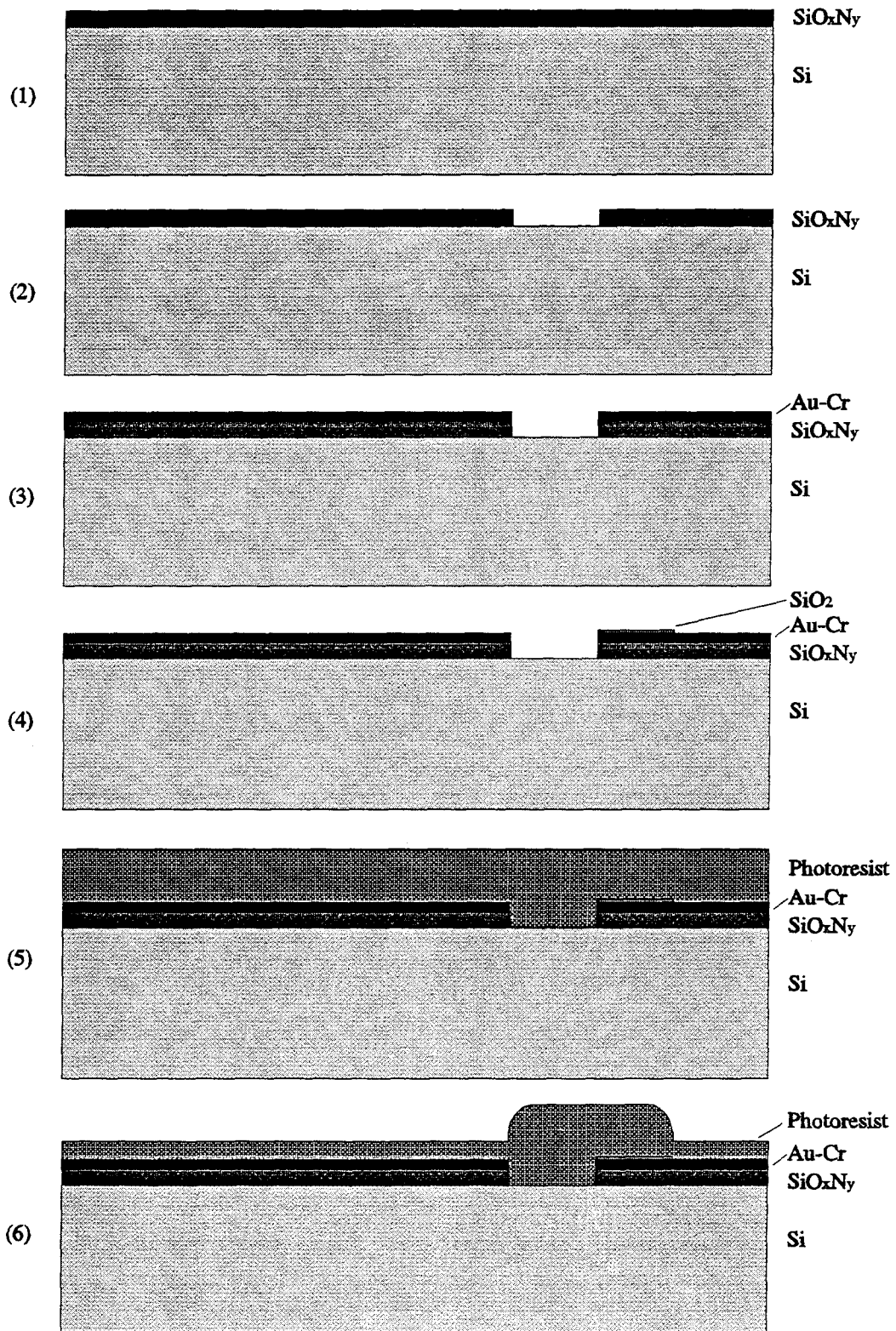
Figure 3.36 Fabrication procedures.

the silicon wafer by using plasma enhanced chemical vapor deposition.

(2) Photoresist is applied and exposed to define an opening for silicon etching. Then SiO_xN_y in the opening is etched away using buffered-HF solution. Resist is removed.

(3) Photoresist is applied again to cover the exposed silicon and a layer of chromium/gold is evaporated and lifted off.

(4) Photoresist is applied and exposed to define an area for SiO_2 deposition. A rectangular pattern of SiO_2 is deposited using thermal evaporation on the edge of contact-electrode. The purpose of this SiO_2 pad is to prevent DC currents flowing through the contact which takes away the charges formed to provide the electrostatic force. Resist is removed afterward.

(5) A thick layer of photoresist is applied on the entire wafer. Several different types of photoresist are used including AZ1350J®, AZ5214®, AZ4330® photoresists and photosensitive polyimides like HTR 3-50® and HTR 3-200®.

Because another layer of photoresist has to be applied later for gold-plating, the first layer of resist may be solved when applying the second layer. Also due to the long period of gold plating, the resist-mask may be attacked by the plating solution. Therefore, a hard-bake process after exposure on this and second resist-layers is required to protect the resist. However, the hard-bake will harden the resist, reduce the height (over which there is evaporated gold covered) and deform the bridge structure. Several failures show the insufficient hard-bake causes the damages. Therefore, we explored the use of several different types of photoresist for a better mesa-forming. Table 3.2 shows the types of resist, spinning speeds used, and the measured thickness's before and after hard-bake. The resists are mostly overbaked for a good protection from plating-solution attack. The thickness is measured by using a Sloan Dektak® IIA surface profiler.
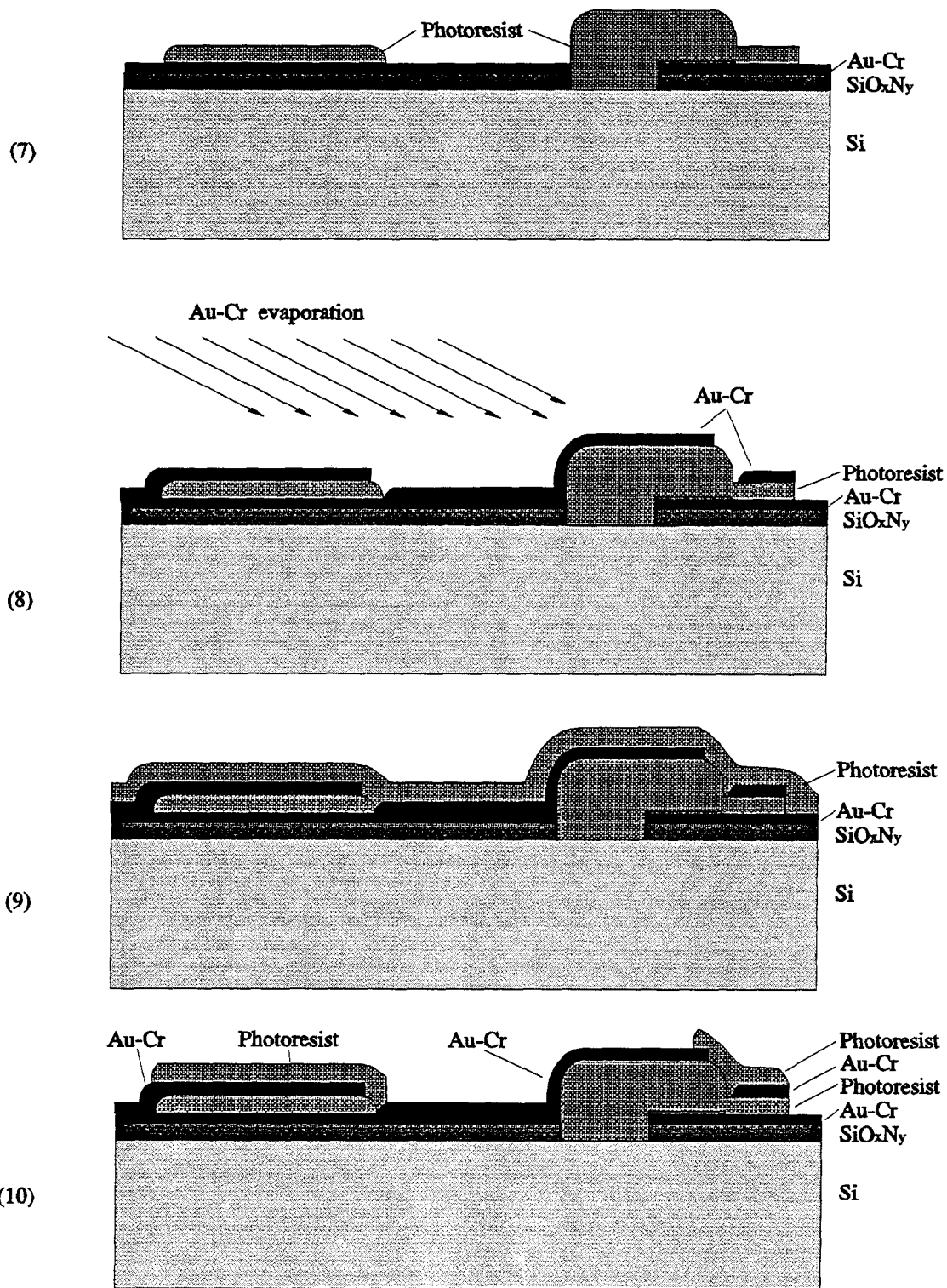
(7)

(8)

(9)

(10)

Figure 3.36 Fabrication procedures. (*continued*)

Resist type	Spinning r.p.m.	Thickness (before) μm	Thickness (after*) μm
AZ1350J	3000	2	~ 1 †
AZ4330	3000	4	3.8
AZ5214	3000	1.6	1.6
HTR 3-50	3000	3.2	1.5 ‡
HTR 3-200	3000	12	5 ‡

Table 3.2 The thickness's of different types of photosensitive resists, used in our laboratory, before and after* the hard-bake process. The thickness is measured by using a Sloan Dektak® IIA surface profiler.

* : The resists are mostly overbaked for protection from plating-solution attack.

† : Due to the highly reflective surface of the highly-doped silicon wafers used, the photoresist is pre-baked at 50° C, which is different from the normal procedure, repeatedly overexposed and overdeveloped which may result in a different thickness.

‡ : The polyimides are cured in a nitrogen-gas blown environment on a hot plate at 150° C.

Due to the highly-reflective surface of the highly-doped silicon wafers, the most commonly-used AZ1350J photoresist is pre-baked at 50° C for 10 minutes, which is different from the normal procedure (at 85° C for 30 minutes), repeatedly overexposed and overdeveloped. This caused a lot of problems during our fabrications and resulted in a lot of failures. Photosensitive polyimide is another option. However, the thickness changes are too big to form a good bridge-structure and it is more difficult to be stripped off than AZ-resists. Our experiences show that a 1.6-μm thick of AZ5214 spun at 3000 r.p.m. ($\sim 1\,\mu$m at 5000 r.p.m.), soft-baked at 90° C for 60 s on a hot plate, and thermally cured (imidized) at 110° C for 60 s on a hot plate gives a uniform profile of contact after hard-bakes and increases resistance to sol-

vents and plating-solution. The thickness doesn't change noticeably after hard-bakes and gold-plating. Also AZ5214 photoresist doesn't cause any trouble when we used it on the highly-reflective surface of highly-doped silicon wafers.

(6) An insufficient UV-exposure is applied to define the mesa over which gold will be plated to form the bridge structure and contact-electrode.

(7) The remaining photoresist then is overexposed to open a window for gold-plating base. The resist then is hard-baked.

(8) A thin ($60\overset{\circ}{A}$-Cr and $400\overset{\circ}{A}$-Au) layer of Cr-Au is evaporated over the entire wafer at an angle of 60° normal to the wafer from the side which the bridge will be formed. This layer serves as a plating base. This oblique evaporation eliminates the requirement of no resist-undercut on the bridge side and undercuts on the rest three sides of the contact-electrode mesa.

(9) Another layer of photoresist is applied.

(10) UV-exposure is used to define the regions to be gold-plated and open a contact area on the edge of wafer for connecting of the plating current.

(11) Gold is plated in a cyanide-based electroplating solution agitated with a magnetic spinner to a thickness of $3\,\mu$m through the photoresist windows. The plating time is 15 minutes with a total current of 0.7 A at 60° C.

(12) The resist and the excessive plating base are stripped in resist-stripper solution and the bridge structure is formed.

(13) The entire wafer is placed in EDP (ethylenediamine-pyrocatechol and water) or KOH (50% of potassium hydroxide flakes in deionized water by weight) solution and the silicon is etched away to form a cantilever beam underneath the SiO_xN_y. The etching rates of EDP (Transene® PSE-300) etchant at 100° C for $\langle 100 \rangle$ and $\langle 111 \rangle$ planes of n-type silicon are $25\,\mu$m per hour and negligible, respectively. This anisotropic feature will result in V-shaped walls ($\langle 111 \rangle$ planes) at an angle of 54.7° from the surface ($\langle 100 \rangle$ plane) under-
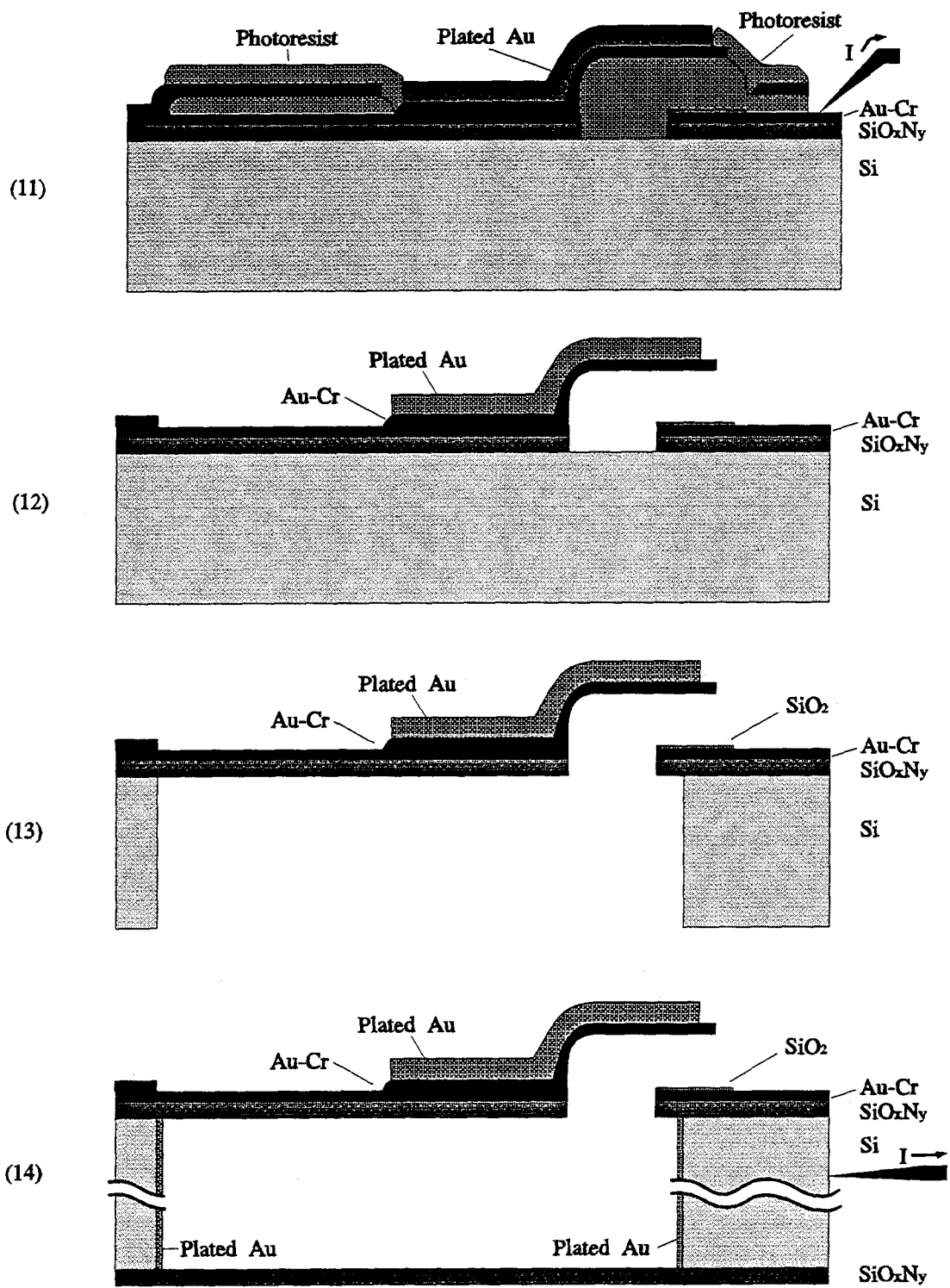
Figure 3.36 Fabrication procedures. (*continued*)

neath the cantilever beam. The etching rates of KOH etchant at 80° C for $\langle 110 \rangle$ and $\langle 111 \rangle$ planes of silicon are 87 μm per hour and 0.5 μm per hour, respectively. The etching will form a vertical-wall cavity underneath.

Then the device is rinsed and carefully dried by blowing air on the wafer. Drying by placing the wafers on hot plates is also used, but heat causes the cantilever bridge bent downward, dries the water between the contact-electrode and the SiO_2-pad, and closes the switches. These switches could not be opened again even by cooling them in a de-humidified liquid-nitrogen-cooled box.

(14) There is a layer of SiO_xN_y on the back of the silicon wafer. Most of the SiO_xN_y membranes in the bottom of the etched cavities are usually broken from the hot silicon-etching. The SiO_xN_y layer on the back provides a good balance of surface-stress with the layer on the front, regardless of broken or good membranes in the windows on the back, and prevents the wafer from tensile or compressive stress bending [37].

The front side of the entire wafer is sprayed (not spun) with photoresist and baked for protection. Gold is plated on the sidewalls of the etched cavities in gold-plating solution. Some SiO_xN_y on the edge of the wafer is removed by dumping only one corner of the wafer into buffered-HF solution and the silicon is exposed for connecting the gold-plating electrode. The highly-doped silicon has very low-resistivity (much less than 0.5 Ω·cm). The switch structures on the front are insulated by the SiO_xN_y-layer and won't be plated. The resist-cover provides extra protection. Low electroplating current is used in order to get a smoother surface.

The device is rinsed after gold-plating. The photoresist is removed using acetone. The device is cleaned in distilled water followed by in methanol and then carefully dried by blowing air on the wafer.

3.7.2 MEMBRANE

Thin-film depositions on silicon such as silicon-dioxide (SiO_2), silicon-oxynitride (SiO_xN_y) and silicon-nitride (Si_3N_4) covered with metallization have been documented well for VLSI applications. However, metallized suspended-membrane in a cavity with only partial connections on the edges has not yet been fully characterized, especially for thin-film cantilever beams.

Using undoped-silicon and polysilicon as the materials of the suspended structures have been demonstrated by Choi *et al.* [38] and Tang *et al.* [39], respectively. Thin (0.2 μm) metal sheets suspended over support structures ($\sim$5 μm high) have been demonstrated by van Raalte [40] and showed that metal-film structure is potentially susceptible to metal fatigue, especially for gold which has a particularly low fatigue strength. Guldberg *et al.* [41] and Thomas *et al.* [42] used 0.35-μm thick thermally-grown amorphous SiO_2-films over a 5-μm epitaxial silicon layer on sapphire substrate to demonstrate a mirror-matrix display. The structures consist of four cloverleaf-shaped thin-film coated with aluminum (300$\overset{\circ}{A}$) with only one corner connected to the center silicon supporting-
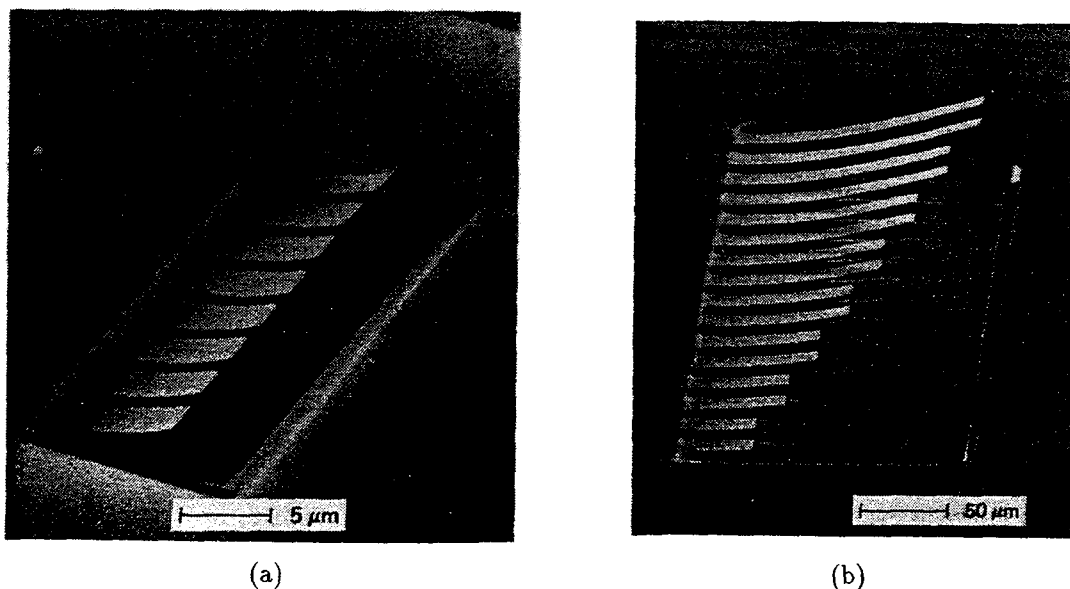

(a)   (b)

Fig. 3.37 (a) The linear cantilever-beam light-modulator array, and (b) with various beam sizes for measuring Young's modulus [25]. K.E. Petersen's works at IBM.

posts. The structure shows that the thermally-grown amorphous SiO_2 films substantially increase the fatigue strengths. A small, linear array of voltage-controlled optical modulators used electrostatically-controlled micromechanical cantilever-beams to deflect light was demonstrated by Petersen [25], as shown in Figure 3.37(a). The structures consist of a metal-coated thermally-grown amorphous SiO_2 film suspended in an anisotropically-etched silicon pit. Figure 3.37(b) shows various beam sizes for measuring Young's modulus [25,43]. These pictures show two concerns: 1. The residual stress of the SiO_2-film coated with metal makes the beams bent upward which indicates there is a compressive stress between the metal and the film. 2. The longer the beams are, the more the stress effect is.

Taking these two considerations into account, we expect to face a bigger technical challenge to fabricate longer cantilever-beam switches. It didn't cause fabrication problems before because those cantilever beams were short (30-118 μm), the silicon etching time was short ($\sim$20 minutes), the etching temperature is low (85° C), and there were no bridge-contact structures on the tips which add more complexities on tension. Actually, on the contrary, the micromechanical optical-modulators utilize the residual stress of the cantilever-beam membranes to achieve a big difference of deflection angles in order to reach a big ON-/OFF-state ratio.

Earlier attempts to build 500 μm-1 mm long cantilever-beam switches using thermally-grown SiO_2-films by wet oxidation in our laboratory (which doesn't have impurity control) failed. After the silicon etching (100° C), most of the cantilever beams broke at the edges connecting to the silicon surface. Changing the thickness of the evaporated gold and using evaporated-silver or evaporated-aluminum for the surface metallization trying to change the residual stress didn't improve the situations. A possible reason is the interaction between the compressive stress of the thermally-grown SiO_2-film on the silicon surface

($\sim 2 - 4 \times 10^9$ dyne/cm^2) [37] and the compressive stress from the metal on the SiO_2-film. Both residual stresses result from the differences among the thermal coefficients of expansion of Si, SiO_2, and metal. Similar conditions were also observed in [44] and [45], which the SiO_2-membranes tend to wrinkle, distort and break when the silicon is etched away, because of the compressive stress.

Si_3N_4 film is an alternative which has been widely used for VLSI applications. However, high-temperature CVD-grown Si_3N_4 on silicon has strong tensile stress [37, pp. 192] which is good for planar circuits on the membrane-windows to avoid rupture, but bad for cantilever-beam applications. The strong tensile stress bends the beams downward and makes the contacts touch permanently.

Silicon-oxynitride (SiO_xN_y) provides a flexible choice. SiO_xN_y films have very different physical and electrical properties depending on their composition [46]. Variations in oxygen and nitrogen concentrations generally have a
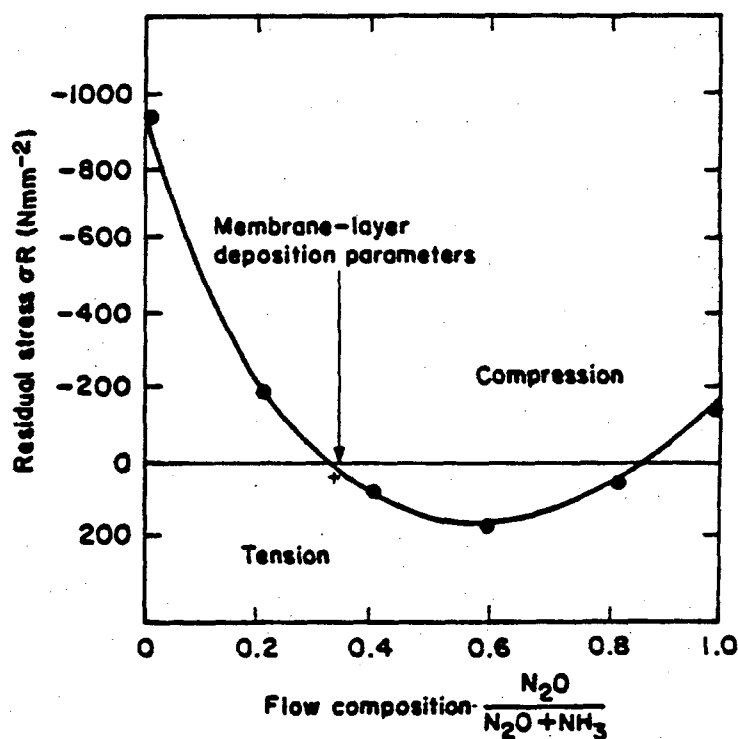
Fig. 3.38 Residual stress as a function of flow composition. The arrow indicates the composition ratio used in our membranes.

strong influence on film properties. To produce the membrane, SiO_xN_y is grown on the silicon wafer using plasma-enhanced chemical vapor deposition. This is done by Kent Potter at Caltech. The deposition parameters are adjusted to produce a membrane on silicon with small tensile stress. Since silicon-oxynitride is considered to be a "low-quality" silicon-nitride film, its tensile strength is lower than that of silicon-nitride. The gases used are silane (SiH_4), ammonia (HH_3) and nitrous oxide (N_2O). The deposition temperature is 300° C. The pressure is 2 mTorr. The RF power density is $0.012 \, W \cdot cm^{-2}$ and the RF frequency is 440 kHz. The residual stress, σ_R, of the film on silicon is a function of flow composition as shown in Figure 3.38. The flow composition is adjusted to obtain a σ_R of $10 \, N \cdot mm^{-2}$.

Another reason to use the SiO_xN_y-membranes is to prevent the thin-films from being attacked by EDP or KOH solutions. We tested the etching rates by measuring the thickness's of SiO_2 and SiO_xN_y films on a Sloan DekTak® IIA surface profiler. The measured etching rate of SiO_2 in EDP (100° C) and in KOH (80° C) are $200 \overset{\circ}{A}$ and $2000 \overset{\circ}{A}$ per hour, respectively. For the 20-minute etching used in the previous cantilever-beam fabrications, the degradation of membranes is negligible. However, in our cases, the silicon wafers have to be etched through and it takes 10-12 hours in EDP solution or 3-4 hours in KOH solution. The thin-film damage from etchants is another possible reason of failures in the earlier attempt of fabricating microswitches on SiO_2 membranes. The measured etching rates of EDP and KOH etchants for SiO_xN_y are $60 \overset{\circ}{A}$ and $500 \overset{\circ}{A}$ per hour, respectively. Therefore, using SiO_xN_y film can reduce the risk of breaking the cantilever beams in long-period etching. The damage can be further reduced by lowering the etching temperatures.

3.7.3 CANTILEVER BEAM

Arrays of cantilever-beams suspended on etched $\langle 100 \rangle$ silicon waveguides are first fabricated to demonstrate the strength of SiO_xN_y films. Figure 3.39
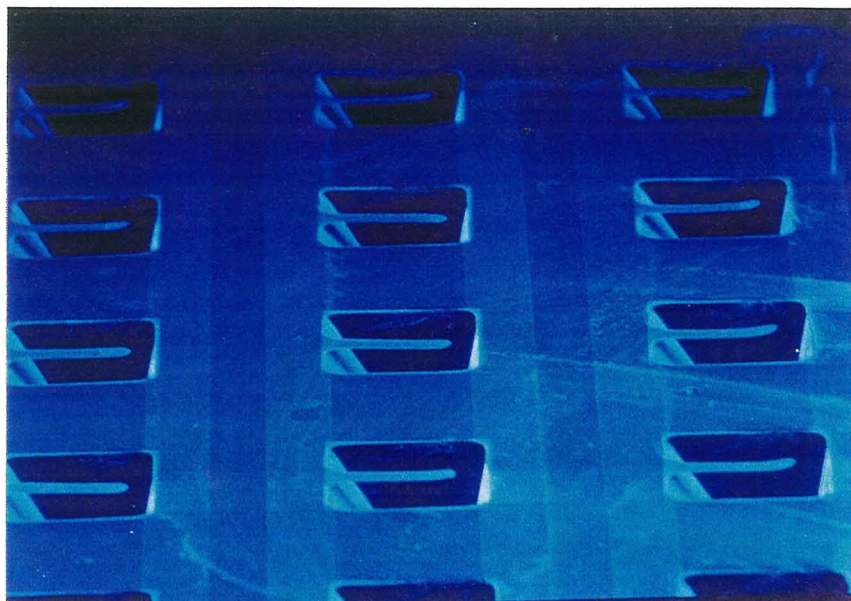
(a)
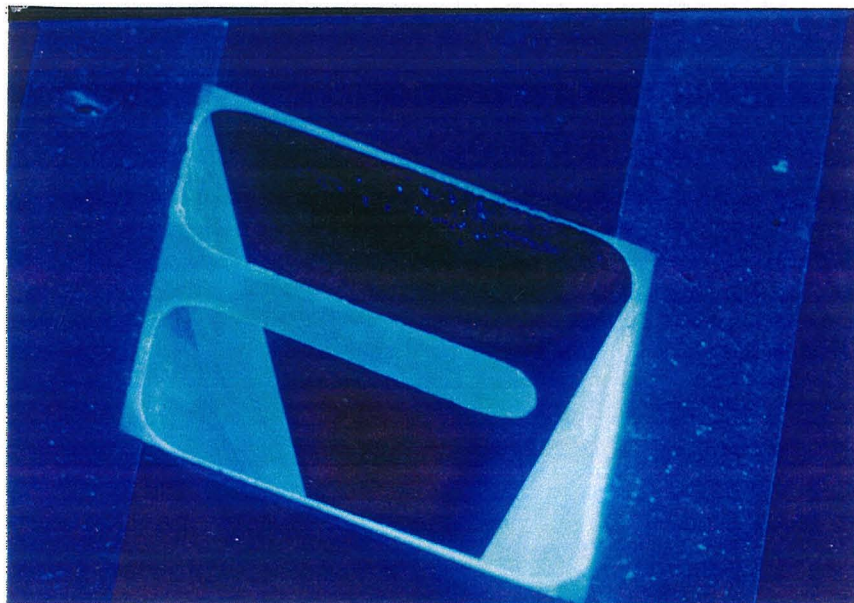
(b)

Figure 3.39 (a) An SEM picture of an array of cantilever-beams suspended in etched silicon cavities; and (b) an SEM picture of a cantilever-beam suspended in an etched silicon cavity. The cantilever beam is a piece of 1-μm thick SiO_xN_y thin-film. A thin (150$\overset{\circ}{A}$) layer of gold is evaporated on the surface for taking SEM pictures. The width of the beam is 160 μm and the length is 800 μm.

shows (a) an SEM picture of an array of cantilever-beams suspended in etched silicon cavities and (b) an SEM picture of a cantilever-beam suspended in an etched silicon cavity. The cantilever-beam is a piece of 1-μm thick SiO_xN_y thin-film. The EDP etching time is 11 hours and, after etching, these SiO_xN_y films stand freely on the edge of the windows like diving boards without any support. Later a thin (150$\overset{\circ}{A}$) layer of gold is evaporated on the surface for taking SEM pictures. The width of the beam is 160 μm and the length is 800 μm. Most of the beams stay flat and several of them bend upward. Due to the highly-reflective surface of the highly-doped silicon, the rounded corners on the tips are caused by overdeveloping AZ1350J photoresist which defines the etching patterns. These diving-board beams are surprisingly robust and survive from long-period hot silicon-etching, water cleaning, compressed-air drying, and travelling between Caltech and NASA-JPL where the SEM pictures were taken.

Figure 3.40 shows a top-view optical picture of another cantilever-beam array. The width of the SiO_xN_y-beams is 200 μm and the length is 900 μm. The front opening of the silicon cavity is 1 mm×1 mm. The silicon wafer with a thickness of 300 μm is etched through, so the back windows are visible underneath the beams. The etching pattern is defined by AZ5214 photoresist which has no exposure problems on highly-reflective surfaces, so the corners of the diving boards are not rounded.

These arrays show that the stress-free high-strength SiO_xN_y-films can provide a good foundation for constructing microswitches.

3.7.4 MICROSWITCHES

Figure 3.41 shows an array of microswitches fabricated using 1-μm thick SiO_xN_y thin-film on $\langle 100 \rangle$ silicon. It is a 5×5 array and 21 out of 25 microswitches are made successfully. One of the bad switches is destroyed by tweezer and the plated bridges on the rest of three are stripped off due to underdeveloped photoresist layers on the plating bases.
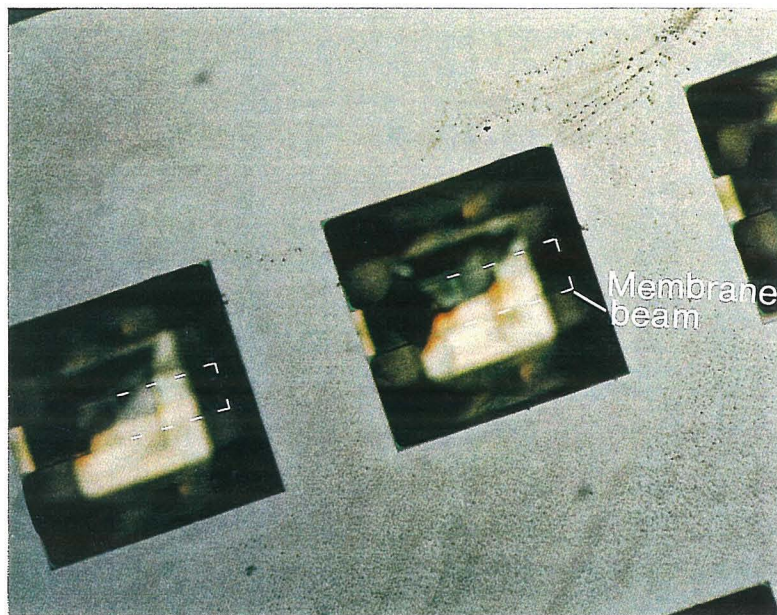
Figure 3.40 A top view of cantilever-beams suspended in etched silicon cavities. This picture is taken using an optical microscope. The cantilever beam is a 1-μm thick SiO_xN_y thin-film. The width of the beam is $200\,\mu$m and the length is $900\,\mu$m. The front opening of the silicon cavity is $1\,mm\times1\,mm$. The silicon wafer with a thickness of $300\,\mu$m is etched through and the back windows are visible.
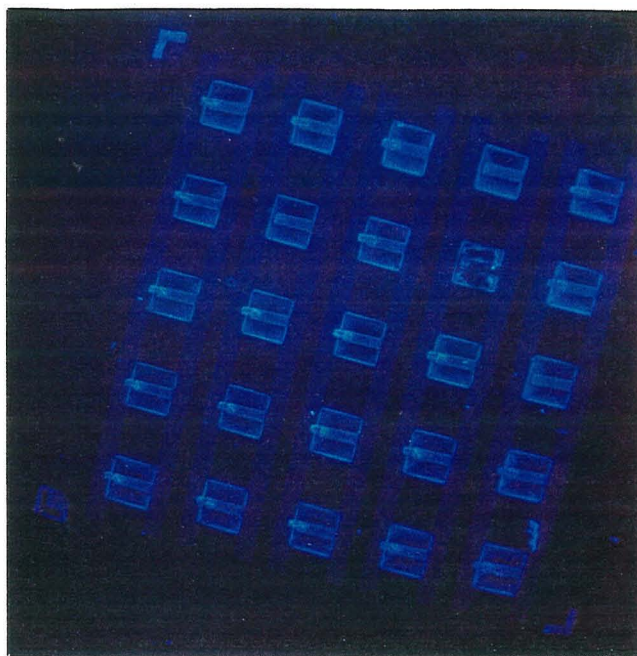

Figure 3.41 An array of microswitches fabricated using 1-mum thick SiO_xN_y thin-film on $\langle 100 \rangle$

Figure 3.42 shows (a) one microswitch and (b) the gap between the contacts. The SiO_2-pad to prevent a DC current path is not fabricated in this switch for testing reasons. The cantilever beam is based on 1-μm thick SiO_xN_y-film and has a width of 100 μm and a length of 440 μm. The total area of the bridge-structure is a 60 μm $\times$ 120 μm. The gap between the contacts is 1 μm which is the height of the photoresist sacrificial-layer. The thickness of the plated gold is 3 μm.

The switch is tested by applying a bias between two electrodes and measuring the resistance across the switch. A minimum voltage of 25 V is required to close the switches at 20° C. When the switches are heated by a heat-gun on the front, they close with less voltage or even without applying a bias. This is caused by the differences in thermal coefficients of expansion between SiO_xN_y film and the Cr-Au metallization. It indicates that the microswitches can also be used as a temperature sensor.

3.7.5 RHOMBIC WAVEGUIDES

Etching $\langle 110 \rangle$ silicon using KOH solution to form a structure with vertical sidewalls have been demonstrated by Bean [26] in 1978. The height of the sidewalls is 80 μm and the misalignment between the protection mask and the crystal planes causes undercutting and makes the sidewalls tilted in deeper etching. The problem was solved by McGrath and Tai [47] who demonstrated micromachined rectangular waveguides on $\langle 110 \rangle$ silicon using the same etching techniques. The height of the etched sidewalls is 1.28 cm.

The misalignment problem is due to the errors of the alignment edges (which indicate the $\langle 111 \rangle$ directions) on the silicon wafers, provided by the wafer manufactures, This misalignment problem was also observed in [48]. These alignment edges usually have errors of several degrees from the exact crystal planes. Figure 3.43 (a) shows the etching result of rhombic waveguides on $\langle 110 \rangle$ silicon using the alignment edges on the wafer. The etching depth is 400 μm. The sidewalls are obviously tilted.
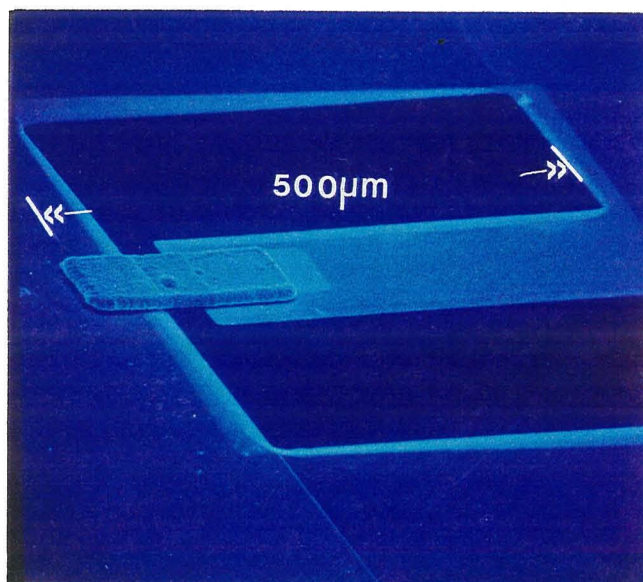
(a)
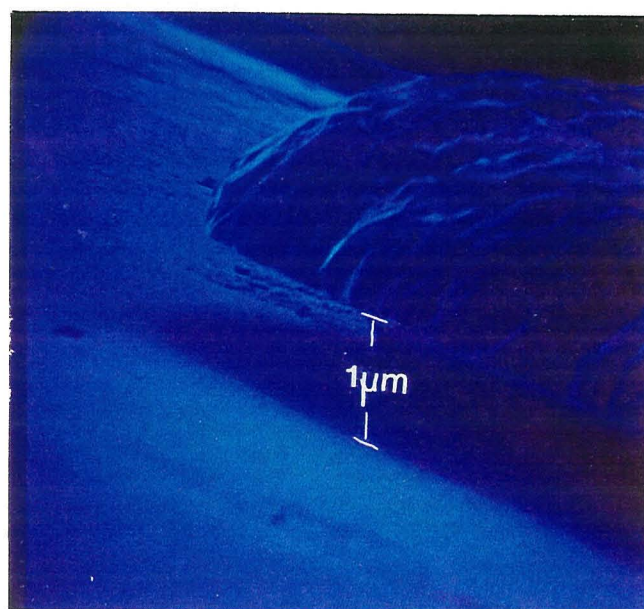
(b)

Figure 3.42 (a) One microswitch and (b) the gap between the contacts.

To overcome this problem but not to purchase expensive custom-made silicon wafers, we used a simple pre-etching alignment technique. A mask is made with patterns of radial straight-lines spaced with an angle of 0.2° between lines. Photoresist is applied on the entire wafer. In an unwanted area on the wafer, the alignment-edge is aligned with one of the straight line and the resist is exposed. Then SiO_xN_y is etched to define the radial-straight-line pattern. Then the unwanted part of the silicon wafer is dumped into KOH solution to etch these lines. After etching, most of the straight lines will show undercuts except the one aligned with the exact $\langle 111 \rangle$ planes. Then we use this line as an alignment mark to define the rhombic patterns. Figure 3.43 (b) shows the result using this technique. The etched depth is about 400 μm and the sidewalls are not tilted.

3.8 MEASUREMENTS

To demonstrate the feasibility of binary phase-shifts utilizing two states of microswitches, several meshes on etched silicon wafers with different metal patterns on membranes imitating different switch-configurations have been fabricated for measurements. The tests are based on the designs for 44-GHz beam-steering grids. Highly-doped $\langle 100 \rangle$ silicon wafers with an average thickness of 310 μm are used to fabricate rectangular windows with equilateral-triangular-lattice arrangements, as shown in Figure 3.24, using EDP etchant. The anisotropic etching creates pyramid-shaped sidewalls in the etched windows. However, according to the simulations, the reflection losses could be minimized with proper spacing parameters.

The silicon is etched through but with SiO_xN_y-membranes suspended on the openings of the windows. The suspended membranes are protected by photoresist. The front and back surfaces of the silicon wafers are deposited with evaporated gold. The sidewalls are also coated with gold by tilting the wafers in the evaporation chamber and evaporating gold on the sidewalls from an angle (45°). The photoresist layer then is lifted-off. The SiO_xN_y-membrane thickness
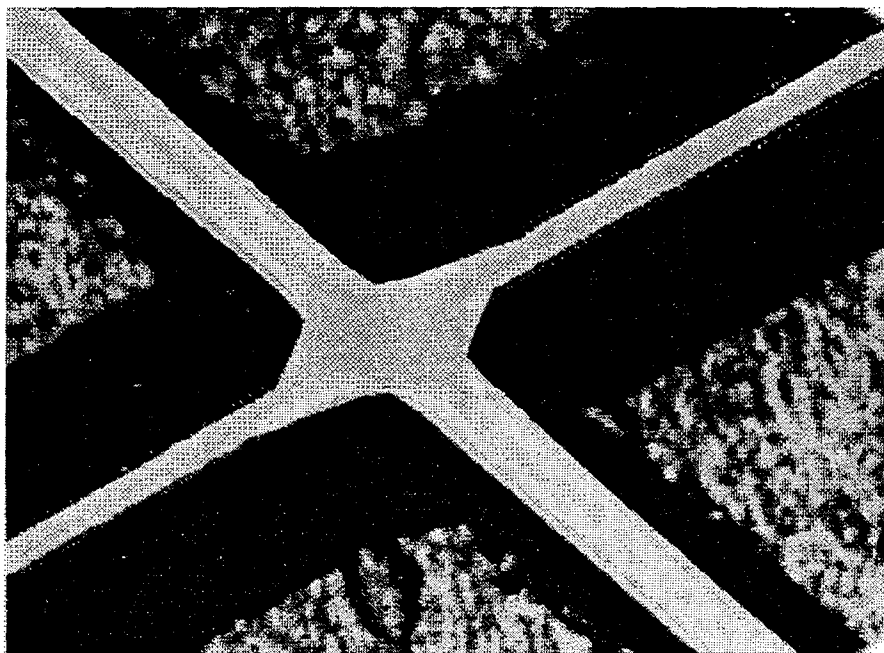
(a)
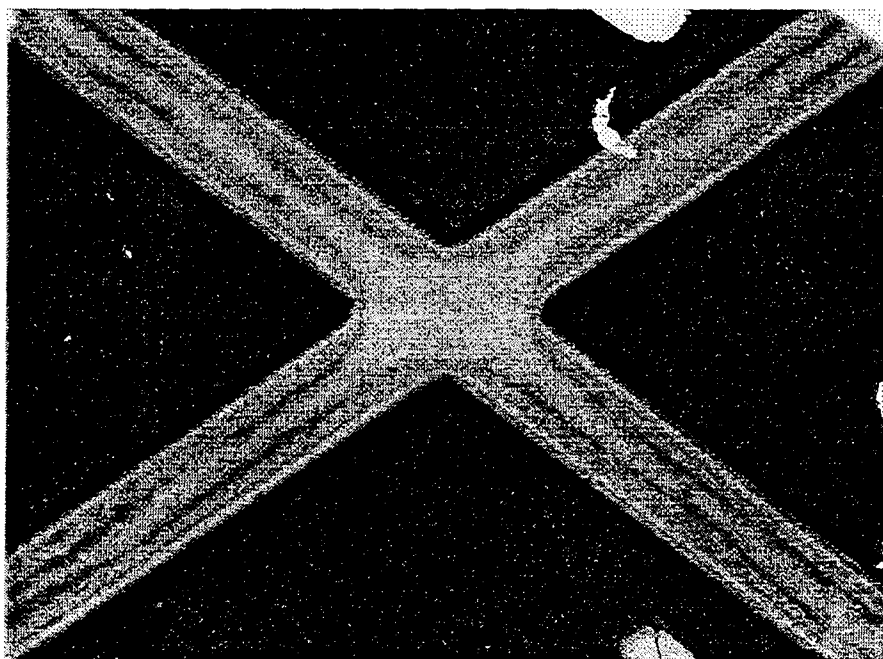
(b)

Figure 3.43 Pictures of etched rhombic waveguides on $\langle 110 \rangle$ silicon wafers (a) using the alignment edge provided by the wafer manufacture; and (b) using the pre-etching alignment technique. The etched depth is about $400\,\mu$m.

is 1 μm which is thin enough to be treated as transparent for 44-GHz signals. For imitating different switch configurations, photoresist is applied and exposed with different masks. Then gold is deposited on the wafer using electron-beam evaporation and lifted-off to form the desired metal patterns on the membranes.

3.8.1 RESONANT FREQUENCIES

The experimental arrangement is shown in Figure 3.44 to measure the transmission. For measuring resonances, reflection measurements are usually used, however, network analyzers with proper operating frequencies are not available at the time, we used transmission measurements instead. Hewlett-Packard millimeter-wave source modules *HP83555A* (35-50 GHz) and *HP83557* (50-75 GHz) with a synthesizer *HP 83620A* are used for sources. Preselected mixers *HP11974Q* (35-50 GHz) and *HP11974V* (50-75 GHz) are used with a spectrum analyzer *HP8563A* for receivers. The grids are placed between the transmitting and receiving horns with absorbers around. Absorbers are also placed around the
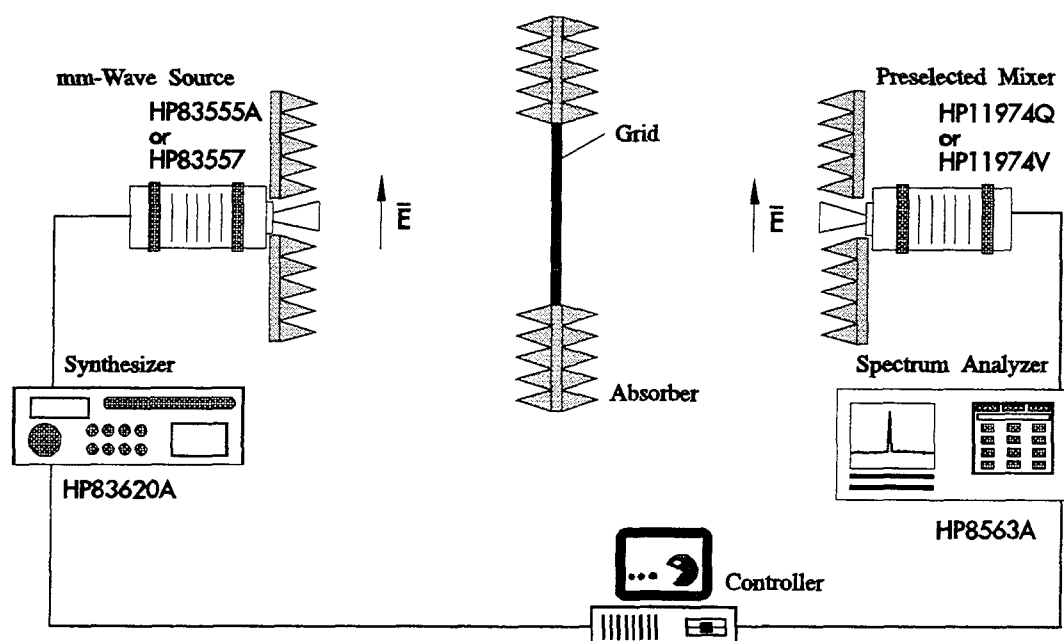

Fig. 3.44 Measurement arrangement.

horns in order to reduce the interferences. The transmission curves are measured as calibration standards without the existence of the grids.

A rectangular-window array without capacitive or inductive metal patterns on the membranes, as shown in Figure 3.24, is first measured to verify the resonance. Calculated and measured transmittances are shown in Figure 3.45. The ripples on the transmission curves come from the interferences between the grid and the receiving horn. The measured transmittance with ripples reaches 0 dB at 44 GHz. Using curve-fitting to smooth the ripples, the measured total-loss is found to be 0.08 dB at 44 GHz. The calculated loss is 4.3×10^{-4} dB. The transmission curve indicates the resonant frequency is about 44 GHz.

Capacitive metal patterns are applied on the membrane windows, as shown in Figure 3.29. The gap between the horizontal strips is 1.11 mm. Adding a shunt capacitance to the resonant impedance, as shown in Figure 3.30, shifts the resonant frequency to 37 GHz. Figure 3.46 shows the calculated and measured
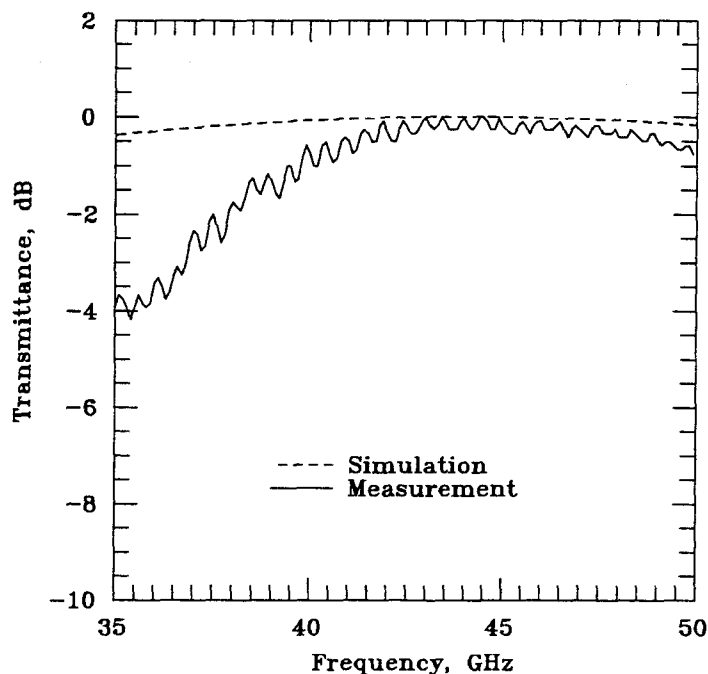
Fig. 3.45 Calculated and measured transmittances of a rectangular-window array without capacitive or inductive metal patterns on the membranes. The structure is shown in Figure 3.24.
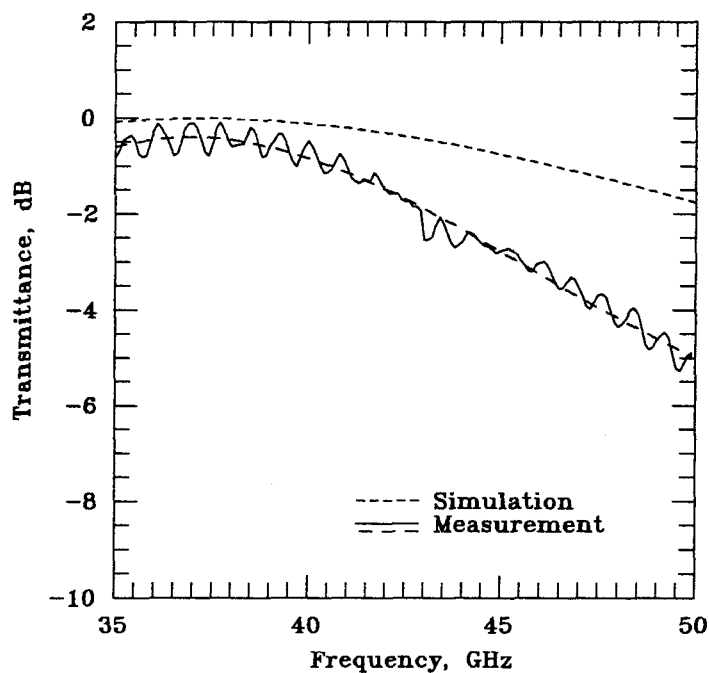
Fig. 3.46 Calculated and measured transmittances of a rectangular-window array with capacitive metal patterns, as shown in Figure 3.29, on the membranes for imitating open switches.
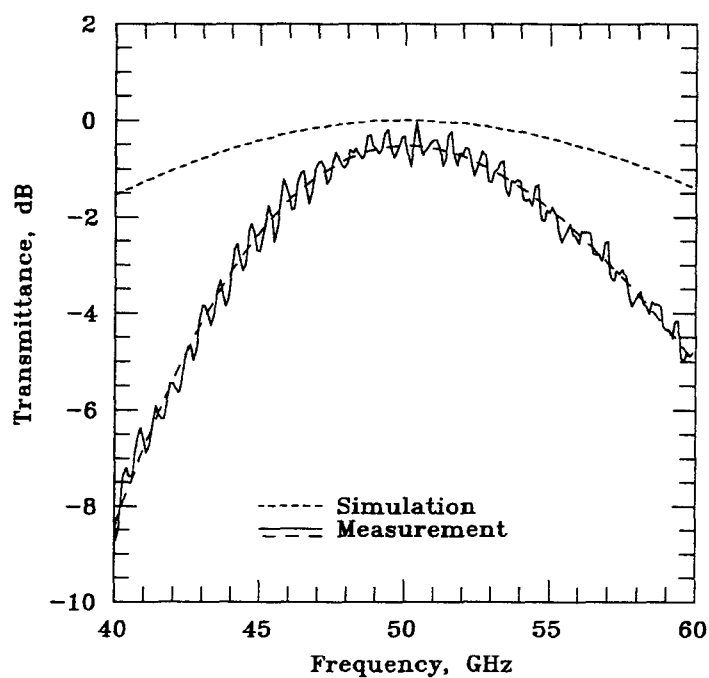

Fig. 3.47 Calculated and measured transmittances of a rectangular-window array with inductive metal patterns, as shown in Figure 3.31, on the membranes for imitating closed switches.

transmittances. The double-dashed line shows a fitting-curve without ripples. The measured total-loss is 0.4 dB at 37 GHz and the calculated one is 0.01 dB.

Inductive metal patterns are applied on the membrane windows for imitating closed switches. The structure is shown in Figure 3.31. The gap between the horizontal strips is 1.11 mm. The vertical strip has a width of 20 μm and a length of 1.94 mm. In the equivalent circuit, a shunt inductive reactance of $+j0.658Z_0$ is added to the impedance of the open-switch configuration by the vertical metal-strip which shifts the resonant frequency to 50 GHz, as shown in Figure 3.32. Figure 3.47 shows the calculated and measured transmittances. The measured total-loss is 0.52 dB at 50 GHz and the Q-factor is also shown greater than that of capacitive configuration, as expected.

3.8.2 BEAM-STEERING

Beam-steering is measured by moving the preselected-mixer on a fixed-distance arc with the grid in the apex of the arc. The length of the arc is 1.5 m to make sure that the measured antenna pattern is in the far-field region. Transmission and the far-field patterns are first measured without the grid between the source and the mixer as calibration standards.

The grid is configured as a "two point-source phased array", with capacitive patterns in one half and inductive patterns in the other half. The capacitive reactance and the inductive reactance will provide $-20.8°$ and $+20.8°$ phase
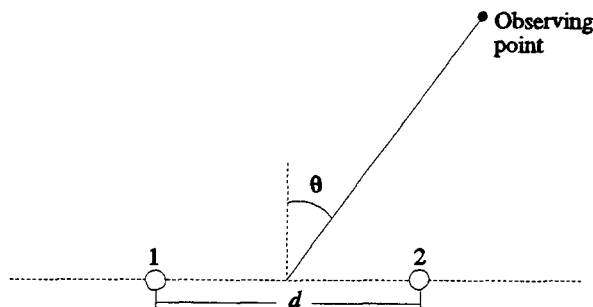

Fig. 3.48 A two point-source phased array.

shifts, respectively, relative to the meshes without any reactive patterns. The analogy of this measurement is shown in Figure 3.48. These two point-sources have unequal amplitudes and arbitrary phase differences. Assuming the point 1 has an electric field amplitude of unity in the far-field range and the point 2 has an amplitude of a and $0 \leq a \leq 1$. The point-sources have a phase difference of δ, then the total field in the same distance is given by

$$E = \sqrt{(1 + a\cos\psi)^2 + (a\sin\psi)^2} \ \angle \tan^{-1}\left[a\sin\frac{\psi}{1 + a\cos\psi}\right] \qquad (3.11)$$

and

$$\psi = \frac{2\pi d}{\lambda}\sin\theta + \delta \qquad (3.12)$$

where θ is the propagation direction, d is the effective distance between these two sources, and the phase angle ($\angle$) is referred to one of the sources. By measuring the E-plane far-field pattern, the relative phase-shifts can be determined.
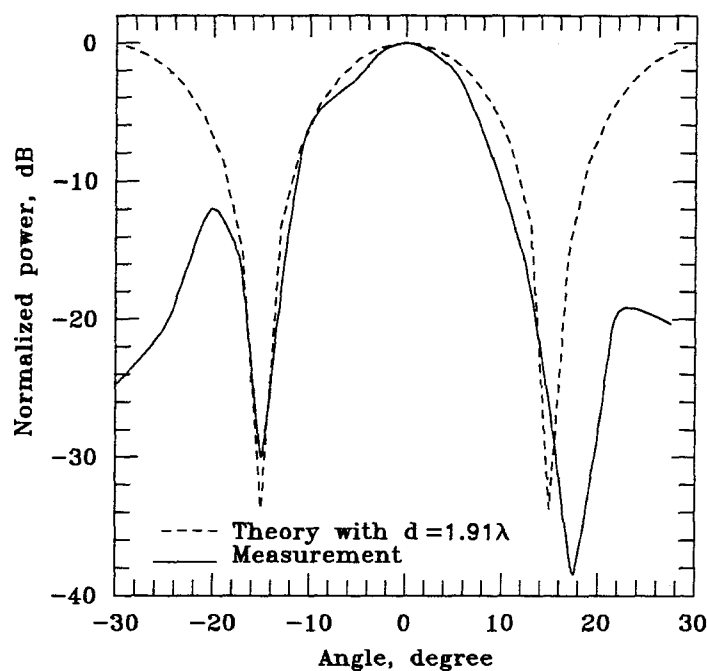

Fig. 3.49 Measured E-plane far-field pattern and theoretical E-plane pattern from two phased-array elements with equal amplitudes and $0°$ phase difference. By comparing these two patterns, we can decide the effective distance, d.

Due to the equilateral-triangular-lattice arrangement of the rectangular pyramid-sidewall windows in the grid, the effective distance between the two phased-array elements will not be the physical separation of the two halves of the reactive metal-patterns. To decide the effective distance, d, the far-field pattern is first measured using a grid with only capacitive metal patterns on all the membranes. This configuration is imitating a grid with all the microswitches opened.

Figure 3.49 shows the measured E-plane far-field pattern and the theoretical pattern calculated from two phased-array elements with equal amplitudes, $a = 1$, and $0°$ phase difference. By comparing these two patterns, the effective distance, d, is found to be 1.91λ.

One layer of beam-steering grid is used to measured the steering angles and
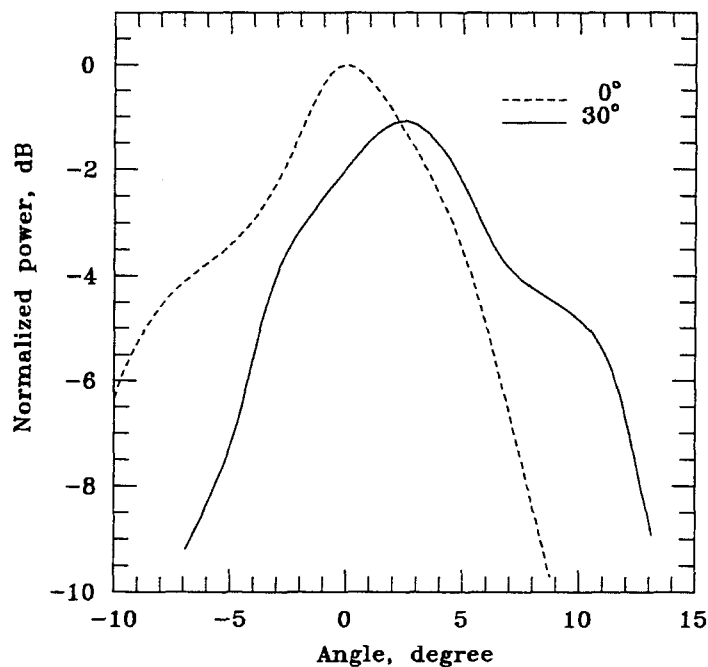

Fig. 3.50 Measured E-plane patterns. The dashed line indicates the grid with only capacitive metal-patterns on the membranes, which the phase difference is $0°$ in the two phased-array elements. The solid line indicates the grid with one half of inductive patterns and the other half of capacitive patterns, which has a $30°$ phase difference decided by the measured steering angle.

phase shifts. Figure 3.50 shows the measured E-plane pattern. The dashed line indicates the grid with only capacitive metal patterns, where the phase difference is 0° in the model of two phased-array elements. The solid line indicates the grid with one half of inductive patterns and the other half of capacitive patterns. The measured steering angle is 2.5° with a loss of 1.08 dB at 44 GHz. This indicates that the phase shift is +30° when the reactance is changed from capacitive to inductive by closing the switch. The estimated phase shift and loss are 41.6° and 0.59 dB, respectively, which should result in a 3.3° steering.

Two layers, which have the same metal patterns - one half of inductive patterns and the other half of capacitive patterns, are stacked together for more phase shifts. These two layers are mounted on a stage with adjustable spacings by a micrometer. The spacing is adjusted to reach a minimum loss. From a
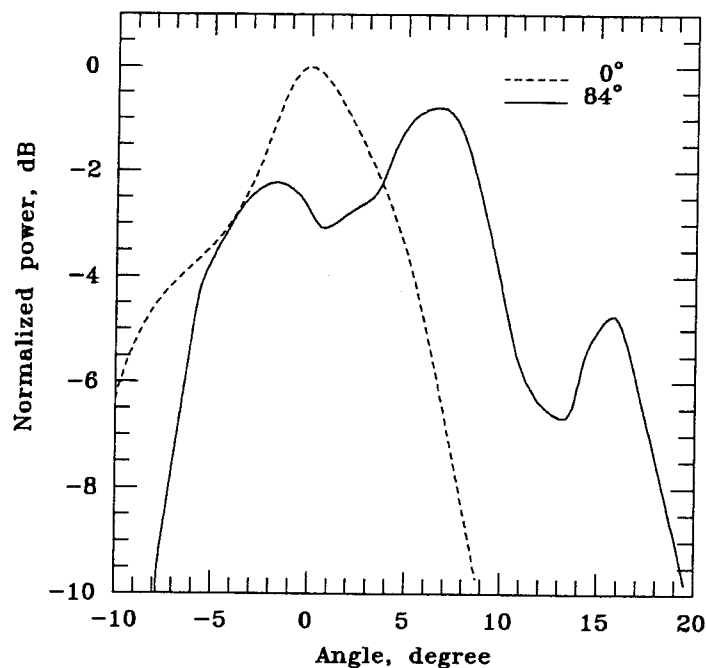
Fig. 3.51 Measured E-plane patterns. The dashed line indicates the 1-layer grid with only capacitive metal patterns, which the phase difference is 0° in the two phased-array elements. The solid line indicates the 2-layer grid with one half of inductive patterns and the other half of capacitive patterns on both layers. The phase difference is 84° decided from the steering angle. The distance between two layers is 1.7 mm, which is an electric length of 90° at 44 GHz.

simple transmission-line model, the minimum theoretical loss should be 0.37 dB with an electrical length of 90°, which will result in a phase shift of 93.6° and a steering angle of 7.8°. Figure 3.51 shows the measured results. The measured loss is 0.8 dB with a steering angle of 7° which indicates a phase shift of 84°. The beam width and the sidelobes of this 2-layer grid are greater than those of the 1-layer grid, possibly due to the multiple reflections, from the metallization on the edges of wafer, between two layers.

A bigger angle of beam steering can be achieved by stacking more layers to allow more phase shifts. The losses can be minimized by adjusting the electrical lengths between layers.

3.9 CONCLUSION

The purpose of this work is to demonstrate the feasibility of discrete beam-steering using microswitch arrays on silicon wafers. Design principles for sub-millimeter and millimeter wavelengths have been shown step-by-step. These two designs include practical considerations of using $\langle 110 \rangle$ and $\langle 100 \rangle$ orientation silicon wafers with anisotropic etchant KOH and EDP solutions, respectively. Because of smaller wavelengths, submillimeter-wave beam-steering grids should have TE_{10}-wave guided in etched vertical-wall rhombic waveguides with micro-switches inside to provide the required shunt reactances for phase-shifting. The dimensions and spacings of rhombic waveguides in the grids have been calculated to minimize the losses. The single-mode rhombic waveguides with inside-angles of 70.6° and 109.4° are also characterized. By changing the settings of micro-switches in different layers, different phase-shifts can be achieved. With a stacked 10-layer structure, a phase-shift resolution of 22.5° over 360° with 4-bit control should be possible. For a 240 GHz-design, calculations predict that the maximum phase error is 5° and the maximum loss is 1.58 dB including reflection loss and RF conduction loss which is calculated by assuming a RF series-resistance of 2 Ω on each switch.

For longer wavelengths, thin $\langle 100 \rangle$ silicon wafers are used for supporting the microswitches and free space between layers is used for providing the proper electrical lengths. The microswitches are suspended on the openings of etched rectangular pyramid-sidewall windows which are arranged in an equilateral-triangular-lattice structure. By adjusting the dimensions and spacings, the reflection losses can be minimized, even with the existence of pyramidal sidewalls. A 10-layer system with proper spacers can provide phase-shifts with a resolution of 22.5° over 360°, controlled by a 4-bit signal. For a 44 GHz-design, calculations predict that the maximum phase error is 4.9° and the maximum loss is 2.42 dB including reflection loss and RF conduction loss which is also calculated by assuming a RF series resistance of $2\,\Omega$ on each switch.

Micromechanical SiO_xN_y-membrane switches are fabricated on $\langle 100 \rangle$ orientation silicon wafers to demonstrate the feasibility of fabricating long (longer than $500\,\mu m$) electrostatically-controlled binary switches on silicon in order to provide the required shunt reactances. Rhombic waveguide arrays are also made by using $\langle 110 \rangle$ orientation silicon wafers and anisotropic etching techniques to show that it is feasible to fabricate vertical-wall waveguides on silicon in order to stack more layers together for more phase shifts.

Measurements are performed for the 44-GHz designs with different metal patterns fabricated on the SiO_xN_y-membranes suspended over etched windows on silicon for imitating open or closed switches. Resonant frequency measurements verify the reactances added by the capacitive and inductive patterns. Beam-steering measurements demonstrated a 7° beam-steering by a 2-layer grid with a minimum loss of 0.8 dB. A bigger angle of beam steering can be achieved by stacking more layers to allow more phase shifts. The losses can be minimized by adjusting the electrical lengths between layers.

3.10 FUTURE WORK

Without doubt, the next step of this work is to integrate the microswitches

into the beam-steering grids since the fabrications of microswitches, the etching of vertical-wall rhombic waveguides on silicon, and the principles of beam-steering have been demonstrated. The operation speeds and voltages of microswitches, which are strongly influenced by the stress and quality of the membranes, would be important issues to study [49-51]. Several research groups including Lucas NovaSensor [52], Texas Instruments Inc. [53], UC Berkeley [54], Tokyo University [55], Stanford University [56] and Rockwell Science Center [57] have shown interest and achievements on this topic. Goldsmith *et al.* [53] demonstrated a different configuration of membrane-switch on a discrete time-delay phase-shifter at 8-12 GHz, which is supported by two posts in the ends of the membrane and has a 30-50 V operation voltage and a series resistance of 1.5 Ω. This switch configuration could be a possible candidate for beam-steering applications.

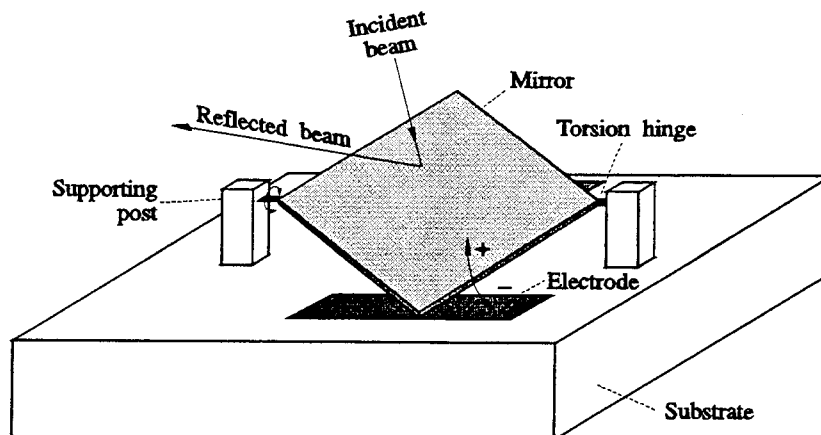With the incredibly fast-launching micromachining technologies and mar-

Fig. 3.51 Micro-mirror on silicon [60]. The height of posts and the lengths of hinges are exaggerated to show the idea. The mirror elements can be highly-integrated to cover the entire reflection surface with very small gaps between adjacent mirrors.

† The name "micro-mirror" is used by two different kinds of optical reflection modulators. Besides the one mentioned in this chapter, the other one is basically a device with a vertical-wall, which is fabricated by etching silicon, coated with metal for the use of reflecting light from a laser diode. There is no motion control in those devices.

kets, the combining of quasi-optical techniques and micromachinery will lead to a new direction of researches. One impressive achievement should be mentioned is the "micro-mirror"[†] array on silicon chips [58,60]. Hornbeck [59] at Texas Instruments Inc. invented the digital micro-mirror devices (DMDs) in 1987 using electrostatically controlled reflection membrane-mirrors as light modulators. These optomechanical devices have been proposed to be used on a thin planar display which should outperform cathode-ray tubes in computer monitors and high-definition televisions [61]. Figure 3.51 shows the idea. The micro-mirror is suspended above the surface by two supporting posts and the torsion hinges. The mirror tilts into the ON- or OFF-state by electrostatic forces which are changed by the bias. The size of the demonstrated micro-mirror is $16\,\mu$m on each side and it is coated by aluminum-alloy. The electrostatic forces tilt the mirror by $\pm10°$ with a voltage of 5 V [60] and reflect the incident light onto a projection lens.

Like at optical wavelengths, the micro-mirror array can be used as a quasi-optical reflection beam-steerer at millimeter and submillimeter wavelengths. Instead of changing the reactances of the propagating waves, the beam direction can be directly changed by the movement of mirrors. This device should also provide advantages of low loss at high frequencies, because of reflections from pure metal surfaces, and simple control circuits, which can be controlled by a CMOS static RAM with a low-power battery like the one demonstrated in [60].

3.11 Acknowledgements

gratitude to Dr. Jason Yao and Dr. Aiden Higgins at Rockwell Science Center, Thousand Oaks, for valuable discussions. I also thank Dr. Phil Stimson (now at DSTO, Australia) and Mark Natzic at JPL for assistance with taking SEM pictures. I appreciate Dr. Neville Luhmann and his students, Dr. Lance Sjogren (now at TRW) and Dr. Xiaohui Qin (now at Hughes), at University of California, Davis, for sharing with me their valuable experiences on beam controllers.

REFERENCES

[1] R.J. Mailloux, "Phased Array Theory and Technology," *Proceedings of IEEE*, Vol. 70, No. 3, pp. 246-291, March 1982.

[2] R.J. Mailloux, "Phased Array Architecture for Millimeter Wave Active Arrays," *Microwave Journal*, Vol. 29, No. 7, pp. 117, July 1986.

[3] D.M. Pozar and D.H. Schaubert, "Comparison of Architectures for Monolithic Pased Array Antennas," *Microwave Journal*, Vol. 29, No. 3, pp. 93-104, March 1986.

[4] K.C. Lim, J.D. Margerum and A.M. Lackner, "Liquid Crystal Millimeter Wave Electronic Phase Shifter," *Applied Physics Letters*, Vol. 62, pp. 1065-1067, No. 10, March 1993.

[5] G. Subramanyam, V.J. Kapoor and K.B. Bhasin, "A Hybrid Phase Shifter Circuit Based on TlCaBaCuO Superconducting Thin Films," *IEEE Trans. on Microwave Theory and Tech.*, Vol. MTT-43, No. 3, pp. 566-572, March 1995.

[6] M. Tsutsumi and A. Alphones, "Optical Control of Millimeter Waves in the Semiconductor Waveguide," *IEICE Trans. Electron.*, Vol. E76-C, No. 2, pp. 175-182, Feb. 1993.

[7] K.B. Bhasin, P.C. Claspy, M.A. Richard, R.R. Romanofsky, M. Bendett, G. Gustafson and W. Waters, "Control of a GaAs Monolithic Ka-Band Phase Shifter Using a High-Speed Optical Interconnect," *IEEE Trans. on Microwave Theory and Tech.*, Vol. MTT-38, No. 5, pp. 686-688, May 1990.

[8] R.A. La Rue, R.E. Colbeth, G.A. Davis, C. Yuen, C. Webb, C. Shih and R.E. Weiss, "Performance of Modulation-Doped Charge-Coupled Devices (MD-CCD's) in the Microwave and Millimeter-Wave Bands," *IEEE Trans. on Electron Devices*, Vol. 41, No. 1, pp. 10-18, Jan. 1994.

[9] J.R. James, G.D. Evans and A. Fray, "Beam Scanning Microstrip Arrays Using Diodes," *IEE Proceedings-H*, Vol. 140, No. 1, pp. 43-51, Feb. 1993.

[10] P. Liao and R.A. York, "A New Phase-Shifterless Beam-Scanning Technique Using Arrays of Coupled Oscillators," *IEEE Trans. on Microwave Theory and Tech.*, Vol. MTT-41, No. 10, pp. 1810-1815, Oct. 1993.

[11] S.W. Lee and T.T. Fong, "Electromagnetic Wave Scattering from an Active Corrugated Structure," *Journal of Applied Physics*, Vol. 33, pp. 388-396, Feb. 1972.

[12] N.G. Alexopoulos, P.L.E. Uslenghi, and G.A. Tadler, "Antenna Beam Scanning by Active Impedance Loading," *IEEE Trans. Antennas Propagat.*, Vol. AP-22, pp. 722-723, Sept. 1974.

[13] C. Chekroun, D. Herrick, Y. Michel, R. Pauchard, and P. Vidal, "Radant: New Method of Electronic Scanning," *Microwave Journal*, pp. 45-53, Feb. 1981.

[14] D.B. Rutledge and S.E. Schwarz, "Planar Mutlimode Detector Arrays for Infrared and Millimeter-wave Applications," *IEEE L. Quantum Electron.*, Vol. QE-17, pp. 407–414, 1981.

[15] W. Lam, C. Jou, H. Chen, K. Stolt, N. Luhmann, Jr., and D. Rutledge, "Millimeter-wave Diode-Grid Phase-Shifters," *IEEE Trans. on Microwave Theory and Techniques*, pp. 902–907, No. 5, May 1988.

[16] W.W. Lam, C.F. Jou, N.C. Luhmann, Jr. and D.B. Rutledge, "Diode Grids for Electronic Beam Steering and Frequency Multiplication," *Int. J. Infrared and Millimeter Waves*, Vol. 7, pp. 27–41, 1986.

[17] W.W. Lam, "Millimeter-wave Monolithic Schottky Diode-Grid Phase-Shifters," *Ph.D. Dissertation*, California Institute of Technology, 1987.

[18] L.B. Sjogren, H.L. Liu, X.H. Qin, C.W. Domier, N.C. Luhmann, Jr., "Phased Array Operation of a Diode Grid Impedance Surface," *IEEE Trans. on Microwave Theory and Techniques*, Vol. MTT-42, No. 4, pp. 565-572, April 1994.

[19] Lance B. Sjogren, "A Multi-Function Millimeter-Wave Schottky Diode Array Electronic Beam Controller," *Ph.D. Dissertation*, University of California, Los Angeles, 1992.

[20] X.H. Qin, W.M. Zhang, C.W. Domier, N.C. Luhmann, Jr., W. Berk, S. Duncan and D.W. Tu, "Monolithic Millimeter-Wave Beam Control Array," *Digest of IEEE Microwave Theory and Techniques Symposium*, MTT-S95, WE3F-F4, pp. 1669-1672, 1995.

[21] Xiaohui Qin, "Monolithic Millimeter Wave Beam Control Array," *Ph.D. Dissertation*, University of California, Los Angeles, 1995.

[22] L.B. Sjogren, H.L. Liu, F. Wang, T. Liu, X.H. Qin, W. Wu, E. Chung, C.W. Domier, N.C. Luhmann, Jr., "A Monolithic Diode Array Millimeter-Wave Beam Transmittance Controller," *IEEE Trans. on Microwave Theory and Techniques*, Vol. MTT-41, No. 10, pp. 1782-1790, Oct. 1993.

[23] K.E. Petersen, "Micromechanical Membrane Switches on Silicon," *IBM J. Res. Develop.*, Vol. 23, pp. 376–385, No. 4, July 1979.

[24] K.E. Petersen, "Dynamic Micromechanics on Silicon: Techniques and Devices," *IEEE Trans. on Electron Devices*, Vol. ED-25, pp. 1241–1250, No. 10, Oct. 1978.

[25] K.E. Petersen, "Silicon as a Mechanical Material," *Proceedings of the IEEE*, pp. 420–457, No. 5, May 1982.

[26] K.E. Bean, "Anisotropic Etching of Silicon," *IEEE Trans. on Electron Devices*, Vol. ED-25, pp. 1185–1193, No. 10, Oct. 1978.

[27] L.D. Clark, Jr. and D.J. Edell, "KOH:H$_2$O Etching of (110) Si, (111) Si, and Ta: An Experimental Study," *IEEE TH0204-8*, 1987.

[28] P.L. Overfelt and C.S. Kennney, "Power-Handling Capability of the Rhombic Waveguide," *IEEE Trans. on Microwave Theory and Techniques*, Vol. MTT-38, No. 7, pp. 934-941, July 1990.

[29] P.A.A. Laura and L. Ercoli, "Comments on 'Power-Handling Capability of the Rhombic Waveguide'," *IEEE Trans. on Microwave Theory and Techniques*, Vol. MTT-40, No. 8, pp. 1733, Aug. 1992.

[30] L.E. Payne, "Inequalities for Eigenvalues of Membranes and Plates," *J. Rat. Mech. Anal.*, Vol. 4, pp. 517-529, 1955.

[31] C.E, Baum, "Some Features of Waveguide/Horn Design," *Sensor and Simulation Notes*, Vol. 314, Air Force Weapons Lab., Nov. 1988.

[32] *American Institute of Physics Handbook*, pp. 5-104 and 5-105, 3rd ed., McGraw-Hill Com., 1972.

[33] G.R. Huguenin, "Millimeter Wave Radar for Automobile Crash Avoidance Systems," *Proceedings of the International Conference on Millimeter and Submillimeter Waves and Applications*, SPIE Proceedings series, Vol. 2250, Jan. 1994.

[34] R. Tribe, I. Westwood and J. Langley, "MM-wave Radar for Advanced Intelligent Cruise Control Applications," *Proceedings of the International Conference on Millimeter and Submillimeter Waves and Applications*, SPIE Proceedings series, Vol. 2250, Jan. 1994.

[35] C.M. Liu, D.B. Rutledge and E.A. Sovero, "40 GHz Monolithic Grid Amplifier," *53rd Annual Device Research Conference*, Charlottesville, Virginia, June 1995.

[36] M.E. Motamedi, "Merging Microoptics with Micromechanics: Micro-Opto-Electro-Mechanical (MOEM) Devices," *Critical Reviews of Optical Science and Technology*, No. 49, pp. 302-328, SPIE, 1994.

[37] S. Wolf and R.N. Tauber, "Silicon Processing for the VLSI Era," Vol. 1, Lattice Press, 1987.

[38] W. Choi and J.G. Smits "A Method to Etch Undoped Silicon Cantilever Beams," *Journal of Microelectromechanical Systems*, Vol. 2, pp. 82–86, No. 2, June 1993.

[39] W.C. Tang, M.G. Lim and R.T. Howe, "Electrostatic Comb Drive Levitation and Control Method," *Journal of Microelectromechanical Systems*, Vol. 1, pp. 170–178, No. 4, Dec. 1992.

[40] J.A. van Raalte, "A New Schlieren Light Valve for Television Projection," *Applied Optics*, Vol. 9, pp. 2225, 1970.

[41] J. Guldberg, H.C. Nathanson, D.L. Balthis and A.S. Jensen, "An Aluminum/SiO_2 Silicon on Sapphire Light Valve Matrix for Projection Displays," *Applied Physics Letters*, Vol. 26, pp. 391, 1975.

[42] R.N. Thomas, J. Guldberg, H.C. Nathanson and P.R. Malmberg, "The Mirror Matrix Tube: A Novel Light Valve for Projection Displays," *IEEE Trans. on Electron Devices*, Vol. ED-22, pp. 765, 1975.

[43] K.E. Petersen and C.R. Guarnieri, "Young's Modulus Measurements of Thin Films using Micromechanics," *Journal of Applied Physics*, Vol. 50, pp. 6761, 1979.

[44] R.J. Jaccodine and W.A. Schlegel, "Measurement of Strains at $Si-SiO_2$ Interface," *Journal of Applied Physics*, Vol. 37, pp. 2429, 1966.

[45] C.W. Wilmsen, E.G. Thompson and G.H. Meissner, "Bulkling of Thermally Grown SiO_2 Thin Films," *IEEE Trans. on Electron Devices*, Vol. ED-19, pp. 122, 1972.

[46] K.K. Schuegraf, "Handbook of Thin-Film Deposition Processes and Techniques," *Noyes Publications*, New Jersey, 1988.

[47] W.R. McGrath, C. Walker, M. Yap and Y.C. Tai, "Silicon Micromachined Waveguides for Millimeter-Wave and Submillimeter-Wave Frequencies," *IEEE Microwave and Guided Wave Letters*, pp. 61–63, Vol. 3, No. 3, March 1993.

[48] R.H. Cornely and R.B. Marcus, "Formation of Silicon Micromirrors by Anisotropic Etching," *Sensors and Actuators, A*, Vol. 29, pp. 241-250, 1991.

[49] S.M. Hu, "Stress-related Problems in Silicon Technology," *Journal of Applied Physics*, 70(6), 15 Sept. 1991.

[50] H. Miura, H. Ohta and N. Okamoto, "Crystallization-induced Stress in Silicon Thin Films," *Applied Physics Letters*, 60(22), 1 June. 1992.

[51] S.M. Hu, "Stress from Isolation Trenches in Silicon Substrates," *Journal of Applied Physics*, 67(2), 15 Jan. 1990.

[52] J. Bryzek and K.E. Petersen, "Micromachines on the March," *IEEE Spectrum*, No. 5, pp. 20-31, May 1994.

[53] C. Goldsmith, T.-H. Lin, B. Powers, W.-R. Wu, and B. Norvell, "Micromechnical Membrane Switches for Microwave Applications," *Digest of the IEEE Microwave Theory and Tech. Sumposium 95*, Vol. MTT-S95, TU1D-6, pp. 91-94, 1995.

[54] W.C. Tang, M.G. Lim and R.T. Howe, "Electrostatic Comb Drive Levitation and Control Method," *Journal of Microelectro-mechanical Systems*, Vol. 1, No. 4, pp. 170-178, Dec. 1992.

[55] M. Ataka, A. Omodaka, N. Takeshima and H. Fujita, "Fabrication and Operation of Polyimide Bimorph Actuators for a Ciliary Motion System," *Journal of Microelectro-mechanical Systems*, Vol. 2, No. 4, pp. 146-150, Dec. 1994.

[56] C.W. Storment, D.A. Borkholer, V. Westerlind, J.W. Suh, N.I. Maluf and G.T.A. Kovacs, "Flexible, Dry-Released Process for Aluminum Electrostatic Actuators," *Journal of Microelectro-mechanical Systems*, Vol. 3, No. 3, pp. 90-96, Sept. 1994.

[57] Private communications.

[58] D.R. Collins, J.B. Sampsell, L.J. Hornbeck, J.M. Florence, P.A. Penz and M.T. Gately, "Deformable Mirror Device Spatial Light Modulators and Their Applicability to Optical Neural Networks," *Applied Optics*, Vol. 28, No. 22, pp. 4900-4907, 15 Nov. 1989.

[59] L.J. Hornbeck, "Deformable-Mirror Spatial Light Modulators," *Spatial Light Modulators and Applications III, SPIE Critical Reviews*, pp. 86, Vol. 1150, August 1989.

[60] J.M. Younse, "Mirrors on a Chip," *IEEE Spectrum*, No. 11, pp. 27-31, Nov. 1993.

[61] M.A. Mignardi, "Digital Micromirror Array for Projection TV," *Solid State Technology*, pp. 63-68, July 1994.

Chapter 4

Metal-Mesh Evanescent-Wave Couplers

Quasi-optical couplers provide functions such as amplitude modulations, beam switching and feedback elements to couple the required feedback to reach oscillation conditions for quasi-optical coherent power-combining. Fabry-Perot interferometers have been widely used as tunable couplers and filters at millimeter and submillimeter wavelengths. These couplers consist of two reflectors and make use of interference between propagating waves to change their coupling coefficient. The large and rapid change of the coupling coefficient with frequency results in a narrow bandwidth. We proposed a metal-mesh evanescent-wave coupler makes use of the coupling effect of evanescent waves to change the transmission. The evanescent waves are induced by an incident wave on the meshes, and decay quickly away from the mesh, normally less than $\lambda/20$ from the surface. Therefore, in contrast to a Fabry-Perot interferometer, the coupling coefficient of the evanescent wave coupler can be significantly changed by small adjustments of spacing. In principle, this type of couplers should have wider bandwidth because the transmission properties of the couplers depend primarily on the mesh parameters.

This work is a joint effort between Dr. Jongsuck Bae and Dr. Koji Mizuno's group, where the couplers were fabricated and tested, at the Research Institute of Electrical Communication in Tohoku University, Sendai, Japan; and the MMIC group at CalTech.

Metal-mesh evanescent-wave couplers have been demonstrated as quasi-

optical amplitude-modulators at millimeter wavelengths. The organization of this chapter is in the following order:

Transmission properties of the inductive and capacitive couplers are first investigated including effective coupling distances, coupling effects and the resonant frequencies. The dependence of the resonant frequencies on the mesh parameters and the thickness of dielectric tuning plates is also studied. A model is presented to explain the relationship between the effective dielectric constant and the evanescent-wave coupling effect, which predicts the behavior of the metal-mesh evanescent-wave couplers. Design principles are also presented to reach maximum amplitude modulations considering the mesh parameters, resonant frequencies and the thickness of the tuning plates. In the end, an optical-controlled metal-mesh evanescent-wave coupler is also demonstrated.

4.1 MOTIVATION

This work serves two purposes: understanding the evanescent-wave coupling effect in order to develop an efficient electronic millimeter/submillimeter-wave amplitude modulator; and explaining some behaviors of slab-tuners and metal-mesh filters used in a quasi-optical grid-amplifier or grid-oscillator system, which are observed when the tuners are placed close to the grids. These behaviors and the discrepancies between measurements and theory can not be explained by a simple transmission-line model.

Construction of a complete quasi-optical system includes amplitude controllers for amplitude modulations and beam switching. The amplitude controllers can also be served as feedback elements to provide the required feedback to reach oscillation conditions for quasi-optical oscillators. Fabry-Perot interferometers have been widely used as tunable couplers and filters at millimeter and submillimeter wavelengths. These couplers consist of two reflectors and make use of interference between propagating waves to change their coupling coefficient. Consequently, the large and rapid change of the coupling coefficient with fre-

quency results in a narrow bandwidth [1]. Also the Fabry-Perot interferometers are mechanically operated which is not suitable for electronic modulations.

The diode grid, a periodic circuit loaded with diodes where the reactances can be varied by controlling the bias on diodes, has been demonstrated as a beam controller. Transmission controls over the range of 20% to 50% at 99 GHz and 20% to 70% at 165 GHz were demonstrated by Sjogren et al. [2,3] using a diode-grid with 8640 Schottky diodes. Qin et al. [4,5] also demonstrated a 24 dB ON/OFF ratio with a minimum transmission loss of 2.2 dB using a single diode-grid and a 42 dB ON/OFF ratio with a minimum transmission loss of 4 dB using two stacked layers at 60 GHz. Quasi-optical diode grids provide many advantages, as mentioned in Chapter 2, including eliminating waveguide losses and high-speed operations. However, the series resistances of the diode increase as the frequencies increase and cause serious losses at higher frequencies, especially at terahertz frequencies. Using passive elements instead of diodes or other active devices to provide amplitude modulations at submillimeter wavelengths is an alternative approach. We proposed a new metal-mesh coupler utilizing evanescent-wave coupling as a new quasi-optical component to overcome the tradeoff between bandwidth and coupling coefficient of the Fabry-Perot couplers and to reduce the transmission losses caused by the series resistances of diodes.

The second purpose of this work is to understand the behaviors of slab-tuners which are commonly used in a quasi-optical grid-amplifier or grid-oscillator system. In a grid-amplifier system, metal-strip polarizers are used to separate the input and output polarizations and dielectric slabs are used to provide independent tuning of the input and output circuits. In a grid-oscillator system, the metal-strip polarizer filters out the desired polarization and feedbacks the other polarization back into the oscillator. Dielectric-slab tuners are also used to match the impedances for delivering maximum output powers. The behaviors of these metal-strip polarizers and dielectric-slab tuners are well predicted by a simple

transmission-line model, however, past experiences show that discrepancies occur when they are placed close, for example, with a spacing less than a half wavelength, to the grids. For instant, De Lisio *et al.* [6] demonstrated a pHEMT grid-amplifier which has nulls in the output pattern, possibly caused by the input polarizer. The nulls disappear when the input polarizer is placed less than a half-wavelength from the grid surface, however, it also causes the peak gain to drop by 3 dB. This behavior can not be explained by the simple transmission-line equivalent-circuit which only considers the propagating mode. The evanescent-wave coupling effect, caused by the changes of the effective dielectric constant, provides a good explanation of this behavior.

In this chapter, mechanical tunable metal-mesh evanescent-wave couplers are first studied to understand the evanescent-wave coupling effect; the dependence of the coupling effects on the mesh parameters, the spacings, the thickness of tuning slab; and the relationships between the coupling effects and the resonant frequencies. A more accurate model then is presented to modify the transmission-line equivalent-circuit taking the evanescent-wave effects into consideration. Finally, we used the same model and design approaches to demonstrate a non-mechanical optical-controlled metal-mesh evanescent-wave coupler for amplitude modulations at millimeter wavelengths.

4.2 CONFIGURATION

The coupler consists of an inductive or a capacitive metal-mesh fabricated on a dielectric plate and a flat dielectric plate placed close to the surface of the mesh, as shown in Figure 4.1. We chose to fabricate the metal meshes on a quartz plate because of the low dielectric constant and low loss at millimeter wavelengths. Low-doped silicon wafer is chosen to be used as the movable dielectric plate because of the higher dielectric constant and low loss. A material with higher dielectric constant is favorable to achieve a bigger difference of dielectric constants between these two plates, such as GaAs, however, it should also satisfy the low-
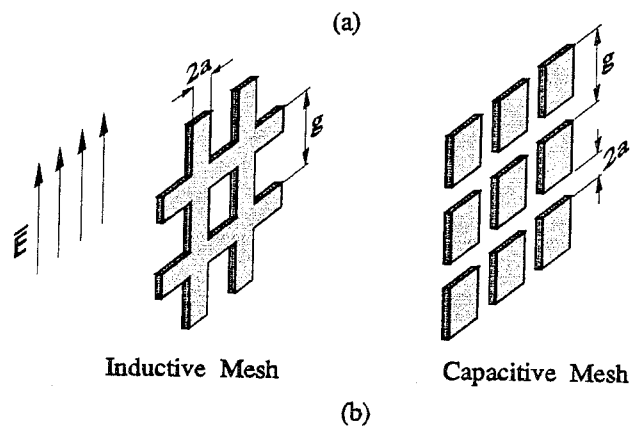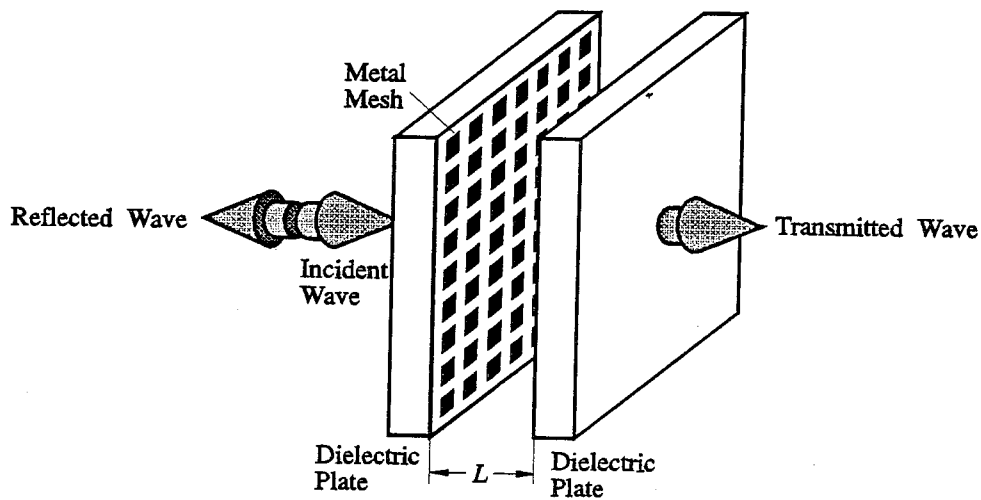
Fig. 4.1 (a) Configuration of a metal-mesh evanescent-wave coupler. (b) Capacitive meshes and inductive meshes.
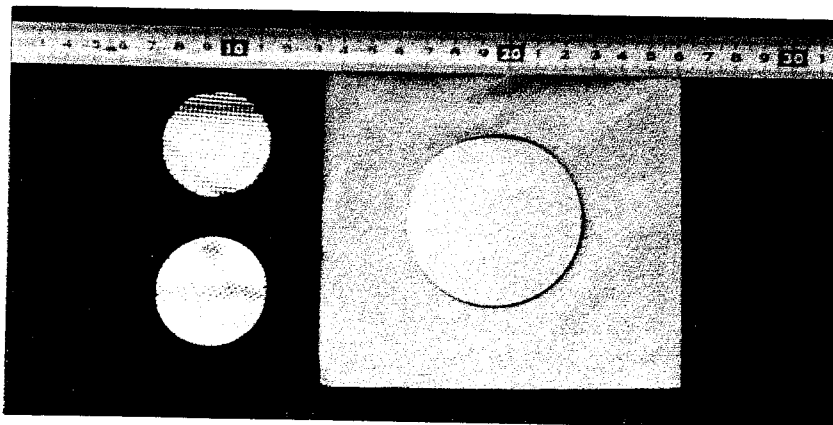

Fig. 4.2 A picture of the silicon plate (right) and the inductive (left, top) and capacitive (left, bottom) metal-mesh quartz plates.

loss requirement.

The metal-mesh evanescent-wave coupler makes use of the coupling effect of evanescent waves to change reflectance and transmittance. The evanescent waves are induced by an incident wave on the meshes, and decay quickly away from the meshes, normally less than $\lambda/20$ from the surface [7]. Therefore, in contrast to a Fabry-Perot interferometer, the coupling coefficient of the evanescent-wave coupler can be significantly changed by small adjustments of spacing, L, between the meshes and the dielectric plate. When the spacing is greater than a half-wavelength, the evanescent-wave coupling effect should vanish due to the strong attenuations of the evanescent waves, the couplers will behave like Fabry-Perot interferometers. In principle, this type of coupler can also have wider bandwidth because the transmission properties of the couplers depend primarily on the mesh parameters. For a vertically-polarized electric field, the transmission properties of an inductive coupler and a capacitive coupler mainly depend on the width of the vertical strips, $2a$, and the gap between the horizontal strips, $2a$, respectively, as well as the unit cell, g, as shown in Figure 4.1.

4.3 CALCULATIONS

The theoretical analysis of the couplers is done assuming an infinitely large periodic grid. The metal strips are assumed to be perfect conductors and have zero thickness. The dielectric materials are assumed to be lossless. To simplify the calculations, one-dimension strips are used. A uniform plane wave is assumed to be normally incident with the electric field polarized perpendicular to the strips for capacitive meshes or parallel to the strips for inductive meshes. The unit-cell waveguide method is used with electric walls on the top and bottom and magnetic walls on the sides to satisfy the boundary conditions for the TEM-wave incidence. Symmetry allows to further reduce the unit-cell waveguide into a quarter-piece waveguide with electric walls on the top and bottom and magnetic walls on the sides as shown in Figure 4.3.

A computer program based on the method of moments is used for simulations. This program is written by Michael De Lisio at Caltech. The calculation results are verified using Hewlett-Packard High Frequency Structure Simulator (*HFSS*), a finite-element electromagnetic-wave solver for 3-D passive structures.

The incident waves induce surface currents on the metal strips. These currents give rise to a reflected, or scattered, wave such that the tangential electric field vanishes on the conducting strips. The surface current distribution is determined using the method of moments [8]. The basis functions have a $\cos^2$ distribution, and the point-matching technique is employed. The Green's function used is a truncated summation of spatial harmonics. In our analysis, ten subdomains give reasonable convergence.

Once the current distribution has been determined, the induced EMF technique is used to calculate the embedding impedance of the metal meshes. This technique is very similar to the one used by Eisenhart and Khan [9] and is further developed by Weikle [10]. Then the embedding impedance is used to find the
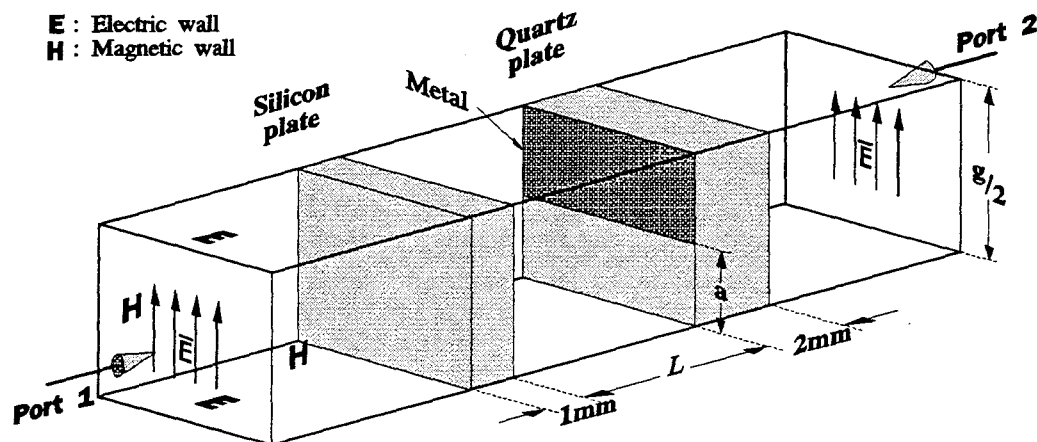
Fig. 4.3 The simulation structure for a capacitive metal-mesh evanescent-wave coupler. Symmetry allows to further reduce the unit-cell waveguide into a quarter-piece waveguide with electric walls on the top and bottom and magnetic walls on the sides. To simplify the calculations, one-dimension strips are used.

reflection and transmission coefficients using a simple transmission-line model.

Figure 4.4 shows the calculated reflectances and transmittances for a capacitive coupler at 60 GHz as a function of the spacing, L, between the meshes and the silicon plate. The quartz substrate has a refractive index of 2.12 and a thickness of 2 mm. The silicon plate has a refractive index of 3.42 and a thickness of 1 mm. The unit-cell size, g, is 1.465 mm ($0.293\lambda_0$) and the gap, $2a$, is 0.585 mm ($0.117\lambda_0$). The results calculated by the method of moments are shown in lines and the results calculated by $HFSS$ are shown in markers. Both results agree well within some errors of convergence. Simulations are also carried out from 40 GHz to 65 GHz with different unit-cell sizes and mesh parameters to verify the agreement of both methods. Results show good agreement, especially when the spacing, L, is small (less than $0.2\lambda_0$). Therefore, we used the method of moments later for calculations in order to reduce the computation time.
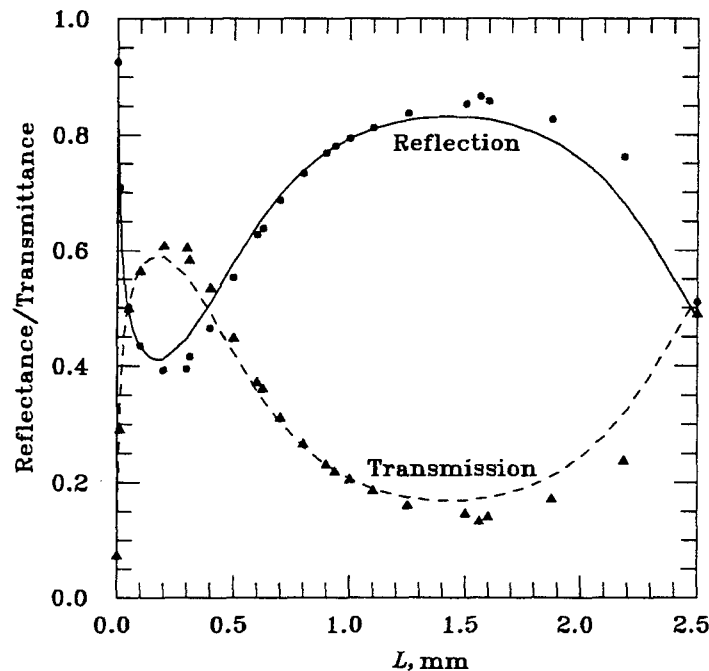
Fig. 4.4 Calculated reflectances and transmittances for a capacitive coupler at 60 GHz. The unit-cell size, g, is 1.465 mm ($0.293\lambda_0$) and the gap, $2a$, is 0.585 mm ($0.117\lambda_0$). The results calculated by the method of moments are shown in lines and the results calculated by $HFSS$ are shown in markers.

Figure 4.4 also shows that the evanescent-wave coupling effect happens when the spacings are small and the transmittances can be varied by more than 50% with a change of spacing only 0.18 mm ($\lambda_0/28$).

Figure 4.5 shows the magnitudes and polarizations of electric fields on the longitudinal plane with a spacing of 0.18 mm between the meshes and the silicon plate. The sizes and tips of pyramids indicate the magnitudes and directions of the electric fields, respectively. The propagating mode is a vertically-polarized
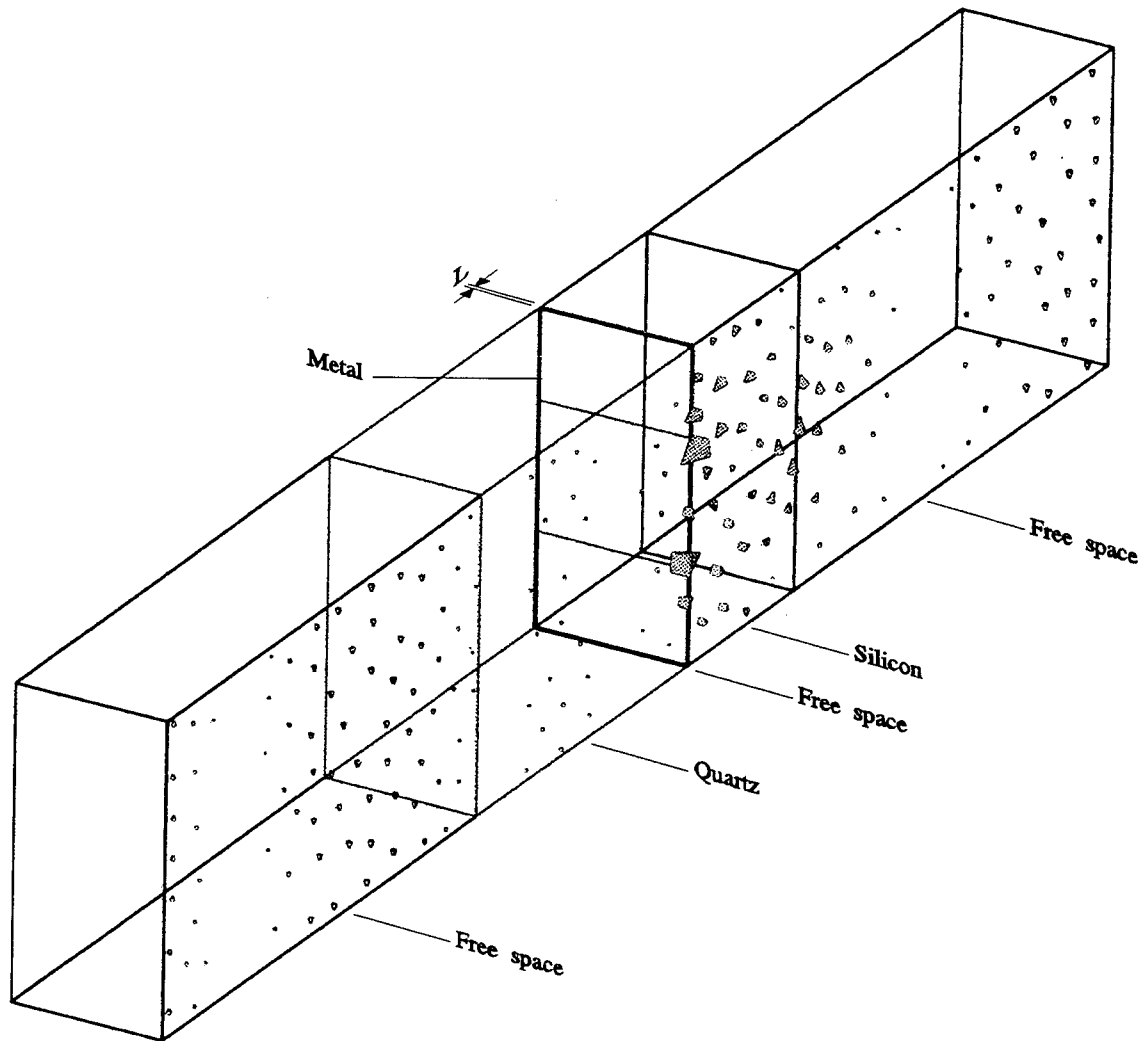
Fig. 4.5 Plot of the magnitudes and polarizations of electric fields on the longitudinal plane. The sizes and tips of pyramids indicate the magnitudes and directions of the electric fields, respectively.

TEM-wave. The horizontally polarized fields in the free space between the meshes and the silicon plate show that there is a strong evanescent-wave interaction which changes the embedding impedance of the metal-mesh grid significantly.

Figure 4.6 shows the calculated transmittances for (a) a capacitive coupler and (b) an inductive coupler as a function of frequency with different spacings, L. The unit cell size, g, is 1.7 mm. The gap of the capacitive meshes, $2a$, is 0.69 mm and the width of the inductive strips, $2a$, is 0.69 mm. The ratio of $2a/g$ is 0.4. Compton *et al.* [11] reported calculation results for strip gratings at a dielectric interface using Babinet's principle and found that, with a ratio of $2a/g = 0.4$, the evanescent waves will be excited the most by the meshes on quartz with a refractive index of 2.1 (Fig. 7 and 8 in [11]). To reach maximum evanescent-wave coupling effects, the ratio of $2a/g$ is always set to be 0.4 in our couplers with different g and $2a$.

Figure 4.6 (a) shows that the evanescent-wave coupling effects change the transmittances more than 40% over a 10% frequency range by varying L within 160 μm. The maximum variation of the coupling effect is 83% at 57 GHz. It is also shown that the capacitive coupler has a relatively flat transmission band in the frequency range between 50 GHz and 57 GHz. The transmittance reaches zero at 57 GHz with zero spacing and increases abruptly when the frequency increases. This is due to the resonant effect in the metal strip gratings [12] and will be discussed later.

The transmission of an inductive coupler should be the complement of that of a capacitive coupler with the same mesh parameters, as shown in Figure 4.6 (b). The coupling effects change less than 20% for a spacing change of 100 μm in the frequency range between 50 GHz and 60 GHz. This shows that the evanescent-wave coupling effect is smaller in the inductive coupler than in the capacitive coupler, verified later by measurements. The resonance also appears at 57 GHz where the transmittance is almost unity.
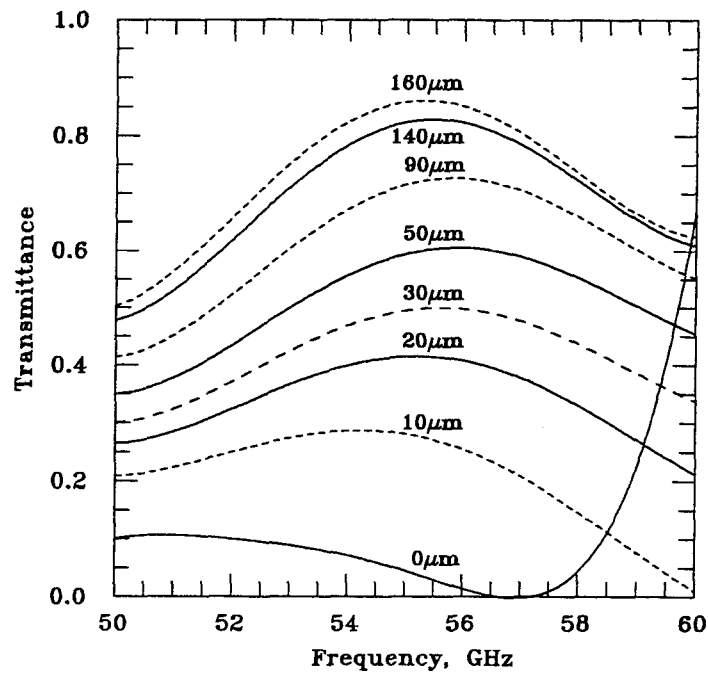
(a)
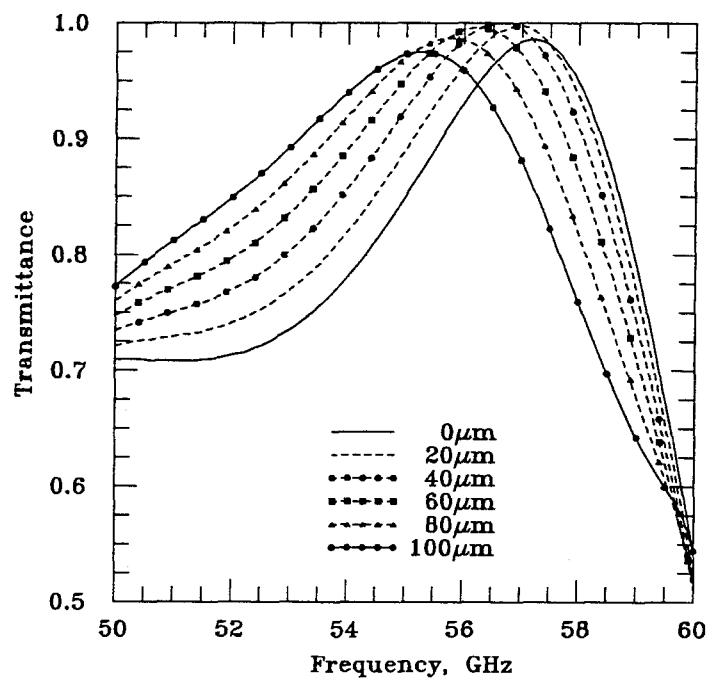
(b)

Fig. 4.6 Calculated transmittances for (a) a capacitive coupler and (b) an inductive coupler as a function of frequency with different spacings, L. The unit-cell size, g, is 1.7 mm. The gap of the capacitive meshes is 0.69 mm and the width of the inductive strips is 0.69 mm.

4.4 MEASUREMENTS

Several capacitive and inductive metal-mesh evanescent-wave couplers are fabricated and tested. The meshes are fabricated on z-cut quartz plates using photolithographic techniques. The metal thickness is $1\,\mu$m. The quartz plates have a thickness of 2 mm and a diameter of 40 mm. Different meshes with dimensions $(g, 2a)=$ (1.465, 0.585), (1.58,0.65), (1.70, 0.69) and (2.12, 0.86) mm are used. The ratio of $2a/g$ is 0.4.

Low-doped silicon wafers are used as the tuning plates. The silicon plate has a diameter of 63.5 mm and a thickness of 1 mm. Later 2-mm and 3-mm thick silicon wafers are also used to verify the dependence of resonance on the thickness of silicon plates.

Figure 4.7 shows the measurement arrangement. The couplers are placed between the transmitting and receiving horns connected to a *HP85106C* millimeter-wave network analyzer. The measurement frequency range is from 40 GHz to 60 GHz. The plates are mounted on micrometers and the spacings are variable with an accuracy of $\pm 10\,\mu$m. The parallelism between the meshes and the silicon plate is adjusted using a He-Ne laser.

The refractive indices of the quartz and silicon plates have first been determined by measuring the transmission properties with the plates placed between horns. The refractive index of the z-cut quartz is 2.12±0.05 and the attenuation constant is 0.5 Np/cm. The refractive index of the low-doped silicon is 3.42±0.05 and the attenuation is negligible in the frequency range of 40-60 GHz.

Figure 4.8 shows the measured transmittances of (a) the capacitive and (b) the inductive couplers with meshes $(g, 2a)$=(1.7,0.69) mm to compare with calculation results. The transmittances are zero and almost unity with the spacing $L = 0$ at 57.4 GHz and 56 GHz for the capacitive and inductive couplers, respectively. For the capacitive coupler, the transmittance variations vary from 10% at 50 GHz to 79% at 57.4 GHz with a spacing change of $130\,\mu$m. For the

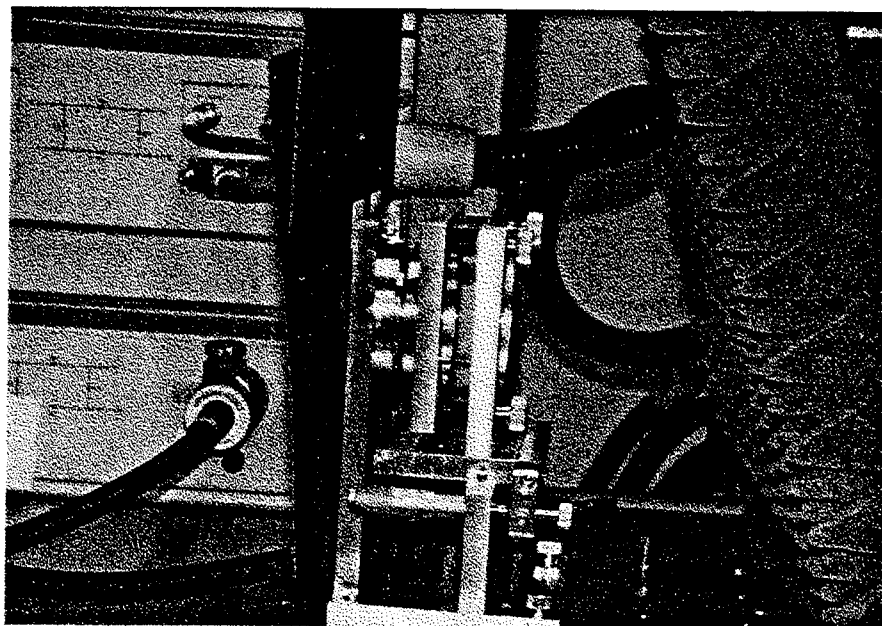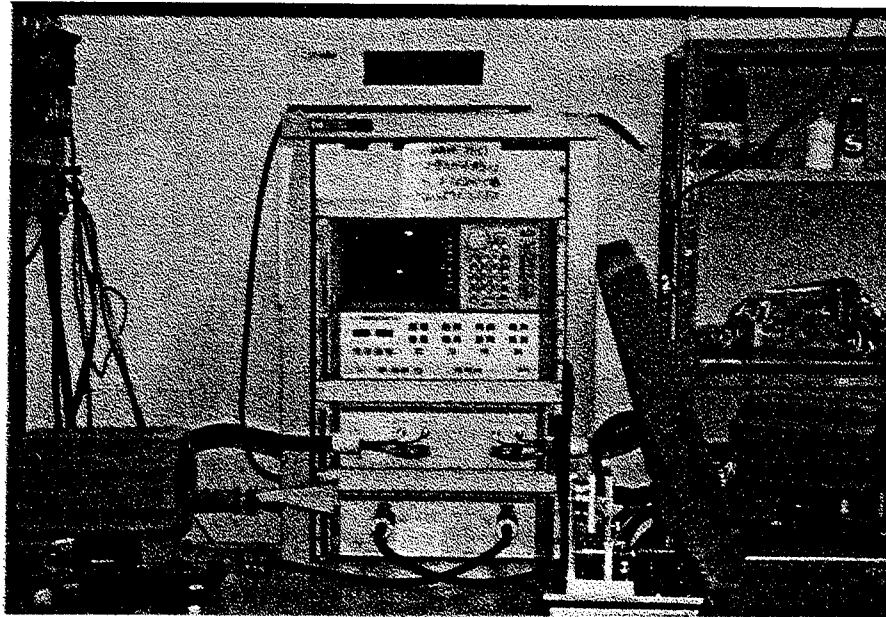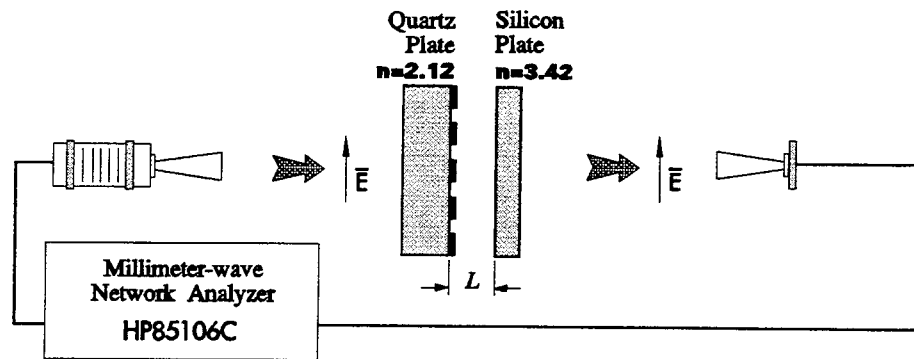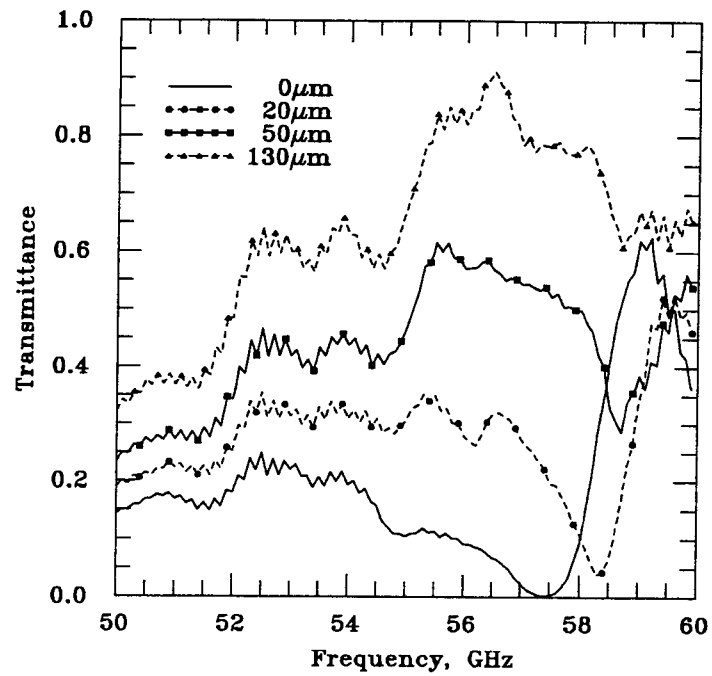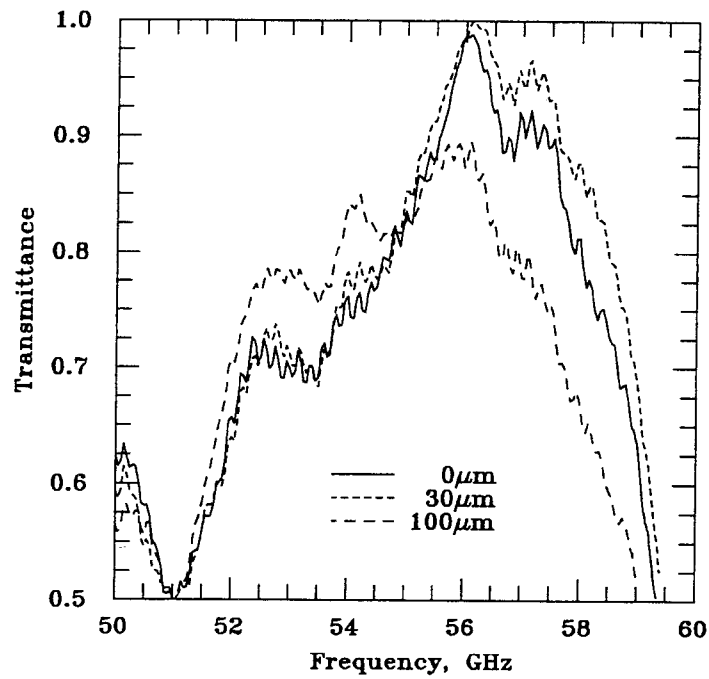Fig. 4.7 Measurement arrangement.

Fig. 4.8 Measured transmittances for (a) a capacitive coupler and (b) an inductive coupler as a function of frequency with different spacings, L. The unit-cell size, g, is 1.7 mm. The gap of the capacitive meshes is 0.69 mm and the width of the inductive strips is 0.69 mm.

inductive coupler, the transmittance variations vary from 8% at 53 GHz to 10% at 56 GHz with a spacing change of 100 μm. The small fluctuations are caused by scattered waves from the mirror-mounts. Although the calculations only use one-dimensional strips, the theory predicts the transmission properties well up to 58 GHz. The measured transmittances for the inductive coupler, however, are 20% lower than the predictions at lower frequencies.

4.5 Coupling Effects

In metal-mesh evanescent-wave couplers, the Fabry-Perot etalon effect always appears together with the evanescent-wave coupling effects, so we have to take both effects into account. Figure 4.9 shows the measured and calculated transmittances at 56 GHz as a function of spacing, from zero to 0.75λ. The Fabry-Perot etalon effect obviously occurs and causes resonant peaks in the transmission. Since the evanescent-wave coupling effect only happens when the silicon plate is very close to the meshes and the coupler behaves like a Fabry-Perot interferometer for larger spacing, by comparing the part of the curve above $\lambda/2$ and the part around the origin, the evanescent-wave coupling effect alone can be isolated by subtracting these two parts. Figure 4.10 shows the transmittances of the couplers (a) with and (b) without the evanescent-wave coupling effect by varying the spacing L from 0 to 4 mm at 56 GHz. The transmittances of the capacitive coupler are 0.1 at $L = 0$ and 0.63 at $L = \lambda/2$, respectively. This shows the evanescent-wave coupling effect decreases transmission by 53%. The transmittances of the inductive coupler are 0.87 at $L = 0$ and 0.54 at $L = \lambda/2$, respectively. It shows the evanescent-wave coupling effect increases transmission by 33%. When the spacing increases to 0.1 mm, by comparing the transmittances at $L = 0.1$ mm with those at $L = \lambda/2 + 0.1$ mm, the transmittance change of the capacitive coupler is 66% and is only 5% for the inductive coupler. This indicates that the capacitive couplers have stronger evanescent-wave coupling effect than inductive ones.
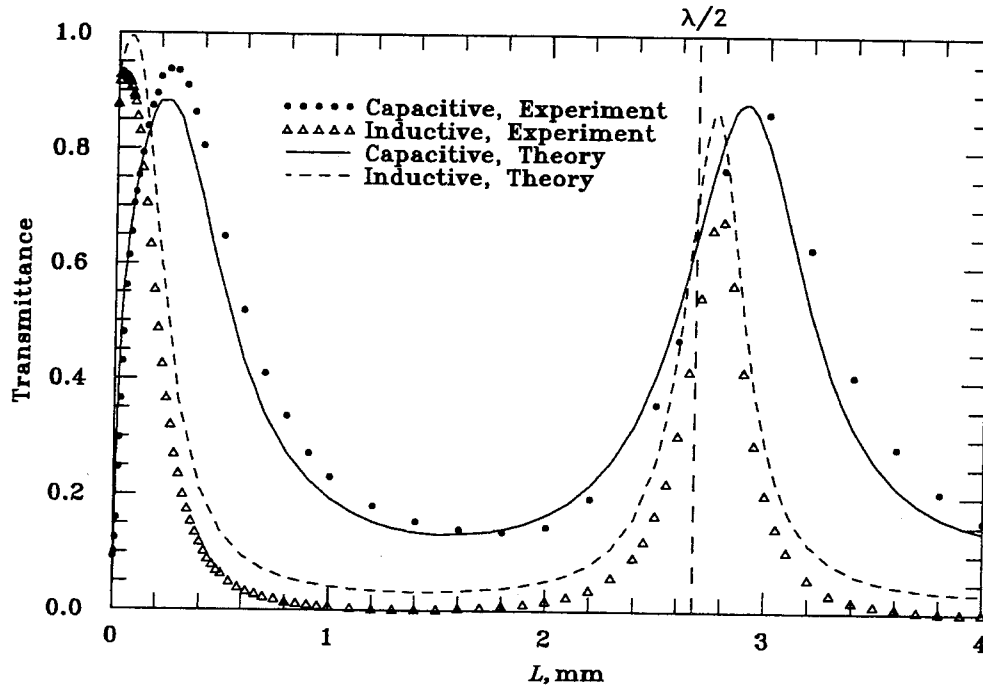
Fig. 4.9 The transmittances of the capacitive and inductive couplers with meshes $(g, 2a) = (1.7, 0.69)$ mm as a function of spacing, L, at 56 GHz.
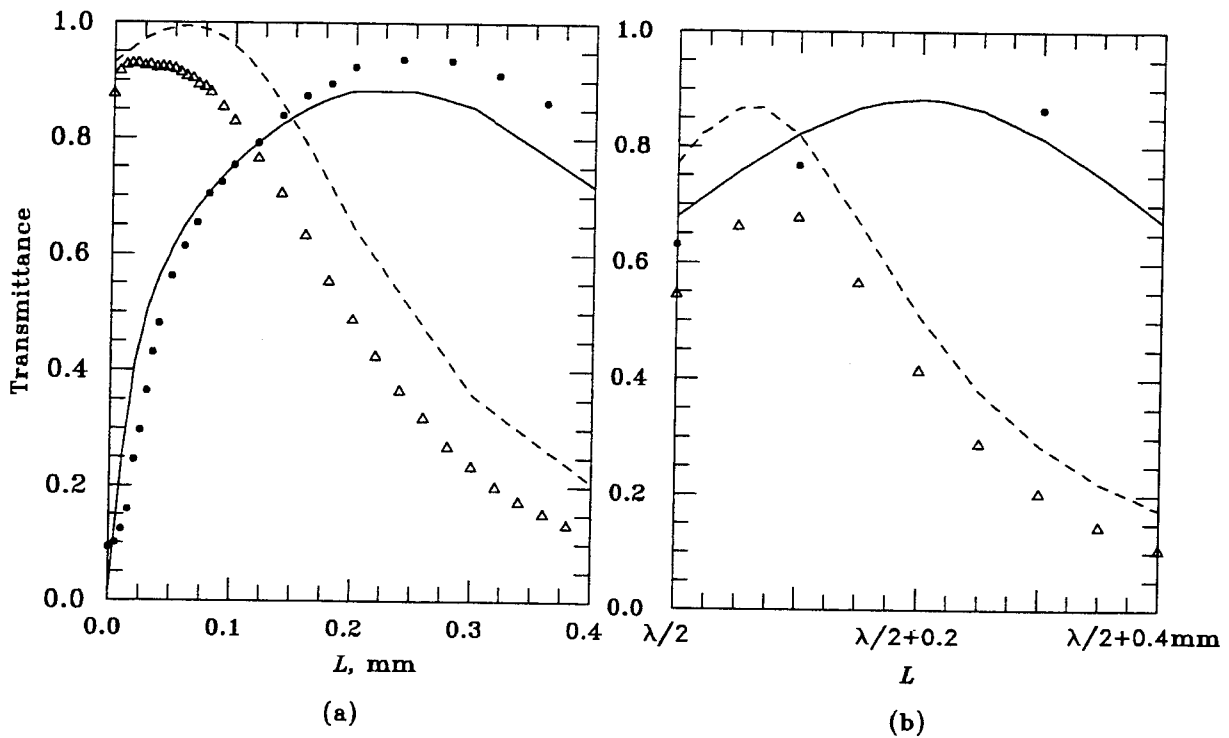

(a)   (b)

Fig. 4.10 The transmittances of the capacitive and inductive couplers (a) with the evanescent-wave coupling effect as the spacing in the range from 0 to 0.4 mm; and (b) without the evanescent-wave coupling effect as the spacing in the range from $\lambda/2$ (2.68 mm) to $\lambda/2 + 0.4$ mm.
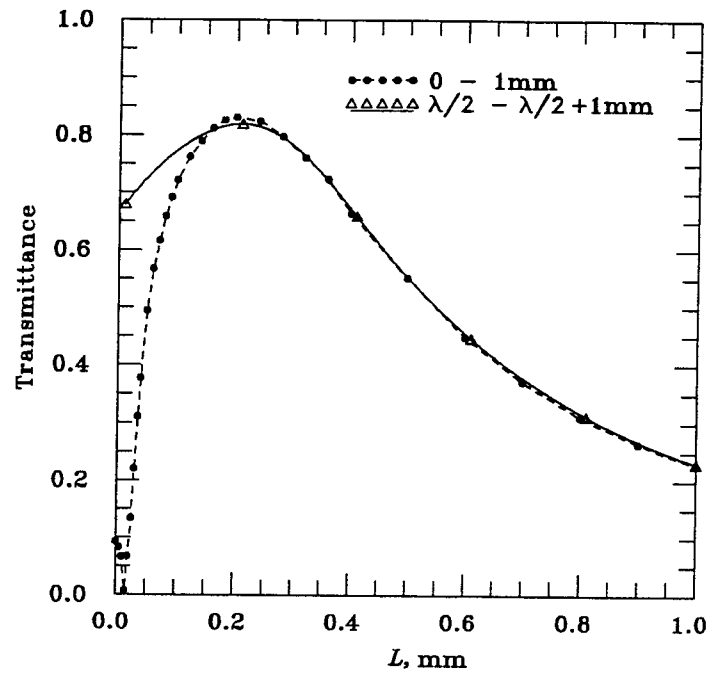
Fig. 4.11 Measured transmittances as a function of spacing, L, at 58 GHz. The dashed line is measured from $L = 0$ to $L = 1$ mm and the solid line is measured from $L = \lambda/2$ to $L = \lambda/2+1$ mm.
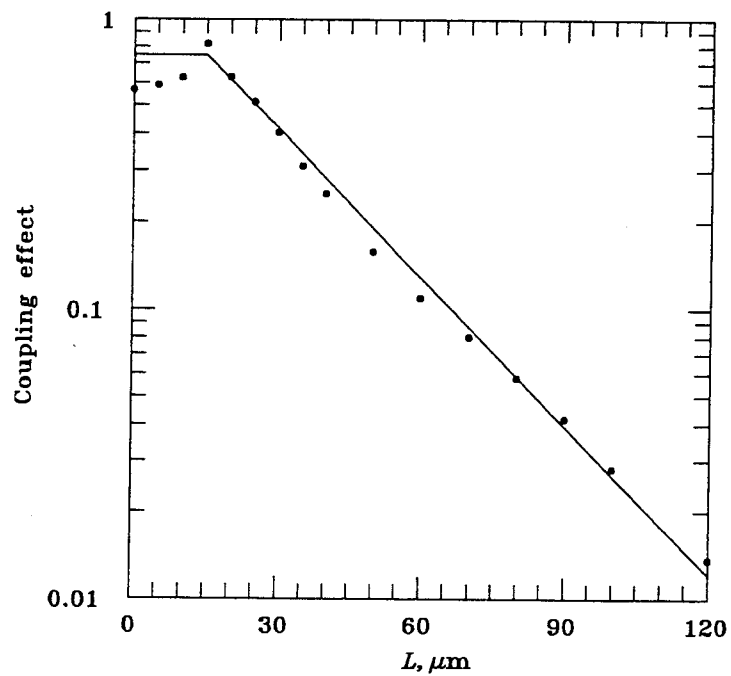

Fig. 4.12 Coupling effect as a function of spacing. With a spacing of 40 μm, the coupling effect drops to e^{-1} of the maximum value.

Figure 4.11 shows the measured transmittances at 58 GHz. The dashed line is measured from $L = 0$ to $L = 1$ mm and the solid line is measured from $L = \lambda/2$ to $L = \lambda/2 + 1$ mm. By comparing the part of the curve above $\lambda/2$ and the part around the origin, the difference is the evanescent-wave coupling effect alone.

The evanescent-wave coupling effect can be defined as

$$C = C_0 \cdot e^{-\alpha(L-L_0)} \tag{4.1}$$

where C indicates the coupling effect, C_0 is the peak value, L is the spacing between the meshes and the tuning plate, L_0 is the effective distance for maximum coupling and α is the attenuation constant of the coupling effect. Figure 4.12 shows the dependence of the coupling effect on the spacing. The attenuation constant is found to be 39 Np/mm and L_0 is 15 μm. With a spacing of 40 μm, the evanescent-wave coupling effect drops to e^{-1} of its maximum value.

To estimate the effective distance of coupling, transmittances of the coupler with meshes $(g, 2a)$=(2.12,0.86) have been measured at 44 GHz (Figure 4.13). The thickness of the silicon plate is 1 mm which is about half wavelength in silicon at 44 GHz, the Fabry-Perot etalon effect between the metal meshes and the silicon plate disappears at this frequency and we can estimate the effective distance of coupling effect more precisely. Supposing there were no evanescent-wave coupling effects in this type of couplers, the transmittances should have stayed flat as the spacings vary. However, abrupt and large changes (more than 20%) of transmittances are observed in both couplers when the tuning plate moves close to the meshes. This clearly shows that the evanescent-wave coupling effects occur and increase the transmittance of the capacitive coupler as the spacing increases while decrease the transmittance of the inductive coupler. The transmittances change exponentially and approach to their final values as the spacing increases. From the measured results, the transmittances are within 10% of their final values at a spacing of 220 μm ($\lambda/31$) for the capacitive coupler and 340 μm ($\lambda/20$) for the inductive coupler, respectively.
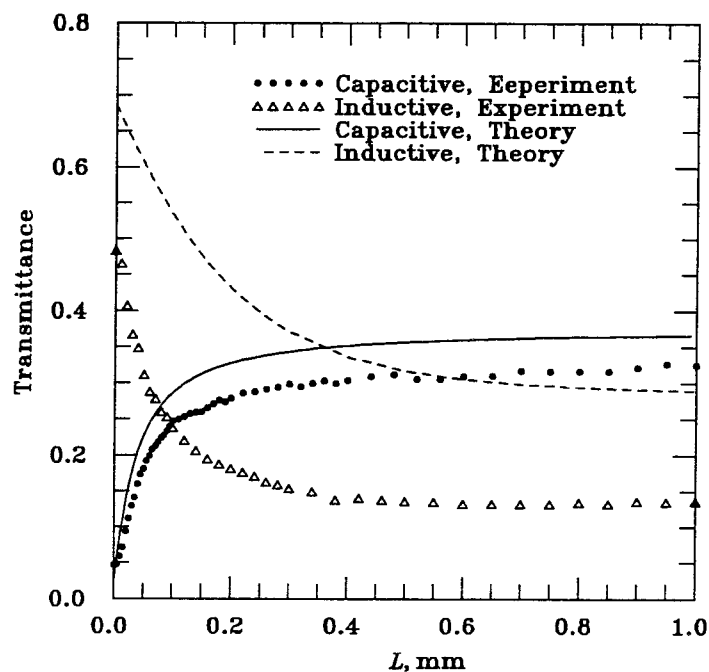
Fig. 4.13 Transmittances of the couplers with meshes $(g, 2a)=(2.12, 0.86)$ mm at 44 GHz.

The decay constants of the coupling effect are 34 and 20 Np/mm for the capacitive and inductive couplers, respectively, which are larger than the intensity decay constant of the first-order evanescent wave, 11.2 Np/mm, predicted from Fourier optics theory [1]. This shows that the changes of transmittance in the couplers do not result from simple coupling between the evanescent fields and the silicon plate. A more complicated model will be presented later. Also the results show that the coupling decays faster and the transmittance variations are larger in a capacitive coupler than in an inductive one. The theoretical transmittances are about twice as large as the measured results in the inductive coupler, which is also observed in Figure 4.8. The discrepancy is possibly due to the RF losses induced by the inductive meshes [13] which are not taken into consideration in our calculations.

In principle, metal-mesh evanescent-wave couplers can have wider bandwidth than Fabry-Perot interferometers because the metal-mesh evanescent-
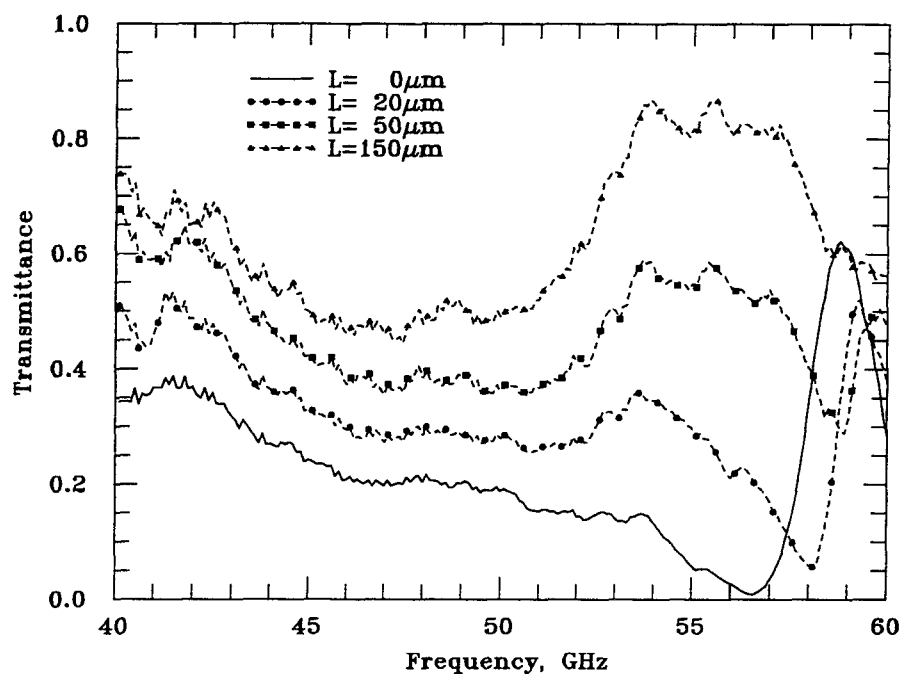
Fig. 4.14 Measured transmittances of the capacitive coupler with meshes $(g, 2a)=(1.7,0.69)$ mm as a function of frequency. The thickness of the silicon plate is 1 mm.

wave couplers make use of the coupling effects of evanescent waves to change transmittance instead of the propagating waves and the transmission properties of evanescent waves primarily depend on the mesh parameters. Figure 4.14 shows the measured transmittances of a capacitive coupler with meshes $(g, 2a)=(1.7,0.69)$ mm as a function of frequency. The coupling coefficient can be changed by 83% at 56.5 GHz with a change of spacing from $L = 0$ to $L = 0.15$ mm. For the same variation of spacing, the transmittance changes are always more than 25% in the frequency range from 40 GHz to 58 GHz. The bandwidth of an evanescent-wave coupler is clearly bigger that of a Fabry-Perot coupler.

4.6 RESONANT EFFECTS

Since diffraction occurs above the resonant frequency and causes transmission losses, the operation of the evanescent-wave couplers is limited below the

resonant frequency. Conventional mesh theory [11,14] has shown that the resonant frequency of metal meshes on a dielectric substrate is determined by

$$f_0 = \frac{c}{g \cdot n} \qquad (4.2)$$

where c is the light velocity, g is the unit-cell size and n is the refractive index of the dielectric substrate. For the evanescent-wave couplers with $L = 0$ and $(g, 2a)=(1.7,0.69)$ mm, the resonant frequency predicted by the conventional mesh theory is 51.6 GHz which is much lower than the measured values, 57.4 GHz and 56 GHz for the capacitive and inductive couplers, respectively, (Figure 4.8). The resonant frequency calculated by the method of moments and *HFSS* is 57 GHz, as shown in Figure 4.6. The discrepancy can be explained by modifying the resonant frequency relationship as

$$f_0 = \frac{c}{g \cdot n_e} \qquad (4.3)$$

where n_e is the effective refractive index. For a resonant frequency of 57 GHz, the effective refractive index is 3.1 which is smaller than the actual index of 3.42. The changes of n_e could be caused by two factors: the evanescent-wave coupling effect between the meshes and the tuning plate; and the finite thickness of the tuning plate. The first factor can be explained by a more complicated coupling model, presented later, which will also explain the disagreements between the decay constant of the coupling effect and the intensity decay constant of the first-order evanescent wave. The second factor is due to the fact that the thickness of the silicon plate used (1 mm) is much smaller than the wavelengths. Several silicon wafers with different thickness's are used to verify our assumption. A design requirement for the silicon-plate thickness is also considered.

4.6.1 DEPENDENCE ON THE MESH PARAMETERS

Figure 4.15 and 4.16 show the measured transmittances of the capacitive and inductive couplers with meshes $(g, 2a)=(2.12, 0.86)$ mm and $(g, 2a)=(1.70,$
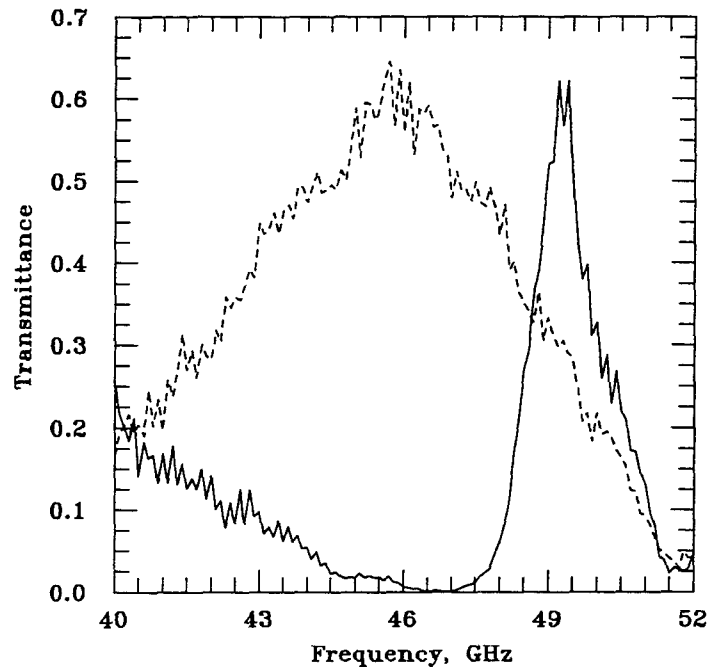
Fig. 4.15 Measured transmittances of the couplers with meshes $(g, 2a)=(2.12, 0.86)$ mm as a function of frequency. The thickness of the silicon plate is 1 mm and the spacing, L, is zero. The dashed line indicates the inductive coupler and the solid line indicates the capacitive coupler.
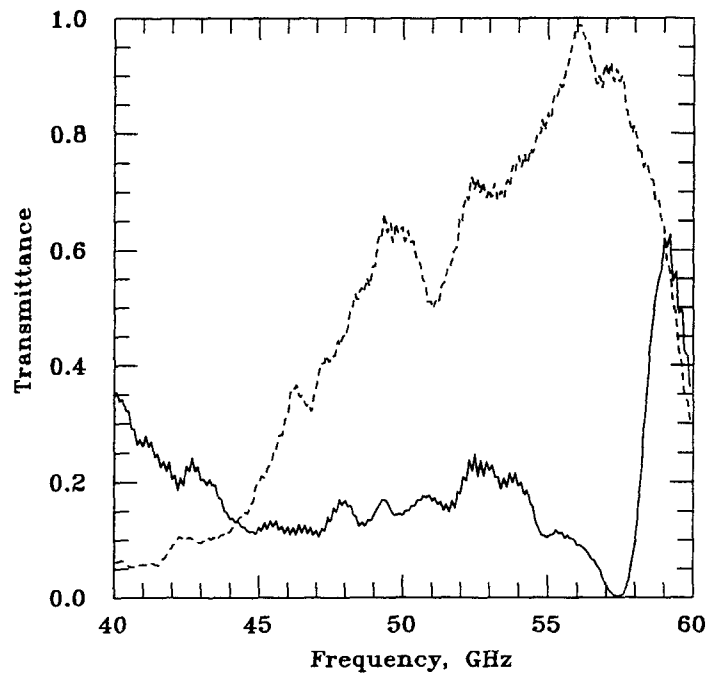

Fig. 4.16 Measured transmittances of the couplers with meshes $(g, 2a)=(1.70, 0.69)$ mm as a function of frequency. The thickness of the silicon plate is 1 mm and the spacing, L, is zero. The dashed line indicates the inductive coupler and the solid line indicates the capacitive coupler.

0.69) mm as a function of frequency, respectively. The thickness of the silicon plate is 1 mm and the spacing, L, is zero. At resonance, the transmittances of capacitive couplers should approach zero while the ones of inductive couplers reach their maximum values, considered the existence of RF losses, instead of unity. Table 4.1 lists the couplers, mesh parameters, resonant frequencies and the effective refractive indices calculated by Eq. (4.3).

Coupler	g, mm	f_c, GHz	f_m, GHz	n_e
Inductive	2.12	46	46	3.076
Capacitive	2.12	46	46.5	3.043
Inductive	1.70	57	56	3.15
Capacitive	1.70	57	57.4	3.074

Table 4.1 The dependence of the resonant frequencies on mesh parameters. g is the unit cell, f_c is the calculated resonant frequency, f_m is the measured resonant frequency, and n_e is the effective refractive index.

The relationship between the measured resonant frequencies and the unit-cell sizes follows the modified mesh theory, however, both results show that the effective refractive index of silicon, which is about 3.1, is smaller than the actual one, 3.42, which is determined by measuring the transmission properties of a 1-mm thick silicon plate in the frequency range of 40-60 GHz. This measurement verifies that the discrepancy should result from the finite thickness of the silicon plate instead of the mesh parameters.

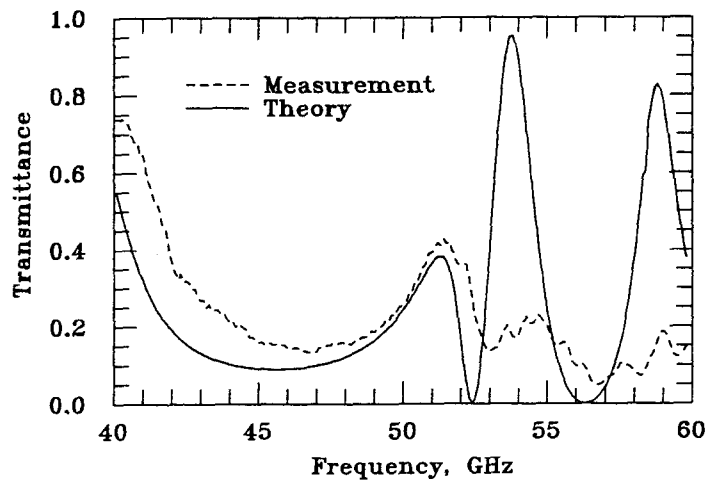## 4.6.2 DEPENDENCE ON THE THICKNESS OF SILICON PLATE

The transmittances of the capacitive couplers with meshes $(g, 2a)=(1.70, 0.69)$ mm are measured at $L = 0$ for different silicon plates with thickness's of 1, 2 and 3 mm to verify the dependence of resonant frequency on the thickness of the tuning plate, as shown in Figure 4.17. The first resonant frequencies, where the transmittances reach to the first nulls as frequency increases, are 57.4, 53.5
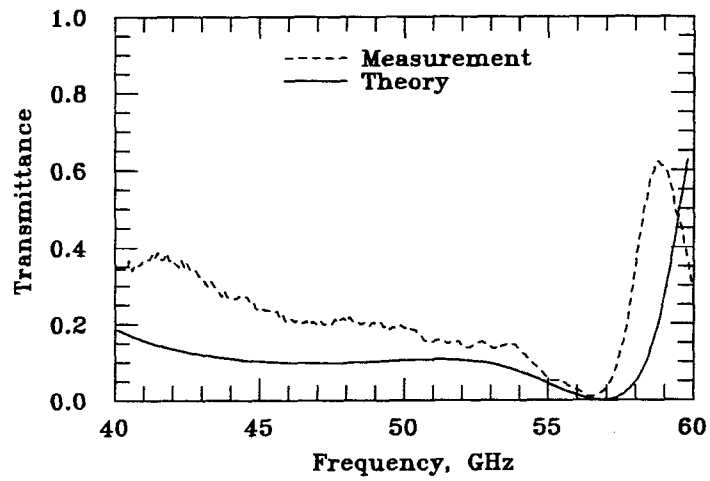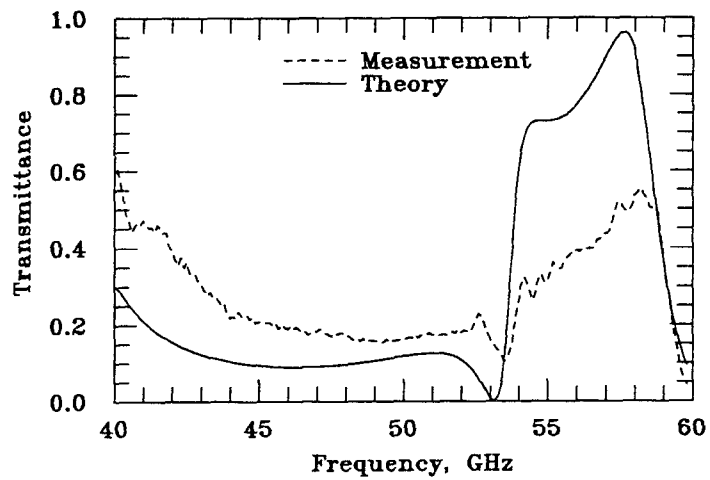
Fig. 4.17 Transmittances of capacitive couplers with meshes $(g, 2a)$=(1.70, 0.69) mm and different silicon plates. The thickness of the silicon plate is (a) 1 mm, (b) 2 mm and (c) 3 mm. The spacing between the meshes and the silicon plate is zero.

and 53 GHz for the thickness of 1, 2, and 3 mm, respectively. Theory has well predicted these resonant frequencies within an error of 1%. Above the resonant frequencies, the measured transmittances are largely different from the calculated values, though their shapes of curves are still similar. The discrepancy between the calculations and the measurements is caused by diffraction losses which have not been taken into account in the calculations. This discrepancy is not important in the designs because the operations of the evanescent-wave couplers should be limited below the resonant frequencies. These results verify our assumption of the relationship between the resonant frequency and the tuning-plate thickness.

Figure 4.18 shows (a) the resonant frequency and (b) the effective refractive index as a function of the thickness of the silicon plate. When the thickness increases, the effective refractive index increases exponentially approaching to the actual value, 3.42. With a thickness of 3.4 mm, which is twice of the unit-cell size $g = 1.7$ mm, the effective refractive index is 3.37 which is 98.5% of the actual value. This can be a rule of thumb for designing an evanescent-wave coupler that the tuning plate should have a thickness at least two times bigger than the mesh period in order to reach the actual refractive index of silicon. When the thickness of the silicon plate goes to zero, the resonant frequency increases and approaches to 83.2 GHz which is determined by the refractive index of the mesh substrate, quartz. This provides a flexibility of choosing the resonant frequencies for different purposes or applications. By adjusting the thickness of the tuning plate, the change of the effective refractive index of silicon can vary the resonant frequency from 51.6 GHz to 83.2 GHz.

The thickness of the quartz substrate is also varied to examine the relationship with the resonant frequencies. However, the resonant frequency doesn't change significantly when the thickness changes from 2 mm to 6 mm because of the lower dielectric constant of quartz.

The resonant frequencies do not only determine the maximum operating fre-

quencies of the couplers, but also change the transmission properties. Figure 4.19 shows (a) measured and (b) calculated transmittances as a function of spacing with different silicon plates. The transmittances are measured at the resonant frequency, f, of the corresponding thickness, d. The capacitive couplers have meshes $(g, 2a)$=(1.70,0.69) mm. The transmittances can be varied 83% with a spacing variation of 200 μm for d=1 mm at 57.4 GHz; 84% with a spacing variation of 120 μm for d=2 mm at 53.5 GHz; and 74% with a spacing variation of 40 μm for d=3 mm at 53 GHz. To compare, the transmittances only change 45% at 53 GHz with a spacing variation of 50 μm for the capacitive coupler with a silicon thickness of 1 mm, as shown in Figure 4.14. Changing the thickness of the silicon plate from 1 mm to 3 mm can increase the coupling coefficient by 1.6 times. Therefore, we can conclude that, by adjusting the thickness of the tuning plate to locate the resonant frequency, a maximum variation of the evanescent-wave coupling effect and a minimum moving range can be achieved at the operating
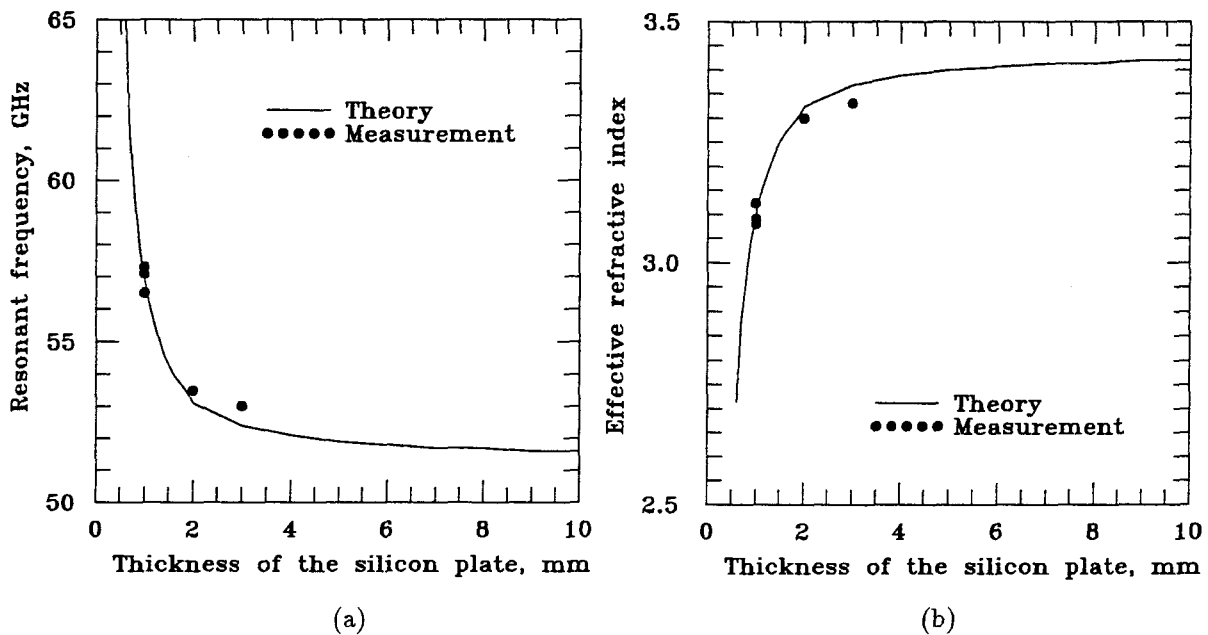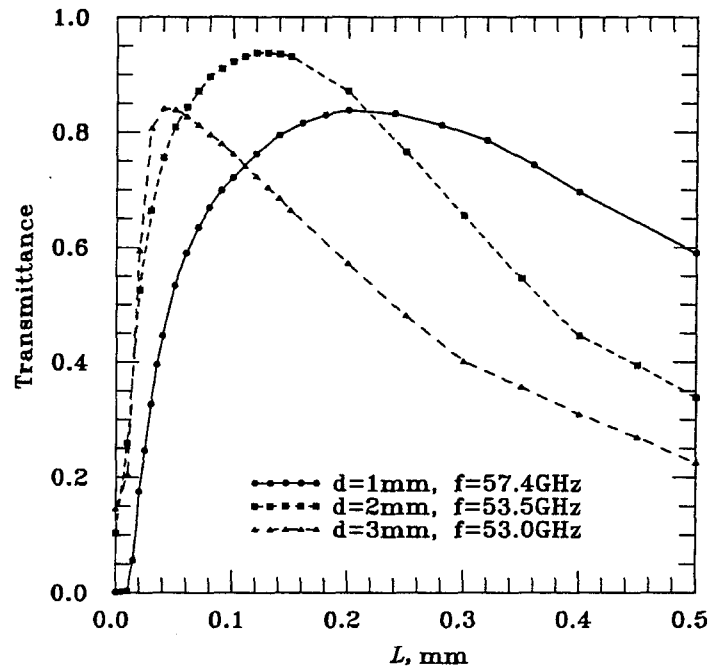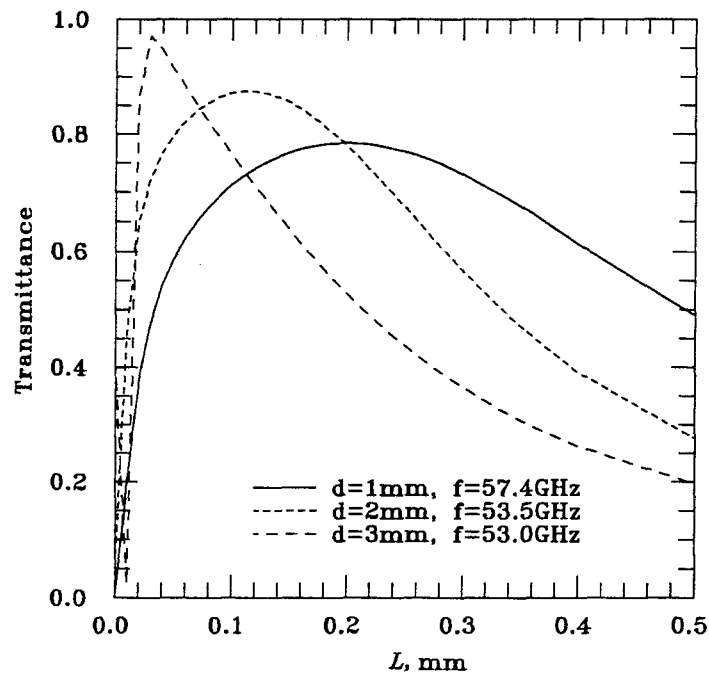
Fig. 4.18 (a) The relationship between the resonant frequency and the thickness of the silicon plate; and (b) the relationship between the effective refractive index and the thickness of the silicon plate. The capacitive couplers have meshes $(g, 2a)$=(1.70, 0.69) mm.

(a)

(b)

Fig. 4.19 (a) Measured and (b) calculated transmittances as a function of spacing with different silicon plates. The transmittances are measured at the resonant frequency, f, of the corresponding thickness, d. The couplers have meshes $(g, 2a)=(1.70, 0.69)$ mm.

frequency. In our case, this can be achieved at any operating frequency between 51.6 GHz, which is the resonant frequency when the thickness of the silicon plate is infinite, and 83.2 GHz, which is determined by the quartz substrate.

4.7 EFFECTIVE DIELECTRIC CONSTANTS

As mentioned before, the abrupt transmittance changes of a metal-mesh evanescent-wave coupler can not be explained by a simple transmission-line model or Fourier optics theory [1]. A more complicated model should be considered. The transmission properties of a metal mesh on a dielectric plate strongly depend on its dielectric constant [11]. Therefore, the changes of the effective dielectric constant of the silicon plate caused by the changes of spacing could explain the large and rapid changes of transmittance in these couplers.

In order to confirm this assumption, transmittances of a coupler with a dielectric tuning plate which has an effective refractive index n_e are calculated as a function of spacing, L. The effective refractive index n_e is determined by

$$n_e = \sqrt{(n_{\text{si}}^2 - 1) \cdot \frac{1}{m} \sum_{i=1}^{m} e^{(-\alpha_i L)} + 1} \tag{4.4}$$

and

$$\alpha_i = k\sqrt{\left(\frac{i \cdot \lambda}{g}\right)^2 - 1} \tag{4.5}$$

where n_{si} is the actual refractive index of the silicon plate, 3.42; α_i is the field decay constant of the i-th order evanescent wave; m is the number of evanescent waves considered; and k is the wave number of the incident wave in free space.

First, n_e is determined for various values of L, then the embedding impedance, $Z_m(L)$, of the metal mesh, which is sandwiched by two dielectric plates with refractive indices of 2.12 and n_e, is calculated by using the method of moments. Infinite thickness of these dielectric plates is assumed to remove the Fabry-Perot
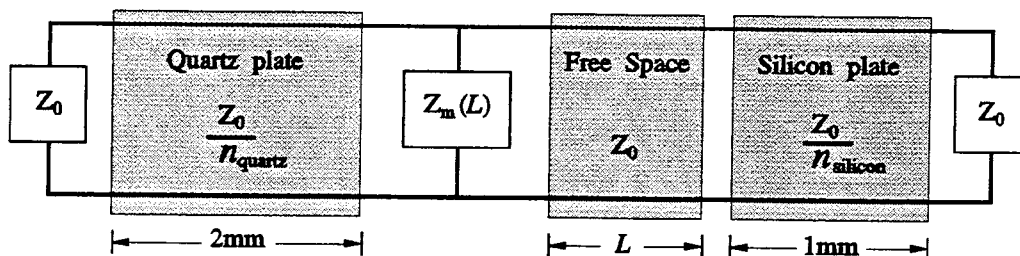
Fig. 4.20 Equivalent circuit of an evanescent-wave coupler.

etalon effect. Finally, reflectance and transmittance of the coupler are computed by using the simple equivalent-circuit shown in Figure 4.20.
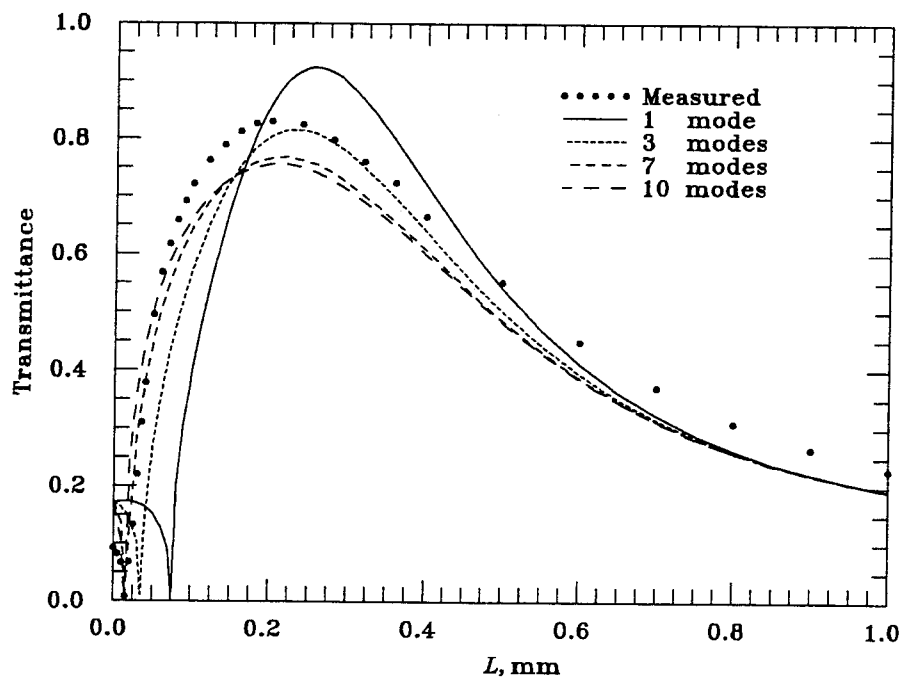
Figure 4.21 shows the measured and calculated transmittances of the (a) inductive and (b) capacitive couplers with meshes $(g, 2a)$=(1.70,0.69) mm as a function of spacing, L, at 58 GHz. The numbers of the evanescent modes considered in calculations are 1, 3, 7 and 10. We assume the considered evanescent modes are equally excited by the metal meshes on the mesh surface. The results show that our assumption on the relationship between the evanescent-wave coupling effect and the effective refractive index of the silicon plate is valid within the experimental error.

4.8 OPTICAL CONTROLLED MODULATIONS

One of the main reasons to study the relationship between the evanescent-wave coupling effect and the effective dielectric constant is to develop an electronic beam controller for amplitude modulations. The abrupt and large coupling effect can be used to vary the transmission powers more efficiently. There are several methods to change the effective refractive indices electronically and these methods have been used on high-speed light modulators such as electrooptic, acoustooptic and magnetooptic effects [15,16]. All these effects produce refractive index changes in response to the modulating electric, acoustic and magnetic fields. At optical wavelengths, these control signals provide good isolation with
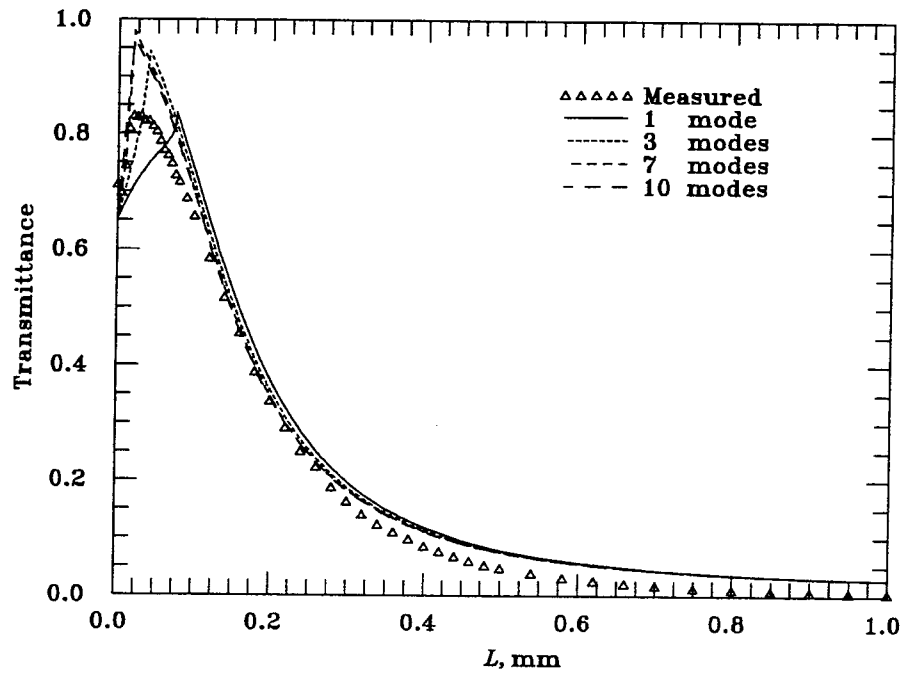
Fig. 4.21 Measured and calculated transmittances of the (a) inductive and (b) capacitive couplers with meshes $(g, 2a)=(1.70,0.69)$ mm at 58 GHz. The numbers of the evanescent modes considered in calculations are 1, 3, 7 and 10.

the propagating signals. At millimeter and submillimeter wavelengths, these methods should also be considered except that the electrooptic effect should be used the other way around, that is, using optical signals to control the propagating millimeter or submillimeter waves. Optical techniques offer many advantages over acoustic or magnetic approaches such as near perfect isolation; low static and dynamic insertion losses; fast responses; high power handling capability and being non-destructive to materials [17]. Using optical injection with the photon energy above the band-gap energy of semiconductor material, a layer of plasma in the material will be generated to change the refractive index. The depth of the free-carrier plasma introduced by light illumination can be controlled by selecting an appropriate combination of optical radiation wavelength and semiconductor absorption properties. For silicon, it has a wider dynamic range of absorption than germanium and a lower photon-energy requirement than GaAs, CdS or GaP. Therefore, low-doped silicon, which has low losses at millimeter wavelengths, has been used as dielectric waveguides in optical-controlled modulators. Lee *et al.* [17] demonstrated a 94-GHz phase-shifter using silicon dielectric waveguides with 1.06-μm pulsed laser illumination. Manasson *et al.* [18] reported a photo-induced plasma grating on silicon slabs to steer a 92-GHz beam by changing the non-equilibrium plasma grating patterns to change the diffraction angles.

The optical injection should have the photon energy above the band-gap energy of silicon, 1.12 ev, to generate enough free-carrier plasma to change the refractive index. In term of wavelength, the optical signal should have a wavelength less than 1.107 μm. The change of refractive index also depends on the intensity and the modulation speed of the light; the injection area; the generation, recombination and diffusion rates of the free carriers in material; and the thickness of silicon. Even for a small change of index, a large intensity of illumination is usually required [19,20]. For example, an intensity of 2.1 mJ/cm^2 with a pulse width of 30 ps at 1.06 μm is required to generate appreciable changes of
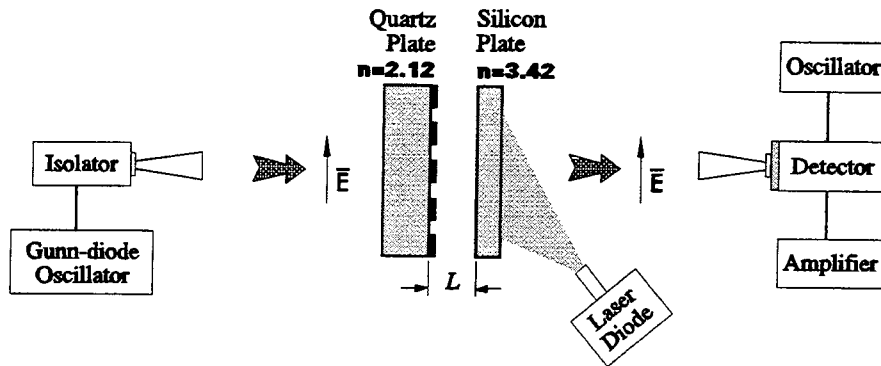
Fig. 4.22 Measurement arrangement for optical-controlled metal-mesh evanescent-wave couplers.

index [17]. The metal-mesh evanescent-wave couplers, as demonstrated, are very sensitive to the changes of effective refractive index, especially when operated at the resonant frequencies. Therefore, we propose to use the evanescent-wave couplers with optical control in order to achieve large modulations and reduce the injection powers.

Figure 4.22 shows the measurement arrangement. The metal-mesh evanescent-wave coupler has meshes $(g, 2a)=(1.7,0.69)$ mm and the thickness of the low-doped silicon plate is 1 mm. The transmitting signal is provided by a Gunn diode oscillator with a frequency range of 48-60 GHz and a CW power of 30 mW. The coupler is placed between the transmitting and receiving horns and illuminated by a laser diode. The laser has a wavelength of 0.88 μm, a peak power of 18 W, a pulse width of 100 ns and a repetition rate of 1 kHz. The laser beam has a radiation angle of 30° which covers the entire silicon wafer. The detector is a Schottky-barrier diode detector with a sensitivity of 10^3 V/W. Due to the experimental setup, only transmittances are measured. The calibrations of the transmittances as well as the relationship between the amplified detection-currents on the Schottky diode and the receiving powers are determined through transmission measurements without the couplers.

Time-responses are first measured to verify the maximum modulation fre-

quency. The modulation frequency is limited by the relaxation time of the free carriers in silicon. By comparing the recovering signals on the Schottky diode with the output pulses from the laser diode, we found that the maximum modulation is about 10 kHz which agrees with the theoretical value predicted from the recombination times of free carriers in silicon [21]. Then the modulation rate is set 1 kHz which is slow enough to give a good ON-/OFF-state isolation.

Transmittances are measured as a function of spacing, L, between the silicon plate and the meshes at 56.5 GHz, with and without the laser illumination. Figure 4.23 shows the transmittance changes between with and without light illumination. The transmittance change is zero when there is no light illuminated
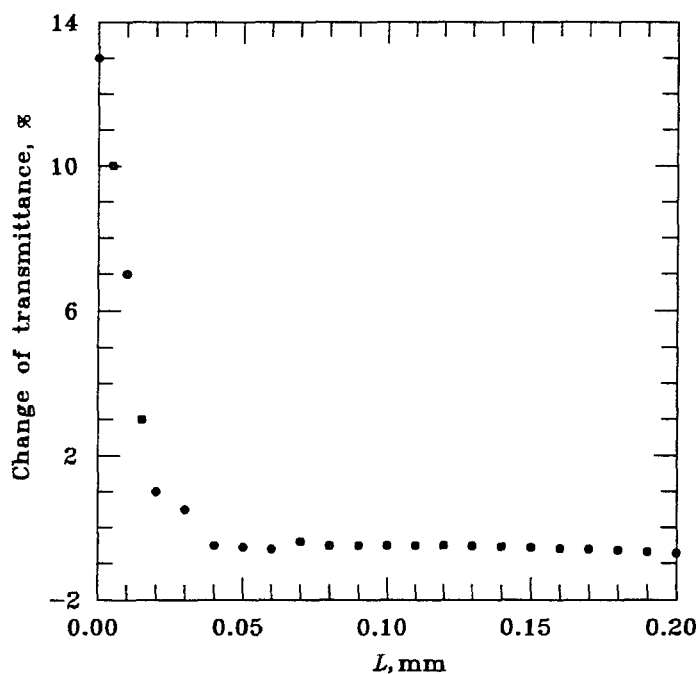

Fig. 4.23 Measured transmittance modulations as a function of spacing, L. The transmittance change is zero when there is no light illuminated on the silicon plate. Positive change means the transmittance increases when the silicon is illuminated. When the spacing is more than 0.03 mm, the evanescent-wave coupling effect is small so that the modulation is only -0.6%. The modulation is increased to $+13\%$ with $L = 0$, which means the transmittance increases 13% with light illuminated, because of the evanescent-wave coupling effect.

on the silicon plate. Positive change means the transmittance increases when the silicon is illuminated. When the spacing is more than $30\,\mu$m, the evanescent-wave coupling effect is small so that the change is only -0.6%. This means the transmittance decreases by 0.6% due to the change of refractive index caused by the photon-induced free carriers. The maximum modulation is $+13\%$ with $L = 0$ where the evanescent-wave coupling effect is stronger.

4.9 CONCLUSION

Metal-mesh evanescent-wave couplers have been demonstrated as quasi-optical amplitude-modulation components at millimeter wavelengths. The transmittance of a capacitive metal-mesh evanescent-wave coupler can be changed from 93% to 10% at 56 GHz by moving a tuning plate only $250\,\mu$m. Transmission properties of the inductive and capacitive couplers have been investigated including effective coupling distances, coupling effects and the resonant frequencies. It is found that the evanescent-wave coupling effect increases the transmittance of a capacitive coupler as the spacing increases while it decreases that of an inductive coupler. By comparing the transmittances with different spacings between the tuning plate and the meshes, the effective coupling distances and the decay constants of evanescent-wave coupling effect can be decided. A model taking evanescent-waves into consideration is presented to explain the relationship between the effective refractive index and the evanescent-wave coupling effect. This model also explains some discrepancies between the conventional mesh theory and the measurements. The wide bandwidth feature of the metal-mesh evanescent-wave couplers is also shown. The coupling coefficient of a capacitive coupler can vary more than 30% over a 13% frequency range by adjusting the spacings less than $\lambda/40$.

Design principles are presented to reach maximum amplitude modulations considering the mesh parameters, resonant frequencies and the thickness of the tuning plates. In a capacitive coupler with the optimal mesh parameters, chang-

ing the silicon plate thickness from 1 mm to 3 mm to tune the resonant frequencies, the coupling coefficient at the operating frequency can be increased from 45% to 70% for a variation of spacing less than $\lambda/100$. The model and design principles presented at millimeter wavelengths, achieve good agreements with measurements, and provide useful information for designing a submillimeter-wave coupler.

An optical-controlled metal-mesh evanescent-wave coupler is also demonstrated. By using a laser diode to modulate the effective dielectric constant with the existence of the evanescent-wave coupling effect, a maximum modulation of 13% is achieved at 56.5 GHz. To compare, the modulation is only 0.6% without the evanescent-wave coupling effect using the same power of light illumination.

4.10 FUTURE WORK

The preliminary works on optical-controlled metal-mesh evanescent-wave couplers show promising signs to develop efficient, low-loss amplitude modulators at millimeter and submillimeter wavelengths using low optical-injection powers. The works continue in two directions: developing a submillimeter-wave metal-mesh evanescent-wave coupler to operate at above 300 GHz and developing an efficient means of controlling optical injections. As mentioned in Chapter 2, the impedance tuning for the THz frequency multipliers is essential to reach high efficiency and high output power. However, due to the small wavelengths, the use of mechanical tuning elements with two quarter-wavelength slabs becomes difficult and less flexible. Using an optical-controlled evanescent-wave coupler to tune the impedances and switch the beams may become an option.

Understanding the dynamic behaviors of the free carriers introduced in silicon by the light illumination is also important to develop an efficient coupler with higher modulation speeds. The changes of the effective dielectric constant of silicon is caused by the temporal and the spatial perturbations of the free-carrier density and the changes include not only the real parts, but also the imaginary

parts of the dielectric constants. The temporal and spatial distributions of the free-carrier density, $n(z,t)$, can be approximated by the continuity equation (in one-dimension form): [22]

$$\frac{\partial n(z,t)}{\partial t} - D\frac{\partial^2 n(z,t)}{\partial z^2} = G(z,t) - R(z,t) \tag{4.6}$$

where z is the direction perpendicular to the surface; D is the coefficient of ambipolar diffusion; and $G(z,t)$ and $R(z,t)$ are the generation and recombination rates of the free carriers, respectively. According to Drude's theory [21], the complex dielectric constant, ϵ, can be expressed as

$$\epsilon = \epsilon_L - \frac{\omega_{p,e}^2\,\tau_e^2}{(1+\omega_0^2\,\tau_e^2)}\cdot\left[1-j\frac{1}{\omega_0\,\tau_e}\right] - \frac{\omega_{p,h}^2\,\tau_h^2}{(1+\omega_0^2\,\tau_h^2)}\cdot\left[1-j\frac{1}{\omega_0\,\tau_h}\right] \tag{4.7}$$

and

$$\omega_{p,e}^2 = \frac{n_e\,q^2}{m_e^*\,\epsilon_0}\,, \qquad \omega_{p,h}^2 = \frac{n_h\,q^2}{m_h^*\,\epsilon_0} \tag{4.8}$$

where ϵ_L is the complex dielectric constant of the silicon; ω_0 is the angular frequency of the propagating wave; the indices e and h indicate the free-carriers of electrons and holes, respectively; the τ_e and τ_h are the collision times; the $\omega_{p,e}$ and $\omega_{p,h}$ are the plasma angular frequencies; the n_e and n_h are the densities; the m_e^* and m_h^* are the effective masses; q is the elementary charge; and ϵ_0 is the vacuum dielectric constant. As one can imagine, the simulations and designs become more complicated when the complex dielectric constants are involved. The calculations using the method of moments and the transmission models need to be re-examined and modified.

4.11 ACKNOWLEDGEMENTS

REFERENCES

[1] V. Balakhanov, "Properties of a Fabry-Perot Interferometer with Mirrors in the Form of a Backed Metal Grid," *So. Phys. Doklady*, Vol. 10, pp. 788-790, 1966.

[2] Lance B. Sjogren, "A Multi-Function Millimeter-Wave Schottky Diode Array Electronic Beam Controller," *Ph.D. Dissertation*, University of California, Los Angeles, 1992.

[3] L.B. Sjogren, H.L. Liu, F. Wang, T. Liu, X.H. Qin, W. Wu, E. Chung, C.W. Domier, N.C. Luhmann, "A Monolithic Diode Array Millimeter-Wave Beam Transmittance Controller," *IEEE Trans. on Microwave Theory and Techniques*, Vol. MTT-41, No. 10, pp. 1782-1790, Oct. 1993.

[4] Xiaohui Qin, "Monolithic Millimeter Wave Beam Control Array," *Ph.D. Dissertation*, University of California, Los Angeles, 1995.

[5] X.H. Qin, W.M. Zhang, C.W. Domier, N.C. Luhmann, Jr., W. Berk, S. Duncan and D.W. Tu, "Monolithic Millimeter-Wave Beam Control Array," *Digest of IEEE Microwave Theory and Techniques Symposium*, MTT-S95, WE3F-F4, pp. 1669-1672, 1995.

[6] M.P. De Lisio, S.W. Duncan, D.-W. Tu, C.-M. Liu, A. Moussessian, J.J. Rosenberg and D.B. Rutledge, "Modelling and Performance of a 100-Element pHEMT Grid Amplifier," submitted to *IEEE Trans. on Microwave Theory and Techniques*.

[7] Z. Agronovich, V. Marchenko, and V. Shestopalov, "The Diffraction of Electromagnetic Waves from Plane Metallic Lattices," *Sov. Phys. Tech. Phys.*, Vol. 7, pp. 277-286, 1962.

[8] R.F. Harrington, *Field Computation by Moment Methods*, Robert E. Krieger Publishing Company, Malabar, Florida, original ed. 1968, reprinted 1982.

[9] R.L. Eisenhart and P.J. Khan, "Theoretical and Experimental Analysis of a Waveguide Mounting Structure," *IEEE Trans. Microwave Theory Tech.*, MTT-19, pp. 706-719, August 1971.

[10] R.M. Weikle II, "Quasi-Optical Planar Grids for Microwave and Millimeter-Wave Power Combining," *Ph.D. Dissertation*, California Institute of Technology, 1992.

[11] R. Compton, L. Whitbourn, and R. McPhedran, "Strip Grating at a Dielectric Interface and Application of Babinet's Principle," *Applied Optics*, Vol. 23, pp. 3236-3242, 1984.

[12] M.S. Durschlag and T.A. De Temple, "Far-IR Optical Properties of Freestanding and Dielectrically Backed Metal Meshes," *Applied Optics*, Vol. 20, pp. 1245-1253, 1981.

[13] R. Ulrich, "Far-Infrared Properties of Metallic Mesh and its Complementary Structure," *Infrared Physics*, Vol. 7, pp. 37-55, 1967.

[14] D.H. Dawes, R.C. McPhedran, and L.B. Whitbourn, "Thin Capacitive Meshes on a Dielectric Boundary: Theory and Experiment," *Applied Optics*, Vol. 28, pp. 3498-3510, 1989.

[15] I.P Kaminow, "Optical Waveguide Modulators," *IEEE Trans. Microwave Theory Tech.,* MTT-23, pp. 57–70, Jan. 1975.

[16] C.H Lee, *Picosecond Optoelectronic Devices,* Academic Press Inc., 1984

[17] C.H. Lee, P.S. Mak and A.P. De Fonzo, "Optical Control of Millimeter-Wave Propagation in Dielectric Waveguides," *IEEE Journal of Quantum Electronics,* Vol. QE-16, No. 3, pp. 277-288, March 1980.

[18] V.A. Manasson, L.S. Sadovnik, A. Moussessian and D.B. Rutledge, "Millimeter Wave Diffraction by a Photo-Induced Plasma Grating," *IEEE Trans. Microwave Theory Tech.,* MTT-43, No. 9, Sept. 1995.

[19] H. Alius and G. Dodel, "Far-Infrared Modulation Techniques Based on Optical Excitation of Semiconductors," *Infrared Physics,* Vol. 35, No. 1, pp. 73-78, Feb. 1994.

[20] H. Alius and G. Dodel, "Amplitude-Modulation, Phase-Modulation, and Frequency-Modulation, of Far-Infrared Radiation by Optical-Excitation of Silicon," *Infrared Physics,* Vol. 32, No. 1, pp. 1-11, 1991.

[21] T. Vogel, G. Dodel, E. Holzhauer, H. Salzmann and A. Theurer, "High-Speed Switching of Far-Infrared Radiation by Photoionization in a Semiconductor," *Applied Optics,* Vol. 31, No. 3, pp. 329-337, 20 Jan. 1992.

[22] S.M. Sze, "Physics of Semiconductor Devices," John Wiley & Sons, Inc., 2nd Ed., 1981.